

*Development of omniphobic and anti-icing coatings
as supported nanomaterials and their
implementation as functional layers in active de-
icing devices*

Doctoral Thesis presented by
Laura Montes Montañez

Supervised by
Dr. M.^a Carmen López Santos
Dr. Víctor J. Rico Gavira

Seville, 2025

Institute of Materials Science of Seville
Spanish National Research Council – University of Seville
Nanotechnology on Surfaces and Plasma (nanoOnSurf)





Ph.D. Thesis

Development of omniphobic and anti-icing coatings as supported nanomaterials and their implementation as functional layers in active de-icing devices

Institute of Materials Science of Seville

(Spanish National Research Council – University of Seville)

A dissertation submitted for the degree of
Philosophiæ Doctor (Ph.D.) in the University of Seville.

Seville, January of 2025

Sgd. Laura Montes Montañez

○ Supervisors:

Dra. M^a Carmen López Santos
University of Seville Tenured Professor
Department of Applied Physics I
Higher Polytechnic School
Institute of Materials Science of Seville

Dr. Víctor J. Rico Gavira
CSIC Tenured Scientist
Institute of Materials Science of Seville

○ Tutor:

Dr. Joaquín Ramírez Rico
University of Seville Professor
Faculty of Physics
Department of Condensed Matter
Physics
Institute of Materials Science of Seville

This doctoral thesis has been developed at the Institute of Materials Science of Seville (CSIC-University of Seville) in the framework of the European project SOUNDofICE, funded by the European Commission through the H2020-FETOPEN-2018-2019-2020, led by Dra. Ana Isabel Borrás Martos and Prof. Agustín R. González-Elipe. The author expresses gratitude due to its hiring as a predoctoral student to work in the doctoral thesis. Also, to thank the Ministry of Science, Innovation, and Universities for enabling my international stay at Institut National des Sciences Appliquées INSA in Lyon (France) through the iMOVE grant and the support of the CSIC Intramural Project Ref. 202160E002, which has contributed to the accomplishment of this thesis.



**SOUNDofICE is a Project funded by the
European Commission through the H2020-
FETOPEN-2018-2019- 2020-01 call**

GA n^o: 899352



<https://fetopen-soundofice.icms.us-csic.es>

“Cuando termina la acción y miramos atrás lo entendemos todo más o menos. Una cosa es cierta, antes del ataque de Doolittle, Estados Unidos sólo conocía la derrota, después llegó la esperanza. Japón se dio cuenta de que podía perder y empezó a retirarse. Estados Unidos se dio cuenta de que podía ganar y avanzó. Fue una guerra que cambió el mundo. Dorie Miller fue el primer negro americano condecorado con la cruz naval pero no sería el último. Entró en la hermandad de los héroes. Para nosotros la II Guerra Mundial empezó en Pearl Harbor y 1117 hombres yacen aún en la tumba del acorazado Arizona. Estados Unidos sufrió, pero se hizo más fuerte, no fue inevitable, los tiempos pusieron a prueba nuestras almas, y fue una prueba que superamos”.

“Tierra de libertad, hogar de valientes”.

7 de Diciembre de 1941, Pearl Harbor (Hawai)

Acknowledgments

Creo que cada una de las personas que está leyendo estas líneas, sabe a cuántas personas tengo que agradecer el poder haber llegado hasta aquí. Me gustaría empezar estos agradecimientos como empezó mi historia dentro del mundo de la investigación, acordándome de Víctor López y Marcela. Gracias por darme la oportunidad y confiar en mí.

Seguidamente dar la enhorabuena a mis directores de tesis por guiarme como lo han hecho, por ayudarme no solo en lo profesional y sobre todo por hacerme crecer como alguien que se quiere dedicar a este mundo. Solo nosotros sabemos lo que nos hemos enseñado el uno al otro. Víctor, gracias por pararme cuando he ido con carrerilla y por hacer más amenos todos los viajes que hemos compartido, sin ti, no hubiese sido igual. Carmen, ¡ay, Carmen!, que relación de madre e hija regañonas más bonita hemos formado en este tiempo. GRACIAS por todo lo que has hecho por mí, por escucharme, por guiarme y sobre todo por saber dirigirme y estar cuando hay que estar. Os voy a echar de menos.

Dentro de esas puertas de color verde que dan luz a la primera planta del Cic-Cartuja 2, no podría olvidarme de todo lo que me has enseñado, Juanra. Gracias por tu paciencia, tu esfuerzo y sobre todo gracias por ser quien eres. No sé qué haríamos sin ti, eres alguien super importante para este grupo. Vanda, que pena que hayamos coincidido y conectado de esta manera en la parte final de esta aventura, pero qué alegría saber que cuento con alguien como tú para siempre. Gracias por cuidarme y escucharme.

Gracias al resto de investigadores seniors: Ángel, Curro, Jorge Gil, Manuel Oliva, Juan Pedro Espinós, Alberto Palmero... porque estoy segura que de una manera u otra habéis contribuido científicamente o dándome apoyo para que esta tesis culminase de la mejor manera. Paula, para mí eres una persona super importante y que, aunque no siempre estemos en contacto, apareces cuando más lo necesito, eres increíble. Agradecer también a todos los técnicos de los servicios del Instituto de Ciencia de Materiales por su gran labor y el gran trabajo que desempeñan para que nuestro trabajo pueda seguir adelante.

Agustín, qué decirte, ¡Cuánto tengo que agradecerte! Siempre pienso en lo afortunada que he sido y espero poder seguir siendo por tener cerca a alguien como tú. Gracias por ser como ese profesor particular experto que, con solo cruzar el pasillo, te soluciona tus dudas e inquietudes. Ha sido un verdadero placer poder aprender de ti y de tu ciencia.

I would like to express my heartfelt gratitude to Prof. Karine Masenelli-Varlot, Prof. Philippe Steyer, Prof. Lucian Roiban and Dr. Victor Trillaud, for giving me the opportunity to undertake a three-month stay at Institut National des Science Appliquées de Lyon (INSA) (Lyon, France), as well as for offering their help and scientific guidance working on new characterization techniques in the “microscopy world”.

Ahora, es el turno de agradecer a mi mini-familia científica, donde mucho de ellos hoy en día son mis amigos y sin ellos, nada de esto hubiese sido como ha sido. Javi, no tengo palabras para agradecerte todo lo que me has ayudado y me has enseñado, gracias por estar siempre. Xabi, fuimos compañeros en el máster y desde ahí supe que serías una pieza importante en este grupo, sin ti y sin tu ayuda, nada sería igual. Fernando, mi Fer, nunca he conocido a alguien tan bueno, tan noble y constante como tú. Gracias por preocuparte por mí y ser siempre tan servicial y AMIGO. Lidia, nuestra madre en la sombra y consejera, gracias por tener siempre las palabras adecuadas en cada momento y por sostener el carro cuando a veces todos hemos tenido tantos “Dramas”. Jose, seguro que cuando estés leyendo estas líneas ya la sonrisa y la alegría que te caracteriza ha vuelto a tu vida, gracias por aportarme y ayudarme. Nerea, gracias por venir al grupo a poner un poco de calma y de orden y a facilitarnos las cosas, no sé qué hubiese hecho sin tu ayuda constante e inmediata.

Juani, mi alegría diaria desde que entró a este grupo de investigación, no sabes la de días en los que solo venía para poder darte un abrazo y que me animases, te voy a echar mucho de menos. Triana, pocas palabras se necesitan para agradecerte el haber formado parte de este proceso. Gloria, todo el mundo necesita una Gloria en su vida, una mujer hecha y derecha que solo con abrir la boca deja las cosas en su sitio, gracias por ser así. Hiedra, querida Hiedra... ojalá todo lo bonito que pueda darte este mundo lo recibas. Eres inocencia, serenidad y la amiga que sabe entenderme y frenarme cuando lo necesito. No sabes lo

importante que eres para mí. Jorge Budagosky, nuestra mente calmada y consejera, gracias por todo lo que me has aportado en esta etapa. Darío, seguro que estás buscando tu nombre en estas líneas y has pensado que me he olvidado de ti, pero eso es imposible. Gracias por tu manera especial de enseñarme día a día que puedes con todo lo que se te ponga por delante y que a veces hay que ver el lado positivo de las cosas para poder seguir avanzando, eres una persona muy especial para mí. Melania, mi Mel, gracias por todas esas mañanas desayunando con prisas y escuchándome. Tú también formas parte de esto.

“Amigo”, te mereces un solo párrafo para ti, por ser tan especial. Jaime, nada de lo que está escrito en esta tesis estaría así sin que antes los dos hubiésemos escrito mil formulitas en las hojas de ese cuaderno, que solo encontrabas cuando Ana te lo pedía. Gracias por acompañarme en este viaje todo el tiempo a mi lado, por ser especial y buen compañero. Gracias por hacer que mis enfados repentinos solo se calmasen con escucharte decir dos frases seguidas. Si tuviese que trabajar otra vez en un proyecto europeo, estoy segura de que lo haría de nuevo contigo.

My dear SoundOffice, you could not be out of these lines of gratitude. Thank you for helping me grow both professionally and personally alongside the incredible team that defines you, like the Consortium. Together, we strive every day to make the world a better place with our scientific ideas and tireless effort. Thank you to the Consortium members for your advices, contributions, and for making this project a rewarding experience filled with great moments. Special thanks to Julio, Paloma and Francisco for your support and for teaching me so much about ice and aviation. Thank you to TECPAR team for the laughter and INMA members for my warm welcome to Zaragoza.

A mis compañeros de carrera y máster: Estrella, Natalia, Vito, Aurora, Aitana, Alfonso, Ángel, Rafa. Tantas horas de biblioteca y de noches de estudio, esto también va para vosotros.

A mi pequeña familia española que Lyon me regaló durante mi estancia predoctoral, gracias por todos los momentos y por hacerme aprender el poco francés que sé, de manera acelerada. Hemos creado un grupo tan bonito que sé que será para siempre, aunque estemos cada uno en una parte del mundo. “Merci beaucoup”.

A mis amigas Yoli, Virginia, Dessi, María, Ana Prados, Ana Morgado, Rocio Chacón por apoyarme y siempre interesarse por mis viajes y resultados. Gracias Carlos, por formar parte de mi vida y apoyarme siempre.

Gracias a mis padres y a mi hermana, por ser los brazos que siempre están abiertos para poder volver en el momento que algo me da miedo o va mal. Gracias por apoyarme en las mejores y peores decisiones sin juzgarme y sobre todo gracias por entender qué es una superficie anti-hielo por plasma y vacío sin ni siquiera saber lo que es plasma. Gracias una y otra vez. A mi familia de cuatro patas, Nilo y Lia, mis mejores compañeros y los que siempre están, ojalá supieseis lo que significáis para mí.

Fran, sé de sobra que estas super orgulloso de donde he llegado, eras una de esas personas que siempre veían más de mi rendimiento que yo misma, y que siempre me has animado a seguir haciendo lo que me gustaba, aunque me costase esfuerzo. Eras, eres y siempre serás una persona clave en mi vida.

Andrés, has aparecido en la etapa más complicada donde estoy segura de que nunca se te olvidará cómo es soportar a alguien en el periodo de escritura de una tesis doctoral. Me has enseñado poco por el breve tiempo que llevo conociéndote, pero qué bonita la manera en la que me has apoyado en silencio solo con estar a mi lado.

Ana Borrás, sabía desde el primer día que te conocí, que serías la última persona en mis agradecimientos, y así será. Gracias Ana por ser mi refugio cuando lo he necesitado, por ser referente para mí y por conocerme tanto que solo con mirarme eres capaz de detectar lo que me pasa. Todas estas palabras son pocas para lo que siento cuando pienso para adentro qué significas para mí. Qué suerte he tenido de poder conocerte más allá de un "Conecta" o de una reunión de grupo. Gracias por ser mi "ángel de la guarda" en este camino y en otros muchos que se me han planteado en mi vida. Para mí, junto con Carmen, sois ejemplo de personas luchadoras, constantes, incansables, ejemplo de madres y de personas protectoras que siempre que puedan estarán para salvar a los suyos. Ojalá la vida me ponga a muchas personas como vosotras, porque vaya suerte. Gracias por estar siempre al pie del cañón.

Finalmente, espero que cuando leáis estas palabras, os venga a la mente todo lo que me voy a acordar de cada uno de vosotros en mi siguiente etapa. Os voy a echar mucho de menos. Tengo la suerte de poder decir que he estado y estoy rodeada de personas maravillosas que me han permitido crecer como persona y como profesional en este mundo.

GRACIAS Y MIL VECES GRACIAS

OUTLINE

Abstract	v
Contributions to the scientific community	vii
Chapter 1. Introduction	2
1.1. General overview about surfaces	4
1.1.1. Wetting control of the surface	6
1.1.2. Design of surfaces	11
1.2. Wetting description	16
1.3. Strategies for liquid-repellent surfaces at room conditions	20
1.3.1 Superhydrophobic surfaces	20
1.3.2 Slippery Liquid Infused Porous Surfaces	23
1.3.3 Other strategies for liquid-repellent surfaces	24
1.4. Icephobicity	26
1.4.1 From wetting to icing phenomena.....	26
1.4.2 General description of icephobic surfaces	31
1.4.3 Water repellence.....	37
1.4.4 Freezing delay and ice accretion	39
1.4.5 Ice adhesion.....	40
1.4.6 Durability of icephobic surfaces	43
1.5. Challenges for the design of repellent surfaces	43
1.6. Objectives and outline of the thesis	48
Bibliography.....	52
Chapter 2. Materials and methods	66
2.1. Introduction.....	67
2.2. Methodology.....	67
2.2.1. Vacuum deposition technology	70
2.2.2. Plasma assisted methodologies	75
2.2.3. Other methodologies for surface modification	82
2.3. Materials used for the fabrication of wetting controlled surfaces.....	86
2.3.1. Substrates	86
2.3.2. Precursors for surface modification and thin films	87
2.4. Characterization of surfaces	89

2.4.1. Physicochemical and morphological analysis	89
2.4.2. Analysis of the wetting and repellent properties.....	91
2.4.3. Characterization of the anti-icing behaviour	95
2.4.4. Stability and durability essays.....	101
Bibliography	105
Chapter 3. Wetting control on porous substrates	110
3.1. Introduction.....	112
3.2. Experimental section	115
3.3. Results and discussion	119
3.4 Conclusions	139
Bibliography	141
Chapter 4. Wetting control of low fluorinated hierarchical SS surfaces	146
4.1. Introduction.....	148
4.2. Experimental section	152
4.3. Results and discussion	156
4.4. Conclusions	184
Bibliography	186
Chapter 5. Superhydrophobic and anti-icing glass surfaces	194
5.1. Introduction.....	196
5.2. Experimental section	197
5.3. Results and discussion	201
5.4. Conclusions	229
Bibliography	231
Chapter 6. Permanent Cassie-Baxter scalable hierarchical surfaces	236
6.1. Introduction.....	238
6.2. Experimental section	242
6.3. Results and discussion	246
6.4. Conclusions	278
Bibliography	281

Appendix A. Water condensation experiments by STEM and ETEM.....	285
Chapter 7. General conclusions and future perspectives	289

ABSTRACT

Given the increasing environmental challenges the society is facing, the interaction of surfaces with the environment through their wettability can be one of the broad fields of studying aiming to find effective solutions to a general protection goal and, particularly ice accumulation.

This thesis introduces a novel proposal for the development of repellent surfaces resistant to severe environmental conditions by means of scalable, clean and efficient vacuum and plasma assisted technologies. Processing of hybrid hierarchical surfaces is supported by mild laser treatments and reasonably ecological surface modification approaches. The fabrication of the developed surfaces is fully compatible with a multitude of functional materials and complex geometries, from porous flexible membranes to aeronautical profiles passing for stainless steel and glass.

The main challenge of this work is to understand the key factors affecting the control of wetting of surfaces considering their interaction with external agents and the intervention of climatic changes to design and develop surfaces that combine self-cleaning, anti-fouling and anti-icing responses of permanent character when applied under real exposure conditions including liquids, ice, solid particles and biological agents. Moreover, functional hybrid hierarchical surfaces must ensure durability and stability under thermal cycling, UV illumination, rain erosion, and strong wind currents.

Additionally, this research explores the integration of the hybrid hierarchical surfaces as functional protective elements in active de-icing devices offering a new approach to address effectively ice prevention and removal ensuring stability while facilitating efficient heat transfer. This approach provides a promising solution for anti-icing technologies in industrial and environmental applications.

Contributions to the Scientific Community

Articles published in peer review international journals resulting from this Ph.D. Thesis are:

1. Plasma-Assisted Deposition of TiO₂ 3D Nanomembranes: Selective wetting, Superomniphobicity, and Self-Cleaning.

Laura Montes, Jose M. Román, Xabier García-Casas, Javier Castillo-Seoane, Juan R. Sánchez-Valencia, Ángel Barranco, Carmen López-Santos* and Ana Borrás*. ***Advanced Materials Interfaces***. **2021**, 8 (21), 2170122. DOI: 10.1002/admi.202170122.

2. A Holistic Solution to Icing by Acoustic Waves: De-icing, Active Anti-icing, Sensing with Piezoelectric Crystals, and Synergy with Thin Film Passive Anti-Icing Solutions.

Jaime del Moral, Laura Montes, Victor Joaquin Rico-Gavira, Carmen López-Santos, Stefan Jacob, Manuel Oliva-Ramirez, Jorge Gil-Rostra, Armaghan Fakhfour, Shilpi Pandey, Miguel Gonzalez del Val, Julio Mora, Paloma García-Gallego, Pablo Francisco Ibáñez-Ibañez, Miguel Ángel Rodríguez-Valverde, Andreas Winkler, Ana Borrás* and Agustín Rodríguez González-Elipse*. ***Advanced Functional Materials***. **2023**, 33, 2209421. DOI: 10.1002/adfm.202209421.

3. Exalted Dual-Scale Surface Roughening in Laser Ablated Aluminum Capped with a Transparent Thin Film: Wetting and Anti-icing Behavior.

Ismail Ghemras, Laura Montes, Carmen Lopez-Santos*, Agustín R. González-Elipse and Victor Rico*. ***Applied Surface Science***. **2023**, 630, 157357. DOI: 10.1016/j.apsusc.2023.157357.

4. Long-lasting Fluorinated Stainless-Steel Hierarchical Surfaces for Omniphobic, Anti-fouling and Anti-Icing Applications.

Laura Montes, Victor Rico*, Fernando Núñez-Galvez, M. Ángeles Arenas, Ana Conde del Campo, Victor Lopez-Flores, Juan Pedro Espinós, Ana Borrás, Agustín R. González-Elipe and Carmen López-Santos*. ***Surfaces and Interfaces***. **2024**, 46, 104167. DOI: 10.1016/j.surfin.2024.104167.

5. Superhydrophobic, Anti-Fogging and Anti-Icing Transparent Glass Surfaces Prepared by Laser Patterning and Fluorination.

Laura Montes, Fernando Núñez-Gálvez, Melania Sánchez-Villa, Luis A. Angurel, Raul Kanter, Niklas Kandelin, Heli Koivuluoto, German F. de la Fuente, Victor Trillaud, Philippe Steyer, Karine Masenelli-Varlot, Ana Borrás, Agustin R. González-Elipe, Carmen López-Santos* and Victor Rico*. **Manuscript under preparation.**

6. Anti-icing and Omniphobic Performance of Scalable Hierarchical Surfaces with Permanent Cassie-Baxter Wettability.

Laura Montes, Victor Rico, Francisco Carreño, Julio Mora, Paloma García-Gallego, Agustin R. González-Elipe, Ana Borrás* and Carmen López-Santos*. **Manuscript under preparation.**

Other articles published in international journals closely related to this Ph.D. Thesis are listed below:

7. Setting a Comprehensive Strategy to Face the Runback Icing Phenomena.

Julio Mora*, Paloma García-Gallego, Francisco Carreño, Miguel González, Marcos Gutiérrez, Laura Montes, Victor Rico Gavira, Carmen López-Santos, Adrián Vicente, Pedro Rivero, Rafael Rodríguez, Silvia Larumbe, Carolina Acosta, Pablo Ibáñez-Ibáñez, Alessandro Corozzi, Mariarosa Raimondo, Rafal Kozera, Bartłomiej Przybyszewski, Agustín R González-Elipe, Ana Borrás, Francisco Redondo, and Alina Agüero. ***Surfaces & Coatings Technology***. **2023**, 465, 129585. DOI: 10.1016/j.surfcoat.2023.129585.

8. Could Superhydrophobic Surfaces be a Realistic Solution for Running-Wet Areas?.

Julio Mora, Paloma García-Gallego, Francisco Carreño, [Laura Montes](#), Carmen López-Santos, Victor Rico, Ana Borrás, Francisco Redondo, Agustín R. González-Elife and Alina Agüero. **SAE Technical Papers. 2023**, DOI: 10.4271/2023-01-1446.

9. Mechanisms of De-Icing by Surface Rayleigh and Plate Lamb Acoustic Waves.

Shilpi Pandey, Jaime del Moral, Stefan Jacob, [Laura Montes](#), Jorge Gil-Rostra, Alejandro Frechilla, Atefeh Karimzadeh, Victor J. Rico, Raul Kantar, Niklas Kandelin, Carmen Lopez Santos, Heli Koivuluoto, Luis Angurel, Andreas Winkler, Ana Borrás, Agustin R. Gonzalez Elife.

Advanced Engineering Materials, 2024, 2401820.

DOI: 10.1002/adem.202401820.

10. Hybrid Icing Protection Strategy with Surface Acoustic Waves propagating on Icephobic and Highly Stable Bilayer Surfaces.

Jaime del Moral, Luke J. Haworth, [Laura Montes](#), Juan R. Sánchez-Valencia, Angel Barranco, Victor Rico, Triana Czermak, Paloma Garcia-Gallego, Julio Mora, Carmen López-Santos, Andreas Winkler, Ana Borrás*, Agustin R. González-Elife and Yongqing Fu*. **Manuscript under preparation.**



A mis padres, a mi hermana

A mis abuelos

***“Si he visto más lejos, es porque estaba sentado sobre
los hombros de gigantes”***

Isaac Newton



Image by IA software

**“Nothing in life is to be feared, it is only to be understood.
Now is the time to understand more, so that we may fear less”**

(Marie Curie)

1

Introduction

Current scientific and technological challenges are directly linked to the consequences of climate change (high-impact rains, extreme frosts, and dry warming seasons), associated with global warming, such as increased environmental pollution and the proliferation of microbial agents. These issues arise from everyday interactions, often unnoticed, but just as important. This thesis focuses on finding solutions to routine problems revolving around the interaction between applied materials' surfaces and environmental factors like rain, airborne particles, biofouling, or frost.

This research demonstrates how surface engineering seeks to remedy the negative impact of severe work environments, which have significant implications for sectors such as infrastructure and transport, particularly in aeronautics, energy sector (wind turbines, power plants), design and conservation of cultural patrimony and decontamination process like water and filtration among others. Surface engineering can control the surface properties that govern the response to interactions with the environment, where we particularly highlight surface wetting. Wetting or wettability, as the solid surface capacity to get wet by a liquid, from the intrinsic perspective of the material, can be addressed through nanotechnology. Nanotechnology is defined as the design, characterization, production, and application of specific structures, devices, and systems with controlled shape and size at the nanometric scale ($\sim 10^{-9}$ m), enabling the exploration of novel properties that make it different from the bulk material. Some of the tools that nanotechnology provides include the ability to control the morphology, structure, and chemical composition as well as functional attributes of materials at the nanometric scale. Therefore, in this thesis, nanotechnology and surface engineering will be used to control the responses to environmental changes through the wetting of multifunctional surfaces.

For the development of robust functional materials, the techniques employed in this work offer significant advantages over traditional methods: top-down (laser) and bottom-up (vacuum and plasma) approaches have been used to enhance the performance of surfaces exposed to environmental interactions. All the resources employed are compatible with bulk properties and complex geometries, environmentally friendly, and scalable.

1.1 General overview about surfaces

Surface defines the boundary between a material and the external environment. Consequently, the first interaction that a material establishes with its surroundings occurs through its surface. At the atomic level, surface atoms experience a distinct environment compared to those within the bulk. While atoms in the interior of a solid interact with neighbouring atoms in all directions, surface atoms lack neighbouring atoms in at least one direction, leading to an excess of energy. This surplus energy of surface atoms relative to the bulk ones is referred to as Surface Free Energy (SFE) or surface tension of solids. Both terms are related to the interactions at a solid's surface, but tension of solids deals more with the mechanical forces on the surfaces, while surface free energy focuses on the energy characteristics and interfacial interactions of the surface¹. Surfaces play a pivotal role in our daily lives because the majority of physical and chemical phenomena occur on them. Common processes such as corrosion, adhesion, wettability, friction, and wear all take place at the surface level^{2,3}. Particularly, surfaces are highly prone to contamination when exposed to the environment, which is a significant concern in materials science due to the critical role that surfaces play in determining material properties such as aesthetics and functionality.

Generally, materials are chosen based on their bulk properties, with a view toward their final application. For example, in a biocompatible material^{4,5}, the surface must be prepared so that the biological environment does not reject it, or in a catalytic reaction^{6,7}, the importance of surface properties is crucial to prevent interference with its conversion efficiency. Other examples may relate to mechanical devices where surface properties such as hardness and passivation are expected. Moreover, for the integration of multilayers, the interface is crucial to relax internal stresses and to compatibilize the physicochemical structure.

However, the surface properties often fall short of the demands on the end application. Surface modification offers a valuable approach to protect, or enhance the adhesion capability or the aesthetic of a material, while also holding great potential to integrate new functionalities without compromising the properties inherent to its nature. Today, surface engineering is playing a key role in the development of new technologies across the sectors, from energy conversions and storage⁸ to semiconductors⁹ and biomedical implants^{10,11},

passing through the control of friction, adhesion, corrosion resistance, thermal barrier, decorative, optical and electrical responses as well as chemical textile and food industries^{12,13}. Surface modification techniques are essential in optimizing materials for specific applications for those who would not initially be good candidates. Today, the development and enhancement of surfaces are guided by design strategies to achieve such desired properties together with the improvement of the durability. Surface design can involve adjusting the physico-chemical properties as well as morphological aspects like topography, and roughness, introducing micro- and nano-scale features. From the point of view of surface modification, it is possible to be able to enhance a functional performance through adjusting their chemical and physical properties by means of these common proposals:

- **Coatings:** A surface can be coated with protective or functional layers to improve specific properties. For instance, anti-corrosive coatings protect against environmental degradation, catalytic coatings are used in chemical reactors or environmental applications¹⁴ or biocompatible coatings are required in implants, biosensors, and surgical devices¹⁵.
- **Surface treatment:** Surface processing encompasses a variety of techniques aimed at enhancing or modifying external material properties, such as cleaning, etching, electric charge generation, and chemical functionalizations, which are achieved through methods ranging from solvents to the application of electromagnetic fields¹⁴. Examples include anodizing and electroplating, which create protective or decorative oxide layers on metals to improve hardness, corrosion resistance, and aesthetic appeal, commonly used in aerospace and architectural applications to protect aluminum¹⁶, and laser modification, which generate surface textures even involving chemical changes to improve wear resistance, hardness, and surface roughness, widely used in industries like aerospace, automotive, and medical devices¹⁷.

Surface modifications today are increasingly sophisticated, combining the precise design of surface geometries with advanced treatments that cater to the specific demands of the application. The integration of surface engineering with fields such as nanotechnology, materials science, and even the current artificial

intelligence are driving innovation in areas ranging from electronics to healthcare¹⁸.

Particularly, this thesis is focused on the advances of surface engineering to control the wetting due to its versatile and transversal utility across various industrial exploitations. The ability to manage how liquids interact with surfaces (either by repelling or promoting spreading) has significant implications for improving surface performance, multifunctionality and durability in applications ranging from self-cleaning materials to biomedical devices¹⁵.

1.1.1 Motivation: wetting control of the surface

Wetting is a critical concept in various fields such as coatings, adhesives, and surface treatments, where controlling the interaction between liquids and solids is essential. Wetting refers to the ability of a liquid to maintain contact with a solid surface, resulting from the interplay between adhesive forces (between the liquid and the solid) and cohesive forces (within the liquid). The degree of wetting is commonly characterized by contact angle measurements, which is the angle formed between a liquid's droplet deposited on the solid surface and the solid surface at the point of triple phase contact (solid-liquid-vapor)¹⁹. The most abundant liquid in nature is water, both as a substance itself, and as a primary component of other substances. So, water is quite interesting designing surfaces to be hydrophobic (water-repellent) or hydrophilic (water-attractive). The surface can be stated as wet if the contact angle value of a water droplet deposited on it goes from 0° to 90° , as a hydrophilic behavior. On the contrast, a hydrophobic surface presents a contact angle value higher than 90° and the contact area between the surface and the water droplet is reduced at the equilibrium. Surfaces having a contact angle value smaller than 20° are considered superhydrophilic and surfaces having a contact angle greater than 150° are called superhydrophobic. In this case, the drop seems to be resting almost spherically on the surface, as illustrated **Figure 1**. Achieving hydrophobic and hydrophilic surfaces is essential across multiple applications due to other properties derived from wetting that they offer: superhydrophobic surfaces, with high contact angles of a liquid droplet deposited on the surface, are valuable for self-cleaning, corrosion resistance, anti-icing, oil-water separation, and reducing drag in fluids^{20,21,22,23}. Conversely, hydrophilic surfaces, with low

contact angles, promote enhanced adhesion, heat transfer, and are critical in biomedical applications, anti-fogging, and water collection²⁴.

Wetting behaviour can be controlled through two main surface aspects²⁵:

- Surface Topography: Modifying the physical structure of a surface, such as creating micro- or nano-scale roughness, can significantly alter wetting properties. For example, rough surfaces can amplify hydrophobicity, as seen in the "lotus effect" shown in Figure 1, where water droplets bead up and easily roll off, or can enhance hydrophilicity, allowing liquids to spread more uniformly²⁶.
- Surface Chemistry: The chemical composition of a surface also plays a major role in wetting when compositions are chosen that are conducive to forming chemical bonds with water or contrary to this. Treatments or coatings can increase or decrease the surface free energy, influencing the balance between adhesive and cohesive forces. For instance, surfaces treated with low-surface-energy materials like fluoropolymers tend to become hydrophobic, while those high surface energy materials such as metals and glass become hydrophilic²⁷.

These properties allow surfaces to be optimized for specific functionalities, whether repelling or absorbing liquids, improving efficiency, safety, and performance in areas like manufacturing, healthcare, and environmental engineering. This is why one of the key motivations behind surface engineering is to develop versatile surfaces of controlled wetting for application in different environmental conditions.

Controlling the wetting of surfaces not only with polar liquids such as water but also considering interactions with other substances like organic liquids, aqueous suspensions, solid particles and biological agents is a significant current motivation due to its impact on performance, efficiency, and sustainability across various sectors such as aerospace, automotive, construction, biomedicine, food storage and electronics among others. For example, in healthcare, surfaces designed to resist bacterial adhesion are crucial for maintaining hygiene and preventing infections²⁸. The construction and textile industries also benefit from advanced surface treatments that improve impermeability and durability^{29,30}.

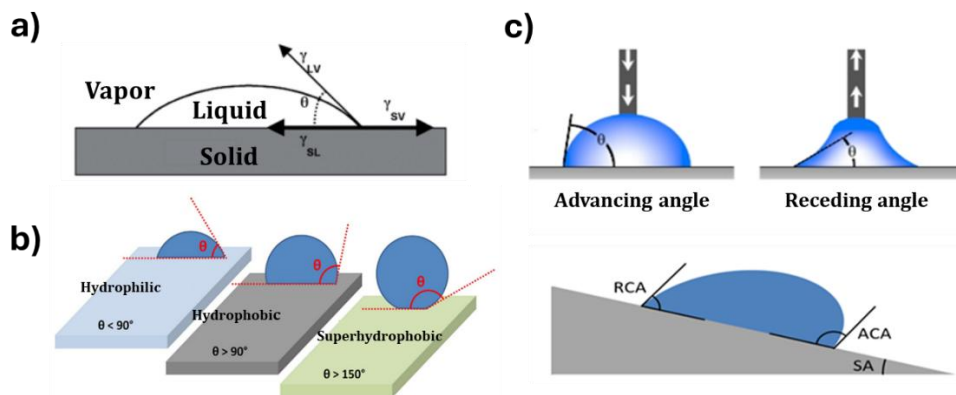


Figure 1. a) Definition of the ideal contact angle of a liquid droplet deposited on a solid surface in equilibrium with the gas phase³¹; b) Schematic representation of a water droplet on hydrophilic, hydrophobic and superhydrophobic surfaces³²; c) Representation of droplet on a tilted surface identifying the advancing(ACA) and receding(RCA) contact angles, as well as the sliding (SA) or rolling-off (RoA) angle³³.

Therefore, by addressing wetting control, i.e. the ability to manage liquid and solid interactions at the interface, the stability, durability and reliability of surfaces can enhance product performance, reduce maintenance costs, and contribute to more environmentally friendly practices. For example, the preservation of transparency in surfaces exposed to extreme weather conditions, such as windows or vehicle and sensor screens, is crucial for maintaining visibility and safety. The accumulation of ice and dust on the surfaces not only compromises aesthetics but also poses a significant risk by reducing the field of vision and increasing the likelihood of accidents³⁴. Thus, it is essential to develop protective technologies and materials but maintaining the optical properties. Research about anti-icing coatings, active heating systems, or preventive solutions by a proper surface design becomes a key area for improving safety and energy efficiency.

Since the surface is the material frontier with the environment, stability and durability can be compromised by aspects such as the contamination. Fluid contaminants, such as oil residues, blood, creams, and fingerprints, are a concern in industries like transportation, textiles and electronic systems^{35,36}. Omniphobic surfaces refer to those that can repel a wide range of liquids droplets, including both polar and non-polar fluids. Achieving omniphobicity, that is a high level of repellence characterized by a high slippery condition of liquids droplets on the surface, typically requires a combination of special

surface chemistry and topography. It is known that surface texturing where micro- and nano-structuration of the surface implies liquid repellence by trapping air in the porosity, allows a reduced contact area between the liquid droplet and the surface³⁷. Other essential features are related to low surface free energy of treated or coated surfaces based on fluorinated compounds to minimize the chemical bonding affinity^{38,39,40}. However, considering that the functionalization strategies currently employed must reduce the number of fluorinated compounds or be replaced by more environmentally friendly alternatives according to safety European regulations^{41,42}, this thesis proposes the minimization of their use while exploring new approaches based on their environmental stability to mitigate their ecological impact⁴³.

Another pursued surface property derived from wetting that affects stability and durability of a functional material when interacts with environmental agents is its self-cleaning capability. Self-cleaning refers to the ability of a surface to clean itself by repelling solid and liquid contaminants like dust or dirt particles, minimizing the need for external cleaning efforts. This property is achieved through specific surface modifications that exploits again both surface chemistry and topography. For example, self-cleaning capacity is interesting in many human-life setups such as glasses⁴⁴, finishing in domestic systems⁴⁵, and facades in building and architectural structures⁴⁶, solar panels⁴⁷, windshields⁴⁸, mirrors⁴⁹, external components of cars and airplanes, and medical devices⁵⁰. It means an option to reduce maintenance costs by minimizing the need for washing in high-rise buildings or hard-to-reach places while keeping surfaces clear and free of dirt, sterilize, and improving visibility, aesthetics, and energy efficiency.

Particularly, the accumulation of fouling agents (organic biological rests on liquid suspension) on surfaces has become a major issue with considerable economic consequences for both industry and society. These contaminants can negatively impact a wide range of applications by compromising safety, health, and performance, leading to increased maintenance costs⁵¹. Fouling can take various forms, including liquid contaminants, solid particles, or biological elements. Solid fouling including dust, chlorates, and salts, affects outdoor operational systems such as solar panels^{52,53} and heat exchangers⁵⁴. Biofouling, which involves the attachment of microorganisms, algae, or proteins has a detrimental impact on sectors such as biomaterials⁵⁵, food processing^{56,57},

marine vessels⁵⁸ and water distribution, and wastewater treatment plants⁵⁹. Therefore, the need arises to develop full repellent surfaces with anti-fouling capability. For that, omniphobic surfaces could be potential candidates referred to the ability of a surface to resist the accumulation of unwanted biological materials.

As a goal extension for surface engineering research, the ability to control the wetting behaviour at low temperatures directly affects new strategies to prevent the accumulation and formation of ice on surfaces. Icing is a widespread climatic issue in regions with sudden seasonal or daily changes and in those with long cold periods, where materials are subjected to abrupt temperature changes between day and night, or across different seasons with significant impact on human activities, services and infrastructure. In the field of aeronautics, ice formation on aircraft wings can lead to increased weight, aerodynamic disturbances (such as reduced lift) and the blockage of mechanical systems. These issues can cause flight delays and cancellations, making anti-icing and de-icing techniques critical in aviation efficiency and safety^{60,61}. Various methods, including chemical de-icing with glycols and sophisticated systems like pneumatic boots^{62,63} are employed to prevent or remove ice, particularly on the leading edges of wings. However, these methods can be costly, energy-intensive and environmentally harmful⁶⁴. Ice accumulation also affects other sectors such as power lines where it can result in power outages and costly damages, while roads experience asphalt fatigue due to freeze-thaw cycles^{62,64,65}. In the energy industry, icing can impair cooling systems⁶⁶ and significantly reduce the efficiency of renewable energy sources, such as wind turbines and solar panels^{67,68}. In addition, ice formation poses challenges for shipping near the poles and for all offshore platforms, compromising safety and productivity. Even in regions with milder climates, such as ski station resorts, freezing rain cause ice accumulation that disrupts operations, like making ski lifts inoperable and obstructing telescopes^{69,70}. This last refers to the challenge posed by transparent as well as robust surfaces, which must be characterized by their ability to withstand long working cycles under varying climatic conditions. Given the broad range of applications affected by icing, the economic impact of infrastructure damage, and the effects on human well-being, the ice protection industry has become a rapidly growing market, valued in the billions of dollars with an anticipated annual growth rate of 4% in the incoming years⁷¹.

In this thesis, proposals will be addressed to implement robust and forceful controlled wetting responses based on the functional interaction with the application environment. These purposes must be compatible with any type of nature, physical-chemical properties and geometry of the material. Particular attention will be paid to obtaining stable and long-lasting repellent surfaces, capable of developing extra performances of self-cleaning, anti-fouling and anti-icing responses. Wetting control will be achieved through surface modification using innovative, scalable and environmentally friendly surface engineering techniques combining the design of suitable surface topography and chemical modifications. Consequently, the parallel challenge will be to establish protocols for characterizing multifunctional behaviours based on the wetting control in simulated work environments and the compatibility as protective exterior surface of active de-icing devices.

1.1.2 Design of surfaces for the control of wetting

From the pioneering works about the nature of solid-liquid interactions in wetting and non-wetting scenarios, surface design engineering has been progressing. In 1805, Thomas Young described the equilibrium behavior of a liquid droplet deposited on an ideal solid surface⁷². Later, differences in the dynamic contact angle of a droplet on a real solid surface, which are crucial for liquids droplets adhesion and mobility, were first described as “hysteresis” by the metallurgy community in the early 20th century⁷³, although the phenomenon had been considered as early as Gibbs’s studies in the thermodynamics properties of surfaces as a discussion of “the frictional resistance to a displacement of the contact⁷⁴. This phenomenon, known as Contact Angle Hysteresis (CAH), continues to be a subject of investigation today^{75,76,77}. This parameter plays a crucial role in understanding the behavior of liquids on non-ideal surfaces. Hysteresis refers to the difference between the Advancing and Receding Contact Angles (ACA and RCA), (Figure 1 c)), related to the energy required for a liquid droplet to spread or retract on a surface. This phenomenon is essential for evaluating the effectiveness and stability of hydrophobic surfaces, which are critical in a wide range of applications, from self-cleaning materials to anti-icing surfaces⁷⁸. Subsequently, the understanding of non-ideal surfaces was further advanced through the Wenzel⁷⁹and Cassie-Baxter⁸⁰ theories related to

the influence of the roughness and the heterogeneous chemistry, respectively, in the wettability. These models, despite being subject to current revisions to include factors like anisotropy⁸¹, impacting and overflowing drop⁸², fractal and re-entrant geometries⁸³ or the droplet volume⁸⁴, remain valid for establishing the basic surface characteristics required to control the wetting behavior, particularly to produce highly effective water-repellent materials.

- **Biomimicry for the wetting control**

As an intrinsic protection and adaptability mechanism, certain nature species have developed surface characteristics, directly related to wettability, to confront or take advantage of the interaction with the environment as it is exemplified in **Figure 2**. A notable illustration is the hydrophobicity of duck feathers thanks to a peculiar nanostructure, which prevent water penetration⁸⁵. The feathers of their wings have a very special structure, with micro- and nano-structures that create a rough texture that traps small air pockets. This, along with an oily layer secreted from their subdermal glands, helps repel water. Other examples of repellent surfaces in nature, are the leaves of various plants^{86,87}, the skin of sharks and springtails⁸⁸, certain insect exoskeletons and the butterfly wings⁸⁹. The term “*biomimicry*” combines “*bio*”, and “*mimicry*” meaning live or living organisms, and to imitate, respectively. Therefore, technology manufacturing inspired in nature can suppose new optimal advances for surface innovative purposes. Traditionally, water repellency strategies go from the selection of natural materials, such as animal furs or natural fibers, which were subsequently enhanced by incorporating natural oils and waxes to withstand harsh environments⁹⁰ to more advanced materials of tunable wettability based on biomimetics.



Figure 2. Left: examples of the most known natural repellent systems in nature (duck feathers, penguin and gecko skin, butterfly wing, and lotus leaf)⁸⁵. Right: top) non-wet kingfisher in the rain and droplet impact on the kingfisher elastic feather⁹¹; medium) contact angle pictures of kale and SEM images of leaf veins⁹¹; bottom) picture of a hydrophobic taro leaf in the natural environment and SEM images showing its micro-nanostructures⁹¹.

Repellent surfaces are recognized by their ability not only to difficult water interaction (superhydrophobic behavior) but also to resist contamination from fouling agents (omniphobic behavior) and solid particles (self-cleaning response). For that, prompting extensive research into strategies for design and creating biomimetic non-stick surfaces. The foundational principles behind bioinspired liquid-repellent surfaces are related to the impact of surface texture and roughness or the heterogeneous chemistry in wettability^{91,92} as presented in Figure 2, established by Wenzel and Cassie and Baxter models in 1936 and 1944, respectively^{93,94}. Therefore, the different scales of roughness found in nature can be replicated through biomimicry to achieve surfaces with specific functionalities related to repellency. From the perspective of theory, design, and the development of new materials for biomimetic repellent surfaces, **Figure 3**, presents a summary of several advances⁶¹.

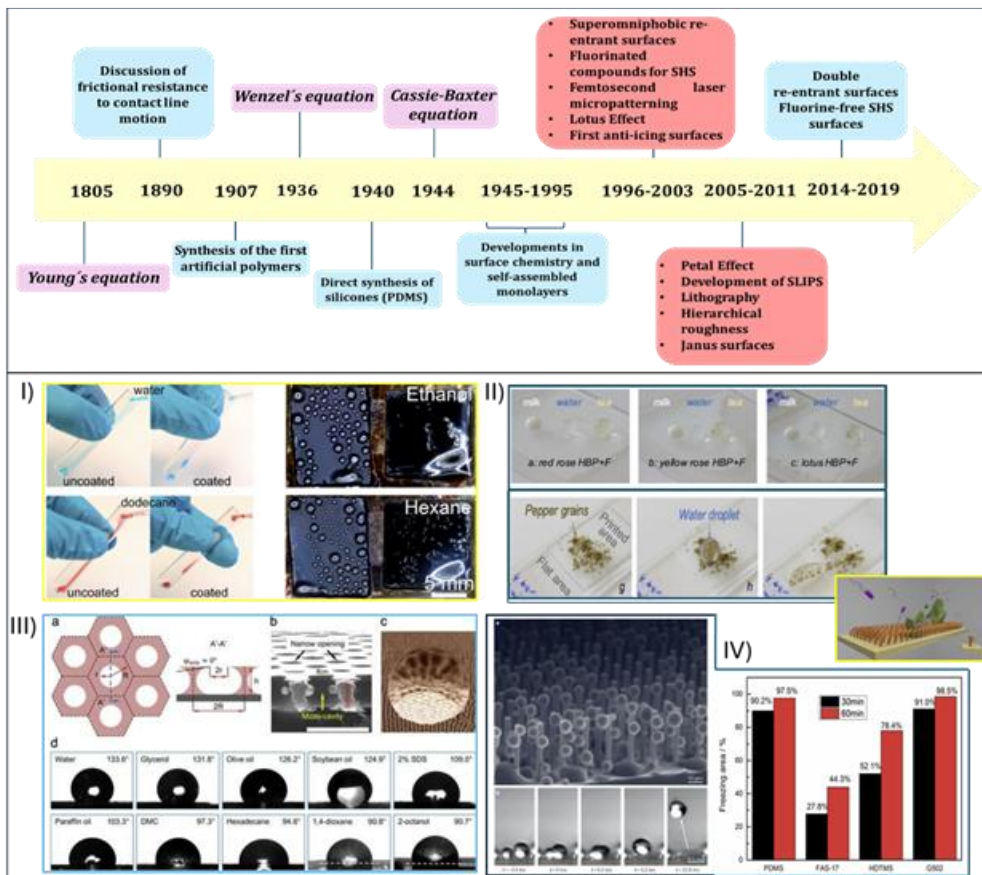


Figure 3. Top: key milestones in the field of wetting control⁶¹. Bottom: state of art of surface response examples related with advanced surface engineering designs⁹⁵: I) experiments about wettability on coated and uncoated surfaces with different solvents, II) self-cleaning capability using real simulants, such as milk, water and tea, III) wettability studies in re-entrant structures with different liquids, IV) ice nucleation studies using re-entrant surfaces.

The timeline highlights theoretical progress in surfaces chemistry, particularly of polymeric nature, as well as the development of Superhydrophobic Surfaces (SHS) and Slippery Liquid-Infused Porous Surfaces (SLIPS) based on the introduction of the hierarchy concept and the lubricant infusion, respectively. Correspondingly, Figure 3 bottom), illustrates examples of the evolution of applied surface designs for omniphobicity (Figure 3 bI)), self-cleaning behavior (Figure 3 bII)), anti-fouling responses (Figure 3 bIII)), and anti-icing capabilities (Figure 3 bIV))^{61,96,97}. Key advancements in the development of water-repellent surfaces include the discovery of natural rubbers and the subsequent development of synthetic polymers in the 20th century⁹⁸. This led to the production of low surfaces energy polymers such as polydimethylsiloxane

(PDMS), a type of silicone rubber, and polytetrafluoroethylene (PTFE), commonly known as Teflon. These polymers have been applied as coatings to modify wettability, particularly as hydrophobic materials. Later, an alternative method for creating low energy surfaces was developed, involving the self-assembly of molecular monolayers, which allowed for precise control at atomistic scale over the surface chemistry and repellency⁹⁹.

In the late 1990s, advancements in visualization and fabrication techniques in materials science, specifically to observe and replicate the nanostructure of the lotus leaf, accelerated the implementation of water repellency by the creation of inspired synthetic superhydrophobic surfaces. Combining micro- and nano-scales topography with high water contact angles ($>150^\circ$), low contact angles hysteresis ($CAH < 5^\circ$), and low rolling-off angles ($RoA < 5^\circ$) were able to be employed in many industrial applications^{100,101}. Although this complex hierarchical structure enhanced water repellency, porosity could become vulnerable under harsh environmental conditions whether under mechanical loads, high humidity, low temperature or presence of corrosive agents. This issue was addressed by developing a new type of functional materials, Slippery Liquid-Infused Porous Surfaces (SLIPS) in which a porous scaffold is infiltrated with an immiscible lubricant to form a smooth, low adhesive, liquid overlayer on the surface. These slippery surfaces are stable under high pressure, exhibit virtually no contact line pinning, and have an omniphobic behavior¹⁰². However, the disadvantages of SLIPS include durability issues, as the liquid lubricant layer can degrade over time due to wear or environmental factors, reducing the surface's effectiveness. Additionally, maintaining a stable and uniform liquid layer across the surface can be challenging, especially in dynamic or harsh conditions. SLIPS can also be sensitive to contamination, as the presence of dirt or oils can disrupt the slippery properties^{103,104,105}. Moreover, low surface tension fluorinated lubricants currently used in SLIPS must be replaced by strategies using silicone, canola, olive, and coconut oils for ecological purposes¹⁰⁶.

Engineered surfaces of low wettability have been designed to offer various benefits, such as minimizing drag in fluid flow, boosting heat transfer, and enhancing self-cleaning properties¹⁰⁷. In the complex domain of ice repellency, these surfaces have shown considerable potential as passive anti-icing or icephobic materials¹⁰⁸. Nevertheless, achieving low wettability with water, even with other non-polar liquids, is insufficient to preserve the repellent capacity at

low temperatures, particularly in environments of high degree of relative humidity. Icephobic surfaces must also possess the ability to inhibit ice nucleation, prevent frost formation and decrease ice adhesion. However, aspects of surface engineering that favor omniphobic behavior, such as porous hierarchical surfaces, may be counterproductive and fail to protect against ice formation when the nanostructure acts as defects conducive to condensation and freezing. Current anti-icing proposals inspired in nature such as oils in plants, and skin of animals (highlighting the study of sea cucumbers, whose skin features a structure with micro and nanofibers that inhibit the adhesion of ice crystals¹⁰⁹) try to address options from self-propelling and bouncing to heat isolation and freezing delay whatever the environmental conditions in search of stable and durable functional surfaces^{110,111}. For instance, new anti-fouling strategies based on the wetting control of the surfaces are being explored to preserve the functional application as well as to enhance the operational life of materials¹¹².

Moreover, from the perspective of smart surfaces, the coupling of these passive protection surfaces to active de-icing systems promises striking efficient advantages. Passive surfaces are ideal to be integrated into active systems because they help to protect and improve energy efficiency based in the wetting behavior. Passive systems, such as self-cleaning coatings or wear-resistant surfaces, protect against abrasion, corrosion, and ice buildup, extending surface life and reducing maintenance needs. In terms of energy efficiency, passive systems can optimize energy use by minimizing the need for active intervention, like heating or defrosting, allowing active systems to work lowering overall energy consumption^{113,114}. Therefore, the scientific community is at the time of defining protocols and characterization standards to evaluate those wetting-based multifunctional properties that serve to establish the quality criteria of this interesting topic of surface engineering.

1.2 Wetting description

As previously mentioned, wetting or wettability of a solid surface provides useful information about the affinity and the interactions of a liquid in contact with a solid surface. It can be characterized by contact angle measurements of a liquid droplet deposited on the surface at the equilibrium condition according to the Young's equation represented in Figure 1 and **Figure 4**. On an ideal surface (i.e.,

completely smooth, rigid, chemically homogeneous, and inert), the Young's equation establishes three interfacial free energies influencing the equilibrium static contact angle (CA): (S-L) solid-liquid, (L-V) liquid-vapor, and (S-V) solid-vapor. The surface energy of the solid-vapor interface and the surface energy to the liquid-vapor interface are often referred to as the solid surface free energy (SFE) and the liquid surface tension, respectively. According to the Young equation, a liquid droplet tends to exhibit lower CA values on a solid surface with high SFE than on a solid surface with low SFE. However, surface geometry, roughness, surface energy and cleanliness of the surfaces as well as droplet size and environmental conditions are factors influencing the contact angle value³¹. Particularly, surface tension, capillarity and gravitational field affect the droplets sliding on the surface¹¹⁵. Under tilting wetting situations as shown in Figure 1 c), an asymmetry occurs between the contact angles measured in both sides of the drop deposited on the surface: the contact angle at the lower side, called Advancing Contact Angle (ACA), becomes greater compared to the one at the upper side, named Receding Contact Angle (RCA). Therefore, a hysteresis of the wetting is appearing, estimated through the difference of these dynamic contact angle values (CAH). Otherwise, the inclination angle of the surface when the liquid droplet starts to move down the tilting direction is known as the Sliding Angle (SA) or Rolling-off Angle (RoA). Hysteresis serves as an indicator of the liquid's adhesion to the surface¹¹⁶. Besides ACA and RCA can be also determined by increasing and decreasing the volume of the droplet until dewetting occurs¹¹⁷ on a horizontal configuration like shown in Figure 1 c). It has been demonstrated in the literature that a liquid droplet will roll off easily from the surface when the static contact angle is greater than 150° and the hysteresis smaller than 5° ¹¹⁸. Consequently, if the solid-liquid contact area is reduced, rolling droplets of specific volume can push, drag and trap dust and dirt particles from the surface in the defined self-cleaning response¹¹⁹.

Other factors influencing the wettability of most solid surfaces range from physical to chemical ones: surface roughness, shape and size of surface motifs and low/high free energy functional groups. Variations in roughness are also caused by impurities and contaminants on the surface. The roughness of the surface is known to influence hysteresis because the surface asperities make different every contact point with the liquid droplet¹²⁰. In consequence, the apparent contact angle, presented in Figure 4 is defined as the angle between the

apparent solid surface and the tangent to the liquid-fluid interface, being different from that of an ideal surface (intrinsic contact angle)^{121,122}.

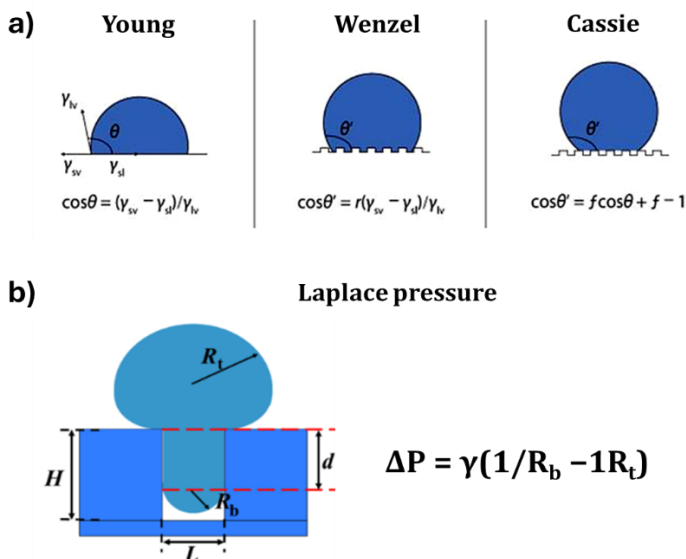


Figure 4. a) Wetting models according to Young, Wenzel and Cassie-Baxter theories¹²³; b) Schematic of the merged droplet tail retracting from the parallel grooved walls of a structure, representing the Laplace pressure as a function of liquid surface tension (γ) and the droplet radius of curvature at the top (R_{top}) and bottom (R_b) of the deformed droplet¹²⁴.

Due to the mentioned defects, real surfaces have a range of stable CA values, also identified with the hysteresis range. It is crucial to emphasize that on smooth surfaces, the reported contact angle (CA) values for water droplets do not surpass 90° due to the chemical nature of them. Therefore, an additional factor, the surface roughness, becomes indispensable for achieving higher CA values.

Two models describe the influence of roughness/heterogeneous topography on the wetting behavior of a liquid droplet deposited on a solid surface: Wenzel's and Cassie-Baxter's theories, presented in Figure 4¹²⁵. The Wenzel's model describes wetting when there is no entrapped air between the solid and liquid. A liquid droplet penetrates the cavities of a rough surface, resulting in a larger surface contact area than a smooth surface by a roughness factor (r). This roughness factor is the ratio of the specific area to the projected area (apparent and intrinsic areas, respectively). According to this model, for a smooth surface with a CA greater than 90° , an increase in the roughness factor increases the

experimental CA and vice versa. It is noteworthy that a droplet in the Wenzel state is often recognized as sticky, given the importance of adhesion between the droplet and the surface, limiting the droplet's mobility on the surface (known as the “*petal effect*” in Figure 3). In contrast, the Cassie-Baxter’s model describes a scenario where the droplet does not fill the cavities of the rough surface. Air pockets are trapped between the solid and liquid, resulting in two interfaces: solid-liquid and solid-vapor below the contact meniscus of the drop, where the droplet wets only the top of the rougher motifs allowing effortless droplet sliding over the surface. According to Figure 4, the f parameter represents the fraction of the solid surface in contact with the liquid. Drawing from the pioneering work of Wenzel and Cassie-Baxter, three requirements must be met to achieve superhydrophobicity, i.e., high contact angle, low contact angle hysteresis, and low rolling-off angle values. This combination results from a well-designed surface chemistry and meticulously crafted topography.

When surface features have an influence in the contour of the liquid droplet-air interface when is deposited on a rough or structured surface, the concept of Laplace’s pressure notably influences the way this interaction occurs. In nature, Laplace effect is used to collect and transport liquids taking advantage of a patterned nanostructure like in the case of cactus spines¹²⁶. Laplace pressure (P) refers to the differential pressure across a curved boundary between a liquid and a gas. It is determined by the surface tension of the liquid (γ) and the radius of curvature (R) of the liquid-air interface.

$$P = \frac{2\gamma}{R} \quad (\text{equation 1})$$

The surface's geometry of a rough or structured surface with entrapped air, led to alterations in the curvature of the liquid-air interface of the droplet affecting the Laplace's pressure experienced by liquid droplets in contact with the surface¹²⁷. Laplace pressure is directly linked to the internal radius of the droplet (Figure 4 b)) and, therefore, to the Three-Phase Contact Line (TPCL) diameter. It highlights that for higher droplet diameter values, the Laplace pressure will be lower, meaning that a larger droplet will have a smaller pressure difference between its interior and exterior. In contrast, when the droplet diameter decreases (usually due to the evaporation process), Laplace pressure increases,

meaning that the surface tension generates higher pressure in a smaller droplet to balance the forces present on the surface. This explains why droplets with less contact with the surface tend to be more spherical and stable against evaporation or collapse if the surface force opposing water penetration is balanced by the Laplace pressure in the drop¹²⁸. Therefore, Laplace pressure is a parameter that allows to identify a wetting regime change from Cassie-Baxter to Wenzel state during the evaporation of a droplet¹²⁹. This parameter also affects the droplet jumping mechanism being useful to develop nanostructured surfaces for easy removal of droplets during steam condensation¹²⁹ and microdroplet manipulation¹²⁶.

1.3 Strategies for liquid-repellent surfaces at room conditions

Over the past two decades, innovative concepts have been explored with the objective of developing multi-repellent surfaces that means omniphobic surfaces with additional multifunctional properties such as anti-fouling, anti-corrosion, anti-fogging, and self-cleaning behaviors. Common strategies can be summarized in three basic approaches shown in **Figure 5**.

1.3.1 Superhydrophobic surfaces (SHS)

Understanding the principles and mechanisms underlying the remarkable liquid repellency of lotus leaves enabled the recompilation of the “*lotus effect*” on synthetic surfaces. This breakthrough served as the foundation for surface engineering such as a wide range of repellent surfaces based on hierarchical micro-nanostructures, capable of maintaining air trapped in the porosity below the liquid solid interface, and consequently minimizing the contact area as previously was commented.

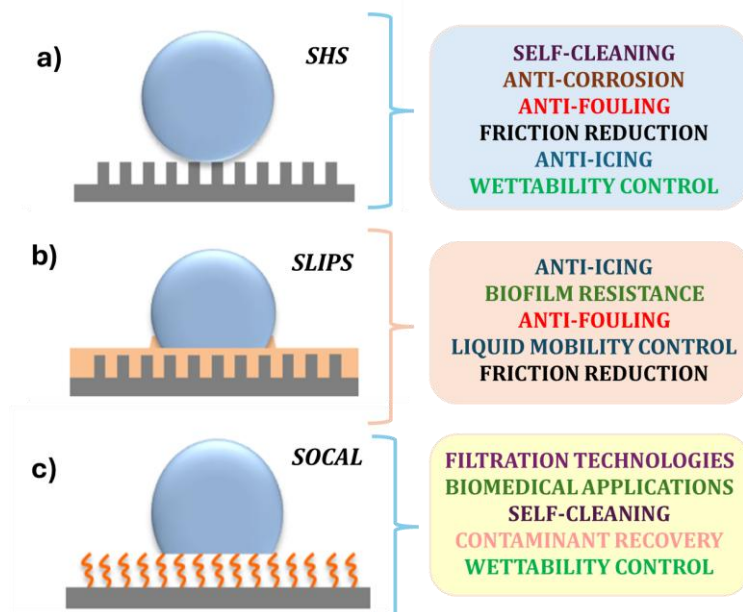


Figure 5. Schematic of different approaches for liquid-repellent surfaces: a) Superhydrophobic surfaces (SHS), b) Slippery Liquid Infused Porous Surfaces (SLIPS) and c) Slippery Omniphobic Covalently Attached Liquid (SOCAL), and their potential applications.

The application of low surface free energy materials is essential to reduce the chemical affinity between the surface and the water droplet. Main scheme of a superhydrophobic surface is shown in Figure 5 a). It is remembered that due to the reduced contact area between the liquid and the surface, SHS exhibit excellent water repellency, characterized by high contact angles, low contact angles hysteresis, and low rolling-off angles. It should be noted that when both CA and CAH are high, a liquid droplet may adhere to the surface due to the “*petal effect*” representing a state of non-wetting but high adhesion¹³⁰. A water droplet experiences strong adhesion on a rose petal surface due to the papillose structure of its epidermis acting as strong pinning sites. This prevents liquid droplets from sliding on the surface even when the petal is inverted. This sticking water-repellent capability has been extensively studied and exploited for various applications, like oil-water separation^{131,132}, anti-corrosion^{133,134}, self-cleaning^{135,136}, anti-fouling^{137,138}, drag reduction^{20,139}, anti-fogging^{140,141} and anti-icing^{22,142}, although there is controversy between static water repellency and anti-icing capability as will be discussed later.

The required micro-/nano-structuration for the fabrication of superhydrophobic surfaces, called hierarchical topography, can be achieved through either top-down or bottom-up approaches¹⁴³. Top-down methods include techniques such as etching (chemical^{144,145}, plasma^{146,147}, laser^{148,149}) lithography^{150,151}, and template-based methods¹⁵². Bottom-up approaches involve techniques like coating¹⁵³, and nanostructures deposition^{154,155}, and sol-gel methods^{156,157}. A combination of both approaches can also be used to create advanced SHS as will be intended in this thesis.

As a peculiar application of superhydrophobic surfaces (SHS)¹⁵⁸, the self-cleaning response allows solid particles to be easily removed by the rolling action of water droplets. In an attempt of explanation at microscopic level, Geyer et al.¹⁵⁹ estimated the lateral adhesion force acting during the self-cleaning of hydrophilic and hydrophobic dirt particles:

$$F_L = 1.1 \frac{\omega \varphi^2 \Delta \gamma^2}{k} \quad (\text{equation 2})$$

considering that the meniscus formed due to the deformation of the interface during the self-cleaning is modelled as a k spring constant, ω being the width of the apparent contact area of the droplet, φ the surface fraction in contact with the particle and $\Delta \gamma$ the work of adhesion between the substrate and the dirt particle.

Currently, the fabrication of SHS is well established and does not present significant technical challenges. However, despite their excellent water repellency, these surfaces have inherent limitations that restrict some practical applications. SHS are ineffective against low surface tension liquids, which can easily spread across the surface, displacing the trapped air content. Moreover, these surfaces cannot withstand pressure, causing liquids to penetrate the porosity and compromising their repellent properties. An important key for SHS is related to micro-nanostructures configuration which can negatively impact the material's mechanical strength depending on the charge, and environmental conditions leading to the loss of wetting functionality when damaged¹⁶⁰. Efforts have been made to extend the unique behavior of SHS to liquids other than water, such as low surface tension liquids (e.g., oils, organic liquids and alcohols). It has been identified that, in addition to the hierarchical morphology required for SHS,

a specific chemical functionality or a sophisticated topography (re-entrant, overhanging or *Janus* structures) is crucial for achieving superomniphobicity, and, by extension, anti-fouling, self-cleaning or anti-icing capabilities¹⁶¹. However, these surfaces still suffer from the general SHS drawbacks, highlighting the fragility of their morphological features that even can lead to mechanical locking issues when ice nucleates within those air traps^{162,163}.

1.3.2 Slippery Liquid Infused Porous Surfaces (SLIPS)

This liquid-repellent methodology, which emerged in 2011 as a novel approach to obtain non-stick surfaces, is particularly effective at repelling low surface tension liquids, addressing some of the limitations of superhydrophobic surfaces. Inspired by the *Nepenthes* plant, commonly known as the pitcher plant, whose penstemon feature a porous structure infused with water or nectar to create a lubricating layer that causes insects to slip into the plant's interior¹⁶⁴. Aizenberg et al. developed the concept "Slippery Liquid Infused Porous Surfaces" (SLIPS)¹⁰², by infusing a low surface tension lubricant into a textured or porous material as it is shown in Figure 5 b). This technology takes advantage of the lubricant's mobility, resulting in exceptionally smooth and defect-free surfaces with very low contact angle hysteresis (CAH) against low surface tension liquids. As a result, liquids and fluids droplets can easily roll off where the surface typically remains hydrophobic due to the wetting behavior of the outermost lubricant layer. For a stable SLIPS system, the lubricant must meet two criteria: 1) it should have a strong affinity for the substrate while repelling liquid or fluid agents, and 2) it must be immiscible with the contact liquid¹⁶⁵. Another key feature of SLIPS is their self-healing capability: when the surface is damaged, the lubricant quickly flows to repair the affected area¹⁶⁶. However, despite this self-healing property, the long-term durability has been questioned and certain limitations still hinder the large-scale practical applications of SLIPS. The effectiveness of these surfaces depends on the mobility of the lubricant at the molecular level, but this same mobility is also their primary limitation. Prolonged use may result in lubricant depletion to evaporation at working operation conditions different from the room temperature or interaction with fluids of different density leading to a displacement and deterioration of the surface's properties¹⁶⁷. Additionally, the textured or porous scaffolds that retain the

lubricant are often fragile, limiting their mechanical robustness. To address this, studies are being focused on the stability of the lubricant, considering the surface energy of the substrate, the lubricant fluid nature, and the repelled liquid one to ensure effective liquid retention. Additionally, it is important to select a lubricant that does not result in drop clogging, as this could cause oil depletion as droplets roll off¹⁶⁸. Furthermore, most efficient lubricants used in SLIPS are composed of fluorine-based chemistry. Therefore, lubricant losses by evaporation and water drop cloaking could cause environmental and human health issues.

1.3.3 Other strategies for liquid-repellent surfaces

One of the methods used to achieve repellent properties is the surface chemical derivatization through molecular grafting. Chemical derivatization is a process in which surfaces are functionalized by incorporating polymeric chains or specific molecules via covalent bonds. This method is widely used to modify properties such as hydrophobicity, chemical resistance, or biocompatibility. Fluorinated compounds are particularly relevant in this context, as they provide unique properties such as low surface energy and high thermal and chemical resistance. Experimentally, molecular grafting can be performed using methods such as radical grafting, photoinitiation, or chemical activation of the surface. According to the literature, typical steps include: 1) surface pretreatment (e.g., cleaning or activation), 2) initial functionalization with a reactive group, and 3) reaction with the fluorinated monomer or compound¹⁶⁹. In chemical derivatization processes through grafting, the molecules most used are fluorinated monomers like Perfluoroalkylsilane (PFAS) compounds characterized by their C-F bonds, acrylates and methacrylates, as well as silanes, among others. **Figure 6** shows a schematic of the main surface chemical reaction that occurs between the functional groups and the surface exposed to their vapors, as well as the result after the reaction.

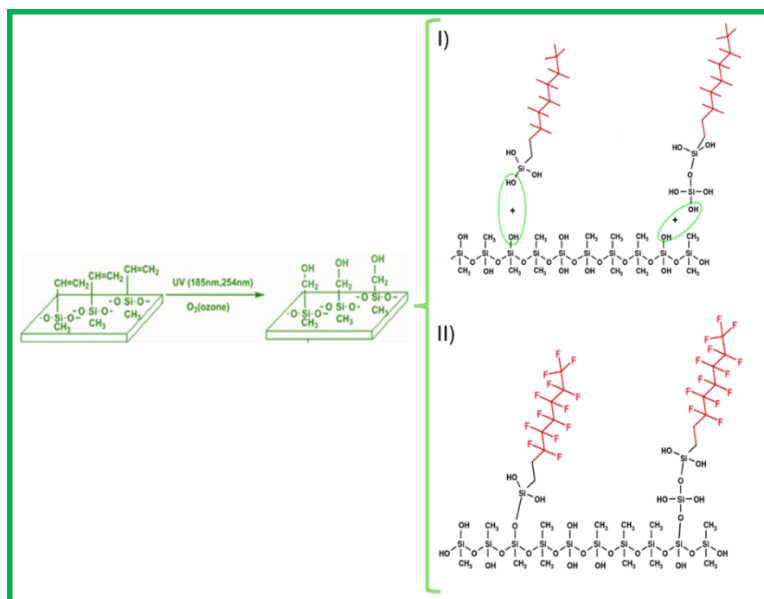


Figure 6. Scheme of chemical derivatization by surface grafting of fluorinated molecules using PFAS to achieve repellent properties. Left: main activation process using O_3 to clean the surface and to obtain $-OH$ chemical groups. Right: formation of stable chemical bond between $O-Si$.

As shown in Figure 6, a surface activation process is necessary to obtain hydroxyl groups on the surface ($-OH$) (Figure 6 I) in order to promote thermodynamically favourable $O-Si$ bonding, that is, a chemical bond is formed between the surface and the functional molecule through the presence of silanol groups ($Si-OH$) in the chosen precursor (Figure 6 II)). In the context of this thesis, this type of strategy will be presented to achieve stable repellent properties. The development of hierarchical surfaces provides a larger available specific surface area to accommodate these types of molecules.

McCarthy's group introduced a new type of liquid-repellent surface called Slippery Omniphobic Covalently Attached Liquid (SOCAL)²⁵. This approach focuses on minimizing contact angle values with different liquids to achieve superomniphobicity by utilizing smooth surfaces grafted with flexible molecular chains that exhibit liquid-like behavior due to their rotational freedom (see Figure 5 c)). Like SLIPS but without the need for a hierarchical support, SOCAL surfaces, despite having only moderate contact angle values, demonstrate excellent slippery properties by leveraging the mobility of the grafted molecules to achieve low CAH^{170,171}. This strategy is a promising solution for developing surfaces with improved mechanical durability and significant liquid repellent

capability. Typically, the surface chemical reactions that occur on these smooth surfaces take place through silane reactions or hydroxyl groups (-OH) induced at the previously activated surface. Some of the used long-chain chemical molecules include chlorosilanes and methoxysilanes, which can be fluorinated or non-fluorinated chains, thereby enhancing the full repellent properties¹⁷². The presence of these flexible, free-moving chains on the surface provides great durability from the perspective of electromechanical tests, and strong mechanical shocks.

Finally, bioinspired porous *Janus* materials, inspired by the banana leaves¹⁷³, have emerged as an innovative solution for applications such as water filtration, and collection, and self-cleaning surfaces. These materials feature hydrophobic and hydrophilic properties on different surface sides or in a gradient way, granting them dual functionality¹⁷⁴. Their porous geometry enhances particle and liquid separation, enabling efficient water contaminant removal. *Janus* configuration leverages an exhaustive control of an asymmetric micro- and nanostructures to achieve water repellence, making them effective for creating new smart functional surfaces¹⁷⁵.

1.4 Icephobicity

Since wetting is affected when the temperature decreases, it cannot be assumed that the affinity or repulsion properties with liquid droplets are maintained when environmental conditions change. To begin to establish the related terminology of the behavior of the three phases: vapor, liquid water and ice when the temperature drops, we will use the term supercooling, also named subcooling¹⁷⁶, referring to a situation where latent heat will not be released when the phase change temperature is reached, but the temperature of the material will gradually decrease until a point where ice crystallization begins.

1.4.1 From wetting to icing phenomena

Commonly, water contact angle tends to decrease from room to sub-zero temperatures what can be related to surface condensation of ambient moisture at temperatures around 0°C near the droplet contour, that increases its volume from its interface when remains deposited on a cold surface. Consequently, a transition from a Cassie-Baxter to a Wenzel state¹²⁵ may usually be observed for

superhydrophobic surfaces that lose such character at low temperatures (Figure 7).

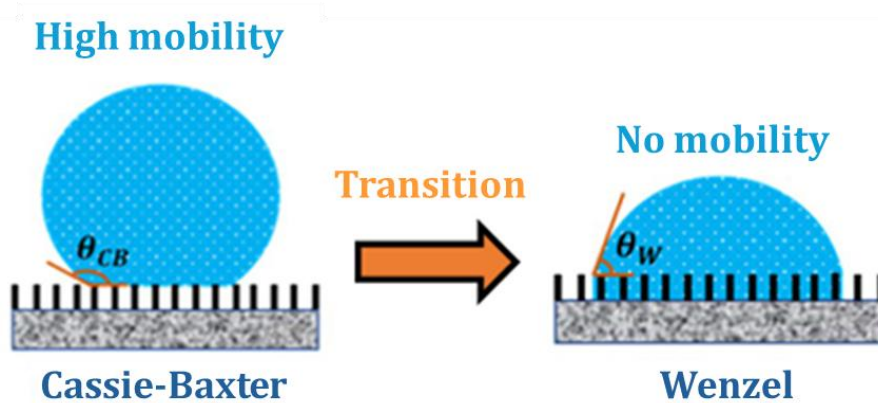


Figure 7. Schematic of the Cassie-Baxter to Wenzel transition at low temperatures¹⁷⁷.

Also, if the drop deposited on a superhydrophobic surface undergoes some evaporation process close to 0°C , its size decreases and the Laplace pressure inside the drop increases, which leads to the impaling of the drop on the surface in a new adopted Wenzel state¹⁷⁸. Moreover, when water droplets are carried by wind currents and impact with high kinetic energy on cooled superhydrophobic surfaces (possible displacement of air pockets from the pores), and/or when the moisture from the environment condenses in the porous surface structure to develop a frost layer, there is also a Wenzel-driven ice formation. At the dew point, droplets can reach a metastable supercooling state whereas at lower temperatures the droplets can freeze when frost begins to be formed around the water droplet and the ice nanocrystals adhere to the surface. The process of freezing of a water droplet deposited on a cold surface is described in 5 stages¹⁷⁹: liquid supercooling, nucleation/recalescence, crystal growth, equilibrium freezing and solid subcooling as it is shown in **Figure 8 a)**¹⁸⁰.

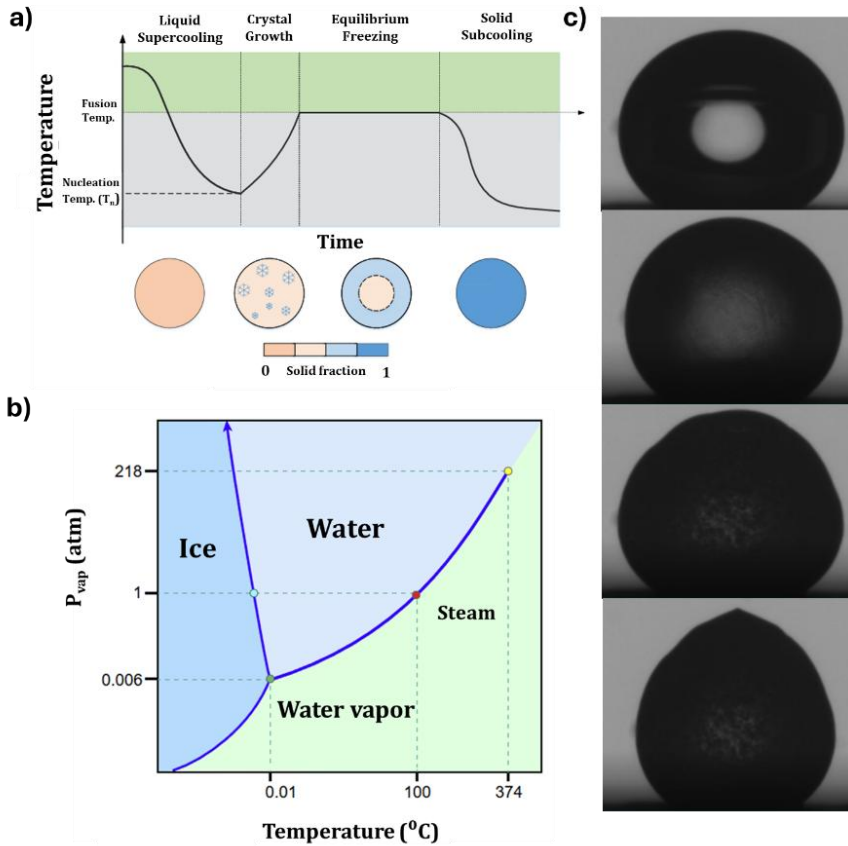


Figure 8. a) Conceptual diagram of the multi-scale droplet solidification framework based on spatial and temporal scales¹⁸⁰; b) General phase diagram of water; c) Pictures of the freezing process of a water droplet deposited on a cold surface identifying the main stages: liquid supercooling, ice nucleation, freezing and ice subcooling.

In the first stage, the temperature of the water droplets in liquid state decreases even below zero. The sudden return of the temperature of the supercooled water droplets to the icing temperature is called the recalescence stage, where crystal nuclei begin to be formed and grow whereas the latent heat is released in a short time until the complete freezing. Then the temperature of the ice particle decreases in the solid subcooling stage.

Prior to the freezing mechanism or during its execution, moist environments can promote water condensation on the cold surface¹⁷⁹. Depending on the wetting behavior and the heat exchange mechanism, film-wise or dropwise condensation can be observed on hydrophilic or hydrophobic surfaces, respectively. Superhydrophobic surfaces may result in a better energy transfer because

reducing the contact area by means of isolated condensed small droplets leaves free spaces for thermal transport and, consequently, for ice nucleation. Moreover, since small water droplets exchange heat with the environment and the cold surface by thermal conduction and radiation, a low thermal conductivity material may promote the generation of ice bridges of adjacent condensed droplets. Therefore, in anti-icing applications it is preferable to have surfaces that facilitate heat conduction and thermal radiation.

Depending on the environmental conditions, particularly the temperature gradient, ice formation may happen in a homogeneous or heterogeneous nucleation mechanism. Homogeneous ice nucleation can be possible at the gas-liquid interface if the evaporative cooling and the supercooled liquid stages are predominant i.e., governed by the difference between the melting temperature and the initial one and regulated by the competition between the decreasing bulk crystal free energy and the increasing surface free energy¹⁸¹. Thus, ice nuclei come from the spontaneous generation of stable and ordered hydrogen bonds between water molecules, what decreases the free energy promoting the increase of the nuclei and increasing the interface free energy between the ice and the liquid water. Both processes compete in the form of a nuclear energy barrier (**Figure 9**). Meanwhile, heterogeneous ice nucleation is commonly observed at the liquid-surface interface if the colder region is the solid material because the presence of the foreign surface decreases the nucleation barrier by reducing the free energy of the interface¹⁸². The temperature for such a process to occur does not have to be so low as that for homogeneous nucleation because of the presence of impurities, roughness or different surface chemistry.

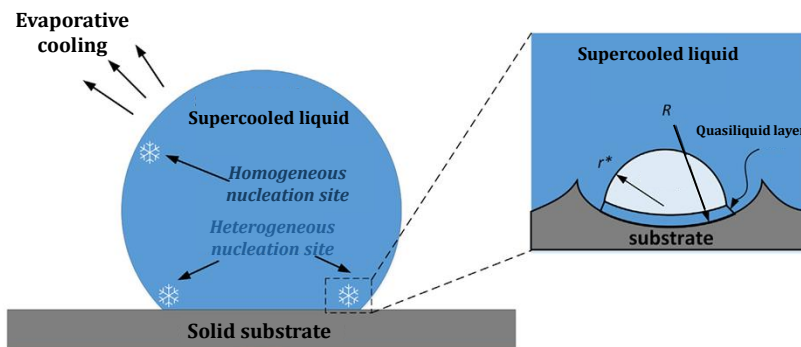


Figure 9. Representation of the homogeneous and heterogeneous ice nucleation mechanisms^{180,183}. R is the radius of curvature for droplet and r^* is the radius of ice particle formed.

These factors influence a lower energy barrier nucleation, and, consequently, the freeze resistance of a surface will be directly related to the surface tension and wetting. According to the classical nucleation theory, the critical size (radius) of ice nucleus¹⁸⁴ can be expressed as:

$$R_c = \frac{2\gamma_{il}T_m}{\rho_i H_{il} \Delta T} \quad (\text{equation 3})$$

being γ_{il} the interfacial energy between ice and liquid water ($\sim 45 \text{ mJm}^{-2}$), H_{il} is the latent heat of freezing, ρ_i the ice density and ΔT the difference between the melting temperature (T_m) and the surface temperature. Theoretically, for ΔT around $5\text{-}10^\circ\text{C}$, the critical radius of the ice nucleus would be around $9\text{-}4.6 \text{ nm}$ ¹⁸⁴. That means that surface roughness in the nanoscale is prone to exposing surface defects that trigger ice nucleation.

After ice nucleation, ice crystals grow and make contact between them in the called ice accretion process. There are three main types of ice that can form under different environmental conditions: glaze, rime, and mixed ice. Glaze (wet) ice forms when supercooled water droplets freeze upon contact with a surface, creating a smooth, transparent ice layer, typically under conditions of freezing rain with calm winds and temperatures near 0°C . Glaze ice is presented as transparent, not completely frozen, highly density ice. Rime (dry) ice, on the other hand, also distinguished like hard or soft, forms when supercooled water droplets freeze on contact with surfaces exposed to cold, humid air, resulting in a frosty, opaque, and rough texture, even with trapped air inside, often occurring in windy conditions with temperatures below freezing (around -15°C). Mixed ice, which is a combination of glaze and rime, forms under conditions where both freezing rain and supercooled droplets coexist, leading to a more complex ice accumulation with both smooth and frosty ice layers on surfaces.

Depending on the environment and surface properties, such as the topography, the Ostwald ripening¹⁸⁵ phenomena could be present during ice accretion. It refers to the transfer of water molecules from smaller sized droplets to larger ice crystals via diffusion through the bulk vapor phase due to the chemical potential difference between the small droplet and the large ice crystal. Finally, the mechanisms governing the ice accretion depend on the release of latent heat during freezing: if it is not possible to remove all the latent heat because the heat

exchange between the surface and the environment is inefficient, glaze ice accretes preferentially, whereas ice rime accretes when supercooled water droplets hit previous ice particles allowing a fast diffusion of latent heat. Therefore, anti-icing surfaces focused on inhibiting ice accretion must be designed to reduce the critical ice nuclei formation together with minimizing the ice crystal growth.

1.4.2 General description of icephobic surfaces

Icephobic surfaces are characterized by four fundamental aspects^{186,187}: freezing delay capability inhibiting ice nucleation, reducing ice adhesion, condensate self-removing and inducing melting of the accumulated ice. However, most of these surfaces do not fully exhibit all these characteristics, leading to optimal performance only under specific conditions. The icephobic properties of a surface are sometimes evaluated based on one or more material properties, such as water repellence or contact angle hysteresis. While these traits can indirectly influence the icephobicity of a surface, they are not, strictly speaking, direct measures of it. Several studies in literature have drawn direct correlations between water repellency and icephobicity. For example, Dalton et al.¹⁸⁸ developed a variety of surfaces ranging from superhydrophilic to superhydrophobic revealing that as the water contact angle increased, ice adhesion decreased, in line with the work of Meuler et al.¹⁸⁹, that suggested superhydrophobic surfaces to prevent freezing. Kulinich et al.¹⁹⁰, noted that the relationship between ice adhesion and water contact angle is only valid when contact angle hysteresis is low (lower ice-solid contact area)¹⁹¹. Meuler et al.¹⁹², examined ice adhesion on a broad set of smooth steel discs coated with different hydrophobic materials, finding that ice adhesion is tied to the value of the work of adhesion and that further reductions in ice adhesion are achievable only with structured surfaces.

Consequently, a comprehensive definition of icephobicity encompasses four key physical principles: (I) thermodynamics governing the phase transition in the supercooled water-surface system, (II) heat transfer involved in the ice formation process, (III) the mechanism of the ice-surface interaction, and (IV) material properties related to long-term mechanical, chemical, and environmental durability. Each of these aspects plays a crucial role in

determining the icephobic performance of a surface. Based on this definition, icephobic surfaces are evaluated by four primary criteria: (1) average ice nucleation temperature (T_N), defined as the temperature at which ice nucleates on a sessile water droplet placed on a surface when the system is slowly cooled under quasi-equilibrium conditions, or the average ice nucleation/freezing delay time (t_f), which refers to the time required for ice nucleation of a supercooled droplet in thermal equilibrium with its surroundings¹⁹³, (2) the rate of ice accretion on the surface; (3) the adhesion strength at the ice-solid interface; and (4) the surface's long-term icephobic durability. **Figure 10** provides a schematic overview. Once a droplet contacts a surface at freezing conditions, it can undergo a phase transformation from water to ice through the process of ice nucleation and subsequent growth. From a thermodynamic standpoint, the heterogeneous ice nucleation temperature, T_N , depends on the Gibbs energy barrier for heterogeneous ice nucleation (ΔG) and the CA (θ) of the water droplet¹⁹⁴ expressed as follows:

$$\Delta G = \pi\gamma_{lv}R^2(2 - 3\cos\theta + \cos3\theta)/3 \quad (\text{equation 4})$$

where γ_{lv} is the liquid-vapor surface tension and R the critical radius. So, the larger the θ when $\theta > 90^\circ$, the higher the ΔG and thus the better the anti-icing performance. The freezing process of water droplets on a solid surface, in addition, follows the principle of energy conservation¹⁹⁵.

$$W_d + m_w L + Q_{exo} = (q_{wa} + \phi + q_r)t_f \quad (\text{equation 5})$$

where W_d is the kinetic energy of the droplet hitting the surface, m_w is the mass of the droplet, L is the latent heat of water, Q_{exo} is the heat released by water in the freezing process, q_{wa} is the natural convective heat transfer between the droplet's contact surface and the surroundings, q_r is the radiative heat transfer between the droplet and the surface, ϕ is the energy dissipated during the impact and t_f is the droplet's freezing time. Another key consideration is the interfacial heat transfer between the water droplet and the surfaces¹⁹⁶ affecting by:

$$t_f = \rho LVHS(T_m - T_s) \quad (\text{equation 6})$$

where t_f is the duration from the water droplet begins phase transition to the solid ice particle is completely formed, ρ water density, V the water droplet volume, H is the heating transfer coefficient, S the contact area between the water droplet and the surface, T_m the equilibrium freezing temperature, and T_s is the temperature of the surface.

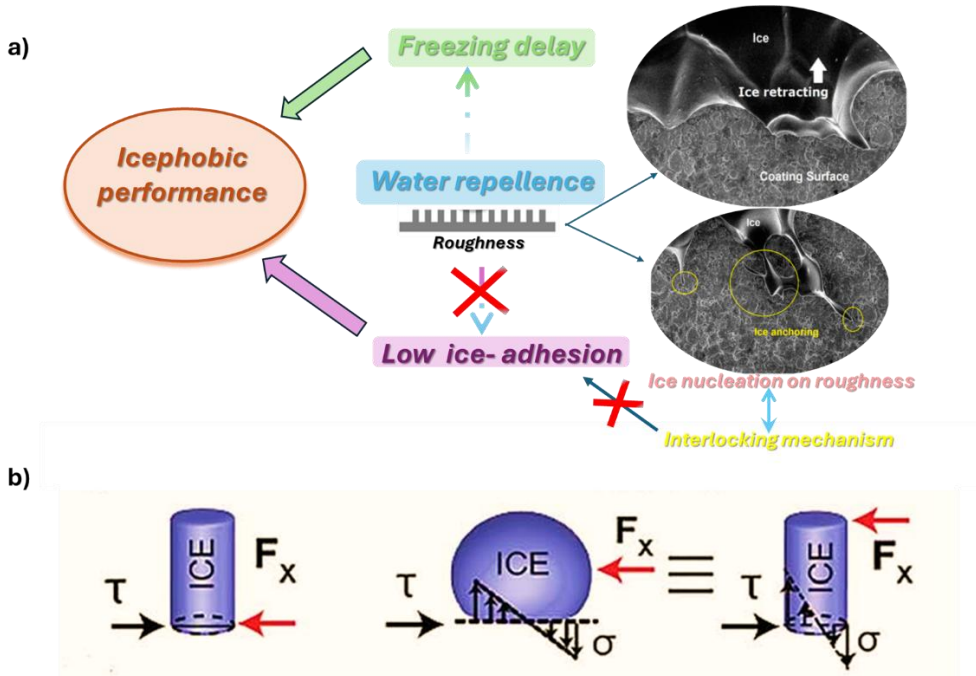


Figure 10. a) Representation of the main factors defining icephobicity: freezing delay time, water repellence and low ice-adhesion properties; b) Ice shedding influencing ice adhesion divided into two models depending upon the wetting state of ice: shear ice removal mode with external force imposed on the ice/substrate surface interface and ice shedding mode with external force applied to keep the ice away from the ice/surface interface.

Additionally, Li et al.¹⁹⁷ demonstrated through molecular dynamics simulations that nano-grooves could decrease the ice nucleation rate and inhibit freezing. For surface roughness higher than 10 nm, increasing the energy barrier for ice nucleation involves modifying surface free energies through the implementation of perfluorinated groups ($-\text{CF}_2$ or $-\text{CF}_3$), for example. Furthermore, other authors proposed that the formation of a quasi-liquid water layer beneath the ice nucleus can be beneficial preventing the ice formation in local nanoconfinements¹⁹⁸. Another extra factors that affect ice nucleation are related to enhanced nucleation sites, such as surface defects, cracks and impurities which can serve as additional and preferential nucleation sites, where water molecules can

cluster together and begin to form an ice nucleus instead of what occur with smooth surfaces which may delay ice nucleation. Since the ice nucleation requires a certain amount of energy to overcome the Gibbs energy barrier, surface defects can reduce this energy activation by providing an easy environment for aggregation of water molecules that may experience stronger interactions than those in a smooth area, promoting the hydrogen bonds and facilitating the phase transition from liquid to solid. In summary, defects can modify the interfacial free energy between the water droplet and surface whereas environmental factors such as temperature condition the ice nucleation as it is shown in Figure 10 a) and b)¹⁹⁹. Nevertheless, icephobicity can be categorized into anti-icing and de-icing functionalities. Anti-icing encompasses attributes aimed at mitigating ice formation, while de-icing pertains to the removal of existing ice, including low ice adhesion and the capability to melt ice²⁰⁰. De-icing strategies have evolved to include passive methods like hydrophobic coatings and thermal techniques such as electrothermal and photothermal systems, as well as active methods like pneumatic and electromechanical de-icing. Electrothermal systems are effective but highly energy-demanding, while photothermal systems offer potential energy savings, though their effectiveness is condition-dependent. Passive methods are of low maintenance but less effective in extreme conditions, while active methods perform better in harsh environments but involve more complexity and maintenance. A key challenge remains improving the exposed surfaces of active devices to enhance their performance, energy efficiency, and long-term reliability in real-world applications²⁰¹.

So, active de-icing technology is the other main method²⁰² to combat the formation and accumulation of ice on surfaces, but using external energy sources. Applications of the active de-icing systems span transportation infrastructure, where heated pavements and bridges prevent ice buildup and enhance vehicle safety, aerospace, where aircraft wings and control surfaces employ active de-icing methods for safe winter operations, and buildings, where heating elements in roofs and gutters prevent ice dams and related damage.

A wide range of ice mitigation actions is available, which can be classified into four well-established categories:

- ✓ Thermal methods include electrical heating systems that utilize electrical resistance as heat dissipative elements by Joule effect embedded in roads, bridges, or aircraft wings to maintain a temperature above freezing to prevent ice formation or detach ice from environmentally exposed surfaces. Also, hydronic heating, which circulates warm water through pipes beneath surfaces, commonly is used in pavement systems to melt snow and ice. Pneumatic systems blow jets of heated air to remove snow and ice, effectively de-icing specific areas like airport runways. Thermal coatings, such as conductive coatings, enhance heat transfer and provide active heating capabilities, reducing ice adhesion. Infrared heating lamps to directly heat responsive surfaces, are particularly useful for targeted applications like de-icing aircraft before take off²⁰³.
- ✓ Chemical methods include systems with chemicals compounds working as icing inhibitors, such as salts or other de-icing agents, to lower the freezing point of water and enhance melting. They are applied as sprays or integrated into heated systems. Some examples of these chemical active systems could be related to self-propelled particles or active colloids, where catalytic and *Janus* elements are able to drive self-propulsion by decomposing chemical fuels. Another example includes autonomous chemical oscillators, which are chemical systems that exhibit oscillatory behavior without external intervention, such as polymer gels. These polymers can undergo rhythmic swelling and deswelling in response to chemical oscillators²⁰⁴.
- ✓ For the mechanical methods, expulsive methods like neumatic boots, high pressure gas flux or piezoelectric pulses to break off ice from the surface are contemplated. If activated with sufficient frequency, some expulsive systems can be used effectively for active anti-icing. Electromagnetic de-icing systems use a spiral coil placed near the inner face of a metallic surface to glue a thin, flexible sandwich²⁰⁵ of conductors and dielectric material to the protected surface¹¹³.

- ✓ Ultrasonic systems use radiofrequency to disrupt ice formation, particularly beneficial for sensitive applications like aircraft. Smart ultrasonic systems incorporate sensors and control devices to monitor environmental conditions and adjust heating or chemical applications, optimizing performance and energy use²⁰⁴. Then, since this thesis has been developed within the framework of an European project called SoundOffice involved in the development of smart efficient de-icing solutions based in the application of acoustic waves, it has been possible to have access to advanced facilities to evaluate passive systems as well as prove its integration in active de-icing devices excited by acoustic waves.

The disadvantages of active systems include their increased complexity, higher weight, and the need for frequent maintenance. Additionally, they tend to consume more energy and may be less durable, especially under extreme conditions. This highlights the need to integrate passive protective surfaces, although there may be risks of physicochemical and thermal and energetic transfer incompatibilities between the two systems and adhesion issues, which requires sufficient scientific and technical efforts to achieve that optimization²⁰⁶. In response to the limitations of current active de-icing systems, there has been a growing interest in developing consonant passive anti-icing materials. These passive methods involve designing surfaces with properties that naturally resist ice formation or facilitate ice detachment without relying on external energy sources or de-icing chemical agents to properly be combined with the benefits of reduced energy consumption through enhanced surface properties^{207,208}. However, many of these efforts have been unsuccessful due to issues related to the continuity of the passive system at the integration interface, energy and heat losses, as well as the lack of stability and durability under work cycling or extreme conditions. This serves as one of the main motivations of this thesis: to develop robust repellent surfaces of remarkable anti-icing capability to be able to be adapted to active de-icing systems while maintaining their efficiency. Therefore, the following section address the main surface properties that must be taken into account when designing icephobic surfaces compatible with active de-icing devices. In the **Figure 11** some of the represented wetting states potentially accepted as icephobic surfaces are shown.

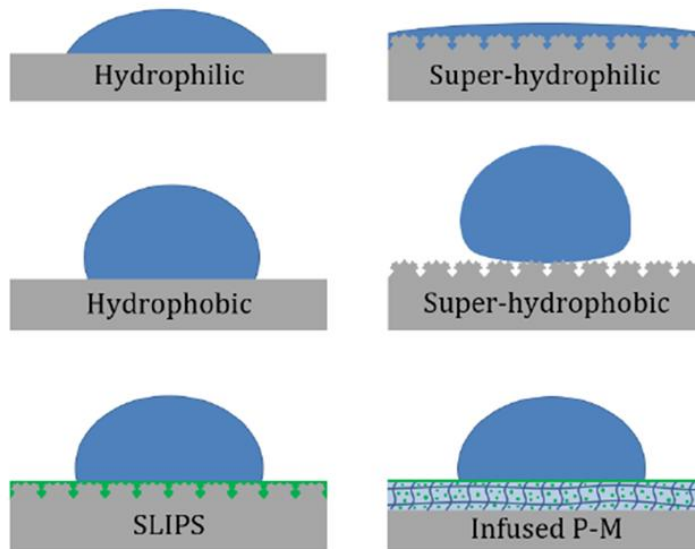


Figure 11. Types of wetting states commonly proposed as icephobic surfaces. SLIPS refers to slippery liquid infused porous surfaces and Infused P-M refers to lubricant infused polymer matrix where green colour represents the lubricant²⁰⁹.

1.4.3 Water repellence

The first influential property of icephobic surfaces is their capacity to repel water droplets at room temperature, as surfaces that remain free of water contact are less prone to water condensation, frost formation and ice accretion under cold and humid conditions. This property can be further divided into two key aspects: the shedding of supercooled water and the reduction of water condensation. When water droplets contact a cold surface, they can freeze making the contact time between the surface and water a crucial factor in preventing ice formation. Surfaces promoting high water mobility enhance the shedding of water, particularly on configurations, thereby minimizing contact time and reducing the likelihood of ice formation^{210,211}. In environmental conditions of supercooled water droplets existing below their freezing point, minimizing surface contact time becomes even more essential, as seen in the formation of glaze ice during freezing rain²¹². Icephobic surfaces often have hydrophilic properties promoting the spreading of water droplets and minimizing droplet retention what could reduce the likelihood of ice formation since making it harder for ice to bond firmly to the surface. However, only if the chemical composition based on ice

inhibitors or a hygroscopic response able to retain a liquid aqueous layer at the ice/surface interface or promote mechanical response to affect ice adhesion, it is found anti-icing behavior of hydrophilic surfaces^{213,214}. Particularly, polymeric matrices of hydrogels infused with substances like ethanol²¹⁵, ethylene glycol²¹⁶ or salty water²¹⁶ instead of traditional lubricants can prevent ice formation even at extremely low temperatures because the antifreezing agents can diffuse to the surface, either melting existing ice or creating a barrier liquid layer between the ice and the substrate. However, these surfaces, classified as semi-active systems, require periodic replenishment of anti/de-icing compounds or substances.

Conversely, non-wetting surfaces, hydrophobic ones, having a low affinity for water interaction, are often considered for icephobic applications. Nevertheless, they do not generally respond extremely well to the anti-icing criteria. Particularly, polydimethylsiloxane (PDMS) is a promising material for anti-icing coatings due to its ability to repel water and allow water vapor permeability²¹⁷. Its permeability to water vapor enables the vapor to evaporate before it condenses and freezes²⁰⁹. Also, due to its elastomeric properties, PDMS enhances the mechanical properties of the surfaces, providing flexibility and resistance. Furthermore, PDMS can be surface-modified to improve its properties, and its durability and efficiency make it a sustainable, low-maintenance choice. This makes it an effective option for applications in aerospace, infrastructure, and heating systems, where ice accumulation could compromise safety or performance.

Superhydrophobic surfaces are anti-icing candidates thanks to the exceptional drop mobility to avoid ice formation from droplets impacts at sub-zero temperatures due to their reduced contact time between droplets and the surface²¹⁸. However, they show limitations under certain conditions. When droplets impact the surface at high velocities, they can penetrate into the surface at low temperatures, transitioning to a Wenzel state, which prevents rebound and facilitates ice nucleation^{219,220}. Additionally, at extremely low surface temperatures, they may fail and allow water droplets to freeze directly onto the surface²²¹. The effectiveness of drop rebound can also be compromised under high humidity due to effects^{222,223}. Also the surface roughness, specifically with dense nano-asperities can improve resistance to drop impalement^{224,225}.

1.4.4 Freezing delay and ice accretion

Another critical property for anti-icing surfaces is the ability to delay the freezing of water droplets deposited on them. This delay is typically quantified either by the time required for droplets to freeze at a specific temperature or by the temperature at which droplets freeze the surface and surrounding environment are gradually cooled (eq. 6). This property is particularly valuable in scenarios where water shedding is not feasible, such as with small droplets or non-tilted geometries. Freezing time can be affected by surface roughness, droplet volume, heat transfer efficiency between the substrate and the droplet, surface free energy, and interface energy barrier of the nucleating droplet. There are two main factors for delaying freezing time: 1) use of low surface free energy chemical materials, and 2) modification of the surface roughness and topography. Thus, superhydrophobic low surface free energy materials act as retardant of the phase transition since the condensed droplets cover small contact surface areas, tiny isolated droplets can grow, coalesce, and being easily removed. Meanwhile, despite that the presence of micro-nano structures can enhance the heterogeneous nucleation, the presence of air in the porosity of hierarchical surfaces can reduce the thermal conductivity^{226,227}. Thus, surface roughness with asperities smaller than the critical ice nuclei radius, can further enhance freezing delay²²⁸.

Optionally, SLIPS also exhibit icephobic properties, contributing to freezing delay due to reduced likelihood of heterogeneous nucleation²²⁹. Infiltrating an oily liquid in a porous solid matrix can hinder heat transfer between water droplets and the surface. However, they are not ideal for shedding supercooled water. Although droplets can roll off SLIPS, they do not bounce, which increases the contact time with the surface. Using a low viscosity lubricant can enhance droplet mobility and reduce the contact time²³⁰. For that, viscosity of the lubricant fluid affects the water droplet sliding velocity according to:

$$v = \frac{V(1-f_l)}{\mu_0} \quad (\text{equation } 7)$$

depending on the droplet volumen V , the area fraction of liquid layer f_i and the viscosity of the infused lubricant μ_o . However, it may also lead to significant lubricant depletion.

A complement to this response is the anti-frosting capability, which refers to the surface's ability to minimize or prevent frost formation. Frost is defined as ice that forms from humid air through desublimation²¹². However, under experimental conditions, the ice that forms may instead be rime ice²⁰⁰, which originates from small water droplets in fog that condense on the surface before freezing. Rime ice represents an intermediate form between frost and glaze ice, and its prevention is closely linked to the previously discussed property of water anti-condensation.

Regarding ice accretion, since simulating natural icing conditions in a climatic chamber is not available to common laboratories, the mass of ice accretion per unit area on the surface can hardly be estimated²³¹. Thus, depending on the environmental conditions, if water droplets can bounce from the surface prior to icing, superhydrophobicity is postulated as a potential reducer of ice accumulated mass. However, under high relative humidity, a frost layer can be formed on the surface suppressing its water repellent properties wich only could be beneficial if a liquid water interlayer remained on the hydrophilic converted surface affecting the ice accretion.

1.4.5 Ice adhesion

Low ice adhesion is a crucial property when ice has already formed on a surface, indicating that the preceding anti-icing mechanisms have been ineffective. When ice adhesion is minimized, mechanical removal of the ice particles via external forces becomes more feasible. Ideally, ice should detach under natural forces such as wind or gravity. A surface is generally classified as having low ice adhesion when the adhesion strength is below 100 kPa, while surfaces exhibiting ultra-low ice adhesion, where detachment can occur naturally, have adhesion strengths below 10 kPa²³². Surface roughness plays a negative role in ice adhesion, due to the fact that ice embedding and growth in roughness create a blocking mechanism (Figure 10 a)). On the contrary, it is preferable to have a lubricating material on the surface, either a liquid water or an oil interlayer between the ice and the surface. The work of adhesion, defined as the ratio of the

shear force of ice separation from a surface to the apparent contact area is related with the wetting of the surface through³³:

$$W_{adh} = \gamma_{LV}(1 + \cos\theta_R) \quad (\text{equation } 8)$$

where γ_{LV} and θ_R are the liquid droplet surface free energy and the receding water contact angle, respectively. However, on rough surfaces the mechanical ice interlock through van der Waals and hydrogen bonds interactions must be taken into account for the ice adhesion strength²³³:

$$W_{adh,r} = W_{coh}x\delta + W_{adh}x(1 - \delta) \quad (\text{equation } 9)$$

being W_{coh} the cohesive strength of ice (~ 1600 kPa), W_{adh} the adhesive strength of ice on an ideal flat surface and δ the ice area fraction interlocked with the micro-/nano- structured surface²³⁴.

Therefore, ice wetting behavior influences the ice detachment by a shear ice removal mode if an external force is applied on the ice/surface interface or by a concurrent ice shedding mode if the external force directed to keep the ice away from the ice/surface interface (Figure 10 b)).

Low adhesion surfaces, many of which are polymeric coatings used in industrial applications (e.g., demolding in the food industry), are proposed for icephobic purposes. These surfaces are generally hydrophobic and of relatively smooth texture. While hydrophobic and low adhesion surfaces can be related to reduced ice adhesion, it is well established that ice adhesion decreases as both water wettability and surface roughness decrease^{189,235}. However, even for very smoother hydrophobic surfaces, the reduction in ice adhesion is not sufficient to classify them as truly anti-icing surfaces, as the adhesion strength remains too high. Otherwise, hygroscopic polymers can absorb and retain moisture from the environment, forming a thin lubricating layer that prevents or reduces ice formation and adhesion. Their chemistry is defined by polar functional groups, such as hydroxyl (-OH), carboxyl (-COOH), and amine (-NH₂), which enable strong hydrogen bonding with water molecules. This hydrophilic nature allows them to dynamically respond to humidity and temperature changes, making them ideal for anti-icing surfaces. Common examples include polyethylene glycol

(PEG), polyacrylic acid (PAA), hydrogels like polyvinyl alcohol (PVA), hygroscopic polyurethane blends, and natural polymers such as chitosan²³⁶. Alternatively, although low ice adhesion has been reported for superhydrophobic surfaces with nanoscale roughness²³⁷, keeping this low adhesion is challenging. Problems such as ice interlocking with surface structure can hinder the reduction of ice adhesion^{238,239}. This issue is further compounded when frost or dew forms between surface textures in humid conditions. But the main peculiar strategy of low ice adhesion are the SLIPS, thanks to the ultra-smooth interface between the solid surface and the lubricant, as well as the mobility of this interface^{240,241}. However, during ice formation, the lubricant can migrate to the droplet or ice surface, leading to lubricant depletion after several freeze-thaw cycles. This migration can result in ice anchoring to the surface scaffold, increasing ice adhesion. To address these challenges, research efforts have focused on enhancing lubricant stability and durability²⁴². A more recent approach involves the use of hydrophobic surfaces with low elastic moduli. The key benefit lies in their deformability, which can result in exceptionally low ice adhesion²⁴³. For instance, elastic surfaces with subsurface hollow structures (macro-crack initiators) have demonstrated ultra-low ice adhesion due to enhanced fracture mechanisms at the interface coupled with the reduced modulus provided by the porous material^{244,245}. Recent advancements have led to the creation of enhanced Liquid-Infused Surfaces (LIS)²³⁶ with elastic porous silicones function as a polymer matrix for SLIPS of microdroplets reservoirs. They can minimize ice anchoring even in cases of oil depletion and improve durability thanks to the flexibility. Finally, liquid layer generators are another approach to reducing ice adhesion, because the presence of ions in an aqueous lubricating liquid layer on hygroscopic polymers blocks the interaction with ice and reduces the melting and freezing point. Hygroscopic polymers can absorb water even from the ice and release to keep an unfrozen liquid layer at the ice/surface interface²⁴⁶, which leads to exceptionally low ice adhesion. Notably, polymer matrix surfaces infused with anti-icing liquids can also be categorized as liquid layer generators²⁴⁷.

1.4.6 Durability of icephobic surfaces

In real life, the good passive anti-icing effect is related to whether the controlled wetting surface can be widely used. Mechanical weakness, chemical corrosion, ultraviolet light exposure, and temperature cycling among others can damage the stability of superhydrophobic surfaces²⁴⁸. Particularly, superhydrophobic surfaces may experience reduced durability due to wear during ice detachment^{249,250}. When the environmental conditions are aggressive, such as in presence of high relative humidity, low temperature, high wind speed or high altitude, water droplets can impact on the surface, get access to the inner porosity of hierarchical structures or condense over already formed ice particles. Furthermore, removal of ice from a surface by means of usual de-icing protocols where hierarchical structures needed for the superhydrophobic behavior may be seriously damaged²⁵¹. Therefore, it is needed to improve the multifunctionality of anti-icing/ice-phobic surfaces, i.e. mechanical, self-cleaning, anti-fouling, and anti-corrosion robust properties²⁴⁸ so as to optimize their practical application. Consequently, establishing stability and durability characterization protocols at laboratory scale becomes really necessary when one wants to evaluate the icephobicity behavior. For that, linear pressure wear and water impact under high pressure tests has been implemented using an Icing Wind Tunnel. Also, the resistance to abrasion and erosion tests, with solid particles and simulated rain, freezing-thawing cycling, chemical corrosion or UV light illumination are crucial aspects to check of a durable anti-icing surface.

1.5 Challenges for the design of robust repellent and icephobic surfaces

The significant technological and economic importance of control of wetting of surfaces applied in any environment, particularly as repellent surfaces, has made chemists, physicists, biologists, and engineers converge on a multidisciplinary research area of great interest. A clear indicator is the fast and substantial increase in the number of scientific publications in peer-reviewed journals, as can be seen in **Figure 12 a**). Additionally, it is important to note that this concern is not limited to academic research but also extends to technological and industrial levels, as reflected in the growing number of patents in recent years (**Figure 12 b**)). However, despite the considerable effort devoted to developing

highly repellent surfaces and the significant progress made in this field, current solutions are far from optimal performance considering stability, durability and multifunctionality criteria. Certain challenges still need to be overcome to successfully transfer surfaces engineering strategies for controlled wetting technologies from laboratories to daily life.

From the earliest superhydrophobic surfaces (SHS), inspired by the *lotus effect*, until today, the field of repellent surfaces has undergone significant interest for the scientific community in last years, leading to a deeper understanding of the principles and mechanisms involved in water-surface interaction, particularly at low temperature. Moreover, to be able to repel different organic liquids, solid particles, and biological agents plays a key role in a wide range of applications (Figure 12 d)).

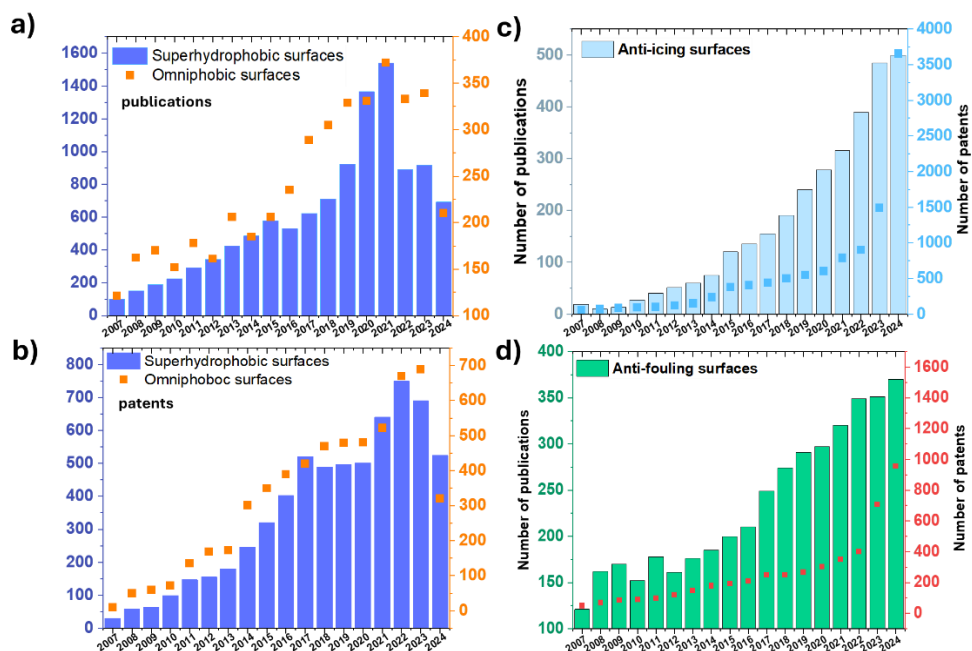


Figure 12. Scientific and technological evolution of the research on liquid repellent and anti-icing surfaces. a) Number of published papers in scientific journals, and b) number of published patents using superhydrophobic (purple bar) and omniphobic surfaces (orange spot). Scientific (bar) and technological (spot) evolution of the research on c) anti-icing surfaces and d) anti-fouling surfaces. (Source: spacemen patent research and Scopus).

Challenges associated to anti-icing surfaces primarily revolve around material performance, durability, energetic cost, and environmental impact²⁵². These factors have significantly influenced research output, leading to an increase in publications and patents over the two past decades as can be observed in Figure 12. The main challenges for anti-icing surfaces are related to material performance, finding configurations that effectively prevent ice adhesion while maintaining, or even offer, other functional properties. Emerging technologies represented through the number of patents in Figure 12 for the research on nanomaterials, biomimetic surfaces and smart systems prove the impact of the topic. For these reasons, along with strong industrial interest, a promising future for repellent and anti-icing surfaces can be anticipated. The state of the art is looking for contamination-free, stable and anti-icing surfaces what requires a series of scientific and technological challenges:

- **Durability**: one of the primary issues of repellent surfaces is their limited durability. Required structures, hierarchical porous topography, to achieve superhydrophobic or superomniphobic responses often lack mechanical strength. For the low-adhesion alternative, SLIPS, the durability largely depends on the stability of the lubricant layer, which can be easily depleted through leakage or evaporation, and the nanostructured container. Additionally, durability is a significant concern in terms of operating conditions, as these surfaces must endure extreme temperatures cycling, chemical environments, or liquid and solid abrasion. Therefore, the limited reliability is a crucial weakness that must be addressed to enable practical applications with optimal performance. Moreover, a consensus on common protocols for characterizing the interaction of the wetting controlled surfaces with the environment is trying to consolidate since the difficulty in accessing large facilities for extreme environment simulators and to establish standard values.
- **Multifunctionality**: currently, developments in highly repellent surfaces tend to focus on preventing the adhesion of specific liquids or fouling agents, and ice, at the cost of degenerating the functionalities of the material, especially if it is applied at severe environmental conditions. A

more universal technological integrated solution, capable of addressing a protective action, adaptable to the environment, compatible with multifunctional applications would mean impact a broad range of sectors.

- Surface compatibility and scalability: from a manufacturing perspective, scalability and energetic processing cost are also key issues. Advanced surface properties, like dual liquid and solid repellence, often require complex fabrication processes and simple geometric configuration of substrates, making real, and large-scale production difficult. Moreover, surface compatibility is required when repellent surfaces are to be generated on chemically and physically different substrate materials where functional integration and adhesion at the interface must withstand environmental changes such as temperature, pressure and humidity, as well as the impact of external agents. Particularly, surfaces of controlled wetting on thermally sensitive, flexible or transparent substrates without affecting their intrinsic properties is still a main research challenge. Modifying a surface to be repellent may compromise the genuine properties like heat resistance, adhesion, or optical transparency. Nowadays, techniques for fabricating repellent coatings through wet methods, such as dip-coating, spray-coating, and spin-coating, are widely used due to their versatility and low cost. These techniques enable the formation of functional coatings by applying precursor solutions that solidify or polymerize on the surface. However, difficulties in achieving uniform coverage on complex or large surfaces, limited coating adhesion to certain substrate materials, or low ecological waste generation point to the use of alternatives. Additionally, precise control of surface roughness required for repellence often demands rigorous processing optimization and sophisticated installations hardly scalable, which can increase development times and energy consumption. Other issues like inconsistent solvent evaporation, sensitivity to environmental conditions, and the tendency to generate defects, such as cracks or bubbles, can affect the quality and durability of the final coating²⁵³. Particularly, plasma treatment enhances surface cleaning, activation, and adhesion, improving coating bonding while

when assisted vacuum deposition techniques, allow precise, uniform deposition of thin films controlling the generation of new stoichiometries and improved surface properties preserving the bulk ones. Plasma and vacuum technologies also emerge as suitable for coating complex geometries and three-dimensional structures as well as compatible with flexible, soft, and sensible substrates thanks to the reduction of the working temperature until room conditions. Additionally, plasma deposition eliminates the need for solvents, making the process more environmentally friendly by reducing chemical waste and health risks. This solvent-free approach supports sustainable and safer manufacturing practices²⁵⁴.

- Environmentally friendly perspective: sustainability standards often limit the use of certain substances suitable for the desired functionality. The utilization of environmentally friendly materials for the design of repellent surfaces presents several issues regarding the current regulatory compliance about strict restrictions on fluorinated chemical compounds due to their environmental impact and potential bioaccumulation (the current framework is governed by Regulation (EU) 2024/573. Identifying alternatives that reduce the required content for optimal performance, be stable under operation avoiding release to the environment, or deliver similar performance without negative ecological consequences can be difficult. Ongoing research and development are necessary to find innovative material configurations that provide an effective liquid repellence while remaining sustainable. Lastly, new strategies must undergo rigorous testing to ensure they meet performance standards, a process that can be both time-consuming and costly, especially for those seeking eco-friendly certifications. Moreover, regarding the experimental processing techniques from an environmental perspective, wet deposition methods have significant drawbacks due to the use of organic solvents, which are often volatile, toxic, or non-biodegradable, contributing to air pollution and health risks. Additionally, these processes generate substantial chemical waste, as leftover solutions often require specialized disposal, increasing environmental impact and costs. These approaches also demand large

amounts of water or solvents for cleaning, further raising resource consumption and waste production. Without mitigation strategies, such as eco-friendly solvents or recycling processes, these techniques are not sustainable in the long term²⁵⁵. Therefore, feasibility must focus on the use of dry, clean processing techniques.

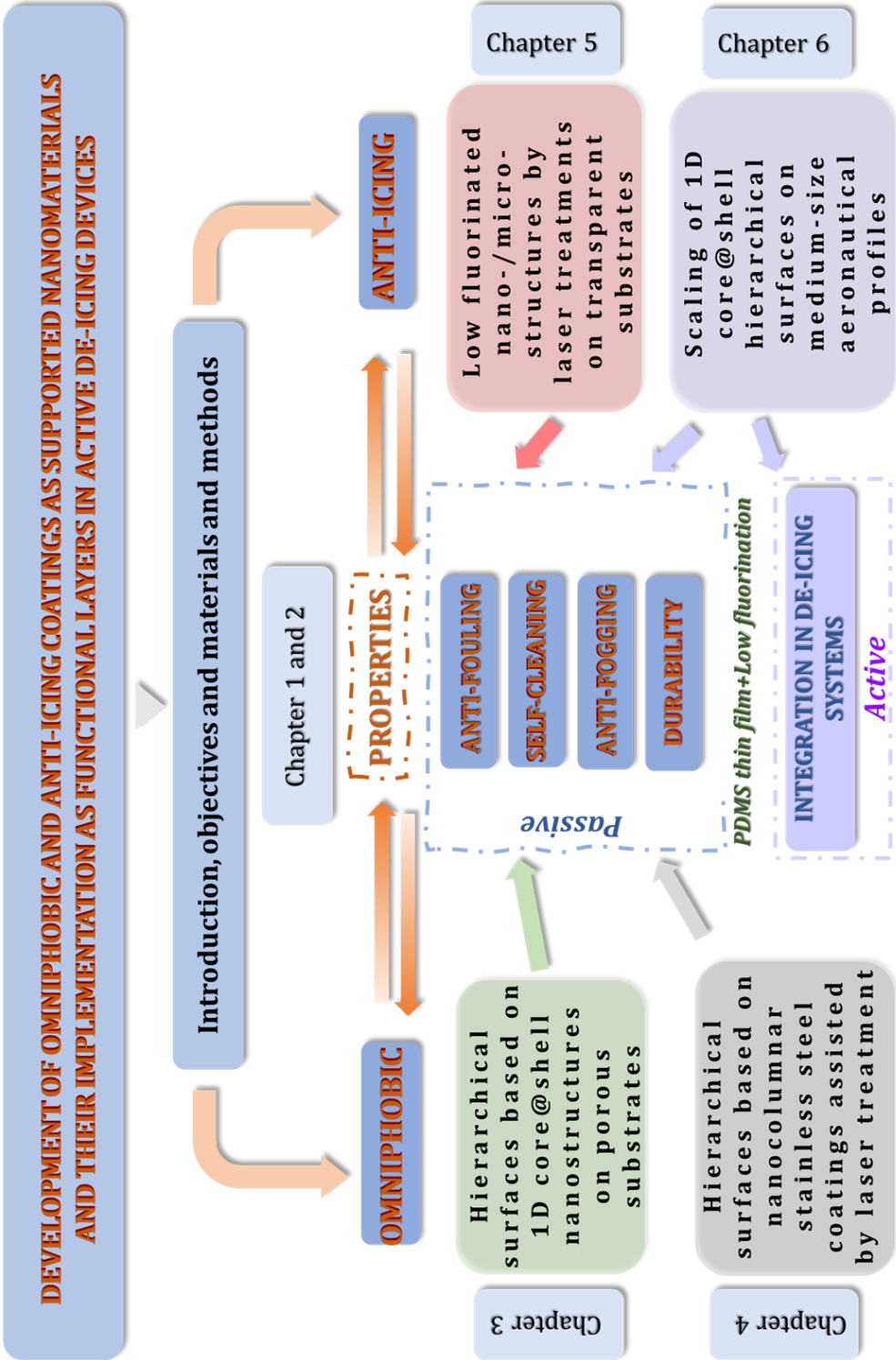
1.6 Objectives and outline of the thesis

The interaction between surfaces and the environment, including fluids, and solid external agents, particularly ice, poses significant challenges with high scientific and technological impacts. Novel mitigation strategies for wetting control and, especially ice accumulation, are being claimed from a practical point of view for different application fields such as energy production, transport, construction, city life and household facilities. Mainly new alternatives for providing stable protective surfaces against environmental changes must respect the specific functionality of the material, ensure good adaptable integration and be resistant to severe working conditions, an efficient and sustainable manufacturing route. This thesis proposes the development of robust passive surfaces of controlled wetting to work under simulated harsh environmental conditions. Particularly, the overall goal aims to be able to combine and tune superhydrophobic, omniphobic, anti-fouling, self-cleaning, anti-fogging and/or anti-icing properties compatible with multitude of functional materials. As innovative proposal, the integration of hierarchical structures with distinctive chemical modification proposals that respond to the challenges described above on different systems, from porous substrates to aeronautical profiles of complex geometries, highlighting ecological processing methodologies, will be intended. Thus, vacuum and plasma-assisted technologies offer key advantages for novel applications in materials science, electronics, optics, and biomedicine among others. These methods ensure high cleaning by operating in controlled environments, minimizing contamination and producing high-quality material properties. The second approach of this thesis is to be able to characterize under simulated environmental conditions the new wetting-derived properties at lab scale, particularly the anti-icing response, as well as at large scale advanced facilities (icing wind tunnel). And the third main objective is to integrate the multifunctional surface strategies on de-icing active systems.

A critical challenge in the development of wetting controlled surfaces implemented as passive anti-icing systems, besides the compatibility from the multi-stacking and energetic points of view, is their stability and durability working under real environmental conditions, such as temperature and humidity cycles or exposure to abrasive and corrosive agents like UV light, rain erosion, and liquids chemical immersion. Therefore, this thesis aims to develop surfaces with robust protective characteristics by ensuring omniphobic wetting behavior persistent at severe environmental conditions. This is achieved through an advanced surface nanoengineering approach capable of incorporating repellent, anti-fouling, and anti-icing functionalities using scalable thin film technologies based on vacuum and plasma techniques, compatible with any substrate and geometry. The objectives proposed in this thesis will be focused on:

- ❖ Development of robust functional surfaces of controlled wetting by means of the generation of a hierarchical structure. Particularly, three levels of roughness scale based on the fabrication of supported one dimensional (1D) core@shell nanostructures by vacuum and plasma technologies, compatible with porous substrates will be explored to provide wetting selectivity, and superhydrophobicity of potential application in liquid separation and self-cleaning (**Chapter 3**).
- ❖ Combination of special chemical modification through flexible polymeric coatings and low surface fluorination approach with hierarchical topography to get omniphobicity for a stable multi-repellency response of porous membranes (**Chapter 3**).
- ❖ Generation of durable repellent multifunctional hierarchical stainless steel surfaces by the combination of laser treatment with nanocolumnar coatings and the chemical surface modification by different low fluorination strategies: from solid coatings to SLIPS passing for chemical grafting to achieve anti-fouling, anti-corrosive, self-cleaning and anti-icing capabilities (**Chapter 4**).

- ❖ Fabrication of stable superhydrophobic, omniphobic, anti-fogging and anti-icing transparent surfaces through the combination of patterned micro-/nano-structuration of glass by laser treatment with low fluorinated surface functionalization (**Chapter 5**).
- ❖ Scaling at medium substrate size and complex geometries of the multifunctional hierarchical surface fabrication, based on the supported core@shell nanostructures strategy, controlling the surface aspect ratio for durable icephobic passive properties tested under realistic environmental conditions at large advanced facilities (**Chapter 6**).
- ❖ Demonstration of the compatibility of the passive anti-icing multifunctional hierarchical surfaces integrated in active de-icing devices, based on electrothermal effect and on surface acoustic waves, as robust repellent protective external elements (**Chapter 6**).



Bibliography

1. Marmur, A., Della Volpe, C., Siboni, S., Amirfazli, A. & Drelich, J. W. Contact angles and wettability: towards common and accurate terminology. *Surf Innov* **5**, 3–8 (2017).
2. de Oliveira, R. K., Correa, O. V., de Oliveira, M. C. L. & Antunes, R. A. Surface Chemistry and Semiconducting Properties of Passive Film and Corrosion Resistance of Annealed Surgical Stainless Steel. *J Mater Eng Perform* **29**, 6085–6100 (2020).
3. Kato, K. Wear in relation to friction - A review. *Wear* **241**, 151–157 (2000).
4. Castner, D. G. & Ratner, B. D. Biomedical Surface Science: Foundations to Frontiers. *Surface Science* **500**, 28–60 (2002).
5. Khalili, A. A. & Ahmad, M. R. A Review of cell adhesion studies for biomedical and biological applications. *International Journal of Molecular Sciences* **16**, 18149–18184 (2015).
6. Singh, B. *et al.* Single-Atom Catalysts: A Sustainable Pathway for the Advanced Catalytic Applications. *Small* **17**, 1–27 (2021).
7. Tao, F. (Feng) & Crozier, P. A. Atomic-Scale Observations of Catalyst Structures under Reaction Conditions and during Catalysis. *Chem Rev* **116**, 3487–3539 (2016).
8. Zhao, C. X. *et al.* Multiscale Construction of Bifunctional Electrocatalysts for Long-Lifespan Rechargeable Zinc–Air Batteries. *Adv Funct Mater* **30**, (2020).
9. Vilan, A. & Cahen, D. Chemical Modification of Semiconductor Surfaces for Molecular Electronics. *Chem Rev* **117**, 4624–4666 (2017).
10. Saini, M. Implant biomaterials: A comprehensive review. *World J Clin Cases* **3**, 52 (2015).
11. Rupp, F., Liang, L., Geis-Gerstorfer, J., Scheideler, L. & Hüttig, F. Surface characteristics of dental implants: A review. *Dental Materials* **34**, 40–57 (2018).
12. Bell, T. Surface Engineering: Past, Present and Future. *Surface Engineering* **6**, 31–40 (1990).
13. El-Awadi, G. A. Review of effective techniques for surface engineering material modification for a variety of applications. *AIMS Mater Sci* **10**, 652–692 (2023).
14. Mozetič, M. Surface modification to improve properties of materials. *Materials* **12**, 22–29 (2019).
15. Swarn, S., Santosh K., and Khanna V. A review on surface modification techniques. *Mater Today* **19**, Preprint (2024).
16. Mehta, A., Vasudev, H. & Singh, S. Recent developments in the designing of deposition of thermal barrier coatings – A review. *Mater Today Proc* **26**, 1336–1342 (2020).
17. Schmidt, V. & Belegreatis, M. R. *Biological and Medical Physics, Biomedical Engineering Laser Technology in Biomimetics Basics and Applications* (2013).
18. Yang, H., Zheng, H. & Zhang, T. A review of artificial intelligent methods for machined surface roughness prediction. *Tribology International* **199**, Preprint (2024).
19. Hu, Y., Ou, J. & Amirfazli, A. Application of Surface Wettability to Control Spreading of an Impacting Droplet. *Langmuir* **40**, 4623–4634 (2024).
20. Bhushan, B. & Jung, Y. C. Natural and biomimetic artificial surfaces for superhydrophobicity, self-cleaning, low adhesion, and drag reduction. *Progress in Materials Science* **56**, 1–108 (2011).
21. Barati Darband, G., Aliofkhaezaei, M., Khorsand, S., Sokhanvar, S. & Kaboli, A. Science and Engineering of Superhydrophobic Surfaces: Review of Corrosion Resistance, Chemical and Mechanical Stability. *Arabian Journal of Chemistry* **13**, 1763–1802 (2020).
22. Cao, L., Jones, A. K., Sikka, V. K., Wu, J. & Gao, D. Anti-Icing Superhydrophobic Coatings. *Langmuir* **25**, 12444–12448 (2009).
23. Zhang, Y., Zhang, Z., Yang, J., Yue, Y. & Zhang, H. A review of recent advances in superhydrophobic surfaces and their applications in drag reduction and heat transfer. *Nanomaterials* **12**, 44 (2022).
24. Etale, A., Onyianta, A. J., Turner, S. R. & Eichhorn, S. J. Cellulose: A Review of Water Interactions, Applications in Composites, and Water Treatment. *Chemical Reviews* **123**, 2016–2048 (2023).

25. Wang, L. & McCarthy, T. J. Covalently Attached Liquids: Instant Omniphobic Surfaces with Unprecedented Repellency. *Angewandte Chemie International Edition* **55**, 244–248 (2016).
26. Spori, D. M. *et al.* Beyond the lotus effect: Roughness influences on wetting over a wide surface-energy range. *Langmuir* **24**, 5411–5417 (2008).
27. Callow, M. E. & Fletcher, R. L. *The Influence of Low Surface Energy Materials on Bioadhesion a Review. International Biodeterioration & Biodegradation* (1994).
28. Mu, M. *et al.* Influence of Surface Roughness, Nanostructure, and Wetting on Bacterial Adhesion. *Langmuir* **39**, 5426–5439 (2023).
29. Nadi, A., Boukhriss, A., Bentis, A., Jabrane, E. & Gmouh, S. Evolution in the surface modification of textiles: a review. *Textile Progress* **50**, 67–108 (2018).
30. Mozetič, M. Surface modification to improve properties of materials. *Materials* **12**, 441 (2019).
31. Chau, T. T. A review of techniques for measurement of contact angles and their applicability on mineral surfaces. *Miner Eng* **22**, 213–219 (2009).
32. Oberli, L. *et al.* Condensation and freezing of droplets on superhydrophobic surfaces. *Advances in Colloid and Interface Science* **210**, 47–57 (2014).
33. Gao, L., McCarthy, T. J. & Zhang, X. Wetting and Superhydrophobicity. *Langmuir* **25**, 14100–14104 (2009).
34. Wahab, I. F. *et al.* Fundamentals of antifogging strategies, coating techniques and properties of inorganic materials; a comprehensive review. *Journal of Materials Research and Technology* **23**, 687–714 (2023).
35. Zhou, L., Li, X., Zhu, B. & Su, B. An Overview of Antifouling Strategies for Electrochemical Analysis. *Electroanalysis* **34**, 966–975 (2022).
36. Belhadjamor, M., El Mansori, M., Belghith, S. & Mezlini, S. Anti-fingerprint properties of engineering surfaces: a review. *Surface Engineering* **34**, 85–120 (2018).
37. Wu, X., Chu, F., Orejon, D. & Mouterde, T. Superhydrophobic surfaces: Fundamentals, manufacture, and applications. *Appl Phys Lett* **124**, 8–11 (2024).
38. Farag, A. A., Mohamed, E. A. & Toghian, A. The new trends in corrosion control using superhydrophobic surfaces: a review. *Corrosion Reviews* **41**, 21–37 (2023).
39. Ashok, D. *et al.* Superhydrophobic Surfaces to Combat Bacterial Surface Colonization. *Adv Mater Interfaces* **10**, (2023).
40. Psarski, M. *et al.* Vapor phase deposition of fluoroalkyl trichlorosilanes on silicon and glass: Influence of deposition conditions and chain length on wettability and adhesion forces. *Mater Chem Phys* **204**, 305–314 (2018).
41. Fiedler, H., Kennedy, T. & Henry, B. J. A Critical Review of a Recommended Analytical and Classification Approach for Organic Fluorinated Compounds with an Emphasis on Per- and Polyfluoroalkyl Substances. *Integr Environ Assess Manag* **17**, 331–351 (2021).
42. Han, J. *et al.* Chemical Aspects of Human and Environmental Overload with Fluorine. *Chemical Reviews* **121**, 4678–4742 (2021).
43. Ezeorba, T. P. C. *et al.* Emerging eco-friendly technologies for remediation of Per- and poly-fluoroalkyl substances (PFAS) in water and wastewater: A pathway to environmental sustainability. *Chemosphere* **364**, (2024).
44. Chabas, A. *et al.* Behaviour of self-cleaning glass in urban atmosphere. *Build Environ* **43**, 2124–2131 (2008).
45. Palmisano, P., Hernandez, S. P., Hussain, M., Fino, D. & Russo, N. A new concept for a self-cleaning household oven. *Chemical Engineering Journal* **176–177**, 253–259 (2011).
46. Liu, G. *et al.* A review of various self-cleaning surfaces, durability and functional applications on building exteriors. *Construction and Building Materials* **409**, 134084 (2023).
47. Wang, P., Yan, X., Zeng, J., Luo, C. & Wang, C. Anti-Reflective superhydrophobic coatings with excellent durable and Self-cleaning properties for solar cells. *Appl Surf Sci* **602**, (2022).
48. Latthe, S. S. *et al.* Self – cleaning superhydrophobic coatings: Potential industrial applications. *Prog Org Coat* **128**, 52–58 (2019).

49. Adak, D., Bhattacharyya, R. & Barshilia, H. C. A state-of-the-art review on the multifunctional self-cleaning nanostructured coatings for PV panels, CSP mirrors and related solar devices. *Renewable and Sustainable Energy Reviews* **159**, 112145 (2022).
50. Wu, P., Xue, Z., Yu, T. & Penkov, O. V. Transparent Self-Cleaning Coatings: A Review. *Coatings* **13**, 1270 (2023).
51. Dalili, N., Edrisy, A. & Carriveau, R. A review of surface engineering issues critical to wind turbine performance. *Renewable and Sustainable Energy Reviews* **13**, 428–438 (2009).
52. Matthews A., *Advanced Surface Coatings: a Handbook of Surface Engineering* (1191).
53. Kurella A., Dahotre B. *Surface Modification for Bioimplants: The Role of Surface* (2005).
54. Zhao, X. & Chen, X. D. A Critical Review of basic crystallography to salt crystallization fouling in heat exchangers. in *Heat Transfer Engineering* **34**, 719–732 (2013).
55. Percival, S. L., Suleman, L., Vuotto, C. & Donelli, G. Healthcare-associated infections, medical devices and biofilms: risk, tolerance and control. *J Med Microbiol* **64**, 323–334 (2015).
56. Verran, J. Biofouling in food processing: Biofilm or biotransfer potential? *Food and Bioproducts Processing: Transactions of the Institution of Chemical Engineers, Part C* **80**, 292–298 (2002).
57. Goode, K. R., Asteriadou, K., Robbins, P. T. & Fryer, P. J. Fouling and Cleaning Studies in the Food and Beverage Industry Classified by Cleaning Type. *Compr Rev Food Sci Food Saf* **12**, 121–143 (2013).
58. Callow, M. E. & Callow, J. E. Marine biofouling: a sticky problem. *Biologist (London)* **49**, 10–4 (2002).
59. Verran, J. Biofouling in food processing: Biofilm or biotransfer potential? *Food and Bioproducts Processing: Transactions of the Institution of Chemical Engineers, Part C* **80**, 292–298 (2002).
60. Cao, Y., Tan, W. & Wu, Z. Aircraft icing: An ongoing threat to aviation safety. *Aerospace Science and Technology* **75**, 353–385 (2018).
61. Kreder, M. J., Alvarenga, J., Kim, P. & Aizenberg, J. Design of anti-icing surfaces: Smooth, textured or slippery? *Nature Reviews Materials* **1**, (2016).
62. Laforte, J. L., Allaire, M. A. & Laflamme, J. State-of-the-art on power line de-icing. *Atmos Res* **46**, 143–158 (1998).
63. Epa, U., of Water, O. & of Science, O. *Technical Development Document for the Effluent Limitations Guidelines and Standards for the Oil and Gas Extraction Point Source Category*. (2016).
64. Zhang, K. & Kevern, J. Review of porous asphalt pavements in cold regions: the state of practice and case study repository in design, construction, and maintenance. *Journal of Infrastructure Preservation and Resilience* **2**, 1-4 (2021).
65. Wang, L. *et al.* The Causes and Forecasting of Icing Events on Power Transmission Lines in Southern China: A Review and Perspective. *Atmosphere* **14**, 1815 (2023).
66. Machielsen, C. H. M. & Kerschbaumer, H. G. Influence of Frost Formation and Defrosting on the Performance of Air Coolers: Standards and Dimensionless Coefficients for the System Designer (1989).
67. Carriveau, R., Edrisy, A., Cadieux, P. & Mailloux, R. Ice Adhesion Issues in Renewable Energy Infrastructure. *J Adhes Sci Technol* **26**, 447–461 (2012).
68. Edrisy, A. & Carriveau, R. A review of surface engineering issues critical to wind turbine performance. *Renewable and Sustainable Energy Reviews* **13**, 428–438 (2009).
69. Gilaberte-Búrdalo, M., López-Martín, F., Pino-Otín, M. R. & López-Moreno, J. I. Impacts of climate change on ski industry. *Environmental Science and Policy* **44**, 51–61 (2014).
70. Olefs, M. & Fischer, A. Comparative study of technical measures to reduce snow and ice ablation in Alpine glacier ski resorts. *Cold Reg Sci Technol* **52**, 371–384 (2008).
71. Martin J., Damon P., & Nitin H. *Ice Detection System Global Market Report*. (2024).
72. Thomas Y. An essay on the cohesion of fluids. *Abstracts of the Papers Printed in the Philosophical Transactions of the Royal Society of London* **1**, 171–172 (1832).
73. Victor R. Preedy. *Coffee in Health and Disease Prevention*. (1997).
74. Wang, X. *et al.* Research on Mesoscale Nucleation and Growth Processes in Solution Crystallization: A Review. *Crystals* **12**, 12356 (2022).

75. Eral, H. B., T Mannelje, D. J. C. M. & Oh, J. M. Contact angle hysteresis: A review of fundamentals and applications. *Colloid and Polymer Science* **291**, 247–260 (2013).
76. Krasovitski, B. & Marmur, A. Drops Down the Hill: Theoretical Study of Limiting Contact Angles and the Hysteresis Range on a Tilted Plate. *Langmuir* **21**, 3881–3885 (2005).
77. Tadmor, R. Line energy and the relation between advancing, receding, and Young contact angles. *Langmuir* **20**, 7659–7664 (2004).
78. Butt, H. J. *et al.* Contact angle hysteresis. *Current Opinion in Colloid and Interface Science* **59**, (2022).
79. *Industrial and Engineering Chemistry Specific Heats at Constant Volume of Mix-Tures of Methane and Crude Oil* (2002).
80. Milne, A. J. B. & Amirfazli, A. The Cassie equation: How it is meant to be used. *Advances in Colloid and Interface Science* **170**, 48–55 (2012).
81. Ge, P., Wang, S., Zhang, J. & Yang, B. Micro-/nanostructures meet anisotropic wetting: from preparation methods to applications. *Mater Horiz* **7**, 2566–2595 (2020).
82. Si, Y., Yu, C., Dong, Z. & Jiang, L. Wetting and spreading: Fundamental theories to cutting-edge applications. *Current Opinion in Colloid and Interface Science* **36**, 10–19 (2018).
83. Wang, X., Fu, C., Zhang, C., Qiu, Z. & Wang, B. A Comprehensive Review of Wetting Transition Mechanism on the Surfaces of Microstructures from Theory and Testing Methods. *Materials* **15**, 4747 (2022).
84. Kim, D., Pugno, N. M. & Ryu, S. Wetting theory for small droplets on textured solid surfaces. *Sci Rep* **6**, 37813 (2016).
85. S Sreeramagiri, S. V. Biomimetics: Applications in Structural Design an overview Biomimetics: Applications in Structural Design. **10**, (2021).
86. Himel, M. H., Sikder, B., Ahmed, T. & Choudhury, S. M. Biomimicry in nanotechnology: a comprehensive review. *Nanoscale Adv* **5**, 596–614 (2023).
87. Barthlott, W. Self-Cleaning Surfaces in Plants: The Discovery of the Lotus Effect as a Key Innovation for Biomimetic Technologies. in *Handbook of Self-Cleaning Surfaces and Materials* **29**, 359–369 (2023).
88. Wagner, T., Neinhuis, C. & Barthlott, W. Wettability and Contaminability of Insect Wings as a Function of Their Surface Sculptures. *Acta Zoologica* **77**, 213–225 (1996).
89. Helbig, R., Nickerl, J., Neinhuis, C. & Werner, C. Smart Skin Patterns Protect Springtails. *PLoS One* **6**, 25105 (2011).
90. Gupta, S., Ivvala, J. & Grewal, H. S. Development of natural wax based durable superhydrophobic coatings. *Ind Crops Prod* **171**, (2021).
91. Dou, X. Q., Zhang, D., Feng, C. & Jiang, L. Bioinspired Hierarchical Surface Structures with Tunable Wettability for Regulating Bacteria Adhesion. *ACS Nano* **9**, 10664–10672 (2015).
92. Milne, A., Amirfazli, A. The Cassie equation: How it is meant to be used. *Adv. Colloid. Interf.* **170**, 48-55 (2012).
93. *INDUSTRIAL AND ENGINEERING CHEMISTRY Specific Heats at Constant Volume of Mix-Tures of Methane and Crude Oil*. <https://pubs.acs.org/sharingguidelines>.
94. Cassie, B. A. & Baxter, Studies about Surfaces interactions (2003).
95. Wong, T. S. *et al.* Bioinspired self-repairing slippery surfaces with pressure-stable omniphobicity. *Nature* **477**, 443–447 (2011).
96. Boban, M. *et al.* Smooth, All-Solid, Low-Hysteresis, Omniphobic Surfaces with Enhanced Mechanical Durability. *ACS Appl Mater Interfaces* **10**, 11406–11413 (2018).
97. Lazo, M. A. G., Katrantzis, I., Vacche, S. D., Karasu, F. & Leterrier, Y. A facile in situ and UV printing process for bioinspired Self-cleaning surfaces. *Materials* **9**, (2016).
98. Kim, P., Kreder, M. J., Alvarenga, J. & Aizenberg, J. Hierarchical or not? Effect of the length scale and hierarchy of the surface roughness on omniphobicity of lubricant-infused substrates. *Nano Lett* **13**, 1793–1799 (2013).
99. Ulman, A. *Formation and Structure of Self-Assembled Monolayers* (1996).
100. Jiang, G., Hu, J. & Chen, L. Preparation of a Flexible Superhydrophobic Surface and Its Wetting Mechanism Based on Fractal Theory. *Langmuir* **36**, 8435–8443 (2020).

101. Barthlott, W. Self-Cleaning Surfaces in Plants: The Discovery of the Lotus Effect as a Key Innovation for Biomimetic Technologies. in *Handbook of Self-Cleaning Surfaces and Materials* 359–369 (2023).
102. Wong, T. S. *et al.* Bioinspired self-repairing slippery surfaces with pressure-stable omniphobicity. *Nature* **477**, 443–447 (2011).
103. Kim, P. *et al.* Liquid-Infused Nanostructured Surfaces with Extreme Anti-Ice and Anti-Frost Performance. *ACS Nano* **6**, 6569–6577 (2012).
104. Vogel, N., Belisle, R. A., Hatton, B., Wong, T. S. & Aizenberg, J. Transparency and damage tolerance of patternable omniphobic lubricated surfaces based on inverse colloidal monolayers. *Nat Commun* **4**, (2013).
105. Tripathi, D., Ray, P., Singh, A. V., Kishore, V. & Singh, S. L. Durability of Slippery Liquid-Infused Surfaces: Challenges and Advances. *Coatings* **13**, (2023).
106. Kasapgil, E., Erbil, H. Y. & Anac Sakir, I. Multi-liquid repellent, fluorine-free, heat stable SLIPS via layer-by-layer assembly. *Colloids Surf A Physicochem Eng Asp* **654**, (2022).
107. Attinger, D. *et al.* Surface engineering for phase change heat transfer: A review. *MRS Energy and Sustainability* **1**,(2014).
108. Gupta, M. C. & Mulrone, A. Ice Adhesion and Anti-Icing Using Microtextured Surfaces. in *Ice Adhesion* **41**, 389–415 (2020).
109. Feng, X., Zhang, X. & Tian, G. Recent advances in bioinspired superhydrophobic ice-proof surfaces: challenges and prospects. *Nanoscale* **14**, 5960–5993 (2022).
110. Zhu Z., Zhang Y., & Sun D. Biomimetic modification of freezing facility surfaces to prevent icing and frosting during for the food industry. *Trends food Sci. Technol* **111**, 581–594 (2021).
111. Li, Q. & Guo, Z. Fundamentals of icing and common strategies for designing biomimetic anti-icing surfaces. *J Mater Chem A Mater* **6**, 13549–13581 (2018).
112. Rasitha, T. P., Krishna, N. G., Anandkumar, B., Vanithakumari, S. C. & Philip, J. A comprehensive review on anticorrosive/antifouling superhydrophobic coatings: Fabrication, assessment, applications, challenges and future perspectives. *Advances in Colloid and Interface Science* **324**, Preprint (2024).
113. Rekuviene, R. *et al.* A review on passive and active anti-icing and de-icing technologies. *Applied Thermal Engineering* **250**, Preprint (2024).
114. Wang, T. *et al.* Passive Anti-Icing and Active Deicing Films. *ACS Appl Mater Interfaces* **8**, 14169–14173 (2016).
115. Xu, S., Wang, Q. & Wang, N. Chemical Fabrication Strategies for Achieving Bioinspired Superhydrophobic Surfaces with Micro and Nanostructures: A Review. *Adv Eng Mater* **23**, 1–21 (2021).
116. Puls, S. *et al.* Benchmarking the reproducibility of all-solid-state battery cell performance. *Nature Energy* 2024 **13**, 1–11 (2024).
117. Behnoudfar, D., Dragila, M. I., Meisenheimer, D. & Wildenschild, D. Contact angle hysteresis: A new paradigm? *Adv Water Resour* **161**, (2022).
118. Quéré. Non-sticking drops. (2005).
119. Quan, Y. Y., Zhang, L. Z., Qi, R. H. & Cai, R. R. Self-cleaning of Surfaces: The role of surface wettability and dust types. *Sci Rep* **6**, (2016).
120. Roura, P. & Fort, J. Comment on ‘effects of the surface roughness on sliding angles of water droplets on superhydrophobic surfaces’. *Langmuir* **18**, 566–569 (2002).
121. Wolansky, G. & Marmur, A. *Apparent Contact Angles on Rough Surfaces: The Wenzel Equation Revisited. Colloids and Surfaces A: Physicochemical and Engineering Aspects* **156**, (1999).
122. Spori, D. M. *et al.* Beyond the lotus effect: Roughness influences on wetting over a wide surface-energy range. *Langmuir* **24**, 5411–5417 (2008).
123. Nakajima, A. *et al.* Transparent superhydrophobic thin films with self-cleaning properties. *Langmuir* **16**, 7044–7047 (2000).
124. Liu, C. *et al.* Laplace Pressure Difference Enhances Droplet Coalescence Jumping on Superhydrophobic Structures. *Langmuir* **38**, 6923–6933 (2022).

125. Hejazi, V., Moghadam, A. D., Rohatgi, P. & Nosonovsky, M. Beyond Wenzel and Cassie-Baxter: Second-order effects on the wetting of rough surfaces. *Langmuir* **30**, 9423–9429 (2014).
126. Wu, L., Dong, Z., Li, F. & Song, Y. Designing Laplace Pressure Pattern for Microdroplet Manipulation. *Langmuir* **34**, 639–645 (2018).
127. Edward Yu. Bormashenko. *Wetting of Real Surfaces* **19** (2013).
128. Lecointre, P. *et al.* Unique and universal dew-repellency of nanocones. *Nat Commun* **12**, (2021).
129. Bayat, A., Ebrahimi, M., Ardekani, S. R., Iranizad, E. S. & Moshfegh, A. Z. Extended Gibbs Free Energy and Laplace Pressure of Ordered Hexagonal Close-Packed Spherical Particles: A Wettability Study. *Langmuir* **37**, 8382–8392 (2021).
130. Feng, L. *et al.* Petal Effect: A Superhydrophobic State with High Adhesive Force. *Langmuir* **24**, 4114–4119 (2008).
131. Chu, Z., Feng, Y. & Seeger, S. Oil/Water Separation with Selective Superantiwetting/Superwetting Surface Materials. *Angewandte Chemie International Edition* **54**, 2328–2338 (2015).
132. Gu, J., Fan, H., Li, C., Caro, J. & Meng, H. Robust Superhydrophobic/Superoleophilic Wrinkled Microspherical MOF@rGO Composites for Efficient Oil–Water Separation. *Angewandte Chemie International Edition* **58**, 5297–5301 (2019).
133. Vazirinasab, E., Jafari, R. & Momen, G. Application of superhydrophobic coatings as a corrosion barrier: A review. *Surf Coat Technol* **341**, 40–56 (2018).
134. Xie, J. *et al.* Robust and anti-corrosive PDMS/SiO₂ superhydrophobic coatings fabricated on magnesium alloys with different-sized SiO₂ nanoparticles. *Appl Surf Sci* **457**, 870–880 (2018).
135. Latthe, S. S. *et al.* Self – cleaning superhydrophobic coatings: Potential industrial applications. *Prog Org Coat* **128**, 52–58 (2019).
136. Manoj, T. P. *et al.* A simple, rapid and single step method for fabricating superhydrophobic titanium surfaces with improved water bouncing and self cleaning properties. *Appl Surf Sci* **512**, 145636 (2020).
137. Bixler, G. D., Theiss, A., Bhushan, B. & Lee, S. C. Anti-fouling properties of microstructured surfaces bio-inspired by rice leaves and butterfly wings. *J Colloid Interface Sci* **419**, 114–133 (2014).
138. Sun, Q. *et al.* Facile preparation of superhydrophobic PVDF microporous membranes with excellent anti-fouling ability for vacuum membrane distillation. *J Memb Sci* **605**, 118106 (2020).
139. Rajappan, A. *et al.* Influence of textural statistics on drag reduction by scalable, randomly rough superhydrophobic surfaces in turbulent flow. *Physics of Fluids* **31**, (2019).
140. Wang, L. *et al.* Anti-fogging performances of liquid metal surface modified by ZnO nanoparticles. *J Taiwan Inst Chem Eng* **95**, 65–70 (2019).
141. Varshney, P., Lomga, J., Gupta, P. K., Mohapatra, S. S. & Kumar, A. Durable and regenerable superhydrophobic coatings for aluminium surfaces with excellent self-cleaning and anti-fogging properties. *Tribol Int* **119**, 38–44 (2018).
142. Zhao, C. *et al.* Multiscale Construction of Bifunctional Electrocatalysts for Long-Lifespan Rechargeable Zinc–Air Batteries. *Adv Funct Mater* **30**, (2020).
143. Li, X., Reinhoudt, D. & Crego-Calama, M. What Do We Need for a Superhydrophobic Surface? A Review on the Recent Progress in the Preparation of Superhydrophobic Surfaces. *ChemInform* **38**, (2007).
144. Kim, J. H., Mirzaei, A., Kim, H. W. & Kim, S. S. Facile fabrication of superhydrophobic surfaces from austenitic stainless steel (AISI 304) by chemical etching. *Appl Surf Sci* **439**, 598–604 (2018).
145. Qian, B. & Shen, Z. Fabrication of Superhydrophobic Surfaces by Dislocation-Selective Chemical Etching on Aluminum, Copper, and Zinc Substrates. *Langmuir* **21**, 9007–9009 (2005).

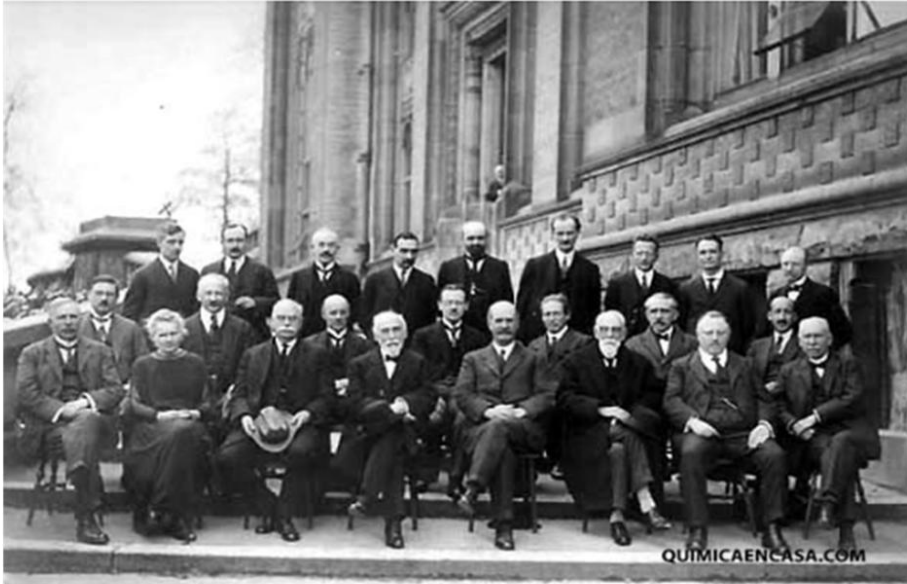
146. Dimitrakellis, P. & Gogolides, E. Hydrophobic and superhydrophobic surfaces fabricated using atmospheric pressure cold plasma technology: A review. *Advances in Colloid and Interface Science* **254**, (2018).
147. Kostal, E., Stroj, S., Kasemann, S., Matylitsky, V. & Domke, M. Fabrication of Biomimetic Fog-Collecting Superhydrophilic-Superhydrophobic Surface Micropatterns Using Femtosecond Lasers. *Langmuir* **34**, 2933–2941 (2018).
148. Boinovich, L. B. *et al.* Combination of Functional Nanoengineering and Nanosecond Laser Texturing for Design of Superhydrophobic Aluminum Alloy with Exceptional Mechanical and Chemical Properties. *ACS Nano* **11**, 10113–10123 (2017).
149. Yang, Z., Liu, X. & Tian, Y. A contrastive investigation on anticorrosive performance of laser-induced super-hydrophobic and oil-infused slippery coatings. *Prog Org Coat* **138**, (2020).
150. Rose, M. A., Bowen, J. J. & Morin, S. A. Emergent Soft Lithographic Tools for the Fabrication of Functional Polymeric Microstructures. *ChemPhysChem* **20**, 909–925 Preprint (2019).
151. Gao, X. *et al.* The Dry-Style Antifogging Properties of Mosquito Compound Eyes and Artificial Analogues Prepared by Soft Lithography. *Advanced Materials* **19**, 2213–2217 (2007).
152. Maghsoudi, K., Momen, G., Jafari, R. & Farzaneh, M. Direct replication of micro-nanostructures in the fabrication of superhydrophobic silicone rubber surfaces by compression molding. *Appl Surf Sci* **458**, 619–628 (2018).
153. Chen, S., Lin, D., Li, H., Lai, X. & Zeng, X. Facile fabrication of superhydrophobic, flame-retardant and conductive polyurethane sponge via dip-coating. *Mater Lett* **287**, 129307 (2021).
154. Karunakaran, R. G., Lu, C.-H., Zhang, Z. & Yang, S. Highly Transparent Superhydrophobic Surfaces from the Coassembly of Nanoparticles (≤ 100 nm). *Langmuir* **27**, 4594–4602 (2011).
155. Latthe, S. S., Terashima, C., Nakata, K. & Fujishima, A. Superhydrophobic surfaces developed by mimicking hierarchical surface morphology of lotus leaf. *Molecules* **19**, 4256–4283 (2014).
156. Rao, A. V., Latthe, S. S., Mahadik, S. A. & Kappenstein, C. Mechanically stable and corrosion resistant superhydrophobic sol-gel coatings on copper substrate. *Appl Surf Sci* **257**, 5772–5776 (2011).
157. Yang, M. *et al.* Fabrication of superhydrophobic cotton fabric with fluorinated TiO₂ sol by a green and one-step sol-gel process. *Carbohydr Polym* **197**, 75–82 (2018).
158. Ragesh, P., Anand Ganesh, V., Nair, S. V. & Nair, A. S. A review on 'self-cleaning and multifunctional materials'. *Journal of Materials Chemistry A* **2**, 14773–14797 (2014).
159. Geyer, F. *et al.* When and how self-cleaning of superhydrophobic surfaces works. *Sci Adv* **6**, (2020).
160. Wen, Q. & Guo, Z. Recent Advances in the Fabrication of Superhydrophobic Surfaces. *Chem Lett* **45**, 1134–1149 (2016).
161. Tuteja, A. *et al.* Designing Superoleophobic Surfaces. *Science (1979)* **318**, 1618–1622 (2007).
162. Wang, C. & Guo, Z. A comparison between superhydrophobic surfaces (SHS) and slippery liquid-infused porous surfaces (SLIPS) in application. *Nanoscale* **12**, 22398–22424 (2020).
163. Zeng, Q., Zhou, H., Huang, J. & Guo, Z. Review on the recent development of durable superhydrophobic materials for practical applications. *Nanoscale* **13**, 11734–11764 (2021).
164. Bohn, H. F. & Federle, W. Insect aquaplaning: *Nepenthes* pitcher plants capture prey with the peristome, a fully wetttable water-lubricated anisotropic surface. *Proceedings of the National Academy of Sciences* **101**, 14138–14143 (2004).
165. Cremaldi, J. & Bhushan, B. Fabrication of bioinspired, self-cleaning superliquiphilic/phobic stainless steel using different pathways. *J Colloid Interface Sci* **518**, 284–297 (2018).
166. Yong, J. *et al.* *Nepenthes* Inspired Design of Self-Repairing Omniphobic Slippery Liquid Infused Porous Surface (SLIPS) by Femtosecond Laser Direct Writing. *Adv Mater Interfaces* **4**, (2017).

167. Baumli, P. *et al.* The challenge of lubricant-replenishment on lubricant-impregnated surfaces. *Adv Colloid Interface Sci* **287**, 102329 (2021).
168. Yeganehdoust, F., Amer, A., Sharifi, N., Karimfazli, I. & Dolatabadi, A. Droplet Mobility on Slippery Lubricant Impregnated and Superhydrophobic Surfaces under the Effect of Air Shear Flow. *Langmuir* **37**, 6278–6291 (2021).
169. Kujawa, J. *et al.* Efficiency of grafting of Al₂O₃, TiO₂ and ZrO₂ powders by perfluoroalkylsilanes. *Colloids Surf A Physicochem Eng Asp* **420**, 64–73 (2013).
170. Wang, X., Wang, Z., Heng, L. & Jiang, L. Stable Omniphobic Anisotropic Covalently Grafted Slippery Surfaces for Directional Transportation of Drops and Bubbles. *Adv Funct Mater* **30**, (2020).
171. Zhao, C. *et al.* Multiscale Construction of Bifunctional Electrocatalysts for Long-Lifespan Rechargeable Zinc–Air Batteries. *Adv Funct Mater* **30**, (2020).
172. Wong, T. S. *et al.* Bioinspired self-repairing slippery surfaces with pressure-stable omniphobicity. *Nature* **477**, 443–447 (2011).
173. Gong, J., Xiang, B., Sun, Y. & Li, J. Janus smart materials with asymmetrical wettability for on-demand oil/water separation: a comprehensive review. *J Mater Chem A Mater* **11**, 25093–25114 (2023).
174. Söz, Ç. K., Trosien, S. & Biesalski, M. Janus Interface Materials: A Critical Review and Comparative Study. *ACS Materials Letters*, (2020).
175. Yan, L. *et al.* Porous Janus materials with unique asymmetries and functionality. *Materials Today* **51**, 626–647 (2021).
176. Shamseddine, I., Pennec, F., Biwole, P. & Fardoun, F. Supercooling of phase change materials: A review. *Renewable and Sustainable Energy Reviews* **158**, Preprint (2022).
177. Shamim, J. A. *et al.* Suppression of wetting transition on evaporative fakir droplets by using slippery superhydrophobic surfaces with low depinning force. *Sci Rep* **13**, (2023).
178. Reyssat, M., Yeomans, J. M. & Quéré, D. Impalement of fakir drops. *EPL (Europhysics Letters)* **81**, 26006 (2008).
179. Jingru, H., Jingbin, L., Zhongwei, H., Kang, C. & Haojun, X. Experimental study on the freezing process of water droplets for ice air jet technology. *Sci Rep* **14**, (2024).
180. Akhtar, S., Xu, M., Mohit, M. & Sasmito, A. P. A comprehensive review of modeling water solidification for droplet freezing applications. *Renewable and Sustainable Energy Reviews* **188**, 113768 (2023).
181. Feng, X., Zhang, X. & Tian, G. Recent advances in bioinspired superhydrophobic ice-proof surfaces: challenges and prospects. *Nanoscale* **14**, 5960–5993 (2022).
182. Li, Q. & Guo, Z. Fundamentals of icing and common strategies for designing biomimetic anti-icing surfaces. *J Mater Chem A Mater* **6**, 13549–13581 (2018).
183. Schutzius, T. M. *et al.* Physics of icing and rational design of surfaces with extraordinary icephobicity. *Langmuir* **31**, 4807–4821 (2015).
184. Guo, Q. & Cheng, P. Effects of non-uniform temperature of the ice nucleus on heterogeneous ice nucleation. *Int J Heat Mass Transf* **163**, 120404 (2020).
185. Tokuyama, M. Statistical Physics Theory of Ostwald Ripening. in *Dynamics of Ordering Processes in Condensed Matter* 63–70 (1988).
186. Hejazi, V., Sobolev, K. & Nosonovsky, M. From superhydrophobicity to icephobicity: Forces and interaction analysis. *Sci Rep* **3**, (2013).
187. Jiang, S., Diao, Y. & Yang, H. Recent advances of bio-inspired anti-icing surfaces. *Adv Colloid Interface Sci* **308**, 102756 (2022).
188. He, Z., Xiao, S., Gao, H., He, J. & Zhang, Z. Multiscale crack initiator promoted super-low ice adhesion surfaces. *Soft Matter* **13**, 6562–6568 (2017).
189. Meuler, A. J. *et al.* Relationships between water wettability and ice adhesion. *ACS Appl Mater Interfaces* **2**, 3100–3110 (2010).
190. Kulinich, S. A. & Farzaneh, M. How wetting hysteresis influences ice adhesion strength on superhydrophobic surfaces. *Langmuir* **25**, 8854–8856 (2009).
191. Farhadi, S., Farzaneh, M. & Kulinich, S. A. Anti-icing performance of superhydrophobic surfaces. *Appl Surf Sci* **257**, 6264–6269 (2011).

192. Meuler, A. J. *et al.* Relationships between water wettability and ice adhesion. *ACS Appl Mater Interfaces* **2**, 3100–3110 (2010).
193. Eberle, P., Tiwari, M. K., Maitra, T. & Poulikakos, D. Rational nanostructuring of surfaces for extraordinary icephobicity. *Nanoscale* **6**, 4874–4881 (2014).
194. Huang, D., Wang, W., Xu, J. & Wang, A. Mechanical and water resistance properties of chitosan/poly(vinyl alcohol) films reinforced with attapulgite dispersed by high-pressure homogenization. *Chemical Engineering Journal* **210**, 166–172 (2012).
195. Zhang, H. *et al.* Solar anti-icing surface with enhanced condensate self-removing at extreme environmental conditions. *Proceedings of the National Academy of Sciences* **118**, 78118 (2021).
196. Liu, Y. *et al.* Robust Photothermal Coating Strategy for Efficient Ice Removal. *ACS Appl Mater Interfaces* **12**, 46981–46990 (2020).
197. Li, C. *et al.* Enhancing and Impeding Heterogeneous Ice Nucleation through Nanogrooves. *Journal of Physical Chemistry C* **122**, 25992–25998 (2018).
198. Sarma, J., Zhang, L., Guo, Z. & Dai, X. Sustainable icephobicity on durable quasi-liquid surface. *Chemical Engineering Journal* **431**, (2022).
199. Irajizad, P., Nazifi, S. & Ghasemi, H. Icephobic surfaces: Definition and figures of merit. *Advances in Colloid and Interface Science* **269**, 203–218 (2019).
200. Dhyani, A., Choi, W., Golovin, K. & Tuteja, A. Surface design strategies for mitigating ice and snow accretion. *Matter* **5**, 1423–1454 (2022).
201. Parent, O. & Ilinca, A. Anti-icing and de-icing techniques for wind turbines: Critical review. *Cold Reg Sci Technol* **65**, 88–96 (2011).
202. Jiang, S., Diao, Y. & Yang, H. Recent advances of bio-inspired anti-icing surfaces. *Advances in Colloid and Interface Science* **308**, 102756 (2022).
203. He, Z., Xie, H., Jamil, M. I., Li, T. & Zhang, Q. Electro-/Photo-Thermal Promoted Anti-Icing Materials: A New Strategy Combined with Passive Anti-Icing and Active De-Icing. *Adv Mater Interfaces* **9**, 108298 (2022).
204. Wang, F. *et al.* Dynamic Anti-Icing Surfaces (DAIS). *Advanced Science* **8**, (2021).
205. Zhao, Z. *et al.* Novel sandwich structural electric heating coating for anti-icing/de-icing on complex surfaces. *Surf Coat Technol* **404**, 126489 (2020).
206. Koutsoloukas, L., Nikitas, N. & Aristidou, P. Passive, semi-active, active and hybrid mass dampers: A literature review with associated applications on building-like structures. *Developments in the Built Environment* **12**, 145-153(2022).
207. Ibrahim, Y., Kempers, R. & Amirfazli, A. 3D printed electro-thermal anti- or de-icing system for composite panels. *Cold Reg Sci Technol* **166**, 102844 (2019).
208. Zhao, C. *et al.* Multiscale Construction of Bifunctional Electrocatalysts for Long-Lifespan Rechargeable Zinc–Air Batteries. *Adv Funct Mater* **30**, 147-158 (2020).
209. Ibáñez-Ibáñez, P. F., Montes Ruiz-Cabello, F. J., Cabrerizo-Vílchez, M. A. & Rodríguez-Valverde, M. A. Ice adhesion of PDMS surfaces with balanced elastic and water-repellent properties. *J Colloid Interface Sci* **608**, 792–799 (2022).
210. Goy, C. *et al.* Shrinking of Rapidly Evaporating Water Microdroplets Reveals their Extreme Supercooling. *Phys Rev Lett* **120**, (2018).
211. Kim, K. H. *et al.* WATER THERMODYNAMICS Maxima in the Thermodynamic Response and Correlation Functions of Deeply Supercooled Water
212. Ryerson, C. C. Ice protection of offshore platforms. *Cold Reg Sci Technol* **65**, 97–110 (2011).
213. Zhou, X., Sun, Y. & Liu, J. Designing Anti-Icing Surfaces by Controlling Ice Formation. *Advanced Materials Interfaces* **8**, (2021).
214. Mousavi, S. M. *et al.* The potential for anti-icing wing and aircraft applications of mixed-wettability surfaces - A comprehensive review. *Cold Regions Science and Technology* **217**, Preprint (2024).
215. Wang, F. *et al.* Liquid layer generators for excellent icephobicity at extremely low temperatures. *Mater Horiz* **6**, 2063–2072 (2019).
216. Liu, F., Wang, Z. & Pan, Q. Intelligent Icephobic Surface toward Self-Deicing Capability. *ACS Sustain Chem Eng* **8**, 792–799 (2020).

217. Shi, X. *et al.* Advanced strategies for marine antifouling based on nanomaterial-enhanced functional PDMS coatings. *Nano Materials Science* **6**, 375–395 (2024).
218. Khedir, K. R. *et al.* Temperature-dependent bouncing of super-cooled water on teflon-coated superhydrophobic tungsten nanorods. *Appl Surf Sci* **279**, 76–84 (2013).
219. Bartolo, D. *et al.* Bouncing or sticky droplets: Impalement transitions on superhydrophobic micropatterned surfaces. *Europhys Lett* **74**, 299–305 (2006).
220. Maitra, T. *et al.* Supercooled water drops impacting superhydrophobic textures. *Langmuir* **30**, 10855–10861 (2014).
221. Mishchenko, L. *et al.* Design of ice-free nanostructured surfaces based on repulsion of impacting water droplets. *ACS Nano* **4**, 7699–7707 (2010).
222. Khedir, K. R. *et al.* Temperature-dependent bouncing of super-cooled water on teflon-coated superhydrophobic tungsten nanorods. *Appl Surf Sci* **279**, 76–84 (2013).
223. Wang, Y., Xue, J., Wang, Q., Chen, Q. & Ding, J. Verification of icephobic/anti-icing properties of a superhydrophobic surface. *ACS Appl Mater Interfaces* **5**, 3370–3381 (2013).
224. Zhang X. *et al.* Impacting-freezing dynamics of a supercooled water droplet on a cold surface. *Int. J. Heat Mass Transf* **158**, 119997 (2020).
225. Bahadur, V. *et al.* Predictive model for ice formation on superhydrophobic surfaces. *Langmuir* **27**, 14143–14150 (2011).
226. Feng, X., Zhang, X. & Tian, G. Recent advances in bioinspired superhydrophobic ice-proof surfaces: challenges and prospects. *Nanoscale* **14**, 5960–5993 (2022).
227. Boinovich, L., Emelyanenko, A. M., Korolev, V. V. & Pashinin, A. S. Effect of wettability on sessile drop freezing: When superhydrophobicity stimulates an extreme freezing delay. *Langmuir* **30**, 1659–1668 (2014).
228. Jung, S. *et al.* Are superhydrophobic surfaces best for icephobicity? *Langmuir* **27**, 3059–3066 (2011).
229. Wilson, P. W. *et al.* Inhibition of ice nucleation by slippery liquid-infused porous surfaces (SLIPS). *Phys. Chem. Chem. Phys.* **15**, 581–585 (2013).
230. Guo, L., Tang, G. H. & Kumar, S. Droplet Morphology and Mobility on Lubricant-Impregnated Surfaces: A Molecular Dynamics Study. *Langmuir* **35**, 16377–16387 (2019).
231. Wei, K., Yang, Y., Zuo, H. & Zhong, D. A review on ice detection technology and ice elimination technology for wind turbine. *Wind Energy* **23**, 433–457 (2020).
232. Hejazi, V., Sobolev, K. & Nosonovsky, M. From superhydrophobicity to icephobicity: Forces and interaction analysis. *Sci Rep* **3**, 2194 (2013).
233. Lv, J., Song, Y., Jiang, L. & Wang, J. Bio-inspired strategies for anti-icing. *ACS Nano* **8**, 3152–3169 (2014).
234. Li, Q. & Guo, Z. Fundamentals of icing and common strategies for designing biomimetic anti-icing surfaces. *J Mater Chem A Mater* **6**, 13549–13581 (2018).
235. Memon, H., Liu, J., De Focatiis, D. S. A., Choi, K. so & Hou, X. Intrinsic dependence of ice adhesion strength on surface roughness. *Surf Coat Technol* **385**, (2020).
236. Erbil, H. Y. Improvement of lubricant-infused surfaces for anti-icing applications. *Surf Innov* **4**, 214–217 (2016).
237. Piscitelli, F. *et al.* Superhydrophobic coatings as anti-icing systems for small aircraft. *Aerospace* **7**, 2 (2020).
238. Varanasi, K. K., Deng, T., Smith, J. D., Hsu, M. & Bhate, N. Frost formation and ice adhesion on superhydrophobic surfaces. *Appl Phys Lett* **97**, (2010).
239. Chen, J. *et al.* Superhydrophobic surfaces cannot reduce ice adhesion. *Appl Phys Lett* **101**, (2012).
240. Subramanyam, S. B., Rykaczewski, K. & Varanasi, K. K. Ice Adhesion on Lubricant-Impregnated Textured Surfaces. *Langmuir* **29**, 13414–13418 (2013).
241. TAS, M., Memon, H., Xu, F., Ahmed, I. & Hou, X. Electrospun nanofibre membrane based transparent slippery liquid-infused porous surfaces with icephobic properties. *Colloids Surf A Physicochem Eng Asp* **585**, 124177 (2020).
242. Wang, J., Kato, K., Blois, A. P. & Wong, T.-S. Bioinspired Omniphobic Coatings with a Thermal Self-Repair Function on Industrial Materials. *ACS Appl Mater Interfaces* **8**, 8265–8271 (2016).

243. Zhang, K. *et al.* UV-curable POSS-fluorinated methacrylate diblock copolymers for icephobic coatings. *Prog Org Coat* **93**, 87–96 (2016).
244. He, Z., Xiao, S., Gao, H., He, J. & Zhang, Z. Multiscale crack initiator promoted super-low ice adhesion surfaces. *Soft Matter* **13**, 6562–6568 (2017).
245. He, Z., Zhuo, Y., Wang, F., He, J. & Zhang, Z. Understanding the role of hollow sub-surface structures in reducing ice adhesion strength. *Soft Matter* **15**, 2905–2910 (2019).
246. Grizen, M. & Tiwari, M. K. Icephobic Surfaces. in *Ice Adhesion* 417–466 (2020).
247. Wang, F. *et al.* Liquid layer generators for excellent icephobicity at extremely low temperatures. *Mater Horiz* **6**, 2063–2072 (2019).
248. Feng, X., Zhang, X. & Tian, G. Recent advances in bioinspired superhydrophobic ice-proof surfaces: challenges and prospects. *Nanoscale* **14**, 5960–5993 (2022).
249. Farhadi, S., Farzaneh, M. & Kulinich, S. A. Anti-icing performance of superhydrophobic surfaces. *Appl Surf Sci* **257**, 6264–6269 (2011).
250. Kulinich, S. A., Farhadi, S., Nose, K. & Du, X. W. Superhydrophobic surfaces: Are they really ice-repellent? *Langmuir* **27**, (2011).
251. Golovin, K. *et al.* Designing durable icephobic surfaces. *Sci Adv* **2**, (2016).
252. Zeng, C. *et al.* Coatings for the Enhanced Icephobicity toward Large-Scale Ice (2021).
253. Cirisano, F. & Ferrari, M. Sustainable materials for liquid repellent coatings. *Coatings* **11**, Preprint (2021).
254. Kadhim, M. M., Shehab, M. M. & Abdalaamer, N. kh. Plasma Vacuum Systems: A Review Article. *MINAR International Journal of Applied Sciences and Technology* **06**, 325–342 (2024).
255. Batan, A. *et al.* Comparison between wet deposition and plasma deposition of silane coatings on aluminium. in *Progress in Organic Coatings* **69**, 126–132 (2010).



“Everyone is a genius, but if you judge a fish by its ability to climb a tree, it will live its whole life believing it is stupid”

(Albert Einstein)

2

Materials and Methods

2.1 Introduction

The goal of this chapter is to present the chosen methodologies, and materials within the context of this doctoral thesis. The diverse methods employed in surface modification and coating synthesis within this research are comprehensively addressed as well as the surface engineering and nanotechnology strategies utilized for the achievement of an exhaustive control of the wetting and derived surface properties, particularly omniphobicity, anti-fouling and anti-icing. Finally, the consolidation of new characterization protocols of the proposed multifunctional surfaces, particularly the water/surface interaction under realistic simulated environmental conditions as well as their stability and durability performances, encompass a detailed exposition of the employed analytical techniques.

2.2 Methodology

Surface modification is defined as a set of processes through which the chemical, physical, or properties of a material's surface are altered to enhance its performance in specific applications. Unlike bulk modifications, surface focus exclusively on the outermost region of the material, which directly interacts with its environment or other materials, leaving the core properties largely unaffected. A key aspect of surface modifications is their ability to generate new surface chemistry, inducing the formation of novel phases, compounds, or structures do not present in the original material. This is achieved through physical or chemical treatments or the application of coatings. Changes may include controlled oxidation (forming protective oxide layers to resist corrosion), or nitriding (introducing carbon or nitrogen atoms to enhance surface hardness), ion implantation (introducing specific ions to create localized chemical compositions), or chemical functionalization (adding specific functional groups to improve adhesion, reactivity, or biocompatibility). Common methods for surface modification include thermal surface treatments, chemical processes, coatings, and advanced techniques such as plasma or laser processing¹.

Deposition, as a concept, frames a series of techniques employed to incrementally build thin or thick layers on a solid surface, either atom-by-atom or molecule-by-molecule. The resulting layer functions as a coating, thereby modifying the properties of the substrate surface in accordance with the

intended application. The thickness of these deposited layers varies across a spectrum from nanometres to hundreds of micrometres depending on the chosen method and material type. The properties of thin films exhibit significant differences from the bulk materials, especially as thickness approaches the nanometric scale, due to the specific processes inherent in the layer growth. Crucial parameters governing deposition control include growth rate, gas pressure, temperature, surface stability, and the nature of the deposited material.

Modification of surfaces can be achieved through two primary approaches: bottom-up and top-down techniques, each offering distinct methodologies. Bottom-up techniques focus on assembling structures atom by atom or molecule by molecule, leveraging natural self-organization or chemical processes to form nanostructures. Examples include sol-gel processes, vapor phase deposition and electrochemical deposition. In contrast, top-down techniques involve the removal or shaping of material from a larger substrate to achieve nanoscale features, employing methods such as chemical etching, mechanical milling, and soft lithography. Both approaches provide versatile options for fabricating nanometric surfaces, depending on the desired structure, material properties, and processing condition².

Current surface modification techniques can be classified into dry methods and wet methods, each offering distinct processes for altering surface properties. Dry methods involve the use of physical or chemical processes in gaseous or solid states, often under controlled atmospheres, and include techniques such as plasma treatments, ion implantation, laser processing, and physical vapor deposition. On the other hand, wet methods rely on liquid-phase processes to modify surfaces, including chemical etching, electrochemical treatments, sol-gel techniques, and dip-coating. The primary differences between these approaches lie in their operational conditions and material interaction mechanisms: dry methods typically offer high precision, localized control, and are suited for applications requiring minimal environmental contamination, whereas wet methods are often more cost-effective, scalable, and suitable for complex geometries but may involve challenges such as waste management, uniformity and material compatibility³.

Some of the popular techniques used for coating growth are vapor-phase deposition methods, which can be either physical or chemical. The main

difference between Physical Vapor Deposition (PVD) and Chemical Vapor Deposition (CVD) lies in their mechanisms: PVD relies on physical processes, such as evaporation or sputtering, to deposit, while CVD uses chemical reactions to form a coating on the substrate. PVD typically requires a vacuum environment to ensure the controlled transport of vaporized material, whereas CVD can occur at atmospheric pressure or under reduced pressure, depending on the process⁴. The thermodynamically intricate gas condensation process leading to layer formation involves the vapor atoms to the surface, culminating in the aggregation of ordered or disordered atomic structures, ultimately determining the resultant nanostructure, composition and crystallinity⁴.

The combination of plasma and vacuum technologies⁵ can enhance the precision, quality, and efficiency of various processes in industries such as microelectronics, material science and aerospace⁴. It allows better control over the reaction environment, and to improve results in terms of material properties, surface treatments and product quality⁶. Moreover, looking for the development of hybrid surface engineering strategies, vacuum deposition methods will be employed in combination to non-vacuum methodologies of surface modification based on wet chemical routes: the spin coating method devoted to the coexistence of liquid and solid phases on the surface and the grafting of macromolecules for the most external surface termination. In summary, the addressed strategy for the obtention of hierarchical surfaces involves exhaustive control and compatibility of the surface topography with different roughness levels and the chemical termination using a low surface energy agent, particularly fixing the focus on fluorinated strategies, but in reduced concentrations.

Addressing the challenge of wetting control, fluid repellence and icephobicity, three methodologies have been explored in this thesis: 1) first level of roughness at scale of several hundred of microns on the substrate, whether by using porous substrates or laser technology in order to modify the surface topography; 2) growth of nanostructures through vacuum and plasma technologies to be able to achieve the roughness levels at scale of a few microns and at the nanoscale associated to the external configuration that governs pursued functionality; 3) an extra surface modification in chemical or structural format like multi-shell of nanostructures and/or using different SFE agents to enhance the repellent

properties as well as the anti-icing behavior, as stable and durable properties in simulated real application conditions.

2.2.1 Vacuum deposition technology

"Vacuum" is etymologically derived from the Latin word "*Vacua*," signifying emptiness, the absence of matter. However, operationally, absolute vacuum is not attainable, so working at vacuum conditions implies a confined space with a lower gas density per unit volume than that of the encompassing atmospheric air. The practical applications of vacuum span diverse fields, including electronics, optics, packaging, and solar cells among others. Their utilisation imparts distinctive advantages, like notably precision, and uniformity of the surface modification, and a marked reduction in external contamination. In materials science, vacuum deposition emerges as a versatile and extensively employed process. This technique involves the deposition of thin films onto a substrate within a vacuum environment. The precision of this method allows for the gradual deposition of specific materials of controlled thickness below the microscale, following an atom by atom or molecule by molecule assembly. The indispensability of vacuum thin film deposition lies in its capacity to employ control over the chemical-physical reactivity of the deposition processes while minimizing gas collisions. This reduction in collisions facilitates the involvement of higher energy particles to promote adhesion, diffusion or etching processes, among others. Notably, when oxygen is generally perceived as a potential contaminant due to the alteration of the coating properties or degrading the adhesion to the substrate, vacuum deposition serves as a crucial strategy to mitigate this effect^{7,8}. The operational pressure values at which vacuum deposition is conducted from a technical point of view typically span from 10^{-1} mbar to 10^{-12} mbar known as low to high vacuum conditions, respectively. This extensive pressure range enables the production of coatings with varying characteristics, such as the structural control ranging from entirely compact to porous morphology⁹. In essence, vacuum deposition stands as an imperative methodological approach, offering a spectrum of applications and benefits in the realm of precision surface engineering and materials science⁴.

Particularly, vacuum deposition methods executed from the vapor phase of a target material, by two overarching categories mentioned above, PVD and CVD, are delineated based on the desired functional surface project.

- ***Physical Vapor Deposition***

PVD processes comprise a category of atomic controlled deposition techniques based on the sublimation phenomena wherein material transforms a solid source into atoms or molecules. Subsequently, these vapor species are transported through a vacuum or low-pressure gaseous environment, ultimately condensing onto a substrate. Coating thickness spectrum ranges from a few nanometres up to thousands of nanometres to be utilized in diverse applications, including semiconductor manufacturing, food storage, and protective purposes^{4,10}. The vacuum PVD method involves environmentally friendly processes, markedly reducing the reliance on toxic raw materials, chemical reactions, and chemical disposal. Notably, one of its salient features is the high purity of the deposited thin films and the capability to control the structural composition from inorganic to organic materials growth. Adaptability is a hallmark of the PVD process, to cover substrates spanning an extensive range of sizes and geometries, like silicon wafers, cutting tools, and windows¹¹. PVD processes are broadly scalable in all its versions: sputtering and thermal evaporation, which include vacuum evaporation, Pulsed Laser Deposition (PLD), Molecular Beam Epitaxy (MBE), Ion Plating, Activated Reactive Evaporation (ARE), and Ionized Cluster Beam Deposition (ICBD)¹².

But PVD methods have some disadvantages, such as a relatively low deposition rate, which can make them time-consuming and less efficient for large-scale production. Additionally, PVD is not suitable for polymers, as the high temperatures involved can degrade or damage these materials⁴.

Within the scope of this thesis, the emphasis will be directed towards two distinctive PVD variants employed for the fabrication of organic, inorganic, and hybrid materials: Glancing Angle Deposition (GLAD) and Organic Physical Vapor Deposition (OPVD), both encompassed within the framework of thermal vacuum evaporation.

❖ Glancing Angle Deposition

Physical vapor deposition at oblique or glancing angles represents two variations of physical vapor deposition, wherein the vapours of the sublimated material impinge upon the substrate at a highly acute angle to the perpendicular direction of vapor incidence. When this angle falls below 80° , it is referred to as Oblique Angle Physical Vapor Deposition (OAPVD or simply OAD), whereas if it surpasses 80° , it is named Glancing Angle Physical Vapor Deposition (GAPVD or simply GLAD). Both approaches allow the production of thin films with different morphologies, characterized by alternating tilted, oriented columnar structures, interspersed with open gaps of comparable dimensions. At GLAD configuration, it is possible to fabricate thin films of columns of nanometric widths with a high degree of microstructural control and open porosity. This evaporation technique is usually assisted by electron beam of a specific material to improve the deposition rate. Directional nanocolumnar growth is a phenomenon that occurs because of a process known as “shadowing” on the substrate’s surface¹³. In the early stages of growth, atoms and atomic clusters can condensate on the substrate, conforming separate seeds or nuclei. When the substrate is positioned at an oblique angle respect to the vapor flux direction, these nuclei create a geometric shadow over the substrate areas behind them. This shadowing effect prevents new material growth on those hidden regions, avoiding the formation of a continuous layer. In addition, the nuclei accumulate the incident atoms that should be deposited in shadowed areas, forming columns that can grow in the direction of the vapor source and preventing lateral diffusion¹⁴ (**Figure 1 a**)). This methodology has been applied in this thesis to fabricate metal oxides oriented nanostructured porous coatings like stainless steel oriented nanocolumns (Chapter 4).

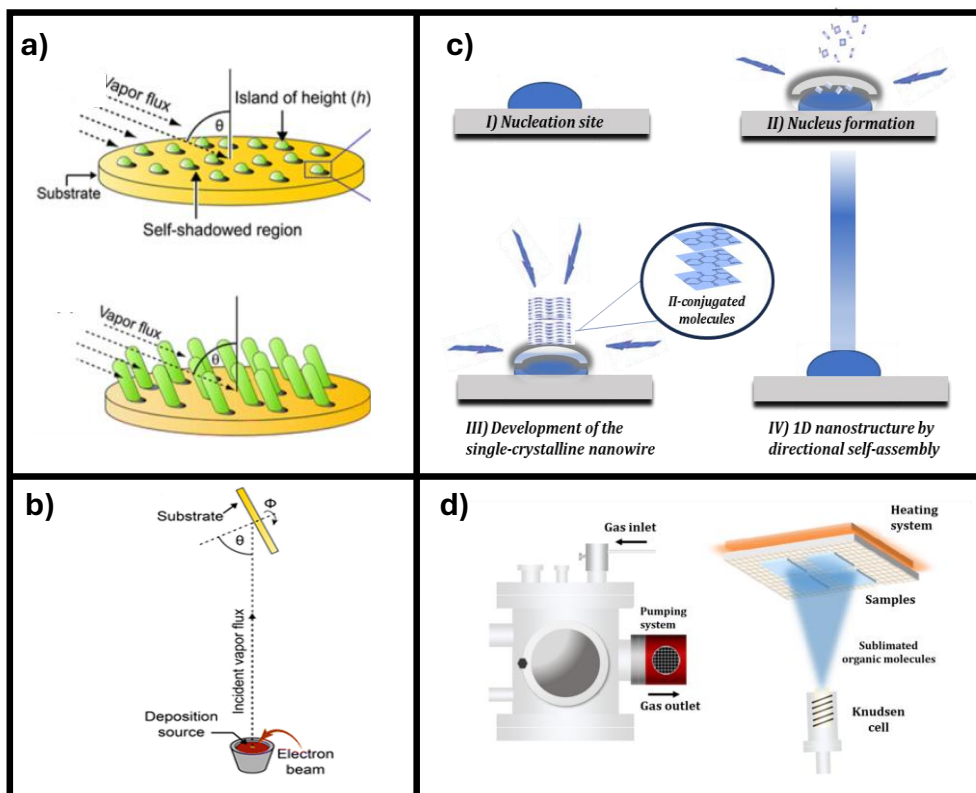


Figure 1. a) Illustration of the growth mechanism in GLAD configuration¹⁵, b) geometric representation of a GLAD evaporation process, c) different steps for the organic nanowires (ONWs) growth using π -conjugated molecules¹⁶ and d) scheme of a OPVD reactor¹⁷.

❖ Organic Physical Vapor Deposition

Organic Physical Vapor Deposition (OPVD) utilizes stable organic precursor of low sublimation temperature, T_s . Particularly, organic vapors whose molecules can be re-condensed by π -conjugated stacking such as metalloporphyrin, metallophthalocyanines and perylenes allow the generation of one-dimensional (1D) nanostructures. The formation of organic nanowires (ONWs) involves the vapor condensation of the π -conjugated molecules onto a substrate, through supersaturation and crystallization process as it is shown in Figure 1 c). Some key substrate aspects to promote the obtention of ONWs are the surface previous state and the temperature. Regarding the first one, morphology, roughness and chemical nature are factors that influence the surface free energy and the sticking coefficient of the arriving organic molecules. Particularly, rough morphologies and ordered topographical defects can provide nucleation sites.

Therefore, before the organic nanowire's growth by thermal sublimation, an activation surface process (UV illumination, oxygen plasma, ozoniser) must be employed¹⁶. For the second point, substrate temperature is determinant to achieve a free movement of molecules when arriving to the surface. If there is not enough available energy to promote a freely movement of the molecules to ensure a self-assembly mechanism, a continuous film will be formed. However, if the temperature is too high, the molecules do not stick to the substrate and no nucleation will be initiated. There is a specific temperature range where the density and width of the ONWs can be controlled¹⁸.

The different steps shown in Figure 1 c) for the growth of organic nanowires begin with the nucleation of the π -conjugated organic molecules on the pre-activated substrate¹⁶. Once the roughness parameter and the temperature for the self-assembly of these molecules are suitable, a monocrystalline growth of an organic nanowire occurs. The OPVD methodology (Figure 1 d)) has been employed in this thesis as part of a soft-template method for the obtention of supported 1D core@shell nanostructures¹⁷.

- ***Chemical Vapor Deposition***

CVD is an interesting process in material science due to its ability to produce high-purity, high-performance coatings with precise control over composition, thickness, and uniformity, essential for semiconductor and microelectronics industries¹⁹. The versatility of CVD allows for the deposition of a wide range of materials, including metals, semiconductors, and insulators. Additionally, CVD processes can be tailored to achieve desired properties such as high hardness, corrosion resistance, and thermal stability²⁰. Its scalability and adaptability make CVD indispensable for both research and industrial applications. In this deposition technique, the substrate is exposed to one or more vapors to generate a solid layer deposited on it with the desired chemical composition. The precursors within the chamber either decompose or suffer chemical reactions on the substrate's surface. Most CVD processes work within a pressure range from 10^{-3} mbar to 10^2 mbar values. But the main CVD requirement is operating at elevated temperatures typically around 1000°C . CVD processes can be categorized into three main types⁴: thermal, plasma, and laser CVD.

In this thesis, the CVD method employed for thin film deposition has been Plasma Enhanced Chemical Vapor Deposition (PECVD), which will be described below.

2.2.2 Plasma assisted methodologies

Plasma discharge, commonly known as the fourth fundamental state of matter, consists of an ionized gas wherein positive and negative ions, neutral particles, and electrons coexist responding collectively to the action of electromagnetic fields. A significant feature of a plasma discharge is the prevalence of particles in an electrically charged state⁶. The transformation of matter into plasma happens as a sequence initiated by applying thermal energy. Following the heat transfer path between phase transitions, upon the application of a substantial amount of further energy to a gas, an electrical breakdown occurs. In this highly energetic phase, gas ionization is promoted and electrons and ions within the gas undergo significant chemical-physical reactivity resulting in an ionized state commonly known as plasma^{6,21}. Plasma is broadly characterized by basic parameters like density and temperature of electrons, ions, and neutral species²¹. In the quasi-neutral state of plasma, the densities of electrons and ions are typically equal, as plasma density whereas the energy distribution can be different for each species collectivity. Considering these parameters, plasmas discharges can be systematically categorized into three distinct classes based on their thermal equilibrium⁶:

- Plasmas in a state of full thermodynamic equilibrium (**thermal equilibrium plasma**): the electron, ion, and neutral particle temperatures are similar. However, their practical significance is diminished due to their non-existence under controlled laboratory conditions. Instances of relevance arise in contexts such as the fusion reactor²¹ or the laser confinement of plasma, where these temperatures provide insights into the dynamics of such phenomena.
- Plasmas in a state of partial thermodynamic equilibrium (**local thermal equilibrium plasma**): the temperatures of electrons, ions, and neutral particles are confined to a similar range. In the specific context of local thermal equilibrium plasma, the ion temperature typically spans from

3000 K to 10000 K, corresponding to 0.4 - 1 eV. This range stands notably higher than the temperatures observed in non-thermal plasmas. Conversely, the electron temperature in local thermal equilibrium plasma is significantly lower. The establishment of a plasma in a state of partial thermodynamic equilibrium can be achieved through various methodologies, such as direct current (DC) or radiofrequency (RF) arcs, or by utilizing an inductively coupled torch. Noteworthy applications include processes like plasma spraying and thermal plasma-based chemical and physical vapor deposition²¹.

- Plasmas out of local thermodynamic equilibrium (**non-thermal equilibrium plasma**): also known as cold plasmas, the temperatures of ions and neutral particles are lower than those of electrons, in the range of 2 - 10 eV. Non-thermal equilibrium plasmas are produced through various methods, including corona discharge, glow discharge, arc discharge, and wave-heated plasma. The realm of non-thermal equilibrium plasmas finds application across diverse fields such as aeronautic and environmental engineering, biomedicine, textile technology, and analytic chemistry. The utilization of non-thermal equilibrium plasmas in these domains serves the purpose of minimizing temperature range processes⁶. Many advantages in using cold plasmas or non-thermal equilibrium plasmas have been studied since electron temperature is higher than gas temperature and plasma reactions can proceed at low temperatures, even room temperature. In this thesis, only non-thermal equilibrium plasmas are involved to assist the surface engineering processes.

The combination of plasma and vacuum reactor technologies represents a patent strategy for specific fields. This synergy is often denoted such as “plasma-enhanced vacuum processing”²² and it finds utility across diverse applications taking advantages of some important processes controlled by it:

- **Surface modification** and **thin film deposition** are interesting procedures in semiconductor manufacturing²³ and materials science. In these domains, a vacuum chamber is established at low-pressure to induce the deposition of thin films onto substrates improving surface performance without altering the bulk characteristics. This process enables meticulous control over film thickness (below the micron), composition, and inherent properties. Noteworthy in this field is the Plasma-Enhanced Chemical Vapor Deposition (PECVD)⁵.
- **Plasma cleaning** constitutes a technologically advanced method by means of the combination of vacuum and plasma reactors. Within these configurations, the vacuum environment meticulously precludes the presence of adsorbed impurities and gases at the surface and/ or porous structure, thereby facilitating the action of plasma in purging and eradicating surface contaminants²⁴ adhered to substrates²⁵.
- **Vacuum plasma sterilization** represents a sophisticated application that combines vacuum technology with plasma to attain exceptionally efficient sterilization²⁶ of medical devices. Taking advantage of high-energy UV photon generation and reactive species, mainly oxidizing ones, in the plasma discharge, the low-pressure environment guarantees the elimination of biological contaminants.
- **Surface activation** is a crucial preparatory step achieved through plasma treatment⁶, designed to prime surfaces for subsequent processes, including adhesion, bonding, or coating. The controlled and uniform activation of surfaces is facilitated by the vacuum environment²⁷, which effectively mitigates undesired interactions with atmospheric gases, ensuring a pristine and well-regulated activation process. Subsequently, the action of plasma through soft etching processes or chemical functionalization improves the adhesion of coatings and the adaptation of interfaces in the manufacture of multilayers.

- *Plasma etching and sputtering processes*, integral to microfabrication, frequently entail the utilization of vacuum chambers coupled with plasma discharge generation²⁸. Low pressure facilitates the work of highly energetic species and lengthens their mean free path to improve the range of meticulous removal or surface roughness generation²⁹ all the while enabling vigilant control over the reaction environment. It plays a pivotal role in functional material science and surface engineering, wherein vacuum chambers are complemented by plasma reactors³⁰.

- *Plasma Enhanced Chemical Vapor Deposition*

Originally designed to lower the processing temperature in CVD, (PECVD) is one of the most widely used procedures due to multiple advantages offered by using a plasma discharge as reaction medium in numerous applications, such as a higher deposition rate and uniform thickness, new stoichiometries, and compatibility with all type of substrates, particularly temperature-sensitive ones, and geometries³¹. Different applications and functions are shown in **Table 1**^{4,32}.

For usual PECVD processing, cold low-pressure discharge plasmas are sustained within chambers providing energy to facilitate CVD reactions simultaneously to activate and direct the film growth. The plasma discharge composed of electron and positive-ion concentrations with energies from 1 to 10 eV facilitates the decomposition of gas molecules from the chemical reactive species into a variety of constituent components (atoms, molecules, free radicals, electrons, ions, etc). All these molecular fragments interact with each other, through chemical reactions to occur at temperatures lower than 300 °C, compared to a CVD process¹².

Table 1. Examples of PECVD applications and functions.

Applications	Functions
Aerospace and outer space	Protective coating for storage media Protective coating against solid particle erosion and corrosion
Automotive	Protective coatings for engine components (low friction and wear)
Biomedical and biosensors	Protective coatings for implants Protective coatings for surgical tools
Manufacturing	Protective coatings on cutting tools (high-speed machining, dry machining, non-metal, and composites)
Textiles	Hydrophobic coatings
Packaging	Barriers against gas and vapor permeation coatings on flexible substrates
Controlled fusion research	Control of plasma/wall interactions for the performance on fusion devices (tokamaks and stellarators)
Fuel cell materials	Development of electrodes and membrane electrolytes
Solar cells	Development of microcrystalline silicon films

Applied power needed to generate a plasma discharge can be supplied by electrodes located inside the vacuum chamber or by inductive coupled antennas in remote configurations. Therefore, the plasma discharge can be generated by DC, Alternating Current (AC), RF, Micro-Wave (MW) or Electron Cyclotron Resonance (ECR) approaches. Particularly, in this thesis work have been employed two of them: RF- and MW- PECVD systems. RF plasma reactors commonly use a plano-parallel configuration where one of the electrodes is grounded and the other is connected to the power supply, although alternately exchanges its role as anode and cathode of the discharge. At frequencies between kHz to hundred MHz, electrons respond instantaneously to the oscillations of the electric field, while plasma ions, due to their greater mass, only respond on average to the oscillation period. Thus, the active electrode, usually used as substrate holder, becomes electrically polarized according to a capacitor model (self-bias voltage) that allows to increase the ion bombardment energy on the surface from several to hundred eV. RF plasmas have lower charge density 10^{10} cm^{-3} at pressures of 10^{-2} - 10^{-1} mbar. Other technological interesting approach is the use of microwave excitation source combined with magnetic confinement, ECR-MW, working by a slot antenna configuration³³. In this operational mode, microwave energy is synchronized with the inherent resonant frequency of the

electrons while a static magnetic field is present. It means that physically, electrons undergo helical paths during a single period of incident microwave oscillation³⁴. ECR-MW discharges are employed in a remote configuration that allows to regulate the ion bombardment of the film and decrease the temperature of the substrate during the deposition. Thus, ECR-MW plasmas easily occur at lower pressures 10^{-5} to 10^{-3} Torr with higher ionization degree and available ionic energy^{34,35}. **Figure 2** shows the schemes of the PECVD reactors employed in this thesis^{17,36}: RF-PECVD system for the development of conformal fluorinated polymer coatings (CF_x coating) and ERC-MW-PECVD reactor for the growth of conformal oxide layers as part of the soft-template method used for the fabrication of 1D core@shell nanostructures, either as a precursor seed for the generation of nanostructures or as a functional coating for them.

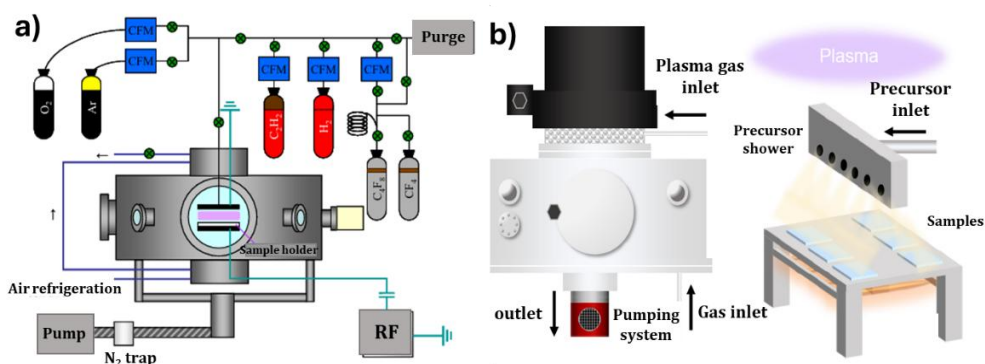


Figure 2. a) RF PECVD reactor scheme working at 13.56 MHz³⁶, b) ERC-MW PECVD SLAN I reactor scheme working at 2.45 GHz¹⁷.

▪ *Soft template method for hybrid 1D nanostructures fabrication*

One of the pioneering methods developed by the Nanotechnology on Surfaces and Plasma group where this thesis was conducted involves the use of PVD, specifically OPVD and PECVD techniques for the growth of supported 1D multifunctional core@shell nanostructures. These hybrid 1D nanostructures have been employed for the implementation of Chapter 3 and 6. There are three fundamental steps involved in the production of 1D nanostructures detailed in the **Figure 3** and additional steps that may or may not be necessary depending on the application of these nanostructures.

1) Formation of nucleation centres

The growth of ONWs follows a seed-mediated process (Figure 3 a)). In this context, the term “seed” is used broadly, referring to nucleation centres, essentially through a certain level of roughness, for promoting the organic crystal formation. This roughness can be achieved through various methods, such as plasma etching, laser surface treatments or the deposition of microstructured, non-percolated thin films or nanoparticles, preferably by vacuum and plasma techniques. In this context, for both Chapters 3 and 6, TiO₂ microstructured metal oxide thin film of 150 - 200 nm thickness was employed to provide the required seed roughness.

2) Growth of supported ONWs

The formation of ONWs is carried out by a temperature controlled (OPVD). The growth of these organic crystalline nanowires from different molecules (π -stacking mechanisms) is compatible with a wide variety of seed surfaces (Figure 3 b)) such as commercial substrates (SS grids, cellulose filters, metallic alloys....). Additional reference materials are employed for the fundamental characterization such as Si (100) and Fused Silica.

3) Deposition of a conformal shell

The third step involves PECVD process to generate a functional metal oxide (MO_x) shell of controlled properties, such as its topography, onto the grown ONWs, as shown in Figure 3 c), resulting in a hybrid core@shell nanostructures referred as ONW@MO_x. It is worth noting that TiO₂ has been chosen as shell coating in this thesis. It is also important to emphasize that the PECVD shell deposition plays a crucial role in the vertical alignment³⁷ of the nanowires, as opposed to their random orientation.

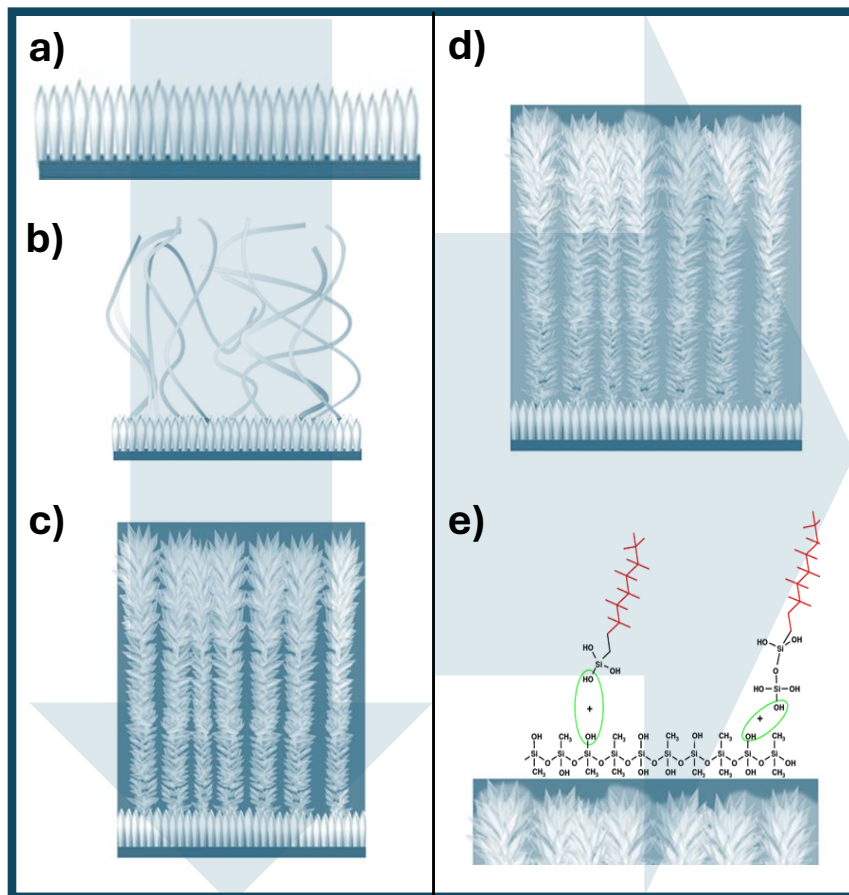


Figure 3. Representation of the soft-template method phases and other hybrid surface modification processes. a) Seeds formation by ECR-MW PECVD, b) Growth of ONWs by OPVD, c) Fabrication of core@shell nanostructures by ECR-MW PECVD, d) Deposition of polymeric coating/infusion of lubricant liquids by spin-coating, e) Surface functionalization of hybrid core@shell nanostructures using functional macromolecules.

2.2.3 Other methodologies for surface modification

To produce hybrid hierarchical surfaces of multifunctional behaviour, two additional non-vacuum techniques have been implemented in the context of this thesis.

- *Laser surface treatments*

Wettability is profoundly influenced by surface properties, particularly topography and morphology³⁸. Among the top-down etching strategies, laser treatments represent fast and effective approaches for generating roughness and surfaces²⁸. Greater control and precision playing with laser irradiation over various regions of the electromagnetic spectrum allows the creation of complex and detailed patterns at micro and nanoscales³⁹ in different kind of substrates as exemplified in **Figure 4**. Infrared (IR) lasers are effective for engraving and texturing materials, whereas Ultraviolet (UV) lasers, like excimer lasers operating between 193 nm and 248 nm, allow the fabrication of very fine and precise surface patterns. Additionally, green pulsed lasers at 532 nm are effective for engraving and modifying metallic and plastic surfaces enable the achievement of either more or less aggressive conditions for surface modification. Nanosecond pulses generate more heat invested in causing a stronger thermal effect, making them ideal for removing material of a randomly roughness surface. Picosecond pulses offer greater control and reduce thermal damage, pointing up to more selective treatments. Femtosecond pulses, being extremely short, minimize heating effects being suitable for complex structures of unaltered underlying material focused under the laser beam⁴⁰. The combination of laser pulse duration with the spectral region energy, together with other laser parameters such as power, repetition frequency, scan rate, hatching type, distance between scanning lines, and number of cycles, is adapted to the type of surface roughness and the specific patterns.

The morphology and roughness of metal alloys (Chapters 4 and 6) were modified by laser treatment at room temperature with a 20 W diode-pumped Nd:YAG (Powerline E, Rofin-Baasel Inc.) unpolarized laser emitting at 1064 nm with 100 ns pulse width and 20 kHz repetition rate. In contrast, laser patterns in transparent glass (Chapter 5) were generated with a femtosecond (fs) laser (Carbide model, Light Conversion, Lithuania), using its third harmonic (UV range) at 343 nm.

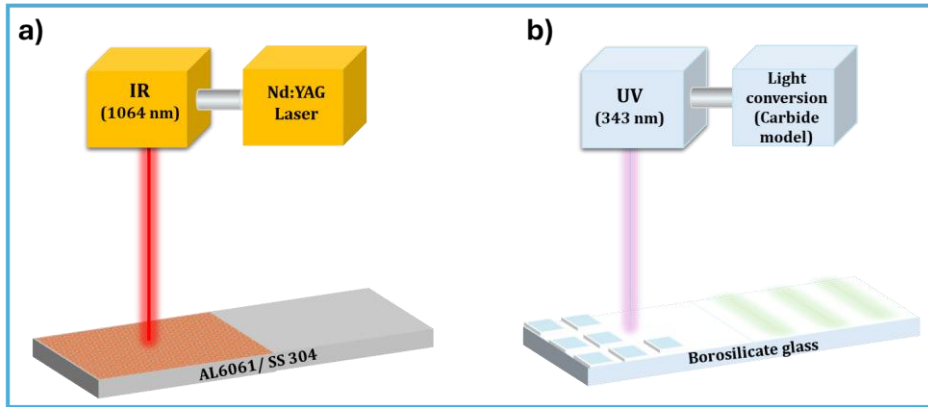


Figure 4. Schemes of a) the Nd:YAG IR laser treatment on metallic alloy substrates (AL6061 and 304 SS), and b) Light Conversion fs laser working at UV region (343 nm) on transparent glass.

At the working distance, the laser beam exhibited a spatially Gaussian energy profile with an elliptical spot, where $1/e^2$ beam dimensions were $2a = 60 \mu\text{m}$ and $2b = 36 \mu\text{m}$, with e being the eccentricity of the ellipse. This laser also offers the option of using a Pulse Peak Divider (PPD) to reduce the effective frequency of the laser treatment. The following working conditions were used for the treatments: 6.07 W laser power, 200 kHz oscillator frequency, 10 kHz effective frequency, 25 mm/s laser scan rate, and 238 fs pulse duration. With these laser processing parameters, the energy per pulse was estimated as 30.35 $\mu\text{J}/\text{pulse}$.

The use of IR nanosecond laser in Chapter 4 and Chapter 6 was devoted to achieve aggressive laser treatments generating great surface roughness at the microscale, and the use of UV femtosecond laser in Chapter 5 to create soft focused laser treatment on transparent surfaces to achieve specific patterns. The laser machining conditions required are more aggressive to generate significant roughness in metal surfaces, while a much more focused and precise laser is needed for more fragile materials like glass, where the abrasion conditions of IR in nanoseconds pulsed could damage it.

- ***Spin coating deposition***

Spin coating involves the fabrication of a thin layer of the desired material onto a flat substrate. Typically, a certain quantity of liquid precursor is dispensed at the center of the substrate. The substrate is set into high-speed rotation, making the liquid material, depending on its density and viscosity, spread over the substrate thanks to centrifugal force, covering it completely and being cured at relatively low temperatures (almost room). This technique is strategically applied to introduce low surface tension lubricant liquids like fluorinated oils (Krytox) and silicone oils in the porous hierarchical surfaces to perform Slippery Liquid Infused Porous Surfaces (SLIPS). Furthermore, it is utilized for embedding nanostructures into polymeric matrices or generate polymeric coatings in a multishell 1D nanostructure configuration as represents Figure 3 d). This non-vacuum technique has been employed in Chapter 3, 4 and 6. The obtention of embedded nanostructures into polymeric matrices aims mainly to enhance the adhesion to the substrate as well as the mechanical and impact properties for durability and stability performance of the proposed multifunctional surfaces if their wetting properties are preserved or even reinforced. The spin coating depositions were carried out using a spin speed of 3500 rpm.

- ***Grafting of fluorinated molecules***

The grafting consists of a chemical derivatization method that involves the anchorage of functional organic molecules on exposed surfaces⁴¹. It is a technique that ensures the chemical functionalization of porous hierarchical surfaces since the vapor precursor can interact with the entire exposed specific surface. For the binding of functional molecules to be effective, it is advisable to clean and activate the surface to generate available radicals. Particularly, grafting of fluorinated molecules provides numerous benefits from the point of view of a repellent surface, as the grafted molecules become an integral part of a surface of modified low free energy⁴². This process entails the utilization of fluorinated precursors of low vapor pressure to produce free-movement and flexible fluorocarbon molecule chains on the

surface's uppermost layer at room conditions⁴¹ as it is presented in Figure 3 e). This experimental method comprises two main steps: 1) after a primary pumping reactor, surface pre-activation by a soft oxygen plasma or ultraviolet ozonized system treatment (around 10 min), possibly leaving exposed hydroxyl radicals, 2) exposition to a fluorinated reactive vapor in a sealed desiccator maintained in a thermal bath at 80°C for two hours inside an extractor hood. This technique has been employed in all the chapters.

2.3 Materials used for the fabrication of wetting controlled surfaces

To be able to fabricate different superhydrophobic, omniphobic and anti-icing passive systems based on vacuum and plasma techniques, the used materials description includes substrates of applied interest, different organic and inorganic precursors for the fabrication of thin films and hierarchical structures, and low surface free energy terminations.

2.3.1 Substrates

Doped silicon 4" wafers Si (100) (TOPSIL) were employed as reference material for fundamental characterization of the fabricated multifunctional surfaces. Also fused silica 1.5 x 1.5 cm² plates (VIDRASA S.A.) were used to be able to analyze the optical properties.

As they are presented in the next chapters, commercial substrates of applied interest were employed. Commercial membranes like stainless steel S0770 SS grid filter (Sigma-Aldrich), of 40 mm diameter and 70 µm pore size, employed to treat pollutant water, and Whatman cellulose filters, grade 4m of 40 mm diameter and 11 and 25 µm pore size, typical of filtration processes, are proposed here as templates for the generation of hierarchical surfaces.

Regarding metal alloy substrates, stainless steel 304 (~98% purity) polished austenitic substrates pieces (20 x 20 mm²) with a thickness of 3 mm and aluminum alloy Al6061 (~98% Al) surface-polished substrates pieces (15 x 15 mm²) with 1.5 mm of thickness were supplied by Goodfellow.

To demonstrate the ability to fabricate functional hierarchical surfaces on transparent substrates, Borofloat® 33 supplied by VIDRASA S.A, is a flat borosilicate glass with a thickness of about 1 mm and 10 x 5,5 cm² size format has been employed.

2.3.2 Precursors for surface modification, thin film and nanostructures deposition

Two different nanostructure configurations have been employed to obtain hierarchical surfaces: tilted nanocolumnar and 1D core@shell nanostructures coatings from the following precursors:

- Stainless Steel (SS) nanocolumnar coatings: SS alloy AISI (99.99% purity) pellets (Equipment Support Company U.S.A., Inc) of 1/4'' diameter x 1/2'' long were used in the electron beam evaporation (GLAD) process.
- Organic@metal oxide 1D core@shell nanostructures: Titanium tetraisopropoxide (TTIP) supplied by Sigma-Aldrich has been the precursor utilized to synthesize seed and shell metal oxide layers, of specific microstructure crystallinity, by PECVD (**Figure 5**). For the organic nanostructured scaffold, the Π -conjugated Phthalocyanine (H_2Pc) and 1,5-diaminoanthraquinone (DAAQ) molecules were used in the soft-template method deposition, supplied by Sigma-Aldrich.

To achieve omniphobic and anti-icing properties, as well as other functional properties such as adhesion to the substrate, flexibility, or robustness, materials with low surface free energy (SFE) are required. For a hydrophobic behaviour, the SFE should be lower than 72.8 mN m^{-1} , which is the value associated to the surface tension of liquid water at room conditions. Besides, due to the low surface tension ($20 - 30 \text{ mN m}^{-1}$) of most solvents, lubricants, and oils, an SFE surface value lower than 20 mN m^{-1} is required to achieve oleophobicity⁴³. For example, materials made of silane base are recognized for having surface free energy around $19 - 21 \text{ mN m}^{-1}$ ⁴⁴. However, these silicone-based surfaces do not usually present slippery conditions. On the contrary, fluorinated precursors have been more effective. Zisman et al. proposed this classification of surface free energy of specific functional groups: $-\text{CH}_2$ (36 mN m^{-1}) > $-\text{CH}_3$ (30 mN m^{-1}) > $-\text{CF}_2$ (23 mN m^{-1}) > $-\text{CF}_3$ (15 mN m^{-1})⁴⁵. For the latter, the strong difference between fluorine and carbon electronegativities ensures a low polarizability, weak intramolecular forces, and low surface free energy.

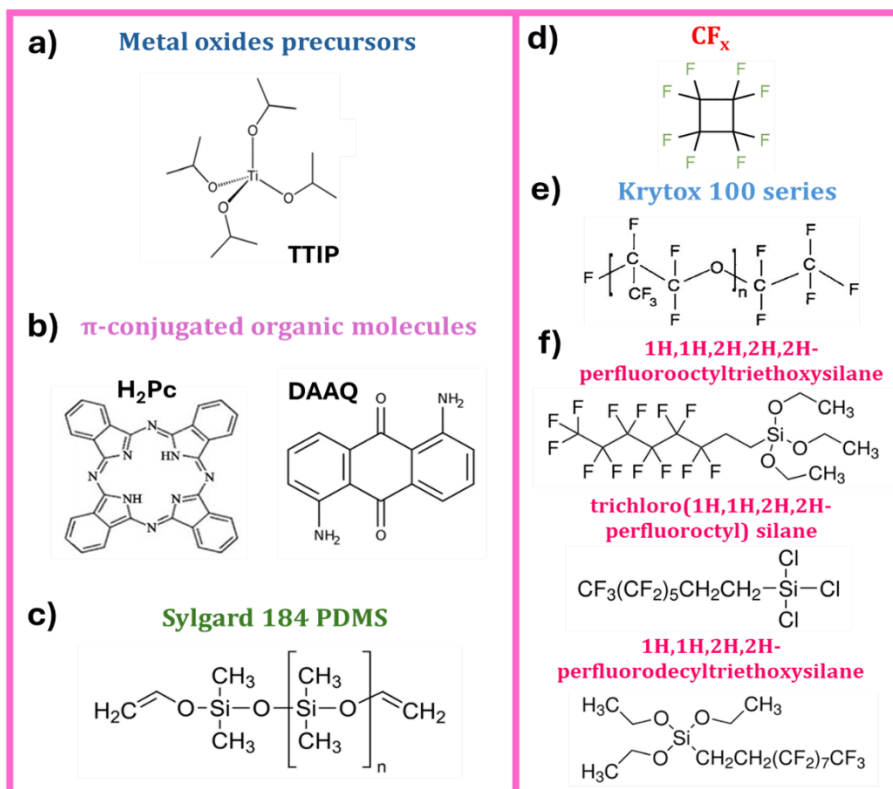


Figure 5. Molecular representation of main used precursors to develop the hybrid hierarchical surfaces: a) Titanium tetraisopropoxide (TTIP), b) Free metal phthalocyanine (H_2Pc) and 1,5-diaminoanthraquinone (DAAQ), c) Sylgard 184 PDMS composition formula, d) C-C₄F₈ organic gas cyclic fluorinated precursor for CF_x coatings, e) Krytox 100 series chemical formula, and f) chemical composition of fluorinated molecules used in grafting: 1H,1H,2H,2H,2H-perfluorooctyltriethoxysilane, trichloro(1H,1H,2H,2H-perfluorooctyl) silane and 1H,1H,2H,2H-perfluorodecyltriethoxysilane.

Therefore, a silicone-based compound and different fluorinated ones were used in this thesis under the format of thin films (thickness lower than 300 nm), infused lubricants (in porous matrices of thickness lower than 1 μm) and anchored fluorinated macromolecules looking for an eco-friendlier multifunctional proposal of reducing the required fluorine amounts in wetting control applications:

- **Silicone-based coating:** SYLGARD 184 Curing agent and SYLGARD 184 Silicone base for the fabrication of polydimethylsiloxane (PDMS) coatings by spin coating distributed by Sigma-Aldrich.

- CF_x conformal thin film: C-C₄F₈ gas organic precursor (Linde) has been employed for the fluoropolymer coating deposition by PECVD.
- Fluorinated precursors for grafting: three different synthetic fluorinated hydrocarbons that contain fully fluorinated carbon chains, supplied by Sigma-Aldrich were tested for surface chemical derivatization: 1H,1H,2H,2H,2H-perfluorooctyltriethoxysilane, trichloro(1H,1H,2H,2H-perfluorooctyl) silane 97% and 1H,1H,2H,2H-perfluorodecyltriethoxysilane 97% in order to check the possibility of reaching repellent properties minimizing the fluorine content or through the establishment of lower number of C-F bonds in shorter chains, and stable chemical bond (O-Si) to the hierarchical surfaces.
- Perfluoropolyether lubricant: compounds used as general lubricant agents in the aerospace industry due to high temperature resistance like Krytox^R 100 (DuPont) high molecular weight fluorinated lubricant was employed to get slippery (SLIPS) surfaces.

2.4 Characterization techniques of multifunctional wetting controlled hybrid hierarchical surfaces

In this section, the used characterization techniques are detailed, distinguishing between techniques that provide physicochemical and morphological information about the surface and those that offer insights into wetting and anti-icing behaviour. The characterizations have been carried out thanks to access to advanced facilities of the Nanotechnology on Surfaces and Plasma group, the Institute of Materials Science of Seville (ICMS) and the University of Seville Research, Technology and Innovation Centre (CITIUS), in addition to other relevant collaborations.

2.4.1 Physicochemical and morphological analysis

Examination of surface morphology has been performed by Scanning Electron Microscope (SEM) to investigate micro/nanostructures and thicknesses using a Hitachi S4800 microscope, employing different acceleration voltages ranging from 2 - 5 kV. Also, the topography of laser surfaces was examined using Confocal

microscopes Sensofar PL μ 2300 and Sensofar S Neox. In a confocal microscopy, the S_a and S_q arithmetic and root mean square roughness parameters, respectively, have been determined: the first one represents the arithmetic mean of the topography heights relative to a baseline, providing a general measure of roughness, whereas the second one is the square root of the mean of the squares of the topography heights relative to the baseline. This parameter is more sensitive to variations in roughness, emphasizing contributions from larger irregularities⁴⁶.

The surface chemical composition (first 3-5 nanometers thickness) was determined through X-ray Photoelectron Spectroscopy (XPS) analysis, employing a SPECS Phoibos 100-DLD electron spectrometer at ultra-high vacuum chamber ($<10^{-9}$ mbar). Spectra were acquired in the pass energy constant mode at 50 eV and 20 eV for survey and high binding energy resolved regions, using a non-monochromatic Al K α source. Chemical composition was also studied by Energy Dispersive X-ray (EDX) spectroscopy, which is a microanalysis technique that provides information on the chemical composition of ~ 3.0 μm surface depth. In the EDX-SEM analysis, we worked with a Hitachi S4800 at 15 kV and 10 mA provided with a Bruker $\text{\textcircled{C}}$ X-Flash Detector 4010.

Optical properties of the developed surfaces were studied using Ultraviolet-visible-Near InfraRed (UV-vis-NIR) spectroscopy. One significant effect to consider during the interaction of light with a nanostructured layer, if the light wavelength is comparable to the size of the material features, is light scattering. This scattering phenomenon involves random changes in the direction of the incoming photons, typically occurring without any loss of energy. Therefore, to fully characterize nanostructured samples, the use of an integrating sphere is often necessary to effectively capture the full components of the transmission and reflection spectra^{47,48}. UV-Vis-NIR optical properties of samples deposited on reference and commercial transparent substrates were measured between 200 - 1100 nm using a PerkinElmer Lambda 750 spectrometer equipped with a 60 mm diameter integrate sphere and a Cary 100 spectrometer in the range from 200 to 900 nm.

2.4.2 Analysis of the wetting and repellent properties at room and low temperatures

Wetting behavior was characterized at room temperature and under simulated environmental conditions, i.e. low temperature and high relative humidity.

- **Room environmental wetting analysis:**

Static contact angle (CA) values were measured using an OCA 20 DataPhysics setup (goniometer instrument) presented in **Figure 6 a)** by varying volumes of bi-distilled water and non-polar liquids (diiodomethane) droplets dispensed onto the surface sample, from 2 to 10 μl . This instrument features a computer-controlled droplet-shape analyzer and dispensing syringes. Wetting properties were determined by analyzing optical images of the deposited water droplet through both frontal and vertical cameras (3250 f/s and 2450 f/s). These measurements were averaged based on a minimum three to ten data points per sample. Dynamic contact angles were determined by hysteresis and sliding experiments. Rolling-off angles (RoA) were measured using the tilting function of the goniometer from 0° to 90° to precisely determine the angle at which the sample facilitates water droplet sliding. Meanwhile, contact angle hysteresis was assessed as the difference between the advancing and receding angles when 5 μl of water volume is controllably injected or removed from the surface. In **Figure 6 b)**, OCA 25 DataPhysics system is shown, what includes an environmental chamber with a thermoelectric module TPC160, for temperature control ranging from -30°C to 150°C and a humidity generator (HGC 30) to simulate real conditions and condensation experiments.

- **Anti-fouling tests by wetting measurements:**

The proposed anti-fouling tests were conducted using the OCA 20 DataPhysics equipment with 2 μl volume of the different bio-fouling simulant liquids: humic acid (65 mNm^{-1})⁴⁹, and sodium alginate (60 mNm^{-1})⁵⁰ solutions in water at 10 mg ml^{-1} concentration, and bovine serum albumin protein (51.5 mNm^{-1})⁵¹ to determine different liquid contact angles when droplets are deposited on the surface. Subsequently, using drop volumes between 5-15 μl , RoAs measurements were taken to determine the minimum angle values at which sliding of these fouling agents occurred.

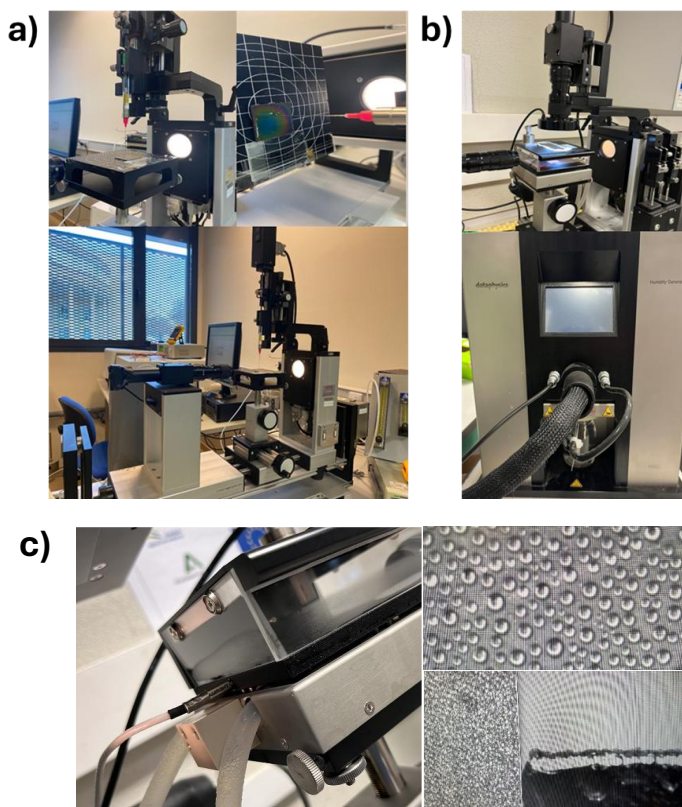


Figure 6. Pictures of the different wetting goniometers: a) OCA 20 DataPhysics equipment, b) OCA 25 DataPhysics for environmentally controlled wetting analysis, c) detail of the environmental chamber from external view during a water condensation experiment (left) and images taken with the top (middle and zoomed image) and the lateral (right) cameras.

- **Self-cleaning response characterization:**

For the study of the self-cleaning properties of the surfaces developed in this thesis, an experimental holder was used to position the samples in a fully horizontal position, but with the option to adjust the tilting angle. Once the different dirt simulants, graphite powder and common salt crystals were applied, we could check their removal with water droplets of a few microliters volume, which highlighted the superhydrophobicity of the surface by dragging the particles.

- **Laplace pressure effect on droplet evaporation at low temperature:**

The experiments conducted to evaluate the stability of the superhydrophobicity of the developed hybrid hierarchical surfaces by measuring the Laplace pressure evolution in an evaporation test, were carried out in chamber of the OCA 20 goniometer. A volume of 5 μl of bi-distilled water was deposited on the cold surface under a dry atmosphere with a constant N_2 flow. The evaporation event, where drop diameter and WCA measurements were monitored was performed at 0 °C of substrate surface (at those conditions, it is expected to have a water surface tension value of 75.5 mNm^{-1} compared to 72.8 mNm^{-1} at 20 °C).

- **Study of the water condensation on developed surfaces:**

Observation of water droplet condensation on the fabricated surfaces was performed under severe climatic conditions in the environmental chamber of the OCA 25 goniometer. The sample was set to a temperature of 2 °C, and then exposed to controlled environmental humidity levels, as shown in Figure 6 c). This experiment has been conducted with the sample at horizontal position (0 ° tilt) or tilted 90 ° to study the sliding of the condensed droplets on the surface.

Analysis of the water condensation on the functional surfaces from a microscopic point of view has been performed by Environmental Scanning Electron Microscope (ESEM) using a Quanta FEG 250 microscope located at Biomedical Research Institute of Malaga in

Nanomedicine Platform, IBIMA (BIONAND Malaga, Spain) and Thermofisher QuattroS ESEM with a STEM3+ detector located at the National Institute of Applied Sciences (INSA) in Lyon (France). ESEM experiments in INSA were conducted during my international stay of 92 days in Lyon (France) with the objective of characterizing the interaction between water and hybrid hierarchical surfaces. An ESEM can operate at higher pressure conditions than a conventional SEM, allowing it to analyze delicate samples under simulated environments. Typically, an ESEM operates in a pressure range from low vacuum (around 10^{-4} Pa) to relatively high pressures, approximately 10 to 2000 Pa. This pressure range is sufficient to maintain a controlled gaseous environment, enabling the observation of samples with moisture content and processes involving liquids, such as evaporation or condensation⁵². In this type of environmental microscope analysis, the electron beam voltage was around 25 - 30 kV. The experiments realized in INSA using ESEM were also performed in a STEM mode, whose technology was developed by the microscopy group at INSA^{53,54} and helped to improve the resolution of the experiments involved water. For all these experiments, the sample was held on a cooled sample holder to act as a cold focus, promoting condensation in a range of 2–6 °C, 98-100% relative humidity, and water vapor pressure ranges from 300 Pa to 1200 Pa.

To unravel in a deeper sense the interaction of water with the hierarchical surfaces, Environmental Transmission Electron Microscopy (ETEM) was employed in INSA. The ETEM provides advanced information at atomic level imaging, capable of performing “*in-situ*” studies of chemical reactions and phase changes, and better control of environmental conditions for specific temperature and pressure studies. The equipment was a FEI Titan 80-300 ETEM equipped with a lab-made gas unit and a Gatan Elsa cryo-sample holder⁵³. The experiments were carried out at temperature ranges from -2 °C to 7 °C of the surface while making the necessary adjustments for inducing water condensation on it. The working pressure was between 600 and 900 Pa to observe water condensation. Besides, the samples were pre-treated in an “*in-situ*” plasma cleaning service equipment to tune the wetting of the 1D

core@shell nanostructures for comparison between repellent and spreading surface predisposition.

2.4.3 Characterization of the anti-icing behaviour

Analysis of the icephobic response of the developed surfaces covers different aspects: from delaying freezing to ice accretion, that have been studied at laboratory scale and in large, advanced facilities, particularly Icing Wind Tunnel (IWT) in the National Institute of Aerospace Technology (INTA, Madrid, Spain).

- **Freezing delay time measurements:**

Wetting contact angle at low temperatures and Freezing Delay Time (FDTs) experiments of a water droplet deposited on a cold surface were conducted in the controlled environmental chamber of the OCA 20 system under dry atmosphere allowing real-time monitoring of the phase transformation (**Figure 7**). The substrate temperature was precisely regulated and maintained using a Peltier device, monitored through a thermocouple positioned 1 mm from the water droplet on the surface. Dry nitrogen at approximately ten standard cubic centimetres per minute (sccm) was cooled at 0 °C and passed through the chamber to simulate a dry environment, allowing equilibrium between water vapor and supercooled water droplets or ice particles. A syringe containing distilled water was introduced into the chamber at 0 °C, and a 2 µl water droplet was deposited onto the surfaces at room temperature (25°C), after which the temperature was reduced to the predetermined value (-5 °C or -10 °C). The temperature was decreased at a rate of -1 °C/s until reaching 0 °C and then at -0.1 °C/s for subzero temperatures.

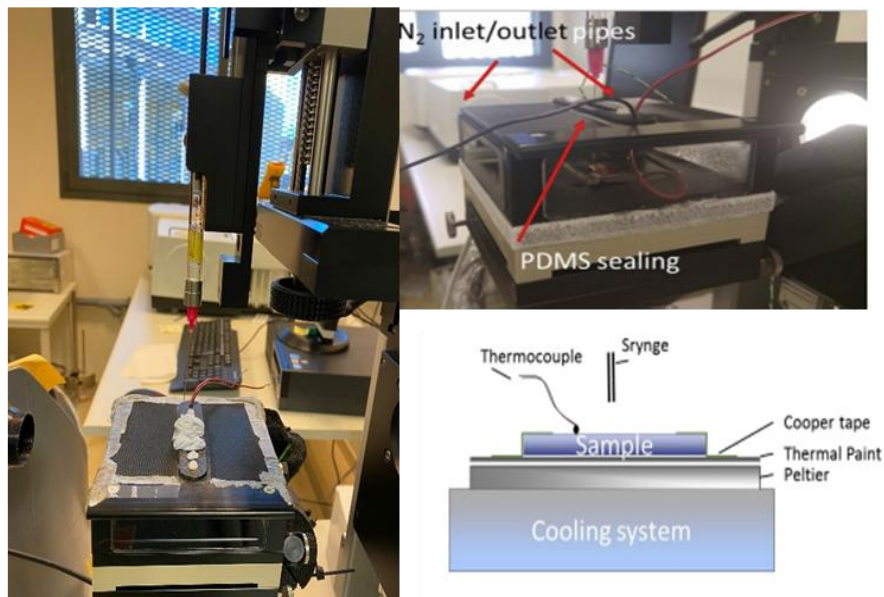


Figure 7. Picture of the controlled environmental chamber accessory of OCA 20 DataPhysics conditioned for freezing experiments and main scheme of FDT experiments using a cooling and Peltier system.

- **Ice adhesion tests on the developed surfaces:**

Pull-off and push-on ice adhesion tests both assess the bond strength between ice and the surface but differ in the direction of applied force. The pull-off test applies a perpendicular force to detach the ice from the surface, measuring adhesive strength, while the push-on test applies a parallel force to evaluate the ice's resistance to sliding or shear failure, providing insights into its stability under lateral forces. Ice adhesion measurements were performed using two different methods: pull-off and push-on tests, in collaboration with the Applied Physics Department of the University of Granada (UGR), the Materials science and environmental engineering Unit of the University of Tampere (TAU, Finland) and INTA. For pull-off ice adhesion experiments, the setup presented in **Figure 8 a)**⁵⁵ consisted of a pulling probe featuring a hollow Teflon cylinder situated on the top of the surface. This cylinder had specific dimensions: an internal diameter of 9.86 ± 0.12 mm and an area of 76.4 ± 1.9 mm², with a water level of approximately 13 mm. An integral component of this setup was a freezing chamber designed to achieve a

temperature of $-13\text{ }^{\circ}\text{C}$. The critical element for the pull-off ice adhesion test was the dynamometer (IMADA ZTA-200n/20N), positioned outside the freezing chamber and linked to a motorized linear stage (IMADA MHZ-500N-FA). The experimental procedure consists of placing the sample in the fridge and waiting for the complete solidification of the water cylinder around 30 minutes. After the rime ice had formed, the dynamometer was engaged, and a pulling force, perpendicular to the sample, was applied to measure the force required to lift the ice from the surface sample following a tensile mode. Considering the area of the cylinder, adhesion strength was expressed in kPa (Force (N)/Area (m^2)). The same experimental set-up for ice adhesion measurements in pull-off configuration in tensile mode has been implemented in a large climatic chamber, a Universal Material Testing Machine with controlled temperature and humidity for assessing wetting, ice formation, accumulation, and adhesion intended for research in the framework of the European SoundofIce project, established in the Nanotechnology on Surfaces and Plasma laboratory.

Push-on ice adhesion tests, these were conducted at Tampere University (Finland). The rime ice type was created in the icing wind tunnel (a specialized facility that combines both ice formation and wind flow to simulate real-world conditions involving freezing temperatures, humidity and air flow), and the ice adhesion strength was examined using a dynamometer setup described in Figure 8 b). These experiments were carried out in shear mode to push the ice accumulated at $-20\text{ }^{\circ}\text{C}$ previously. Value of 25 m/s of airspeed was imposed in this facility for the previous ice rime formation.

To complement the characterization, centrifugal ice adhesion experiments were also conducted in the IWT facilities of INTA (Figure 8 c)). In this case, glaze ice was formed at $-5\text{ }^{\circ}\text{C}$. The methodology involves placing $50 \times 50\text{ mm}^2$ samples in a specific holder before ice formation, using collimators to direct the ice formation to the selected area (around $2.75\text{ cm} \times 5\text{ cm}$). The sample is weighed before and after the experiment to determine the ice mass by difference. During the ice adhesion test, the surface is fixed in the arm of a Centrifugal ice Adhesion Test (CAT) system. The arm is then accelerated at 300 rpm until the ice detaches.

Knowing the angular velocity, the ice weight, and the ice adhered area, the adhesion value is calculated using shear stress^{56,57}.

- **Ice accretion tests on the developed surfaces:**

Ice accretion measurements in the IWT at INTA consist of evaluating how ice forms and accumulates on a surface exposed to cold conditions and airflow. During these experiments, winter weather conditions are simulated, where wind and low temperatures promote the freezing of water droplets or vapor on the surface of interest. INTA's IWT (**Figure 9**) is a laboratory scale facility meticulously designed to simulate icing conditions "*in cloud*" for the comprehensive study of ice accretion on aeronautical materials. This wind tunnel boasts an open section configuration and is housed within a 54 m³ cold climate chamber, ensuring temperature stability down to -20 °C for prolonged testing periods.

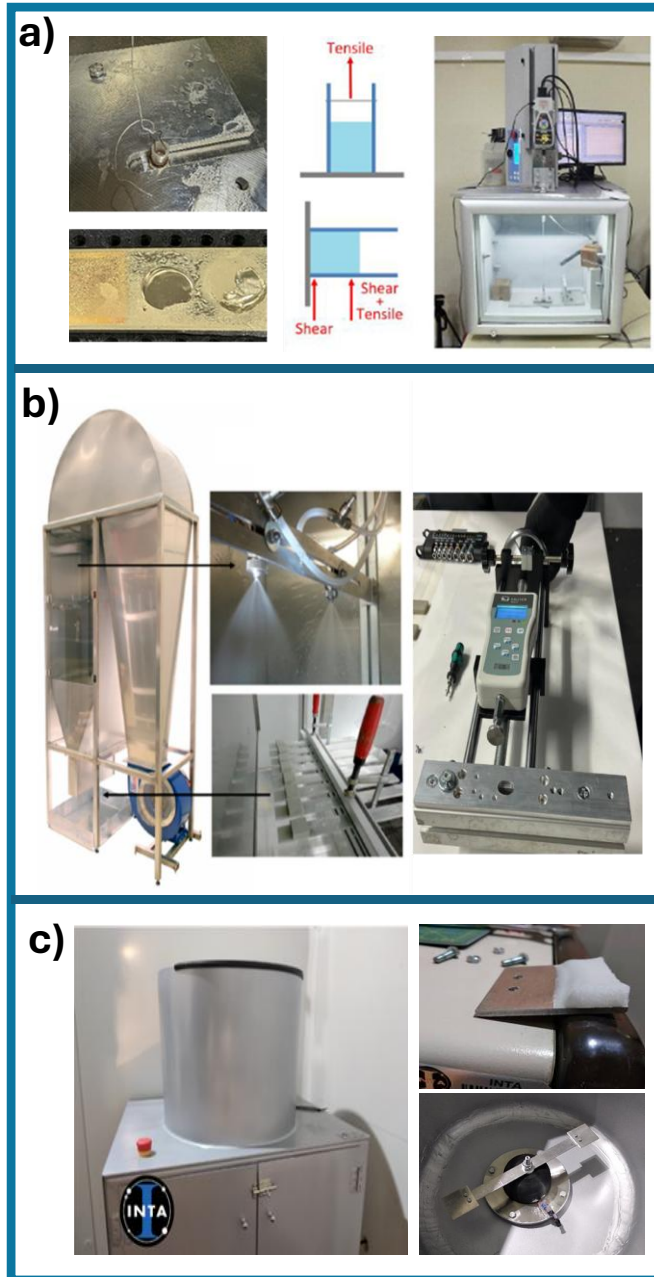


Figure 8. Pictures of some ice-adhesion testing devices: a) Ice adhesion experimental set-up in pull-off configuration (UGR): left) zoomed surface regions before and after the ice detachment, medium) tensile and shear mode schemes, right) general view of the tensiometer and the refrigerator chamber; b) Ice adhesion setup in push-on shear mode performed in IWT (TAU): left) general view of IWT with zoom on the supercooled water droplet dispenser and the sample holders, right) tensiometer configuration for shear mode measurement, and c) Centrifugal Ice Adhesion Test system from INTA⁵⁸: left) general view, right) example of ice accreted block (top) and sample mounting (bottom).

Within the same INTA's IWT facilities, a specific ice accretion test was conducted. Depending on the temperature and the liquid water content (LWC) (water mass per unit volume of air), two different ice crystals can be formed on a surface. Glaze ice forms when liquid water droplets impact cold surfaces and freeze rapidly, resulting in a smooth, glass like appearance that is dense and heavy, typically occurring during freezing rain and when the temperature is around $-5\text{ }^{\circ}\text{C}$. Meanwhile rime ice develops from the condensation of water vapor that freezes upon contact with cold surfaces, characterized by a rough texture and irregular crystal formations. This one is less dense than glaze ice and forms in high humidity and low temperature conditions around $-15\text{ }^{\circ}\text{C}$. Mixed ice consists of a combination of both glaze and rime ice, displaying features of both types, with varying density influenced by rapid changes in temperature and humidity⁵⁹.

The test facilities are situated within the cold climate chamber, which allows for temperature adjustments ranging from room temperature down to a minimum of $-40\text{ }^{\circ}\text{C}$ ⁶⁰. Before ice accretion process, the samples were allowed to cool in a cold room.

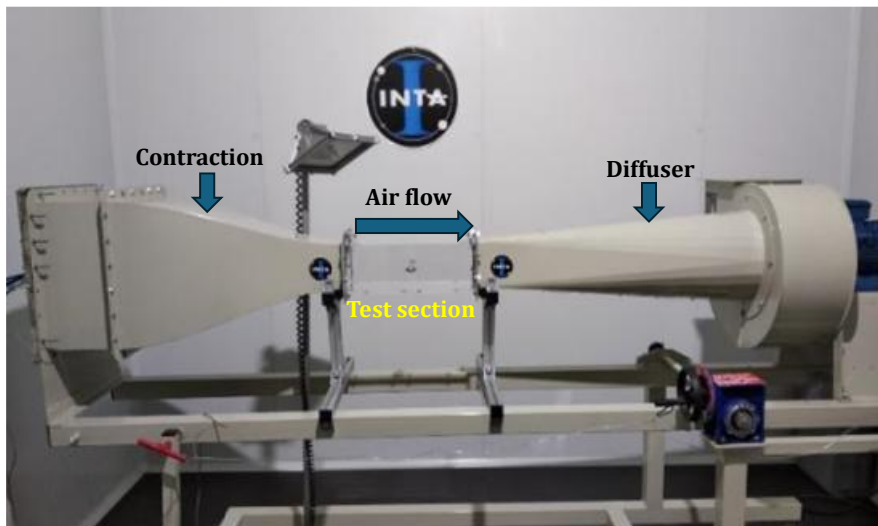


Figure 9. Picture of the ice-wind tunnel (IWT) from INTA with indicated main parts: contraction, test section where the sample is facing to the air flux containing supercooled water droplets and diffuser⁶¹.

An important parameter for this type of experiment in large facilities simulating real conditions is the wind speed, which specifically is set at 25, 50, and 70 m s⁻¹ at INTA. During an ice accretion experiment in the IWT, besides the LWC and the wind speed, the mean volume diameter (MVD) is another key parameter in the simulation of adverse environments. For the current experiments, the LWC value was 25 ml min⁻¹ (1 g of water /1 m³ of air), and the MVD values depended on the type of ice formed. Although the specific conditions are detailed in Chapter 6, it is important to highlight that the type of ice formed was glaze ice at -5 °C (simulating the most aggressive wind speed conditions, with the highest possible water content from an experimental perspective, and common temperature in cold areas). The methodology consisted of placing the samples in tilted position around -5 °C facing an air/water flow maintained at temperatures between -5 °C and -10 °C. A controlled water flow was dispensed using a peristaltic pump, combined with air flowing at 70 m s⁻¹. The samples were placed at a 45° angle to facilitate observation of ice accretion onto the surface through a camera. The amount of accreted ice was determined by weighing the sample, before and after the experiment. All these experiments and measurements were carried out in the same cold room where IWT is located.

2.4.4 Stability and durability essays

Aging, regarding working under cycling and aggressive environmental conditions, is a key factor which checking a surface must pass to demonstrate its level of reliability and stability. In this thesis, robustness and durability have been verified by visual inspection, measuring reproducible wetting and, in some cases, chemical composition, after the developed surfaces have been subjected to special tests, following the current protocols established in the literature according to performed applications^{62,63}. Durability tests have consisted of immersion for 30 minutes in different organic liquids like isopropyl alcohol, humic acid and bovine serum (biofouling agents), two different thermal cycles: 3 cycles of heating at 150 °C for 2 hours and cooling at room temperature, and 5 freezing-thawing cycles from -5 °C to room temperature, as well as irradiation

with UV-vis light for one and a half hours at a distance of 30 cm from the light source (ASB-XE175 Xenon lamp with power of 300 mW/cm²).

- **Corrosion test for functional hierarchical stainless steel surfaces:**

In Chapter 4, the developed surfaces of low fluorinated hierarchical stainless steel have been subjected to corrosion essay. The anti-corrosive properties were assessed through electrochemical analysis, employing the potentiodynamic polarization technique available in the Department of Surface Engineering Corrosion and Durability of the National Center for Metallurgical Research, CENIM-CSIC (Madrid). The electrochemical measurements were conducted in a conventional three-electrode cell, where the deposited thin films served as the working electrode. A stainless-steel rod constituted the counter-electrode, while a saturation calomel electrode (SCE) served as the reference electrode⁶⁴. The identification of relevant electrochemical parameters, such as corrosion potential, pitting potential, and corrosion/passive current, followed the procedures outlined in literature and represented in **Figure 10 a)**⁶⁵. Corrosion potential (E_c) is the electric potential at which a metal's rate of oxidation (corrosion) and reduction reactions at its surface are balanced⁶⁶. This potential indicates the tendency of a material to corrode in a specific environment, with more negative values generally signifying a higher likelihood of corrosion. Pitting potential (E_p) is the specific electric potential at which a localized corrosion initiates on a metal's surface in an aggressive environment. When the potential reaches this threshold, it overcomes the protective oxide layer on the metal, leading to the formation of small, deep pits. Pitting potential is an important indicator of a material's resistance to pitting corrosion, (higher values generally indicating better resistance⁶⁷). Finally, the values of corrosion/passive current (I_p) refer to the electric current that flows through a corroding material when it is in a passive state. This occurs when the material has developed a protective oxide layer that inhibits further corrosion⁶⁵. Further details of the experimental corrosion tests will be defined in Chapter 4, where the corrosive medium employed was NaCl solution.

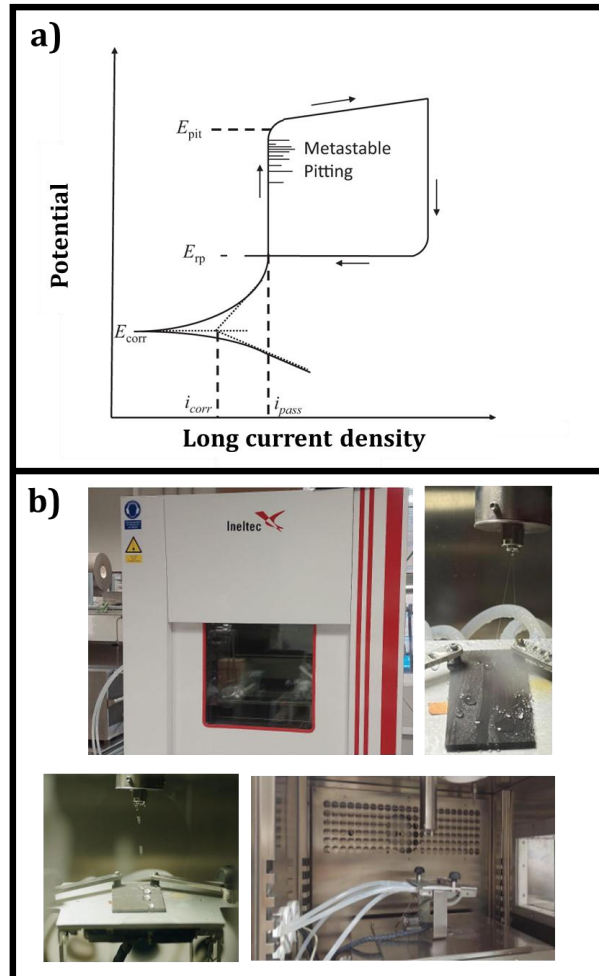


Figure 10. a) Representation of main parameters involved in the corrosion potentiodynamic polarization test⁶⁶; E_{pit} : Pitting corrosion potential and E_{corr} : Corrosion potential, b) Climatic chamber images, detailing both water dispensers (spray-top right and dripping-bottom left).

- **Durability and stability at icing conditions:**

Additional durability and reproducibility tests were carried out using the Universal Material Testing Machine with controlled temperature and humidity for assessing wetting, ice formation, accumulation, and adhesion, shown in Figure 10 b). Several important specific parts of the climatic chamber can be highlighted: an adjustable motion platform for regulating and moving the position of the desired sample within the plane, a rotatable support allowing positioning from horizontal to 90° without the need for external access to the climatic chamber, a tray of associated electrothermal Peltier modules for

independently controlling the sample's temperature, separate from the chamber's temperature, a thermostatically controlled water dosing system for conducting long and cycling water interaction as well as performing ice formation experiments under two possible working modes: water spray or continuous dripping on the surface at a fixed temperature. Visual inspection is possible due to transparent windows (quartz or ZnS) and a thermographic camera. Durability, stability and reproducibility tests using this climatic chamber were carried out, for simulated rain erosion and thermal/humidity cycles working between 2 °C -5 °C with the default value of relative humidity (3 cycles of 2 hours). The evaluation of the appearance and the wetting behavior before and after these experiments under simulated real conditions inside the climatic chamber allowed the evaluation of permanent anti-icing performance.

Bibliography

1. Singh, S., Kumar, S. & Khanna, V. A review on surface modification techniques. *Mater Today Proc* (2023).
2. Biswas, A. *et al.* Advances in top-down and bottom-up surface nanofabrication: Techniques, applications & future prospects. *Advances in Colloid and Interface Science* **170**, 2-27 (2012).
3. Mehta, N. Overview of Coating Deposition Techniques. *Tribology and Characterization of Surface Coatings*, 1-32 (2022).
4. J.M. Albella. *Introducción a La Ciencia de Materiales: Técnicas de Preparación y Crecimiento*. (1993).
5. Chu, P. K., Chen, J. Y., Wang, L. P. & Huang, N. Plasma-surface modification of biomaterials. *Materials Science and Engineering, Reports* **36**, 143-206 (2002).
6. Alfred Grill. *Cold Plasma in Materials Fabrication* (1994).
7. Charles A. Bishop. *Vacuum Deposition onto Webs, Films and Foils* (2011).
8. Donald M, M. *The Foundations of Vacuum Coating Technology* (2003).
9. Bárdos, L. & Baránková, H. Plasma processes at atmospheric and low pressures. *Vacuum* **83**, 522-527 (2008).
10. Rossnagel, S. M. Thin film deposition with physical vapor deposition and related technologies. *Journal of Vacuum Science & Technology A: Vacuum, Surfaces, and Films* **21**, S74-S87 (2003).
11. Murr, L. E. *et al.* Metal Fabrication by Additive Manufacturing Using Laser and Electron Beam Melting Technologies. *J Mater Sci Technol* **28**, 1-14 (2012).
12. A.David, A. G. *Handbook of Thin Film Process Technology* (1998).
13. Barranco, A., Borrás, A., Gonzalez-Elipe, A. R. & Palmero, A. Perspectives on oblique angle deposition of thin films: From fundamentals to devices. *Prog Mater Sci* **76**, 59-153 (2016).
14. Matthew M. Hawkeye M.M., J. W. and S. *Glancing Angle Deposition of Thin Films*. (2014).
15. Sánchez-Valencia J.R. Fabricación de láminas delgadas porosas con emisión fluorescente para aplicaciones fotónicas. *A Thesis by*. (2010).
16. Borrás, A., Gröning, O., Aguirre, M., Gramm, F. & Gröning, P. One-step dry method for the synthesis of supported single-crystalline organic nanowires formed by π -Conjugated Molecules. *Langmuir* **26**, 5763-5771 (2010).
17. Castillo Seoane J. Low Dimensional Optoelectronic Devices Enabled by Vacuum and Plasma Technologies. *A thesis by*. (2024).
18. Won Chung J., Hoichang Y., *et al.* Single-Crystal Organic Nanowires with Large mobility and strong Fluorescence emission: a conductive-AFM and space **21**, 10488 (2009).
19. Mittal, M., Sardar, S. & Jana, A. Nanofabrication techniques for semiconductor chemical sensors. in *Handbook of Nanomaterials for Sensing Applications* 119-137 (2021).
20. Sathiyarayanan, S., Rajagopal, G., Palaniswamy, N. & Raghavan, M. Corrosion Protection by Chemical Vapor Deposition: A Review. *Corrosion Reviews* **23**, 355-370 (2005).
21. Paul K. & Chu X. *Low Temperature Plasma Technology (Methods and Applications)* (2013).
22. Kadhim, M. M., Shebab, M. M. & Abdalameer, N. Plasma Vacuum Systems: A Review Article. *Minar International Journal of Applied Sciences and Technology* **06**, 325-342 (2024).
23. Vilan, A. & Cahen, D. Chemical Modification of Semiconductor Surfaces for Molecular Electronics. *Chem Rev* **117**, 4624-4666 (2017).
24. Pankaj, S. K. *et al.* Applications of cold plasma technology in food packaging. *Trends Food Sci Technol* **35**, 5-17 (2014).
25. Yi, C. X., Wang, S. K., Xu, X. B., Tian, Y. F. & Bao, M. D. Study on plasma cleaning of surface contaminants on pure copper. *Mater Res Express* **10**, (2023).
26. Sakudo, A., Yagyu, Y. & Onodera, T. Sterilizing surface using plasma technology in medical sector. *Int J Mol Sci* **20**, (2019).
27. Fan, J., Wu, H., Liu, R., Meng, L. & Sun, Y. Review on the treatment of organic wastewater by discharge plasma combined with oxidants and catalysts. *Environmental Science and Pollution Research* **28**, 2522-2548 (2021).

28. Donnelly, V. M. & Kornblit, A. Plasma etching: Yesterday, today, and tomorrow. *Journal of Vacuum Science & Technology A: Vacuum, Surfaces, and Films* **31**, 50825 (2013).
29. Sharma, P. *et al.* Plasma etching of polycarbonate surfaces for improved adhesion of Cr coatings. *Appl Surf Sci* **637**, 157903 (2023).
30. Randhawa, H. Review of plasma-assisted deposition processes. *Thin Solid Films* **196**, 329–349 (1991).
31. Thomas Neubert, M. V. Plasma-Enhanced Chemical Vapor Deposition. in *Handbook of Deposition Technologies for Films and Coatings (Third Edition)* (2010).
32. Gordillo-Vázquez, F. J., Herrero, V. J. & Tanarro, I. From carbon nanostructures to new photoluminescence sources: An overview of new perspectives and emerging applications of low-pressure PECVD. *Chemical Vapor Deposition* **13**, 267–279 (2007).
33. ZHANG, H. *et al.* Recent progress on non-thermal plasma technology for high barrier layer fabrication. *Plasma Science and Technology* **20**, 063001 (2018).
34. Milton Ohring. Deposition and structure. in *Materials Science of Thin Films* (2002).
35. Piallat, F. *et al.* PECVD, RF vs Dual Frequency: investigation of plasma influence on metalorganic precursors decomposition and material characteristics PECVD, RF vs Dual Frequency. *J Phys D Appl Phys* **47**, 185201 (2014).
36. Terriza A., Funcionalización Superficial de Polímeros por PECVD para Uso Biomédico. *A Thesis by.* (2013).
37. Macias-Montero, M. *et al.* Vertically aligned hybrid core/shell semiconductor nanowires for photonics applications. *Adv Funct Mater* **23**, 5981–5989 (2013).
38. Quan, Y.-Y., Chen, Z., Lai, Y., Huang, Z.-S. & Li, H. Recent advances in fabricating durable superhydrophobic surfaces: a review in the aspects of structures and materials. *Mater Chem Front* **5**, 1655–1682 (2021).
39. Sanjay Raja S., Selvakumar P., Dinesh Babu, P., Rubasingh J. & Suresh, K. Influence of laser parameters on superhydrophobicity-A review. *Engineering Research Express* **3**, (2021).
40. Kumar, V., Verma, R., Kango, S. & Sharma, V. S. Recent progresses and applications in laser-based surface texturing systems. *Mater Today Commun* **26**, 101736 (2021).
41. Rico, V. *et al.* Robust anti-icing superhydrophobic aluminum alloy surfaces by grafting fluorocarbon molecular chains. *Appl Mater Today* **21**, 100815 (2020).
42. Kujawa, J., Al-Gharabli, S., Kujawski, W. & Knozowska, K. Molecular Grafting of Fluorinated and Nonfluorinated Alkylsiloxanes on Various Ceramic Membrane Surfaces for the Removal of Volatile Organic Compounds Applying Vacuum Membrane Distillation. *ACS Appl Mater Interfaces* **9**, 6571–6590 (2017).
43. Cansoy, C. E. & Cengiz, U. The effect of perfluoroalkyl and hydrocarbon liquid chain lengths on oleophobic behaviors of copolymer surfaces. *Colloids Surf A Physicochem Eng Asp* **441**, 695–700 (2014).
44. Vudayagiri, S., Junker, M. D. & Skov, A. L. Factors affecting the surface and release properties of thin polydimethylsiloxane films. *Polym J* **45**, 871–878 (2013).
45. Zisman, W. A. Relation of the Equilibrium Contact Angle to Liquid and Solid Constitution. 1–51 (1964).
46. Elliott, A. D. Confocal Microscopy: Principles and Modern Practices. *Curr Protoc Cytom* **92**, (2020).
47. Fraden, S. & Maret, G. Multiple light scattering from concentrated, interacting suspensions. *Phys Rev Lett* **65**, 512–515 (1990).
48. Nedelcu, N. *Thin Films.* (2023).
49. Klavins, M. & Purmalis, O. Surface activity of humic acids depending on their origin and humification degree. *Proceedings of the Latvian Academy of Sciences, Section B: Natural, Exact, and Applied Sciences* **67**, 493–499 (2013).
50. Del Gaudio, P., Colombo, P., Colombo, G., Russo, P. & Sonvico, F. Mechanisms of formation and disintegration of alginate beads obtained by prilling. *Int J Pharm* **302**, 1–9 (2005).
51. Thi-Yen Le, T. *et al.* On the equilibrium surface tension of aqueous protein solutions – Bovine serum albumin. *J Mol Liq* **347**, 118305 (2022).
52. Zhang, Z. *et al.* Applications of ESEM on Materials Science: Recent Updates and a Look Forward. *Small Methods* **4**, 1900588 (2019).

53. Masenelli-Varlot, K. *et al.* Wet-STEM tomography: Principles, potentialities and limitations. *Microscopy and Microanalysis* **20**, 366–375 (2014).
54. Chatre, C. *et al.* Influence of Surface-Active Substances and Substrates on the Wettability of Individual Aerosol Particles during Condensation by Environmental Scanning Electron Microscopy. *Langmuir* **39**, 765–772 (2022).
55. Ibáñez-Ibáñez, P. F., Montes Ruiz-Cabello, F. J., Cabrerizo-Vílchez, M. A. & Rodríguez-Valverde, M. A. Ice adhesion of PDMS surfaces with balanced elastic and water-repellent properties. *J Colloid Interface Sci* **608**, 792–799 (2022).
56. Rehfeld, N., Speckmann, B. & Stenzel, V. Parameter Study for the Ice Adhesion Centrifuge Test. *Applied Sciences (Switzerland)* **12**, (2022).
57. García, P. *et al.* Passive Ice Protection Systems Lab Scale Testing Methodology. *SAE International Conference* (2023).
58. García, P. *et al.* Passive Ice Protection Systems Lab Scale Testing Methodology. *SAE International Technical Paper*. (2023)
59. Wei, K., Yang, Y., Zuo, H. & Zhong, D. A review on ice detection technology and ice elimination technology for wind turbine. *Wind Energy* **23**, 433–457 (2020).
60. Koivuluoto, H., Hartikainen, E. & Niemelä-Anttonen, H. Thermally sprayed coatings: Novel surface engineering strategy towards icephobic solutions. *Materials* **13**, (2020).
61. Mora, J. *et al.* Setting a comprehensive strategy to face the runback icing phenomena. *Surf Coat Technol* **465**, (2023).
62. Malavasi, I., Bernagozzi, I., Antonini, C. & Marengo, M. Assessing durability of superhydrophobic surfaces. *Surf Innov* **3**, 49–60 (2015).
63. Milionis, A., Loth, E. & Bayer, I. S. Recent advances in the mechanical durability of superhydrophobic materials. *Adv Colloid Interface Sci* **229**, 57–79 (2016).
64. Domínguez-Jaimes, L. P. *et al.* Corrosion resistance of anodic layers grown on 304L stainless steel at different anodizing times and stirring speeds. *Coatings* **9**, 706 (2019).
65. Eliyan, F. F. & Alfantazi, A. Mechanisms of Corrosion and Electrochemical Significance of Metallurgy and Environment with Corrosion of Iron and Steel in Bicarbonate and Carbonate Solution. *Corrosion* **70**, 880–898 (2014).
66. Nyby, C. *et al.* Electrochemical metrics for corrosion resistant alloys. *Sci Data* **8**, 58 (2021).
67. Joseph R. D. & Lois A. A. *Properties and Selection: Irons, Steels, and High-Performance Alloys* (1990).



“Dissatisfaction is the first necessity for progress”

(Thomas Edison)

3

**Control of the wetting behaviour
on porous substrates:
hierarchical surfaces through 1D
functionalized nanostructures for
selective wetting, or
omniphobicity**

Abstract

In recent years, there has been a focus on achieving adapted surfaces for microfluidic, vital in biomaterials, and water purification. This study combines a soft-template method assisted by vacuum and plasma techniques to create metallic oxide nanofibers on porous substrates like cellulose membranes and stainless steel (SS) grids. Under mild conditions of fabrication, 3D nanomembranes have been obtained by means of the combination of 3 levels of roughness: the one of the porous supports at the microscale, the one due to the geometry of the nanofibers (from a few micrometers to several hundred nanometers) and the one of the metallic oxide nanostructure surfaces. As a result, the hierarchical surfaces repelling water droplets and allowing oil droplets spreading serve as effective water/oils filters. UV light activation of photoactive metallic oxide nanostructure surfaces lets the wetting tunability from hydrophobic to hydrophilic responses. 3D nanomembranes are compatible with surface modification protocols leading to omniphobic (i.e. full liquid repellence) and self-cleaning surfaces.

3.1 Introduction

Controlling wetting on advanced surfaces is crucial because it allows for the design of materials with specific functionalities across various applications. Wetting behaviour, (how a liquid interacts with a surface), affects processes like cleaning, fluid transport, and heat transfer. For example, in microfluidics, controllable wettability enables precise manipulation of tiny liquid volumes, while in anti-fouling coatings, it helps to prevent the accumulation of unwanted substances on surfaces. Additionally, superhydrophobic materials can repel water efficiently, making them valuable for self-cleaning surfaces, waterproofing, and anti-icing applications. The ability to engineer surfaces with tuneable wetting properties also extends to medical devices, where controlled wetting can reduce bacterial adhesion or optimize drug delivery systems. Furthermore, research into superhydrophobic and superhydrophilic surfaces is driving advancements in energy-efficient water harvesting and innovative heat management solutions, which are particularly relevant for industrial and environmental applications. Achieving effective wetting control often involves manipulating surface chemistry and microstructure, which can create tailored interactions with liquids, leading to enhanced performance in specific conditions^{1,2,3}. For example, the ability to separate liquids in minuscule quantities is a crucial aspect of controlling wetting, particularly in microfluidics and advanced materials applications. This capability presents several significant implications such as surface engineering highlighting surface roughness and chemical modification⁴. Advanced materials, where nanostructured surfaces have shown that manipulating the geometry can lead to effective droplet formation and separation, indicating different textures to achieve desired droplet behaviours^{5,6} which is potential for innovation. For example, to ongoing development in controlling wetting at the microscale offers to drug delivery systems, where precise liquid amounts need to be administered, and in the food industry for ingredient separation⁵.

Control of wetting on porous substrates, such as nanomembranes, presents significant challenges due to the complex interplay between the surface's physical and chemical properties. For these types of porous substrates there are many reasons why controlling wetting can be an issue, highlighting the capillary effects and liquid absorption⁴, surface heterogeneity⁷, instability of surface

coatings and inconsistent wetting state transitions⁸, from Cassie-Baxter to Wenzel states that can be unpredictable on textured porous surfaces⁹.

Moreover, the extended studies of liquid separation within nanotechnology and materials science necessitates the deployment of sophisticated techniques for the manipulation and separation of minuscule quantities of liquids at the nanoscale level¹⁰. This involves the utilization of innovative methodologies like nanofiltration, microfluidics, and nanomembranes to efficiently isolate, sort, and manipulate small liquid samples or volumes for diverse scientific and technological applications. In this context, membranes play a pivotal role in selectively controlling the transfer of matter and/or energy between them. The efficiency and functionality of membranes are contingent upon various factors, including material composition, pore size, structural geometry, distribution, and pertinent physical-chemical aspects such as density and surface tension¹⁰. These elements significantly influence a membrane's efficacy in separation processes, particularly within the realms of microfluidics and nanodevices. Microfluidics, entailing the manipulation of fluids at the microscale, relies on nanodevices for their remarkable responsiveness¹¹, capable of employing both passive and active modes of separation techniques. Hydrophilic membranes, with affinity for water, are frequently employed in gravity-based filtration of emulsions due to their resistance to clogging¹². However, their efficacy diminishes when tasked with separating water-in-oil emulsions. Ongoing developments in membrane technology aim to overcome these limitations, striving to create membranes tailored to diverse separation needs through research in surface modification, advanced materials, and innovative structural designs¹³. These advancements are in fields such as environmental remediation, pharmaceuticals, and industrial processes, where precise liquid separation¹⁴ is indispensable.

Transitioning to the commercial substrate domain, nanomembranes with nanoscale pore sizes find application in various fields such as high-efficiency cathodes in lithium batteries¹⁵, contaminated water filtration processes¹³, and semiconductor devices¹⁶ such as nanotubes or graphene¹⁷. This highlights the emergence of the concept of "*fast flexible electronics*"¹⁸. A noteworthy facet in membrane technology involves nanomembranes, capable of providing high selective wetting. This attribute is particularly pertinent in applications such as self-cleaning phenomena in windows¹⁹, anti-fog coatings for glass, as well as antibacterial and antiseptic coatings²⁰. Nanomembranes with superhydrophobic

but oleophilic properties are of significant interest for wastewater treatment²¹, biomedical²², and veterinary applications²³ as filters, given their ability to repel water while allowing the passage of oils. This unique capability positions them as excellent candidates for filtering biological fluids²⁴, such as blood, where the separation of lipids²⁴ from aqueous components is crucial. In biomedical and veterinary contexts²³, nanomembranes enhance sample preparation, biomolecule separation, and in-vitro diagnostics procedures^{22,25,26}.

Within this expansive framework, we propose a promising methodology to achieve the control over wetting by creating hierarchical surfaces that take advantage of the microporosity of substrates, allowing them to be applied as selective membranes, making them both repellent and self-cleaning. This involves merging a soft-template approach utilizing single-crystalline organic nanowires (ONWs) as vacuum-processable 1D templates with the plasma-enhanced chemical vapor deposition of TiO₂ nanofibers as it is described in Chapter 2. This TiO₂ shell was chosen for their photoactive and wetting properties. These nanofibers are deposited onto high-porosity and rough supports like cellulose and stainless steel (SS) filters. Cellulose filters are highlighted due to their porosity, biodegradability and cost (generally more affordable) and SS filters are employed due to their durability (resistant and long-lasting), corrosion resistance and easy cleaning. The ability to integrate the growth of these repellent and self-cleaning nanofibers onto such substrates is reflected in the demand for these materials in applications such as low-flow-retention filtration processes and liquid. Its versatile applications extend to soil and seed analysis, food drying, and atmospheric gas control²⁷, filtration of juices and beers to eliminate particles without altering flavor and for its application in the treatment of water containing suspended pollutants²⁸. They also play a crucial role in food production, particularly in filtering oils and other edible liquids²⁹, as well as laboratories for filtering solutions in chemical analyses³⁰.

Finally, these hierarchical surfaces fabricated on porous substrates using the previously indicated methodology serve as templates for hosting chemical agents through plasma techniques, spin coating, and vapor phase deposition.

Our study explores the selective wetting characteristics of nanostructured porous materials, highlighting their potential applications as filtration systems and microfluidics valves. We demonstrate how surface modification of these materials enhances controlled wetting behavior, providing high selectivity and

tunability under UV exposure. Additionally, we present an innovative technique for separating small mixed volumes of polar and non-polar liquids through gravitational and surface tension influences. The investigation includes a thorough examination of the chemical alteration of TiO₂ nanostructured membranes with fluorine, integrating them into elastomeric polydimethylsiloxane (PDMS). This integration preserves the unique three-scale roughness achieved through the nanostructuring process, promising the creation of manageable, reliable, and enduring self-cleaning surfaces.

3.2 Experimental Section

3.2.1 Materials

The substrates employed in this study comprised porous supports and reference compact, smooth substrates, namely Si (100) silicon and fused silica, these last measuring 1.5x1.5 cm². The commercial substrates selected for the deposition of 3D nanomembranes were the S0770 SS grid filter from Sigma-Aldrich, featuring a 40 mm diameter and a 70 μm pore size which was chosen. To precede the utilization of flexible filters in subsequent stages, a Whatman qualitative cellulose filter, Grade 1, measuring 42.5 mm in diameter with an 11 μm pore size, was employed. Additionally, another Whatman qualitative cellulose filter, Grade 4, sized at 40 mm in diameter and featuring a 25 μm pore size, was employed.

3.2.2 Methods

3.2.2.1 Fabrication of hierarchical surfaces on porous substrates: 3D Nanomembranes

TiO₂ nanofibers were the result of applying the soft-template method described in Chapter 2. This methodology allows the deposition of single-crystalline nanowires to achieve 1D templates in different commercial substrates: cellulose filters and (SS) grids. **Figure 1** shows a reminder about different steps for the synthesis of nanofibers (NFs) in specific supports (1 to 4 steps) and the result of these nanostructures growth in different commercial substrates. The difference between organic nanowires (ONWs) and nanofibers (NFs) is the presence of the TiO₂ shell, where ONWs of H₂Pc is the organic core as final material.

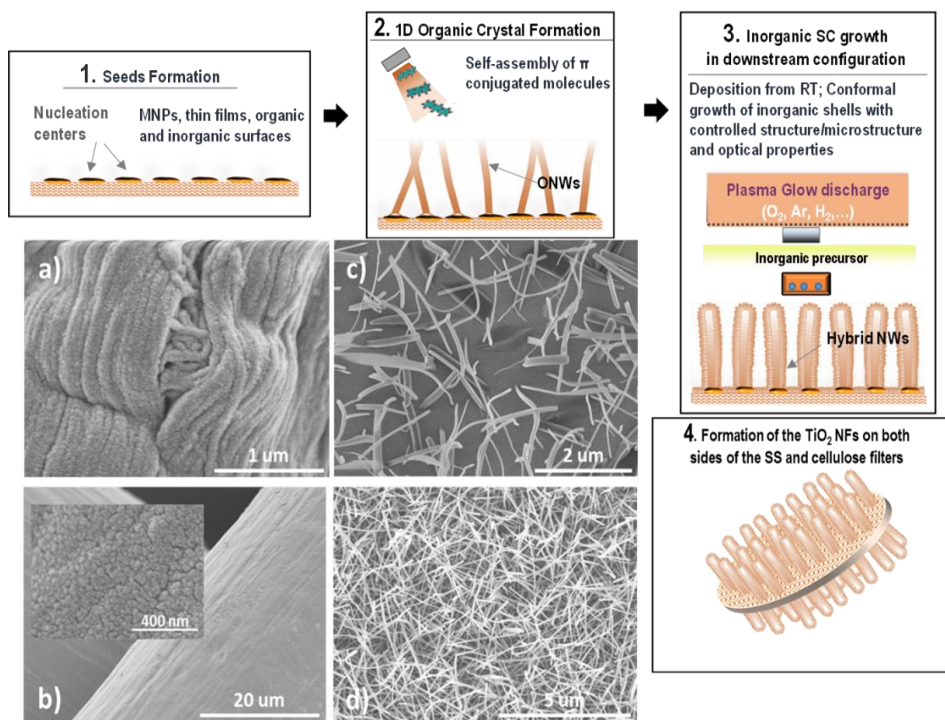


Figure 1. Plasma-assisted deposition of core@shell NFs on 3D supports. Steps 1-4: Pictorial representation of the multistep procedure for the formation of the H₂Pc@TiO₂ nanofibers on flat and 3D supports. a,b) SEM images of a) the cellulose filter and b) stainless steel membrane after the conformal PECVD of the TiO₂ acting as a nucleation layer for the formation of the NFs (step 1), c,d) Top view SEM images of the H₂Pc single-crystalline nanowires growing on the TiO₂ nucleation layer for two different densities (step 2) in cellulose filters.

Figure 1 shows a high conformality of the TiO₂ layer, showing the typical cauliflower morphology according to the deposition conditions: formation at room temperature under 100% oxygen plasma³¹ by (PECVD) technique. Figure 1 c) and d), shows the different densities at different magnifications for the ONWs deposition under two different growth rates namely c) $< 0.5 \text{ \AA s}^{-1}$ and d) $> 1.5 \text{ \AA s}^{-1}$ of H₂Pc nanowires formed on a TiO₂ nucleation layer. H₂Pc nanowires were growing thanks to the driven mechanism for crystallization process led by the high directionality of the self-assembly with specific organic molecules, where π -stacking growth is characteristic for this type of molecules³² and under mild temperatures (being aware of the presence of cellulose in the employed porous substrates) and vacuum conditions, by a simple thermal evaporation process as described in Chapter 2. It is noteworthy that the shell keeps the specific microstructure of the deposited material, in this case, TiO₂. The final step

involves obtaining an inorganic shell by low pressure PECVD (described in Chapter 2) of 200 nm for 1 hour of deposition, resulting in a core@shell nanostructure. The shell's thickness can be adjusted by managing the TiO₂ deposition time. The outcomes presented in this work pertain to the core@shell nanostructure referred to as H₂Pc@TiO₂ nanofibers (NFs). These molecules (H₂Pc) were evaporated using Ar plasma at 2×10^{-2} mbar, with a substrate temperature of 170°C and a growth rate of 1 Å s⁻¹. The existence of the core explains the blue color appearance of the cellulose and metal grids as it will be observed in the next figures, and it is important to indicate that the deposition processes were for both substrates simultaneously. The blue color of these organic molecules results from the characteristic Q-band absorption typical of these organic functional molecules. The final step (step 4) is the repetition of steps 1-3 to get these nanofibers on both sides of the supports, highlighting that these steps did not occlude the pores of these commercial nanomembranes.

3.2.2.2 Modification of hierarchical surfaces on porous substrates

As a final and necessary step to achieve water-repellent properties (superhydrophobicity), the anchoring of fluorinated molecules in the form of chemical functionalization was carried out on these types of nanostructured membranes. This fluorine-based grafting involved chemical derivatization. TiO₂ nanofibers were exposed to 1H,1H,2H,2H-PFTOES for 2 hours following the steps described in Chapter 2. Before it, the surfaces were chemically activated by an oxygen plasma PECVD for 10 minutes, (details were shown in Chapter 2). Otherwise, to reinforce the mechanical stability of the nanofibers, 3D nanomembranes were coated by a thin layer of polydimethylsiloxane (PDMS) using 2:1 ratio of PDMS precursor to curing agent dissolved in a 1:3 toluene solution, using a spin-coater working at 3500 rpm with 2 different steps for the deposition. Eventually, these PDMS-embedded 3D nanomembranes were also subjected to the fluorine-based grafting procedure, respecting the porosity of these nanomembranes, as will be presented throughout this chapter.

Regarding the labeling for these nanomembranes, the label H₂Pc@TiO₂ NFs is used to address the formation of core@shell NFs using H₂-phthalocyanine as the organic core and TiO₂ as inorganic shell. For different surface modifications,

employed labels will be H₂Pc@TiO₂ NFs + F-grafting or H₂Pc@TiO₂ NFs + PDMS + F-grafting, in the same order as experimental procedure.

3.2.3 Characterization of hierarchical surfaces on porous substrates

The morphological aspects and density of the nanofibers were comprehensively investigated through microscopic imaging at varying magnifications, facilitating a meticulous statistical analysis (ImageJ) of the 3D nanomembranes. SEM images were captured utilizing a Hitachi S4800 operating at 2 kV, encompassing both reference and commercial substrates, including cellulose filters and stainless steel grids. Establishing a one-week interval of sample storage in dark conditions to avoid changes in photoactive activities of TiO₂ shell, the wettability properties were systematically evaluated by performing droplet contact angle measurements using polar (bi-distilled water, WCA) and non-polar (CH₂I₂ diiodomethane, DCA) liquids. These measurements were performed using the OCA 20 DataPhysics goniometer, as detailed in Chapter 2. The determination of the static measurements was with 1 µl droplets on the surfaces, while the dynamic sliding, Rolling-off-Angle (RoA), experiments were conducted with 5 and 10 µl droplets with water and diiodomethane. The presentation of statistics encompassing data from five measurements on each surface provides an averaged contact angle value with estimated errors ranging between 3% and 7%. The exploration of wetting selectivity has been carried out by water-diiodomethane separation demonstration through a glass funnel and joint material designed to support nanomembranes of 19 mm in diameter. The photoactivation of the surfaces was achieved through UV-vis (Ultraviolet-Visible) irradiation in an ambient air environment. A comprehensive spectrum emanating from a 175 W ASB-XE175 xenon light source lamp was employed for these experiments with a specific distance between lamp and samples of 30 cm with a power of 300 mW cm⁻², where the key aspect will be the hydrophobic-hydrophilic conversion.

3.3 Results and discussion

3.3.1 Photoactive hierarchical surfaces on porous substrates: 3D nanomembranes morphology

Figure 2 shows SEM images at different magnifications of the hierarchical surfaces obtained by the deposition of $\text{H}_2\text{Pc@TiO}_2$ NFs on 3D porous substrates compared to the reference ones. The synthetic approach is compatible with high-density NFs formation on both cellulose and SS membranes. Minor variations in NFs density, thickness, and length across the different supports are attributed to surface temperature, membrane surface area differences and material membrane roughness. Considering that the roughness of the TiO_2 seed layer is the same for each of the commercial substrates used, the sticking coefficient is also the same, and the substrate temperature is identical for both because it is necessary for nucleation to occur, the characteristic aspect that may result in a higher or lower density of nanowires is the micro/meso-porosity of the commercial membranes. In the case of larger pores, as observed in the metallic nanomembranes, there was more space for the nucleation of the nanowires since this type of nanowire tends to nucleate more rapidly in geometries with high surface defects, such as the corners of these pores in the metallic filters, whereas a conformal density was observed in the case of cellulose substrates. In both, metallic grids and cellulose filters, NFs presented in length and diameter distributions, with maximum around $4 \mu\text{m}/0.20 \mu\text{m}$ and ranging from 2 to $9 \mu\text{m}/0.10$ - $0.35 \mu\text{m}$ for the length/diameters, respectively.

Despite the varied substrates, SEM images revealed a consistent and homogeneous growth of NFs with uniform density. The TiO_2 shell maintained its characteristic globular and cauliflower-like microstructures when they were observed on the porous substrates. Additionally, the application of plasma-assisted technology ensured the alignment and adhesion of NFs on both rigid and soft substrates which are also chemically different.

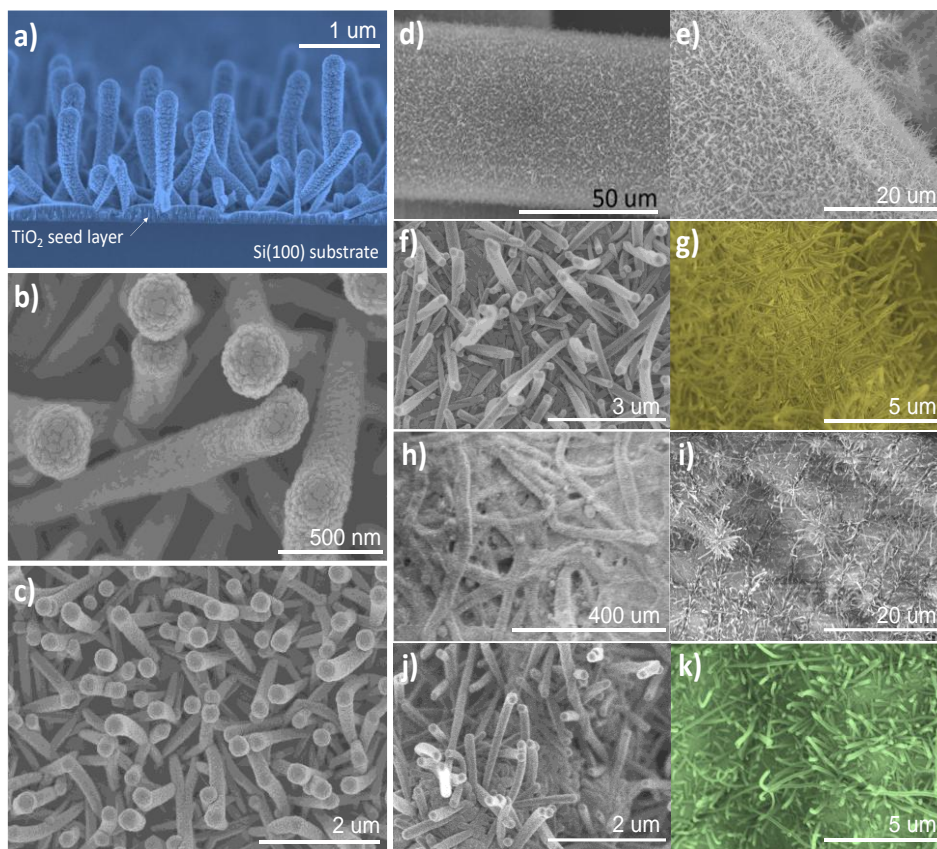


Figure 2. Formation of $\text{H}_2\text{Pc}@TiO_2$ NFs on flat reference and 3D porous substrates. Characteristic SEM images at different magnifications of the a) and c) $\text{H}_2\text{Pc}@TiO_2$ NFs deposited onto Si (100), d) and g) on the stainless steel grid, h) and k) on the 25 μm cellulose membrane.

Although on the Si (100) substrate, vertical alignment of NFs was more pronounced (Figure 2 a)), on the stainless steel grid (Figure 2 e)-g)), they also presented preferential orthogonal alignment and to a lesser extent on cellulose along the topographic undulations. This alignment results from the plasma sheath electric field and the increased nanofiber rigidity during the TiO_2 shell formation³³. Detailed observations of the metallic grids (Figure 2 d)-g)), and cellulose filters (Figure 2 h)-k)), showed an excellent NFs growth conformality achieved through plasma-assisted growth, allowing high-density NF development across the whole exposed geometric features and internal parts of the 3D supports. For the first time, we present that using the soft-template approach with substrates of open porosity, including materials such as stainless steel membranes and temperature-sensitive cellulose filters, we can achieve a

conformal growth of aligned NFs using specific and compatible organic molecules thanks to shell deposition on mild work conditions.

3.3.2 Wettability of photoactive hierarchical surfaces on porous substrates

The initial step of the characterization of the tunable wetting surface involves an assessment of static and dynamic contact angles using diverse liquids, both polar and non-polar in nature. This comprehensive investigation encompasses the examination of the wetting behavior with water, representing a polar liquid, and diiodomethane, representing a non-polar liquid. The outcomes of these analyses are succinctly presented in **Table 1**, collecting the control of wetting behaviors by designing the structure and chemical functionalities based on the deposition of NFs on both flat and 3D supports. Table 1 shows how reference silicon and fused silica substrate presented both hydrophilic (water) and oleophilic (diiodomethane) responses given the low contact angle values. However, thanks to the surface nanostructuring with the $\text{H}_2\text{Pc@TiO}_2$ NFs deposition, an increment in the water contact angles (WCA) on fused silica (134°) and Si substrate (123°) have been obtained, respectively. Diiodomethane contact angle (DCA) cannot be measured, indicating an enhanced oleophilic surface state of the flat reference substrates. In instance of porous substrates, the initial wettability diverges significantly from that of the flat reference materials. Cellulose supports presented complete superhydrophilicity and superoleophobicity, while the metallic grid has displayed high contact angle values with both polar and non-polar liquid droplets. Upon the formation of $\text{H}_2\text{Pc@TiO}_2$ NFs on cellulose, the wetting behavior suffered a transformation, shifting from a membrane that was entirely permeable to water to one that inhibited water absorption. Also the *W-RoA* values, show low sliding values ($\sim 0^\circ$ and 17° for NFs without any chemical functionalization).

Table 1. Values of water and diiodomethane contact angles (WCA and DCA, respectively) and rolling-off angles (RoA) with water (W-) and diiodomethane (D-) droplets for H₂Pc@TiO₂ NFs, H₂Pc@TiO₂ NFs+ F-grafting and H₂Pc@TiO₂ NFs+ PDMS + F-grafting, deposited onto porous membranes and reference substrates for comparison.

Samples	WCA (°)	W-RoA (°)	DCA (°)	D-RoA (°)
Fused Si	24	>90	19	--
Si	27	>90	10	--
11 μm cellulose	0	--	0	--
25 μm cellulose	0	--	0	--
SS grid	133	>90	85	>90
H ₂ Pc@TiO ₂ NFs on fused Si	134	20	0	--
H ₂ Pc@TiO ₂ NFs on Si	123	25	0	---
H ₂ Pc@TiO ₂ NFs on 11 μm cellul.	~180	0	0	--
H ₂ Pc@TiO ₂ NFs on 25 μm cellul.	~180	17	0	--
H ₂ Pc@TiO ₂ NFs on SS grid	~180	10	34	--
H ₂ Pc@TiO ₂ -F NFs on SS grid	~180	5	153	35
H ₂ Pc@TiO ₂ -PDMS-F NFs on SS grid	~180	5	136	15

The uncoated metallic filters exhibit a *petal effect* behavior³⁴ characterized by high WCA and RoA values, whereas with the presence of NFs, the surface presented sliding angles akin to the *lotus effect* (RoA ~ 10°) resulting a good opportunity to achieve a selective wetting with superhydrophobic and oleophilic properties, minimal adhesion against the impact of water droplets and a maximum one for diiodomethane spreading on the surface. These values notably surpass those exhibited by the nanostructured flat references (RoA ~ 20°). The most minimal sliding angles were observed with H₂Pc@TiO₂ NFs on cellulose membranes, even inducing a lack of adhesion for 10 μl water droplets on the lower-porous-size cellulose substrate. Consequently, the fabrication of hierarchical surfaces on porous materials using nanostructures with a high aspect ratio, termed 3D nanomembranes, endows them with superhydrophobic capability and superoleophilic response. These properties find utility in selecting

the liquids passing through the nanomembranes and facilitating the separation of liquid mixtures, particularly those involving water. Moreover, this functionality enables precise control over the directional movement of liquids. Finally, the combination of the hierarchical surface through the core@shell nanostructures with the different surface modifications exhibits high WCA values, with both samples showing superhydrophobic characteristics and W-RoA values below 10° (W-RoA of 5° for $\text{H}_2\text{Pc}@TiO_2\text{-F}$ and $\text{H}_2\text{Pc}@TiO_2\text{-PDMS-F}$). From the perspective of wetting with diiodomethane, a value of 153° for $\text{H}_2\text{Pc}@TiO_2\text{-F}$ -grafting and a value of 136° for the same hierarchical surface but with a thin PDMS layer between the shell and the surface fluorination were reached. Low D-RoA values were detected for these two samples, emphasizing the superoleophobic nature of this proposed combination.

Figure 3 illustrates alterations in wetting behavior, transitioning from a water-permeable membrane to a water-repelling state for cellulose membrane with a transformation attributed to the varying pore sizes under examination. With the fabrication of nanofibers (NFs), the metallic grids showed superhydrophobic behavior, attaining a state of complete water droplet repulsion, as depicted in Figure 3.c) and d). Concurrently, that membrane underwent a noteworthy shift from oleophobic (85°) to oleophilic (34°). Importantly, the nanostructured cellulose substrate maintained consistently high surface free energy when confronted with droplets of low-tension liquids, as detailed in Table 1. This experimental observation substantiates the transition in wetting behavior from Wenzel to Cassie-Baxter surfaces³⁵.

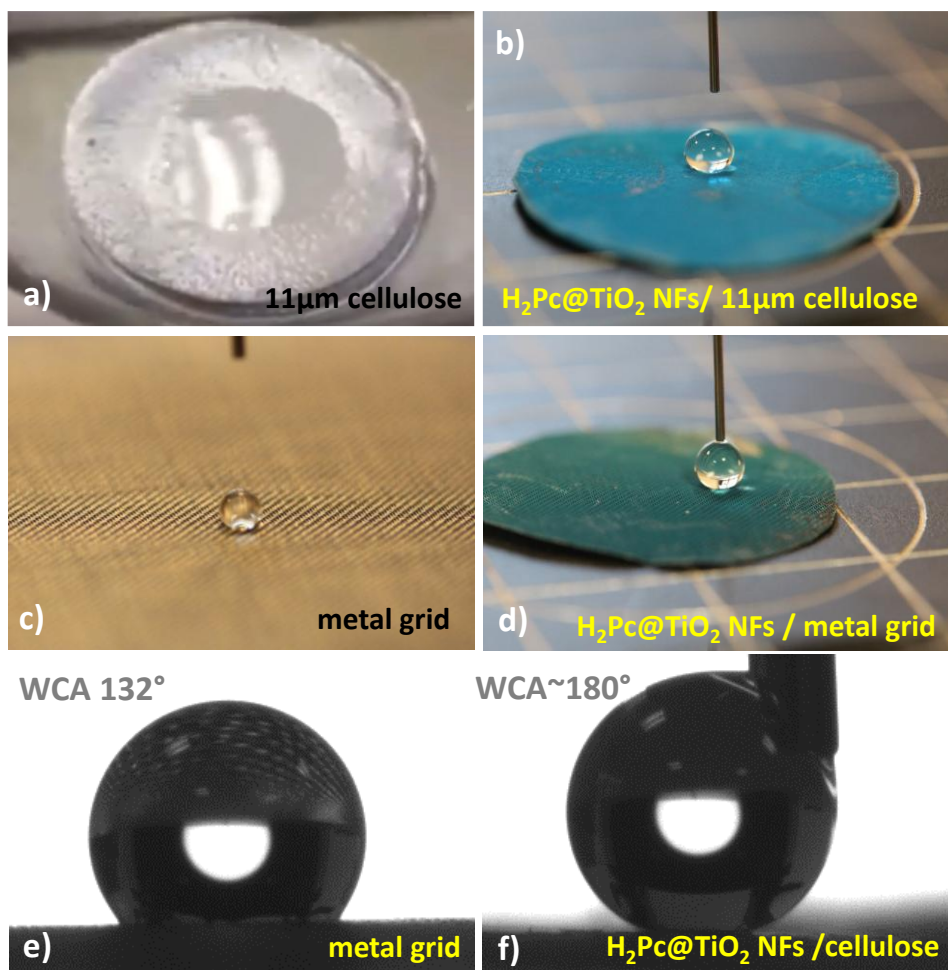


Figure 3. Wetting behavior of the cellulose filter and metallic grid a), c) before and b), d) after the nanostructuring with the $H_2Pc@TiO_2$ NFs. Water droplets of 2 and 10 μ l were used in panels b) and d) and e), f) deposited on the metal grid and the $H_2Pc@TiO_2$ NFs/cellulose surfaces, respectively. (In this last, the tip was kept inside trying to counteract capillarity versus surface repellency).

This phenomenon arises from the combination of three distinct roughness levels: firstly, the porous substrates with dimensions in the order of tens of micrometers; secondly, the micrometer-scale length of the nanofibers; and lastly, the nanoscale morphology of the TiO_2 shell. Consequently, the modification of commercial membranes with $H_2Pc@TiO_2$ NFs, without substantial chemical or physical alterations (beyond a color change), manifests a unique superhydrophobic and superoleophilic response.

3.3.3 Evaluation of the wetting selectivity and liquid filtration of 3D nanomembranes

To demonstrate the superhydrophobic/superoleophilic capability of these nanomembranes, some liquid filtration tests are depicted in **Figure 4**. The panels present a comparison of results involving a) the metallic grid, b) 25 μm , and c) 11 μm cellulose filters nanostructured with $\text{H}_2\text{Pc@TiO}_2$ NFs deposited on their surfaces during a liquid filtration/separation test using a 1:1 emulsion of water and diiodomethane, with a consistent flux controlled by a syringe. As observed in the pictures of Figure 4, the droplets from the emulsion (around 2 μl) tended to primarily spread across the surface, although some liquid retains a semi-spherical shape. This phenomenon has been attributed to the lower surface tension of water in the initial stages of the experiment (Figure 4 a1), b1) and c1)). Conversely, the higher density and surface tension of the non-polar liquid led to an immediate spreading of diiodomethane over the entire surface. This behavior was more pronounced in the cellulose filters, as it is illustrated in Figure 4 b2) and c2), when an increasing number of small droplets coalesced to form a microdroplet that grows until they covered the entire surface, as is shown in Figure 4 a3), b3), and c3). Diiodomethane has been effectively separated from water due to the superhydrophobic/superoleophilic nature of the hierarchical membrane surfaces supported by the gravity effect. Furthermore, it is crucial to emphasize that no alteration of the filtered diiodomethane or the separated water properties (no bluish color) were detected, indicating the absence of hypothetical detachment or dilution of the organic core from the NFs.

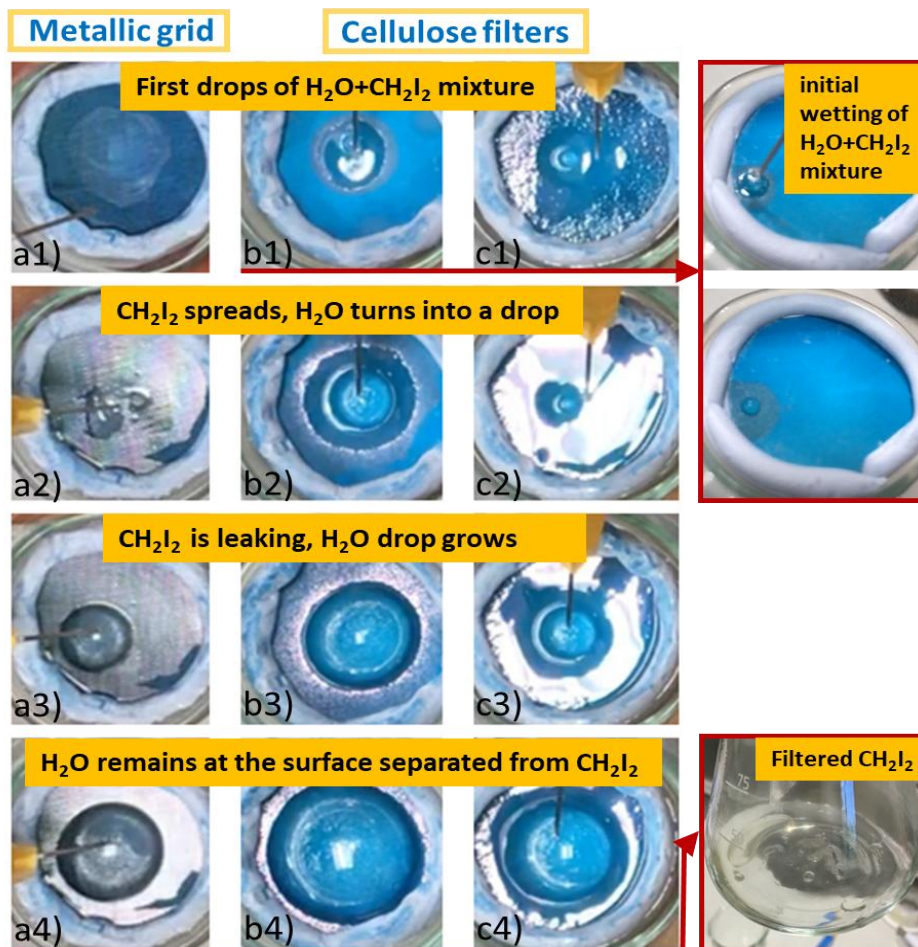


Figure 4. Non-polar/polar liquid emulsion separation and filtration. The photographs show the sequences of a: 1:1 diiodomethane/water emulsion droplets interacting with the 3D nanomembranes of a) metal grid and cellulose filter of b) 25 μm and c) 11 μm decorated with H₂Pc@TiO₂ NFs. Water remains on the surface and diiodomethane leaks out because of the wetting selectivity of these 3D nanomembranes surfaces.

3.3.4 Wetting tunability through photoactivation of the hierarchical surfaces on porous substrates

The ability to craft multifunctional systems through the synergistic integration of materials with distinct functionalities within nanoarchitectures stands as a pivotal advantage inherent in the applied methodology for fabricating core@shell nanofibers. TiO₂ as shell is deposited in its amorphous phase since it is grown under room temperature conditions on an organic nanowire, indicating

that the photoactivity of this amorphous phase may behave somewhat differently compared to the crystalline phase. Particularly the chemical inertness of TiO₂ coating, coupled with the commendable mechanical properties of the organic core in the NFs, serves to fortify the stability of the resulting hierarchical surfaces. In this specific context, the photoactivation capability of the nanostructured TiO₂ shell was demonstrated to facilitate a reversible transition between superhydrophobic to superhydrophilic states upon exposure to UV light^{36,37}. The graph in **Figure 5** presents the evolution of hierarchical porous surfaces water contact angle compared to that on a flat reference under a) visible (Vis) and b) UV-vis illumination.

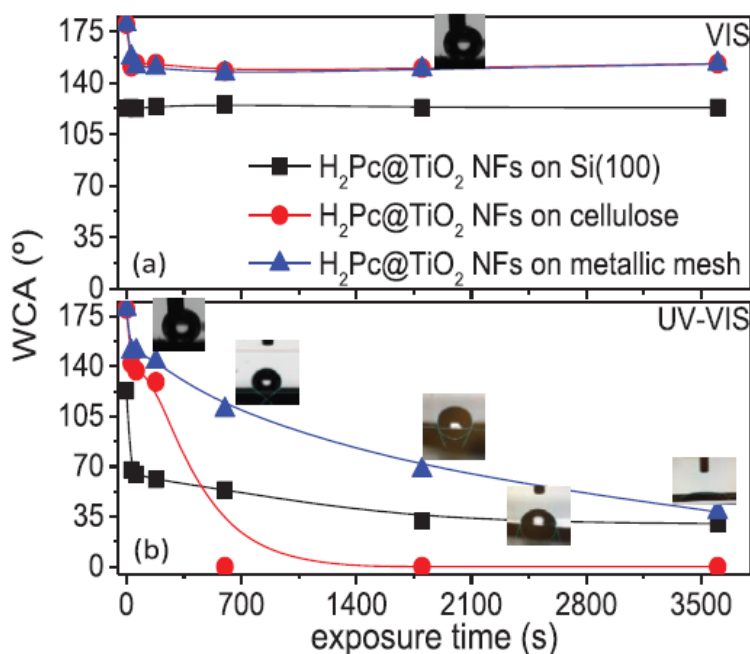


Figure 5. Superhydrophobic-to-superhydrophilic conversion of the hierarchical porous surface, in function of the irradiation wavelength, and support (metallic grid, 11 μm cellulose filter, and Si reference substrate) through the variation of the water contact angle with the irradiation time as labeled with a) visible and b) UV-vis lights.

The water contact angle of surfaces fabricated on cellulose and metallic grids exhibited a decrease within the initial minutes of exposure to visible (Vis) light, a surprising outcome given that TiO₂ traditionally demonstrates photoactivity primarily under excitation at ultraviolet (UV) wavelengths. Consequently, there was a simultaneous reduction of about 20° in the water contact angle by

approximately 200 seconds for both porous supports unlike the Si reference one. Subsequently, the WCA stabilized, maintaining its superhydrophobic nature³⁸. This fact could be related to the presence of active species in the visible region as part of our hierarchical surface. The presence of free phthalocyanines (H_2Pc), which not only provide a blue color to the samples but also exhibits a Q-band in the 600-700 nm region, could be activated when irradiated with these wavelengths. Given the porosity of the TiO_2 shell, these species may migrate through the walls, causing hydroxylation (presence of -OH groups) in the shell. The fact that the samples continued to exhibit a bluish color after the experiment suggests that H_2Pc remained in the pores. The presence of carbon from the air, as well as contaminants captured during the experimental process, may contribute to a decrease of a high WCA of the TiO_2 surface when irradiated^{39,40,41}. This intriguing observation may also be attributed to the light-absorbing capacity of these substrates, compared to the nanostructures deposited on Si (100), which exhibits a stable response under Vis illumination.

This phenomenon underscores differential controls with UV-visible wavelength illumination, inducing a swift transition of all three surfaces to hydrophilic states. Nonetheless, the kinetics response varies contingent upon the support type, with the metallic grid manifesting a comparatively slower decrease in WCA in comparison to silicon and cellulose hierarchical surfaces. It is noteworthy that only on the cellulose filter the conversion was complete within the experimental timeframe, rendering superhydrophilic after 600 seconds of illumination according to amorphous TiO_2 behavior in the literature^{42,43}. Previous studies on hydrophobic membranes adorned with TiO_2 nanoparticles have documented delayed photoactivation or necessitated elevated synthesis temperatures to achieve crystalline TiO_2 phase and enhance the photoactivation performance^{43,44}. The intricate mechanisms governing water condensation on hydrophilic or hydrophobic TiO_2 thin films and highly porous nanostructures have been scrutinized to precisely control the photoactivation of wettability, a phenomenon also observed in other photoactive, low-dimensional metal oxide nanomaterials⁴⁴. The recovery of superhydrophobic properties on the surface can be initiated through heating, extended dark storage, or exposure to low vacuum conditions overnight^{45,38}. The multifaceted capabilities of TiO_2 hierarchical porous surfaces, as evidenced by their tunable wettability

responses, amplify their potential utility across a spectrum of scientific and technological areas.

These findings unveil opportunities for the application of TiO₂ nanomembranes in diverse domains, potentially serving as photonic microfluidic valves for liquid selection under light activation. Furthermore, their prospective roles encompass acting as self-cleaning membranes or sensors, with additional applications in the photocatalytic elimination of water pollutants²¹.

3.3.5 Chemical modification of the hierarchical porous surfaces to achieve omniphobicity

Numerous factors, including the composition of the fibers, mechanical or chemical stability upon contact with liquid drops, and adhesion of the fibers to the support, play pivotal roles in ensuring the stability of NFs on porous surfaces. In a specific context, the TiO₂ composition of the shell imparts high chemical and notable thermal stability to the NFs, while the organic core concurrently confers flexibility to accommodate the impact and motion of drops on the nanomembrane surface. PECVD methods, described in Chapter 2, are renowned for their conformal deposition of metal oxides and polymers on different supports, exhibiting enhanced performance in terms of tunable wetting and compatibility with intermediate layers to enhance material adhesion.

Therefore, critical considerations in our system involve the substrate itself, the hygroscopic cellulose, and the integrity of the NFs after cyclic wetting with polar and non-polar liquids. **Figure 6** presents SEM images illustrating the nanostructured cellulose surface after contact to a 3 μ l water droplet for a duration of 10 minutes. Discernible topographic alterations mainly characterized by swelling are evident.

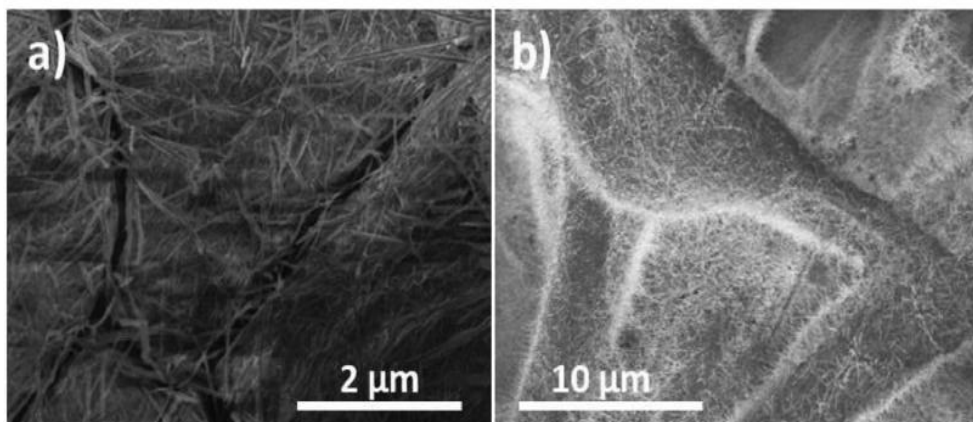


Figure 6. Hygroscopic effect on the cellulose a) 11 μm and b) 25 μm pore-size filters decorated with the $\text{H}_2\text{Pc@TiO}_2$ NFs just after wetted with water droplets of 3 μl volume for 10 min.

However, despite these modifications, the 3D nanostructures exhibit robust adhesion to the cellulose surface, thereby offering tangible evidence of the stability of the nanofibers (NFs) even after undergoing 4 cycles of contact with water and diiodomethane. To fortify mechanical stability further, the forthcoming sections will explore a polymeric embedding of the NFs with elastomeric coatings such as a highly flexible polymer, polydimethylsiloxane (PDMS)⁴⁶. This methodology, previously documented to improve contact angles with non-polar liquids on high-aspect-ratio nanostructured surfaces³⁷, is anticipated to bolster NF adhesion to complex geometrical substrates, mechanical stability, and flexibility of the resulting hierarchical porous surfaces. Consequently, the $\text{H}_2\text{Pc@TiO}_2$ NFs were enveloped with a thin layer of PDMS (details were described in Chapter 2). SEM images for the two surface modifications carried out on these hierarchical surfaces deposited on commercial membranes are presented in **Figure 7** a)-c), depicting the features of the NFs decorated metallic grid followed by the deposition of PDMS. Several key aspects can be emphasized at this point firstly, in panel a), and supported by Energy Dispersive X-ray (EDX) spectroscopy analysis in panels d-i) show that the PDMS coating process does not clog the membrane pores of the metallic grid. Second, although part of the NFs appears completely buried in the polymer, yet the microscale roughness of the surface is high, as the heads of the longest NFs stand out of the PDMS surface.

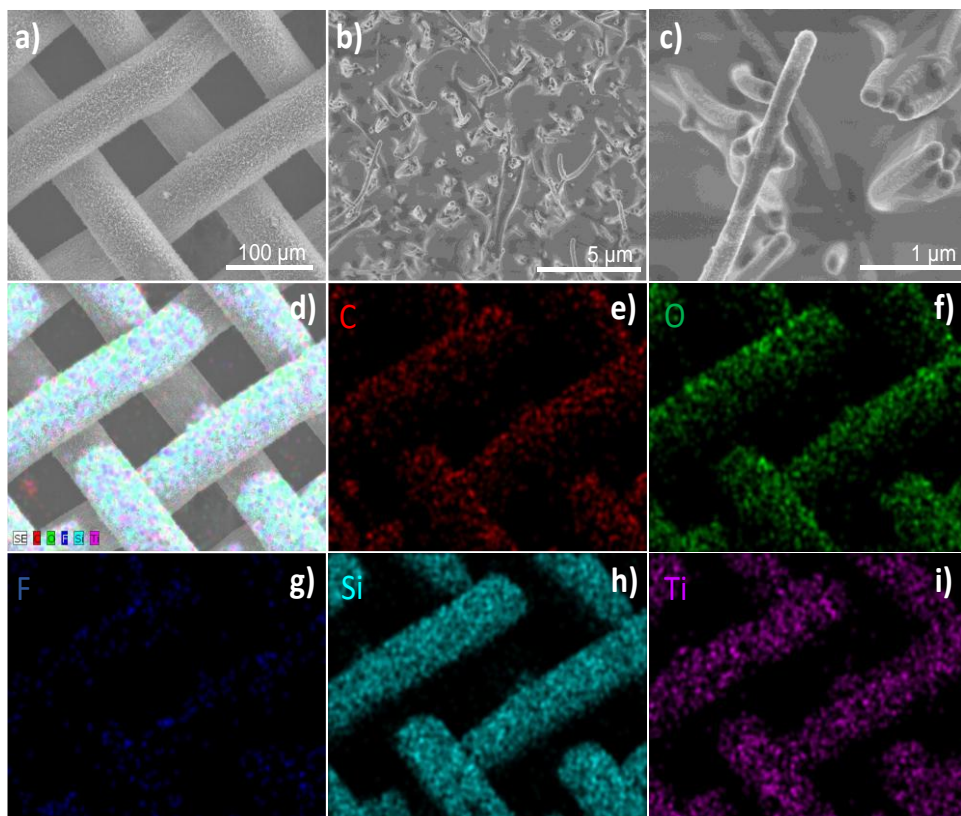


Figure 7. Embedding the $\text{H}_2\text{Pc}@/\text{TiO}_2$ NFs on porous substrates in a stretchable polymeric matrix. a-c) SEM images at different magnifications after the F-grafting and PDMS modification of the metallic grid decorated with NFs. d) EDX combined and e-i) elemental signals' images for the different elements as labeled of the $\text{H}_2\text{Pc}@/\text{TiO}_2$ -PDMS-F NFs on the metal grid.

In Figure 7 d), a general chemical overview can be observed thanks to the different colours representing the various chemical elements, highlighting the presence, as seen in Figure 7 e), of carbon found in the flexible molecules of the fluorinated chemical anchor, as well as the carbon present in the PDMS. Carbon may also appear in the porosity of the shell and originate from the air. Oxygen is associated with the content in the silanol groups (Si-OH) of the chemical reagent for the fluorinated anchoring, as well as that present in the PDMS and TiO_2 shell. Figure 7 g) indicates the percentage of fluorine in the form of C-F bonds formed through the surface derivatization on these hierarchical structures. The presence of Si is attributed to the chemical reagent for the anchoring of fluorine, and to one of the chemical composition of the PDMS, and finally the Ti shown in Figure 7 i), is due to the TiO_2 shell of these core@shell nanostructures.

Since it was previously indicated, it is evident that PDMS coating process does not obstruct the metallic grid micropores. This result is significant since the incorporation of the polymer does not compromise the grid's filtering capability for air or gases. Additionally, while some NFs may appear immersed in the polymer, the microscale surface roughness remains high, even if the heads of the longest NFs are embedded in the PDMS. This effect, despite being able to reduce the solid area fraction and roughness, it can maintain the RoA characterized by low values as shown in Table 1.

A parallel strategy has recently been documented to enhance the performance of 1D nanomaterial layers concerning mechanical robustness under bending, strain, and stress cycling, involving materials such as carbon nanotubes, ZnO³⁸, and Cu and Ag nanowires³³. This is a noteworthy outcome, signifying that the embedding of the nanofibers in the polymer does not compromise the filtering capacity of the grid for air or gases, a crucial aspect demonstrated in the subsequent illustrative **Figure 8**, where an experiment was conducted by introducing some papers into an Erlenmeyer flask and positioning both core@shell nanostructured membranes with PDMS, and F-grafting at the entrance of the flask. The main idea was to use an air gun to pass through these hierarchical nanomembranes and observe movements in the inserted papers, highlighting the non-occlusion of the micropores of the nanomembranes with these fluorinated nanostructures embedded in a polymer matrix.

In this specific context, the creation of the hybrid H₂Pc@TiO₂-PDMS NFs is envisaged to amplify the longevity of the 3D nanomembranes. This enhancement results from the augmented flexibility and robustness of the nanofibers, not only in the face of continuous drop impacts and mechanical stress but also when subjected to prolonged periods of UV and vis light illumination.

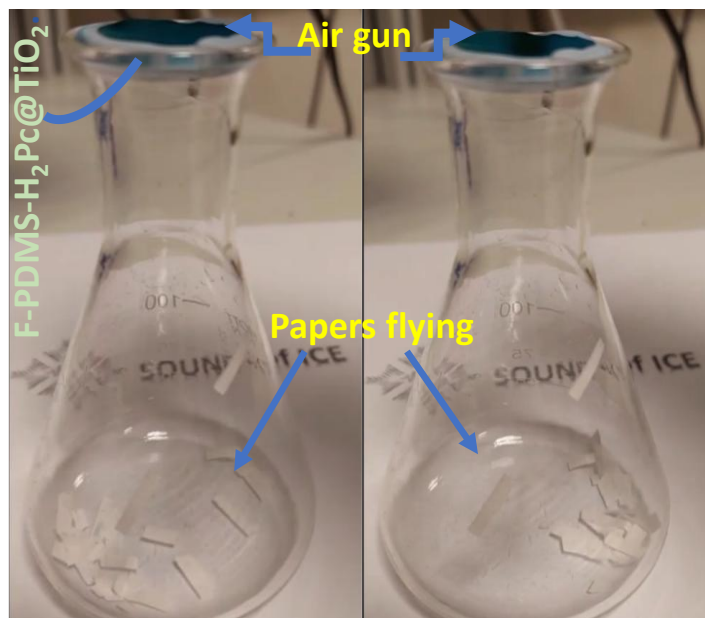


Figure 8. Demonstration of the liquid repellent NFs-PDMS-F 3D nanomembranes as full gas permeable using an air gun.

Moreover, to achieve fully repellent properties in these nanostructured hierarchical surfaces, an extra surface functionalization through chemical anchoring of special molecules has been proposed, particularly the grafting of fluorinated molecules on the TiO_2 shell or the embedded nanostructured surface. It is important to note that this process, as described in the Chapter 2, requires exposing these $\text{H}_2\text{Pc}@TiO_2$ (core@shell) nanostructures to a soft oxygen plasma to ensure the chemical reactivity of the surface to form Si-bonds from the PFOTES molecule and free -OH groups on the surface of the TiO_2 shell or PDMS coating⁴⁷. The chemical anchoring procedure of fluorinated molecules is characterized by being an efficient and uniform process across the surface⁴⁸ of the nanomembranes, as reflected in the EDX colour maps shown in Figure 7. This also induced a notable reduction in the RoA values with water as visually depicted in the photographs presented in **Figure 9 a)**, because of an improved superhydrophobicity and repellence to non-polar liquid droplets, inducing superomniphobicity. This property refers to the extreme resistance of a surface to be wet by various liquids, including both polar and non-polar fluids.

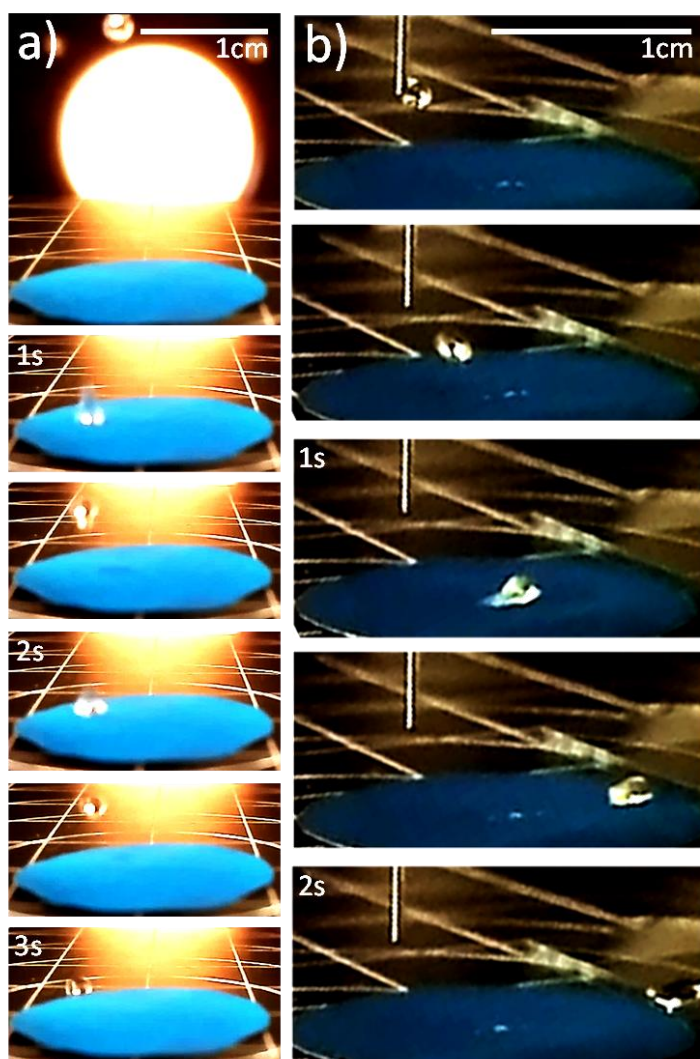


Figure 9. Superomniphobicity of NFs-PDMS-F hierarchical porous surfaces. a) Pictures of 1 μl water droplet repellence of the $\text{H}_2\text{Pc@TiO}_2\text{-F}$ NFs on the metallic grid, b) Pictures of 1 μl diiodomethane droplet sliding and repellence of the $\text{H}_2\text{Pc@TiO}_2\text{-PDMS-F}$ NFs on the metallic grid tilted 5° . (Pictures taken from videos recording at 240 fps). Please note that the focus is settled when the drop is pinning to the needle.

In this event, 1 μl water droplet exhibited a distinctive bouncing behavior on the surface, repeating the action three times before ultimately being expelled from the F-grafted nanofiber (NF) decorated metallic grid in a flat position. Simultaneously, larger water droplets of 10 μl manifested sliding behavior at tilted angles of approximately 5° , as comprehensively outlined in Table 1. This surface modification exerts a substantial influence on the contact angle with non-

polar liquids, yielding a (DCA) as high as 153° and RoAs below 35° for $5\ \mu\text{l}$ diiodomethane droplets. As it is exemplified in Figure 9 b), $1\ \mu\text{l}$ diiodomethane droplet was showcased failing on the tilted F-PDMS membrane and freely rolling out of it. It is imperative to note that prior investigations on alternative fluorine-based membranes, whether fabricated with polymers⁴⁹ or graphene oxides⁵⁰ and applied in ion exchange, have been employed but typically involved complex wet chemical processes and achieved only a hydrophobic state. Notably, polymeric membranes found in literature for distillation^{11,21,51,52}, even if omniphobic, lack complete water repellency and slipperiness. Additionally, in approaches centered around nanostructuring membranes with nanoparticles⁵³, omniphobicity has been restricted to sliding capacity of water droplets.

To demonstrate the superomniphobic behaviour in a more comprehensive way, **Figure 10** presents a sequence of pictures featuring the F- and F-PDMS-nanomembranes exposed to the dosing of $5\text{-}20\ \mu\text{l}$ of a 1:1 emulsion of water and diiodomethane. For the first case, in Figure 10 a1) and a2), the liquid emulsion selectively could filter only at the external-tube edge, with even small water droplets rolling off the surface and adhering to the tube's outer wall (Figure 10 a1)-a6)). Despite diiodomethane exhibiting some wetted surface area on the functionalized membrane due to a contact angle of $\sim 153^\circ$, the non-polar liquid was not filtered through it, instead, it remained within the $\text{H}_2\text{O} + \text{CH}_2\text{I}_2$ mixture as a retained droplet of increasing volume.

In the case of F-NFs (Figure 10 b1)-b6)), the liquid emulsions were retained on the surface with clear liquid separation. As the liquid volumes increased, small droplets detach and roll off the tube's outer walls (Figure 10 b6)). It is noteworthy that during the experiment, diiodomethane remains on top of the porous membrane, even resisting the gravitational force and accumulated water above. Its higher density did not lead to settling at the bottom of the tube, contrasting with the dominant surface free energy effect observed in Figure 4.

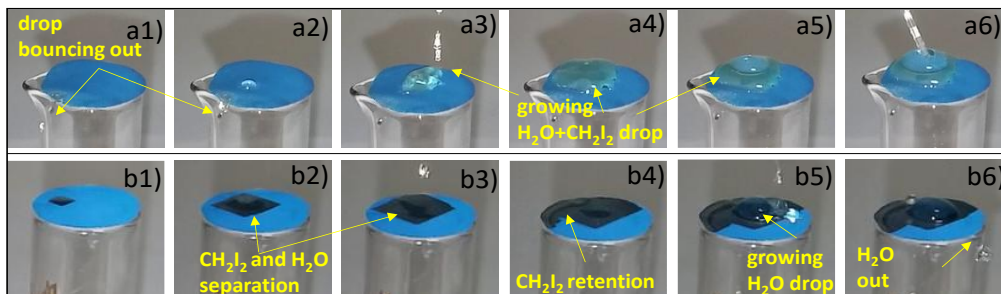


Figure 10. Stability of the superomniphobic 3D nanomembrane. Pictures of the 3D nanomembranes on metallic grid in contact with a 1:1 water/diiodomethane emulsion microdroplets, modified with a) $\text{H}_2\text{Pc@TiO}_2\text{-F}$ NFs, b) $\text{H}_2\text{Pc@TiO}_2\text{-PDMS-F}$ NFs after being UV-Vis irradiated.

An added advantage of both F- and F-PDMS surface modification is the robustness and stability of the omniphobic behaviour. After 1 hour of UV-vis irradiation, the functionalized nanofibers showed a water contact angle (WCA) of 124° and a diiodomethane contact angle (DCA) of 136° highlighting this experiment such as durability test.

3.3.6 Self-cleaning properties of omniphobic $\text{H}_2\text{Pc@TiO}_2$ 3D nanomembranes

In addition to the potential for wetting selectivity for liquids separation or achieving complete liquid repellence, functionalized hierarchical porous surfaces can utilize their omniphobic nature to perform self-cleaning properties⁴². This self-cleaning capability extends not only to both polar and non-polar liquids but also to solid particle pollutants. Unlike alternative self-cleaning methods that rely on external factors⁵⁴, in this chapter, a self-cleaning test has been conducted by impacting water droplets onto the functionalized hierarchical porous surface contaminated with graphite powder. As an example, the different hierarchical surfaces on the metallic grid exhibit different levels of self-cleaning, as illustrated the **Figure 11**. The surface of $\text{H}_2\text{Pc@TiO}_2$ NFs on the metallic grid demonstrates the ability to remove accumulated dirt upon the impact of water droplets.

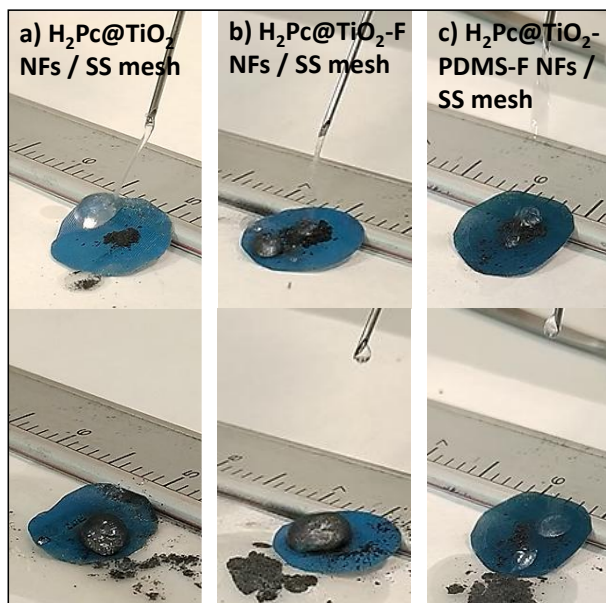


Figure 11. Self-cleaning test pictures of superomniphobic hierarchical porous surfaces contaminated with carbon particles assisted by the impact of water droplets, for the following functionalized cases: a) $\text{H}_2\text{Pc@TiO}_2$ NFs, b) $\text{H}_2\text{Pc@TiO}_2\text{-F}$ NFs, and c) $\text{H}_2\text{Pc@TiO}_2\text{-PDMS-F}$ NFs on the metallic grid.

The droplet persisted on the surface containing graphite powder particles until reaching a certain volume, at which point the droplet detached from the 3D nanomembrane (Figure 11 a)). Similarly, F-grafted NFs on the metallic grid exhibited efficient self-cleaning but in a faster way, requiring smaller droplets to remove dust more swiftly. In the case of F-PDMS-NFs on the metallic grid, Figure 11 c) shows complete surface cleaning after passing the first small drops sliding on the surface, effectively removing graphite particles along their paths. This aligns with the findings in Table 1, indicating lower rolling-off angles and, consequently, lower adhesion of the hybrid $\text{H}_2\text{Pc@TiO}_2\text{-PDMS-F}$ NFs porous surface, where water drops push and drag the polluting particles.

Figure 12 shows the SEM images taken at various magnifications, demonstrating the clean state of the functionalized 3D nanomembranes after the impact of water droplets with the surface contaminated with carbon particles. The self-cleaning feature of these surfaces is particularly advantageous in scenarios where dust particles settle, and new fluid pollutants may be present in liquids or liquid mixtures during separation and filtration processes⁵⁵.

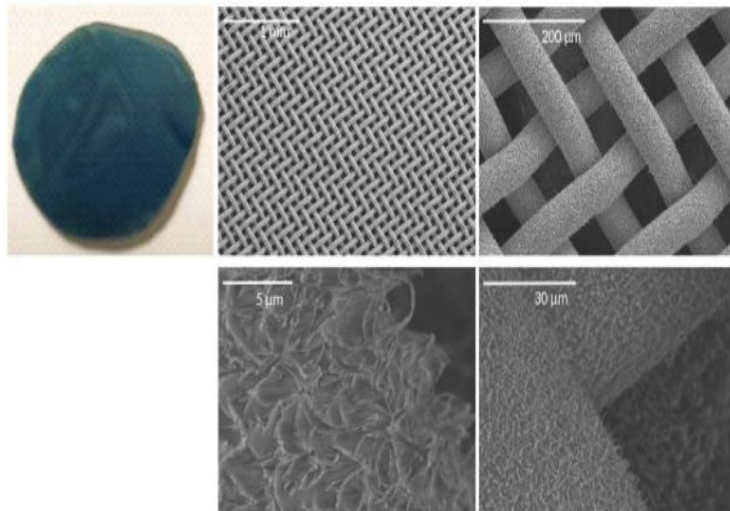


Figure 12. Picture and SEM micrographs of the F-PDMS 3D nanomembrane from the metallic grid after several experiments of self-cleaning. No signal of carbon particles has been found along the entire scanned porous surface area.

3.4 Conclusions

In this work, we have explored the application of the soft-template method combining vacuum and plasma techniques to synthesize core@shell nanowires and nanofibers, successfully adapting it to fabricate hierarchical porous surfaces as 3D nanomembranes. Plasma-enhanced chemical vapor deposition (PECVD) for the formation of metal oxides, particularly for the fabrication of photoactive amorphous TiO_2 , has been proven as an effective protocol to control the roughness needed for organic nanowires seeds and to conform the nanofibers shells. We have showcased the method's adaptability for surface modification on diverse 3D porous substrates, including metal grids and cellulose filters, operating seamlessly at room temperature. From the perspective of potential applications, selective wetting and photoactivity of microvalves have huge importance in various fields. In microfluidics, these properties can be utilized to control fluid movement precisely, enabling advanced lab-on-a-chip technologies for biomedical diagnostics and chemical analysis. By harnessing photoactive materials, microvalves can be designed to respond to light stimuli, allowing for dynamic control over microfluid flow and enabling functions like on-demand release or mixing of reagents. Additionally, selective wetting can enhance the efficiency of droplet manipulation, which is crucial in applications such as inkjet printing and microreactors.

The resulting nanofibers exhibit 3D shells characterized by nanoscale roughness, specifically adopting a distinctive cauliflower-like morphology. This contributes to a triple scale of roughness, encompassing the microscale length of the fibers (in the micrometer scale) and the characteristic morphology of the porous supports (tens of micrometers). This distinctive structure imparts pronounced superhydrophobic behavior, even on hygroscopic cellulose filters.

Leveraging the inherent oleophilic nature of amorphous TiO_2 , we have proposed novel material configurations for effectively separating polar and non-polar liquids microdroplets, showcasing photoactivity under ultraviolet illuminations. Exposition to UV light renders the surfaces hydrophilic in less than one hour.

The synergistic integration of F-grafting with PDMS embedding of the nanofibers emerges as the most effective functionalization, endowing the surfaces with self-cleaning properties against carbon particles, stable even after prolonged exposure to various environmental conditions, including UV illumination.

Importantly, this surface modification does not obstruct the membrane pores, ensuring the air and gases flux across.

In summary, developed hierarchical porous surface not only discriminates between liquid droplets based on surface tension response but also acts against microfluid phases and solid particles. The multifaceted functionalities of the developed 3D nanomembranes, extendable to alternative core@shell nanoarchitectures, make them promising candidates for diverse fields, ranging from advanced liquid separation techniques in the microscale, microfluidics valves, biomedical devices to self-cleaning surfaces with broad practical implications.

Bibliography

1. Song, J., Shi, R., Bai, X., Algadi, H. & Sridhar, D. An overview of surface with controllable wettability for microfluidic system, intelligent cleaning, water harvesting, and surface protection. *Adv Compos Hybrid Mater* **6**, 1–21 (2023).
2. Hosseini, M. & Karapanagiotis, I. Materials with Extreme Wetting Properties. *Methods and Emerging Industrial Applications*. (Springer) (2021).
3. Wu, X., Chu, F., Orejon, D. & Mousterde, T. Superhydrophobic surfaces: Fundamentals, manufacture, and applications. *Appl Phys Lett* **124**, 8–11 (2024).
4. Dang, C., Ding, Y., Jia, L. & Peng, Q. Dynamic wetting behaviour of droplets on the surface of porous materials with micro-airflow. *Kexue Tongbao/Chinese Science Bulletin* **66**, 128–136 (2021).
5. Teng, P., Tian, D., Fu, H. & Wang, S. Recent progress of electrowetting for droplet manipulation: From wetting to superwetting systems. *Mater Chem Front* **4**, 140–154 (2020).
6. Chu, C., Zhao, Y., Hao, P. & Lv, C. Wetting state transitions of individual condensed droplets on pillared textured surfaces. *Soft Matter* **19**, 670–678 (2022).
7. Dubey, P. P., Pham, Q. N., Cho, H., Kim, Y. & Won, Y. Controlled Wetting Properties through Heterogeneous Surfaces Containing Two-level Nanofeatures. *ACS Omega* **2**, 7916–7922 (2017).
8. Yu, M., Zhu, B., Lu, Y., Li, J. & Yang, J. A robust dynamic dewetting coating with omniphobicity, wear resistance, and scratch repairability. *Colloids Surf A Physicochem Eng Asp* **679**, 132659 (2023).
9. Kim, P., Kreder, M. J., Alvarenga, J. & Aizenberg, J. Hierarchical or not? Effect of the length scale and hierarchy of the surface roughness on omniphobicity of lubricant-infused substrates. *Nano Lett* **13**, 1793–1799 (2013).
10. Richard W., B. *Membranes Technology and Applications*. WILEY (2004).
11. Zhu, P., Kong, T., Tang, X. & Wang, L. Well-defined porous membranes for robust omniphobic surfaces via microfluidic emulsion templating. *Nat. Commun* **12**, 15283 (2017).
12. Anil Kumar Pabby, Syed S.H. Rizvi, A. M. S. R. *Handbook of Membrane Separations*. CRC Press (2008).
13. Rehman, F., Thebo, K. H., Aamir, M. & Akhtar, J. *Nanomembranes for Water Treatment. Nanotechnology in the Beverage Industry: Fundamentals and Applications*. Elsevier (2020).
14. Wang, Y. *et al.* Infused-liquid-switchable porous nanofibrous membranes for multiphase liquid separation. *Nat Commun* **8**, 1–7 (2017).
15. Lu, X. *et al.* Pd-functionalized MnO_x-GeO_y nanomembranes as highly efficient cathode materials for LiO₂ batteries. *Nano Energy* **19**, 428–436 (2016).
16. Mittal, M., Sardar, S. & Jana, A. Nanofabrication techniques for semiconductor chemical sensors. *Handbook of Nanomaterials for Sensing Applications* 119–137. Elsevier (2021).
17. Annamalai, A., Boulanger, N. & Thomas, W. *Sustainable Energy & Fuels functionalized graphene oxide membranes under hydrogen proton exchange membrane fuel cell*. 1790–1798 (2019).
18. Yugang Sun, J. A. R. *Semiconductors Nanomaterials for Flexible Technologies*. Elsevier (2010).
19. Wu, P., Xue, Z., Yu, T. & Penkov, O. V. Transparent Self-Cleaning Coatings: A Review. *Coatings* **13**, 1270 (2023).
20. Montali, A. Antibacterial coating systems. *Injury* **37**, 81–86 (2006).
21. Zheng, R. *et al.* Preparation of omniphobic PVDF membrane with hierarchical structure for treating saline oily wastewater using direct contact membrane distillation. *J Memb Sci* **555**, 197–205 (2018).
22. Schuster, C., Rodler, A., Tscheliessnig, R. & Jungbauer, A. Freely suspended perforated polymer nanomembranes for protein separations. *Sci Rep* **8**, 1–11 (2018).

23. Jafary, F., Motamedi, S. & Karimi, I. Veterinary nanomedicine: Pros and cons. *Veterinary Medicine and Science* **9**, 494–506 (2023).
24. Jakšić, Z. & Jakšić, O. Biomimetic nanomembranes: An overview. *Biomimetics* **5**, 24 (2020).
25. Chen, D., Wang, C., Chen, W., Chen, Y. & Zhang, J. X. J. PVDF-Nafion nanomembranes coated microneedles for in vivo transcutaneous implantable glucose sensing. *Biosens Bioelectron* **74**, 1047–1052 (2015).
26. Tonev, D. G. & Momchilova, A. B. Therapeutic Plasma Exchange in Certain Immune-Mediated Neurological Disorders: Focus on a Novel Nanomembrane-Based Technology. *Biomedicines* **11**, (2023).
27. Wang, T. & Wang, Z. Liquid-Repellent Surfaces. *Langmuir* **38**, 9073–9084 (2022).
28. Ávila, A. F. *et al.* A nano-modified superhydrophobic membrane. *Materials Research* **16**, 609–613 (2013).
29. Charcosset, C. Classical and Recent Applications of Membrane Processes in the Food Industry. *Food Engineering Reviews* **13**, 322–343 (2021).
30. Kennedy, V. C., Zellweger, G. W. & Jones, B. F. Filter pore-size effects on the analysis of Al, Fe, Mn, and Ti in water. *Water Resour Res* **10**, 785–790 (1974).
31. Borrás, A., Cotrino, J. & González-Elipe, A. R. Type of Plasmas and Microstructures of TiO₂ Thin Films Prepared by Plasma Enhanced Chemical Vapor Deposition. *J Electrochem Soc* **154**, P152 (2007).
32. Filippin, A. N. *et al.* One-reactor plasma assisted fabrication of ZnO@TiO₂ multishell nanotubes: Assessing the impact of a full coverage on the photovoltaic performance. *Sci Rep* **7**, 1–10 (2017).
33. Macias-Montero, M. *et al.* Vertically Aligned Hybrid Core / Shell Semiconductor Nanowires for Photonics Applications. *Adv. Funct. Mater* **23**, 5981–5989 (2013).
34. Feng, L. *et al.* Petal Effect: A Superhydrophobic State with High Adhesive Force. *Langmuir* **24**, 4114–4119 (2008).
35. Murakami, D., Jinnai, H. & Takahara, A. Wetting Transition from the Cassie–Baxter State to the Wenzel State on Textured Polymer Surfaces. *Langmuir* **30**, 2061–2067 (2014).
36. Xu, Q. F., Liu, Y., Lin, F., Mondal, B. & Lyons, A. M. Superhydrophobic TiO₂- Polymer Nanocomposite Surface with UV- Induced Reversible Wettability and Self-Cleaning Properties. *ACS Appl. Mater Interfaces* **25**, 8915–8924 (2013).
37. Filippin, N. *et al.* Plasma-Enabled Amorphous TiO₂ Nanotubes as Hydrophobic Support for Molecular Sensing by SERS. *ACS Appl Mater Interfaces* **12**, 50721–50733 (2020).
38. Rajab, F. H., Korshed, P., Liu, Z., Wang, T. & Li, L. Applied Surface Science How did the structural ZnO nanowire as antibacterial coatings control the switchable wettability. *Appl Surf Sci* **469**, 593–606 (2019).
39. Etacheri, V., Di Valentin, C., Schneider, J., Bahnemann, D. & Pillai, S. C. Visible-light activation of TiO₂ photocatalysts: Advances in theory and experiments. *Journal of Photochemistry and Photobiology C: Photochemistry Reviews* **25**, 1–29 (2015).
40. Ademola Bode-Aluko, C. *et al.* Photocatalytic and antifouling properties of electrospun TiO₂ polyacrylonitrile composite nanofibers under visible light. *Materials Science and Engineering: B* **264**, (2021).
41. Romero-Gomez, P. *et al.* Enhancement of visible light-induced surface photo-activity of nanostructured N-TiO₂ thin films modified by ion implantation. *Chem Phys Lett* **582**, 95–99 (2013).
42. Zhang, H. *et al.* Visible-Light-Activated Photocatalytic Films toward Self-Cleaning Membranes. **2002847**, 1–9 (2020).
43. Elimelech, M. Reactive, *Self-Cleaning Ultra-filtration Membrane Functionalized with Iron Oxychloride Nanocatalysts*. (2018).
44. Wang, H. & Wang, H. Transition metal nitrides for electrochemical energy applications. *Nanostructures, Functional, and Flexible Materials for Energy Conversion and Storage Systems*, 1354–1390 (2021).
45. Wang, L., Urata, C., Sato, T., England, M. W. & Hozumi, A. Self-Healing Superhydrophobic Materials Showing Quick Damage Recovery and Long-Term Durability. *Langmuir* **33**, 9972–9978 (2017).

46. Chen, C. H., Cheng, I. C. & Chen, J. Z. Facile method to convert petal effect surface to lotus effect surface for superhydrophobic polydimethylsiloxane. *Surfaces and Interfaces* **30**, 101901 (2022).
47. Rico, V. *et al.* Robust anti-icing superhydrophobic aluminum alloy surfaces by grafting fluorocarbon molecular chains. *Appl Mater Today* **21**, (2020).
48. Cai, Y., Li, J., Yi, L., Yan, X. & Li, J. Fabricating superhydrophobic and oleophobic surface with silica nanoparticles modified by silanes and environment-friendly fluorinated chemicals. *Appl Surf Sci* **450**, 102–111 (2018).
49. Gao, X. L. *et al.* Highly conductive fluorine-based anion exchange membranes with robust alkaline durability. *J Mater Chem A Mater* **8**, 13065–13076 (2020).
50. Gong, X., Liu, G., Li, Y., Yu, D. Y. W. & Teoh, W. Y. Functionalized-graphene composites: Fabrication and applications in sustainable energy and environment. *Chemistry of Materials* **28**, 8082–8118 (2016).
51. Wang, W. *et al.* Monolithic Omniphobic Membranes. *Nat Commun* **19**, 1–9 (2019).
52. Li, C. *et al.* Elucidating the Trade-off between Membrane Wetting Resistance and Water Vapor Flux in Membrane Distillation. *Environ Sci Technol* **18**, 10333-10341 (2020).
53. Wang, Y., Zhu, L. & Du, C. Flexible Difunctional (Pressure and Light) Sensors Based on ZnO Nanowires / Graphene Heterostructures. **1901932**, 1–6 (2020).
54. Zhang, H. *et al.* Visible-Light-Activated Photocatalytic Films toward Self-Cleaning Membranes., *Environ Sci Technol* **2002847**, (2020).
55. Baidya, A., Das, S. K., Ras, R. H. A. & Pradeep, T. Fabrication of a Waterborne Durable Superhydrophobic Material Functioning in Air and under Oil. **1701523**, 1–9 (2018).



“Nothing in our lives is to be feared; it is only to be understood”

(Marie Curie)

4

**Control of the wetting behaviour
of stainless steel substrates:
Low fluorinated hierarchical
surfaces for omniphobic, anti-
fouling and anti-icing
applications**

Abstract

Stainless steel (SS) alloys have found widespread applications across various industries, household applications, and commodities where precise control of surface properties is imperative for tailoring their interaction with the environment. In this study, a novel procedure for processing stainless steel surfaces, yielding a multifunctional response encompassing superhydrophobicity, omniphobicity, self-cleaning, anti-fouling and robust anti-icing capabilities resistant to corrosion tests have been presented. The methodology involves a two-step process: generation of dual-scale roughness topography and surface modification based on low fluorination. From the first step SS hierarchical surfaces are obtained through a liquid-free procedure consisting of the deposition of SS nanostructures by electron beam evaporation at oblique angle on a laser-induced microstructured SS surface. Subsequently, the hierarchical surfaces have been subjected to slight fluorination through two different protocols: plasma-assisted deposition of a thin Teflon-like coating or the grafting of fluorinated molecules. Furthermore, potentiodynamic analysis of the corrosion behavior demonstrates the preservation of a corrosion resistance like that of the compact SS substrate. Remarkably, the chemical stability of these low fluorinated hierarchical surfaces supports their versatile application across a wide range of scenarios. From a methodological standpoint, proposals for anti-fouling and anti-icing behavior based on the control of surface wetting are presented for the first time for this type of metallic substrates.

4.1 Introduction

Stainless steel is one of the most in-demand metallic materials today, but to understand its performance as a metallic surface, a wide range of environmental factors must be considered. It is notable that the global impact of corrosion processes is greater than 3% of the Global Gross Domestic Product for this material, and currently, the application of available corrosion control practices may only save about 35% of losses. The environmental factors that this type of material interacts with include humidity, varying temperature values, chlorides and pH acids, different salt levels, and biological fluids¹.

Stainless steel inherently possesses anti-corrosion properties and good thermal conductivity, making it an effective heat dissipation system, while also being economically cost-effective and compatible with a wide range of designs in the market². However, these properties alone are not sufficient to make this type of metallic material completely stable in its environment and against the factors it is exposed to. Therefore, it is essential to seek multifunctionality to equip it with new functionalities, enhancing its energy efficiency, preventing contamination processes, improving safety performance, and increasing sustainability. Classical function of SS requires new capabilities according to improve the wetting control, antibacterial response^{3,4}, self-cleaning^{5,6}, friction resistance^{7,8} or compatibility with food contact⁹ for specific applications. Specially, anti-icing capacity is another “*must*” for many SS engineering pieces highlighting low environmental temperatures. A lot of industrial applications requiring a good anti-corrosive performance rely on the singular properties of stainless steel. Due to the inherent compactness of the surface oxidation layer, this extensive category of iron-based alloys shows an innate self-protective mechanism, enabling prolonged resilience against exposure to authentic industrial environments^{10,11}. Over the intermediate term, severe conditions, including saline and/or humid atmosphere, particulate matter, biological agents, or chemical factory emissions may endanger the anti-corrosive and anti-erosion capabilities of stainless steel. In response to these challenges, strategies involving the incorporation of additional elements through doping to create new alloy properties and/or the implementation of advanced surface treatments are posited as effective measures^{12,13}. In general, the controllable wetting, interaction with environmental agents, and passive anti-icing capabilities of a surface are intricately governed by its topography and chemical composition.

With respect to the former, surfaces exhibiting roughness encompassing both nano-and-micro-scales, demonstrate water and, to some extent, ice repellence since was presented in Chapter 1. Hierarchical surfaces on stainless steel material are generated through the combination of structures at different scales, which can include micro- and nanostructures to enhance properties such as corrosion resistance, and anti-fouling characteristics through the control of wettability. Common methods for creating these surfaces include chemical treatments, laser technology, and different vacuum and plasma deposition techniques¹⁴. In the state of the art for this kind of metallic substrate, the use of functional groups with a polar nature, such as those present in silicone- or fluorine-based compounds, have been studied and it constitutes an additional advantageous factor to avoid the deposition of water or other liquid droplets on surfaces¹⁵. These combined strategies of surface modification, involving both micro/nano roughening and chemical surface functionalization with polar species have been commonly employed in materials such as aluminum metal¹⁶, polymers¹⁷ and composites^{18,19}. However, their standardization for implementation on SS surfaces has been infrequent. Dual-scale and nanostructured topographies generated onto SS surface through laser^{3,7,20} or electrochemical^{21,22} methodologies serve as effective means for tunable wettability and other surface characteristics such as anti-microbial properties²³. The limitations in controlling the wettability of metal surfaces treated chemically or with laser technology are a well-documented challenge. In chemical treatments, wear and insufficient surface penetration can reduce coating adhesion, limiting durability and effectiveness. This occurs because if the chemical substance does not reach the micro-grooves or necessary roughness, delamination or, in more severe cases, a suboptimal surface for wettability control can result. Regarding laser technology, the creation of roughness can present similar issues: a good surface texture is achieved but requires extreme precision in working conditions, especially when aiming to avoid aesthetic imperfections. Achieving effective water repellency in laser-treated metals^{27,20} typically requires employing highly aggressive, high-fluence laser treatments to generate substantial surface roughness. Nonetheless, when applied to stainless steel, these intense treatments often induce alterations in surface stoichiometry, thereby compromising corrosion resistance. Additionally, the microscale roughness produced by both methods does not always achieve a sufficiently fine

structural hierarchy to ensure complete water repellency or resistance to other external agents²⁴, as these properties often require combined nanometric and micrometric textures²⁵. A combination of methods, such as laser treatments followed by specialized nanometric coatings, could be considered to improve structure and adhesion^{20,26,27}.

To attain additional functionalities, surface texturization in different degrees of roughness requires the integration with a suitable chemical functionalization. To illustrate that, SS subjected to laser treatment, in conjunction with fluoroalkylsilane-silica nanoparticles, has been utilized to achieve superhydrophobicity²⁸. This approach concurrently yields a significant reduction in friction within humid environments. Furthermore, the combination of surface nanostructuring and targeted chemical functionalization has been employed to confer anti-fouling properties upon SS^{29,30}, a crucial attribute in sectors such as food processing³¹, and healthcare^{4,13,32,33}. All the strategies mentioned above^{34,35} are reflected in the state of the art from the perspective of achieving distinctive water wettability compared to other surfaces³⁶. However, today, advances in the applications of these types of metallic alloys have made it necessary to develop new strategies that not only exhibit superhydrophobic properties but also achieve complete repellency to any type of liquid, presenting omniphobicity as well as self-cleaning capabilities against solid particles coming from the environment³⁷. Moreover, it is important to highlight the use of this type of material in a wide range of applications where ice accumulation can be a significant issue, emphasizing the need to develop hierarchical superhydrophobic, omniphobic, self-cleaning, and anti-icing SS surfaces³⁷.

In this study, we propose an innovative approach for the development of multifunctional hierarchical SS surfaces characterized by dual-scale roughness. In this approach, the nano-structuring of the stainless steel itself helps avoid internal stress at the interface with the substrate, given that both are of the same material. Additionally, the porous nanostructure increases the specific surface area, which is advantageous for achieving hydrophobic properties and for integrating chemical functionalities, such as anchoring fluorinated molecules or infusing lubricants. This proposed method reduces the use of fluorinated compounds compared to traditional techniques^{38,39}, utilizing small amounts of fluorinated reagents in liquid or solid form. Low fluorination strategies, applied as coatings or anchored molecules, remain stable under the employed

methodology, as the process is conducted in dry conditions. The fabrication process comprises distinctive stages:

- i) Laser texturization of pristine SS flat substrate to generate aligned grooves, as patterns that mimic those found in nature are sought.
- ii) Deposition of a nanocolumnar porous SS layer using electron beam evaporation at oblique angles. These oriented nanostructures allow to work with custom nanoarchitectures and, in our case, to enhance the porosity to be able to increase the performance of surface functionalization^{4,40}.
- iii) Surface modification using low amount of fluorinated agents under stable configurations.

The initial step i) induces micron-sized roughness, subsequently combined to nanostructures in step ii) to achieve an oriented hierarchical surface, following a protocol developed in the research group as documented in prior studies^{16,41}. For step iii), two strategies were employed: the grafting of fluorine-containing molecules or the deposition of a fluorinated thin film by means of plasma-assisted chemical vapor deposition (PECVD). Previous studies have reported the efficacy of fluorination on re-entrant SS surfaces fabricated in foils and meshes using laser or electrochemical methods, showcasing its efficiency in controlling ethylene glycol and decane wettability for liquid separation applications^{42,43}. Thus, the main objective of both present strategies is to minimize the incorporation of fluorine while ensuring the enduring stability of the repellent surfaces. To validate the performance of the designed SS surface, we compare our approach with the infusion of a slippery fluorine-based lubricant (SLIPS)^{44,45} or their integration of fluorinated particles^{46,47} in nanostructured surfaces, that involve substantial amounts of fluorine-containing compounds. They, upon release, can pose significant environmental risk. Our proposal illustrates that the SS hierarchical surfaces shows exceptional liquid-repellent behavior that can be applied in multifunctional applications such as abrasion resistance, anti-icing response and anti-fouling behavior. Furthermore, our investigation confirms that, depending on the treatment, fluorination does not compromise the anti-corrosive properties of SS surfaces.

4.2 Experimental Section

4.2.1 Materials and samples preparation

Austenitic stainless steel 304 polished specimens (15 cm x 15 cm) were provided by Goodfellow. Prior to utilization, these samples underwent a cleaning process involving rinsing with Hellmanex III water solution and acetone. SS pellets (AISI 301, 99% purity) from Equipment Support Company U.S.A., Inc were employed for the synthesis of porous nanocolumnar films by electron beam evaporation. These SS pellets were employed due to their similar Cr/Fe ratio values, ranging from 0.16 to 0.20 for both substrates and pellets⁴⁸, thereby preventing the loss of stainless properties when using for nanostructures growth.

Laser treatments at room temperature were performed using a 20 W diode-pumped Nd:YAG unpolarized laser (Powerline E, Rofin-Baasel Inc.) emitting at 1064 nm with a 100 ns pulse width. Experimental parameters, including an average laser power of 16 W, scanning rate of 100 mm s⁻¹, repetition rate of 20 kHz, and a fixed distance of 40 μm between scanning lines, were chosen after testing different specific conditions according to literature following existing patterns in nature⁴⁹. The resulting samples are denoted as SS-laser.

Nanocolumnar thin films of 700 nm thickness were deposited at room temperature by electron beam evaporation in an oblique angle configuration⁴, at a zenithal angle of 70° relative to the normal direction of the substrates. This method, recognized for producing highly porous nanocolumnar thin films on flat substrates⁵⁰, was used onto laser-treated and flat SS substrates (for comparison) as well as silicon reference substrates. SS target pellets were electron beam evaporated at a pressure below 10⁻⁴ mbar, fixing a deposition rate of 1 Å/s on substrates positioned 50 cm (fixed distance in this reactor) away from the SS crucible. These specific experimental conditions were employed to find a positive compromise between stable and conformal SS nanostructures growth and porous degree according to wetting behavior and anti-corrosion properties previously published for our research group⁵¹. These samples are denoted as 70SS-...

Surface grafting of 1H,1HH,2H,2H-Perfluorooctyltriethoxysilane molecules (Sigma-Aldrich) was carried out according to previous works¹⁴: after a O₂ plasma surface activation under mild conditions (10 min using a remote microwave ERC source at 500 W power and 1x10⁻² mbar pressure), the removal of environmental

water condensed at the sample surface by heating at 80 °C and primary vacuum pumping followed. SS-laser and 70SS-laser substrates were exposed to reactive vapors of this compound in a thermal bath at 80 °C for 2 hours. These samples are labeled as F-70SS-...

Fluorinated polymeric (CF_x) continuous and homogeneous thin films were deposited with approximately 200 nm thickness, estimated from coatings deposited onto a flat silicon reference. This thickness value was chosen as the optimal thickness for conformal deposition on the oriented nanostructures without losing the porosity they contribute to the hierarchical system. This CF_x polymer was deposited by PECVD previously described in Chapter 2. In brief, deposition is performed in a radiofrequency (13.56 MHz) parallel-plate reactor using mixtures of C_4F_8 (50 %) and Ar (50 %) ⁵² at a working pressure of 0.15 mbar, while maintaining a negative self-bias voltage of 200 V at the bottom electrode serving as sample holder. These samples are denoted as CF_x -70SS...

Slippery Liquid-Infused Porous Surfaces (SLIPS) were prepared by infiltrating the low surface tension fluorine-containing liquid Krytox® 100 (DuPont) into the hierarchical SS surfaces. Prior of infiltration, heating was required at 80 °C for 30 minutes to eliminate condensed environmental water within the highly porous SS nanocolumns of the 70SS-laser sample. Subsequently, Krytox was spin-coated for 1 minute at 4500 rpm to ensure the removal of excess liquid at the surface. These samples are referred to as K-70SS-....

4.2.2 Characterization methodologies

Surface morphology was characterized by Scanning Electron Microscopy (SEM) utilizing a Hitachi S4800 field emission microscope operating at 2 kV and 10 mA. Chemical composition analysis of the surfaces was conducted via X-ray Photoelectron Spectroscopy (XPS) using a SPECS spectrometer described in Chapter 2. Non-monochromatic Al $K\alpha$ radiation was used to excite spectra in a normal configuration. Data were recorded employing 50 eV constant pass energy mode for general survey spectra and 30 eV for high-resolution spectra. Calibration in binding energy (BE) was performed using the functional carbon C-H and C-C bonding groups, at 284.5 eV in the C1s region.

Surface topography was characterized by Atomic Force Microscopy (AFM) in a Dulcinea microscope (Nanotec) operating in tapping mode configuration.

Roughness average root Mean Square (RMS) values were determined using a specific free software WsXM⁵³. Confocal microscopy analysis was conducted with a Sensofar Methodology microscope to determine the roughness parameters S_q and S_{ai} ; defined as the mean quadratic height and the average of the maximum height of the peaks in the examined zone respectively.

As part of the quality control process of the samples, environmental resistance was characterized by abrasion, rain, and single particle erosion tests. For the abrasion tests, a standardized 1720 abrasion and washability tester, manufactured by Elcometer and equipped with an abrasive element comprising a sponge and an abrasive textile pad, was used under dry conditions, applying a load of 0.05 Kg cm^{-2} ⁵⁴. Otherwise, samples were subjected to some standardized solid and rain erosion tests according to the following procedures: solid and simulated single particle erosion tests were performed with $50 \text{ }\mu\text{m Al}_2\text{O}_3$ particles of 5 g total mass with a feed rate of $1 \pm 0.5 \text{ g min}^{-1}$, impacting at $30 \pm 2 \text{ m s}^{-1}$ and $20^\circ \pm 2^\circ$ of incidence from a working distance of $20 \pm 1 \text{ mm}$ during 10 min of total testing time (ASTM G76)⁵⁴. The rain erosion tests were carried out basically with a given number of water droplets (diameter of $260 \text{ }\mu\text{m}$), which were sent at different velocities ($165, 180$ and 225 m s^{-1}) on the samples⁵⁵ (collaboration with Airbus Central R&T Materials laboratory, Munich (Germany)).

Electrochemical corrosion tests (in collaboration with the National Center of Metallurgical in Madrid (CSIC)), were carried out on samples of 5 cm^2 area, positioned horizontally, measuring cyclic potentiodynamic curves as it is described in Chapter 2. Before any potentiodynamic sweep, the Open Circuit Potential (OCP) was recorded for 900 seconds . The hierarchical SS samples worked as electrodes, whereas a silver/silver chloride - Ag/AgCl (3 M KCl)-electrode was used as reference electrode and a rolled platinum wire as counter electrode. A cathodic potential of -0.3 V (vs OCP) was applied, followed by an anodic sweep at a scan rate of 0.16 mV s^{-1} until a value of 1.5 V vs. Ag-AgCl (3 M KCl) or a current density limit of 0.25 mA cm^{-2} were reached. These electrochemical tests were carried out in a 0.6 M NaCl solution at room temperature. Corrosion potential (E_c), pitting potential (E_p), and passive current density (I_p) were derived from the potentiodynamic curves and utilized to characterize the anti-corrosive properties of the surfaces.

Wetting properties such as static contact angle (CA) and rolling-off angles (RoA) were determined under room conditions using OCA20 DataPhysics Instrument. Droplets of bi-distilled water (2 μl) and diiodomethane (1 μl) were employed as polar and non-polar liquid references, respectively. The Water Contact Angles (WCA) and Diiodomethane Contact Angles (DCA) were measured for this experiment. The reported values represent an average of 5 measurements involving an error bar of 10%. Also, to demonstrate self-cleaning capability, water droplets were dripped onto the hierarchical SS surfaces contaminated with salt or graphite powders.

To evaluate the repellence capacity of these metallic surfaces, anti-fouling ability was characterized for the first time in hierarchical surfaces through static and dynamic wetting analysis using 2 μl droplets of three distinct fluid fouling simulants⁵⁶ provided by Sigma Aldrich: humic acid (mud simulator), sodium salt solution (10 mg ml^{-1}), alginic acid sodium salt from Brown algae solution (10 mg ml^{-1}), and bovine serum albumin (proteins present in animal blood).

For the first time, to complete the studies of the different functionalities intended to be demonstrated with this type of hierarchical metallic surfaces, the anti-icing efficacy of the samples was evaluated under two proposals: by measuring the Freezing Delay Time (FDT) of a water droplet deposited onto the surface and by assessing the ice adhesion on the surface. For the FD tests, 2 μl supercooled water droplets were employed in a dry atmosphere at $-5\text{ }^{\circ}\text{C}$ using Peltier's systems to be able to evaluate, through this test, how resistant and/or insulating are these hierarchical metallic surfaces, (Chapter 2). Ice adhesion tests were performed at $-13\text{ }^{\circ}\text{C}$ utilizing a pull-off method in our own Universal Material Testing Machine. Upon ice detachment, the applied force was converted into adhesion strength by dividing it by the probe area. The experiments were conducted thrice, revealing maximum deviations of 5% in the determined ice adhesion strengths and freezing delay times.

Durability tests (carried out in our facilities in Seville), were performed on hierarchical SS surfaces involving 5 cycles of freezing/thawing between $-5\text{ }^{\circ}\text{C}$ and $20\text{ }^{\circ}\text{C}$ within an environmental chamber, encompassing the icing and melting of the 2 μl water droplets deposited on the surfaces.

4.3 Results and discussion

4.3.1 Synthesis and characterization of SS hierarchical surfaces

Achieving effective water repellence behavior in laser treated metals typically requires the application of aggressive, high-fluence laser treatments to induce a substantial level of surface roughness. However, when applied to stainless steel these energetically intense treatments can alter the surface stoichiometry and compromise the corrosion resistance. This presents a serious concern for long-term industrial applications that require liquid repellency and/or anti-icing properties in environments where biofilms or other biological agents may expedite corrosion⁵⁷ or compromise the adhesion of interlayer materials, especially at elevated temperatures⁵⁸.

As an alternative, we employed a relatively mild laser treatment designed to create specific grooves while minimizing damage to the overall surface area. Subsequently, the deposition of an additional SS layer onto these patterned surfaces results in the obtention of hierarchical SS surfaces. The laser ablation treatment applied to the SS plates was configurated to produce parallel lines spaced approximately 40 μm , with a morphology composed of rounded motifs having an average size of 15 μm (**Figure 1**).

Confocal microscopy analysis of laser-treated surfaces, compared to untreated ones, revealed the creation of ordered linear patterns with a periodicity of around 45 μm , affecting a surface thickness of approximately 3 μm and promoting increase in roughness. S_a and S_q roughness parameters values varied from 0.19 μm to 0.24 μm for the bare SS substrate to 0.96 μm and 1.19 μm after the laser treatment (i.e., sample SS-laser), respectively.

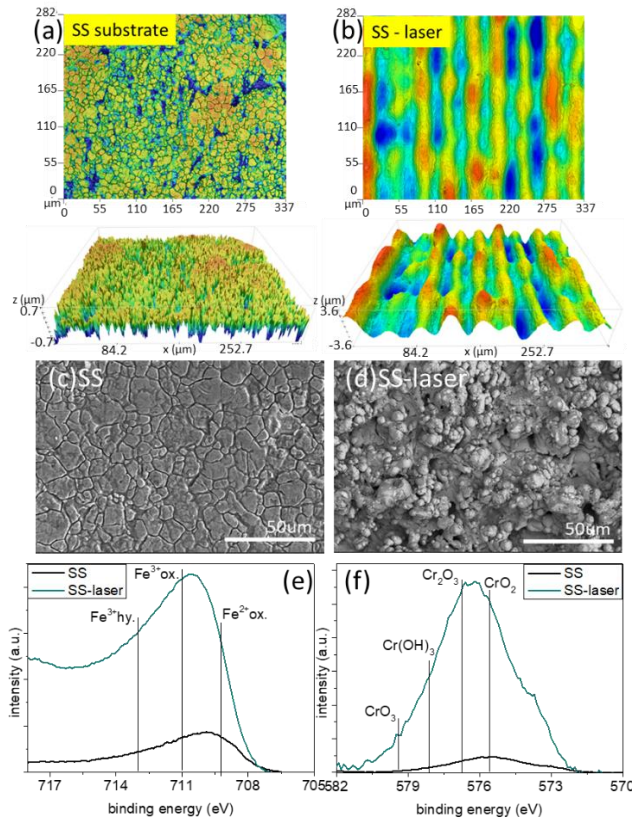


Figure 1. Laser treatment of SS. Confocal microscopy images (a-b) and top view SEM micrographs (c-d) of the SS sample before a), c) and after b), d) laser treatment, respectively. Fe $2p_{3/2}$ e) and Cr $2p_{3/2}$ f) high resolved binding energy XPS spectra of the SS surface before and after the laser treatment. A tentative attribution of chemical species is included to account for the chemical state of Fe and Cr in each case.

SEM images illustrate how laser treatments blurs well-defined SS grain boundaries, leading to the development of an irregular distribution of granular microstructures with diameters below $7 \mu\text{m}$. In addition, surface morphology was modified, as illustrated in Figure 1 a)-d), highlighting the presence of a roughness scale in comparison with the grains of SS surface before laser treatment. It is noted that the laser treatment induced slight alterations in surface chemistry, where surface atomic percentages obtained through XPS analysis of the sample surfaces are presented in **Table 1**.

Table 1. XPS atomic concentration for the SS surface before and after the laser treatment.

% at.	O	C	Fe	Cr	Ni	Si
SS	24.0	70.0	1.0	0,4	-	4.5
SS-laser	54.3	34.2	4.9	3.1	0.9	2.7

The standardized chemical composition of an austenitic 304 stainless steel is characterized by having practically negligible atomic percentage values of O before the environmental passivation that this material undergoes, with values of 1 % for C, 68 – 70 % for Fe, 18 – 20 % for Cr, close to 1 % for Si, and 8 – 10 % for Ni⁴⁸. Based on this analysis, it was observed that cleaned reference stainless steel samples, when exposed to air (environmental passivation), exhibited high content of carbon and oxygen, and a relatively lower content of iron and chromium. This fact supports a surface contamination and oxidation experienced by the SS samples during air exposure. This accounts for the relatively low percentages of iron, chrome, and other metallic elements present in the SS (XPS analysis suggest a thickness of around 3-5 nm from the surface). The laser treatment induced small alterations in the surface metal ratio, accompanied by the partial removal of spurious carbon (laser-treated surfaces are exposed to air before XPS analysis). The SS-laser samples exhibited atomic contents of 5.1 at. % Fe and 3.3 at. % Cr, resulting in a Cr/Fe ratio of 0.65 compared to a ratio of 0.40 in pristine SS samples, both higher than the ~ 0.29 value from the nominal reference⁴⁸. This suggests a certain preferential evaporation of chromium and nickel over iron during laser treatment.

Furthermore, the laser treatment improved the surface oxidation, exemplified in Figure 1 e), and f), which depict the Fe 2p and Cr 2p spectra for both pristine and SS-laser samples. The Fe 2p signal appeared broad, indicating the prevalence of Fe⁺³ oxide and hydroxide, with minor contributions from Fe⁺² (metallic Fe is not observed because it must be buried beneath the oxidized layer)^{59,60,61}. Similarly, the Cr 2p spectrum revealed various oxides and hydroxides of chromium groups^{62,63} in different valence states after laser treatments, although the broad shape of the spectrum hinders a precise quantification of these contributions.

Hierarchical double-roughness SS surfaces were obtained by depositing a nanostructured SS layer through electron beam evaporation at oblique angles. To establish a reference surface, this oriented nanostructured layer was also

deposited on flat silicon substrates, demonstrating an open porous film formed by 45° tilted nanocolumns of SS, as evidenced by the top-view and cross-sectional SEM micrographs depicted in **Figure 2 a)**. The nanocolumnar structure resembles those previously observed in pure metal films^{64,65} evaporated at oblique angles, with the size and tilting angle of the nanocolumns being linked to the zenithal angle of evaporation and the film's thickness⁴⁰.

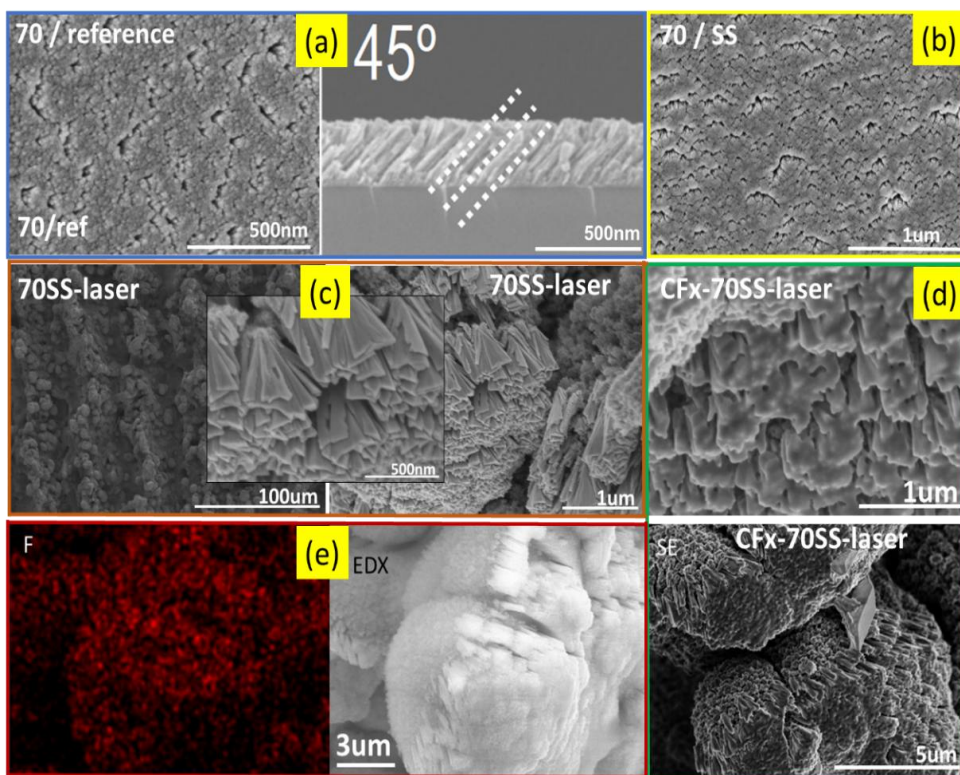


Figure 2. Morphology of SS nanocolumnar thin films deposited at a zenithal angle of 70° analysed by SEM: a) Images on a flat silicon wafer (top view and cross section images). b), c) Images at two different magnifications of SS flat and SS-laser substrates, including a zoomed region in c) (sample 70SS-laser). d) Images at two magnifications of the laser treated SS, after coating with a CF_x fluorocarbon polymer film (sample CF_x-70SS-laser). e) EDX and fluorine surface maps of the sample in d).

It reflected an enrichment in Cr and Ni compared to Fe, when contrasting the film composition with that of the pellets employed for evaporation⁵¹. On flat stainless steel (SS) substrates, the electron beam evaporation of SS replicated the nanocolumnar structure observed on the flat silicon reference, illustrated by the top-view micrographs presented in Figure 2 b). Upon depositing a similar SS

nanocolumnar thin film into the SS-laser sample, a hierarchical surface combining two levels of roughness at both micro- and nano- scales was obtained. This observation was confirmed by SEM examination of the SS-laser sample coated with the SS nanocolumnar thin film (refer to sample 70SS-laser in Figure 2 c)). The low-magnification image in this figure reveals that SS nanocolumns preferentially grow on the hills of the grooves, according to current models about oblique angle deposition on highly rough surfaces^{66,67}. Additionally, this image discloses that the micron-scale roughness defined by the laser-ablated pattern can be modulated at the nanoscale by the accumulation of nanocolumns along the groove's direction. The magnified image in Figure 2 c), confirms the existence of a porous irregularly ordered arrangement of nanocolumns, exposing open pores at the surface, providing a re-entrant-like surface topography. These types of re-entrant surfaces are defined as textured or curved structure designed to repel liquids by creating overhangs that trap air beneath droplets, helping to maintain high contact angles and reducing surface tension effects⁶⁸.

AFM measurements were tested to demonstrate that an increase of approximately 2 nm in the RMS roughness was identified with the 700 nm thick nanocolumnar SS films deposited on SS compared to silicon, shown in **Figure 3**. This discrepancy can be related to the inherent flatness of the silicon wafer relative to the SS substrate.

As mentioned in previous section, the third step involved in the process to achieve distinctive wetting on hierarchical SS surfaces is to have a highly porous SS surface acting as an ideal host for accommodating fluorine-based agents, ranging from molecules to coatings and lubricants liquids. Fluorination of the re-entrant-like surfaces (which were characterized to present overhanging structures for air retention⁶⁸) prepared in this study, combining laser treatment with SS evaporation, was carried out following the experimental procedures outlined in the Chapter 2. Figure 2 d) and e), display selected SEM images and Energy-Dispersive X-ray (EDX) spectroscopy map for the 70SS-laser surface covered by a CF_x thin film (i.e., sample CF_x -70SS-laser). The fluorine (F) mapping shows high conformality of the CF_x coatings and its uniform distribution over the sample. A comparison between Figure 2 d) and e) highlights that coating of the 70SS-laser sample with the CF_x thin film induced a certain smoothing of the surface, mitigating partially the surface irregularities and therefore its hierarchical character.

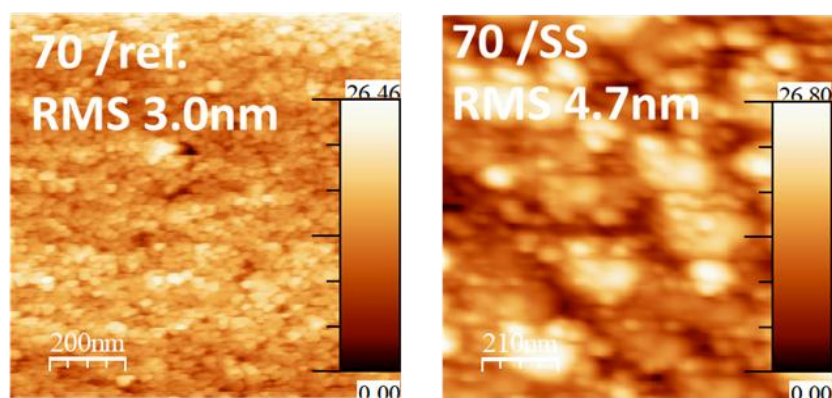


Figure 3. AFM topographical images of SS nanocolumnar thin films at 70° azimuthal deposition angle when they are deposited onto silicon flat and SS substrates. Corresponding average RMS roughness parameter is indicated.

4.3.2 Corrosion behavior of hierarchical low fluorinated SS surfaces

An essential consideration in the application of nanostructured SS surfaces with advanced functionalities is the corrosion resistance. To address this concern, the hierarchical SS samples before and after their fluorination, have been evaluated using a standard potentiodynamic corrosion procedure (details were described in Chapter 2). **Figure 4** and **Table 2** compile pertinent information on the corrosion properties of the examined samples in comparison to the reference flat SS sample. Initial observations reveal that the polarization curves exhibited a similar shape regardless of the surface treatment applied to the samples. They are characterized by a nearly vertical anodic branch, with a slope similar to that observed for the flat SS used as a reference. Both the 70SS and 70SS-laser samples displayed the same passive current density that the reference SS but exhibited higher and lower pitting potentials, respectively (Table 2).

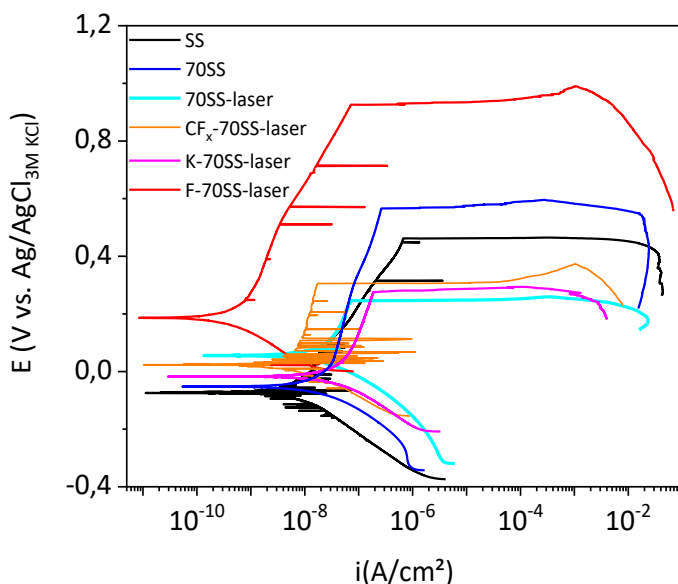


Figure 4. Potentiodynamic polarization curves used as corrosion tests of the micro and nanostructured 70SS and 70SS-laser samples and of this latter sample after fluorination (samples CF_x-70SS-laser, F-70SS-laser, and K-70SS-laser). The curve corresponding for the reference SS is included for comparison.

Table 2. Relevant corrosion parameters derived from the analysis of the potentiodynamic polarization curves (E_c : corrosion potential; E_p : pitting potential; I_p : passive current density).

Samples	E_c (V)	E_p (V)	$E_p - E_c$ (V)	I_p (A/cm ²)
SS	-0.075	0.460	0.535	$1.5 \cdot 10^{-7}$
70SS	-0.055	0.565	0.620	$7 \cdot 10^{-8}$
70SS-laser	0.025	0.150	0.125	$3 \cdot 10^{-8}$
CF _x -70SS-laser	0.025	0.380	0.283	$1 \cdot 10^{-8}$
K-70SS-laser	0.055	0.275	0.220	$9 \cdot 10^{-8}$
F-70SS-laser	0.185	0.925	0.740	$5 \cdot 10^{-9}$

These results indicated a lower localized corrosion resistance for the 70SS-laser sample compared to the SS reference. Pitting corrosion differences in stainless steel are commonly associated with micro-roughness generated by laser treatment, as well as chemical and topographical alterations. A previous study⁶⁹ emphasises that topographical changes have more influence than roughness on the pitting corrosion on stainless steel. This aligns with our observation about that the corrosion resistance decreased reasonably for the 70SS-laser sample, an

effect attributed to the grooves formed by the laser treatment. Notably, the deposition of a nanocolumnar thin film of stainless steel (70SS sample) did not significantly alter the anti-corrosion properties of flat SS, supporting that the negative effect of laser patterning on corrosion behaviour can be compensated by the deposition of the nanocolumnar SS layer. It is important to note that these corrosion tests were carried out in extreme corrosion conditions highlighting that the SS 304 surfaces without any protection can achieve values of E_p around 0.3-0.5 V in saline environments⁷⁰, indicating that enhancements were found for fluorinated hierarchical SS surfaces as it is shown in Table 2.

Remarkably, certain fluorinated surfaces exhibited significantly enhanced corrosion resistance compared to SS. This is exemplified by sample F-70SS-laser, demonstrating improved barrier properties through the reduction of the passive current density by two orders of magnitude and a pitting potential shifted by approximately 450 mV towards nobler values compared to SS reference. Conversely, the other two fluorinated surfaces, CF_x-70SS-laser, and K-70SS-laser, appeared to have a reduced pitting corrosion resistance compared to the reference SS⁷¹. However, although the general response does not exhibit improvement, it does not significantly deteriorate with respect to the anti-corrosive properties of the SS-reference. To justify the superior corrosion resistance of sample F-70SS-laser, we propose that during the initial stage of the tests, the corrosive medium is not able to penetrate the hierarchical surface of F-70SS-laser, acting as a protective barrier. Subsequently, at higher voltages, the corrosive medium may affect the PFOTES molecule and grafted bonds, leading to the release of fluorine atoms and the pitting of the oxidized SS surface. It is also possible that erosion may affect the native oxide regions exposed at the surface of the rough-textured surfaces, enabling that the released fluorine atoms react with Cr or Fe atoms, forming a fluorinated passivation layer⁷². The fate of fluorine after the corrosion experiments will be further studied in the concluding section of this chapter.

4.3.3 Wetting behavior of hierarchical SS surfaces

After laser treatment and SS thin film deposition, the samples were securely stored in a laboratory drawer under ambient conditions for a minimum duration of one month to stabilize their wetting state showing high values of WCA due to

the carbon presence from air⁷³. As illustrated in **Figure 5 a)**, water droplets on the pristine SS and SS-laser samples exhibited a partially hydrophilic behavior, without significant distinctions between flat (sample SS) and micro/nano-structured surfaces, and an incipient hydrophobic character for sample 70SS-laser.

It is noteworthy that all these non-fluorinated samples displayed significant oleophilic trends, as evidenced by DCA values close to zero. Upon fluorination, that partial hydrophilic or hydrophobic behaviors of these samples transformed into highly hydrophobic states for samples K-70SS-laser and CF_x-70SS-laser, and even superhydrophobic for sample F-70SS-laser. Remarkably, the contact angle of diiodomethane on these fluorinated surfaces increased, rendering all these fluorinated hierarchical surfaces oleophobic. The superhydrophobic/oleophobic characteristics were particularly pronounced in sample F-70SS-laser, exhibiting a typical omniphobic nature with contact angles close to 180° and 120° during wetting tests with polar and non-polar liquids droplets, respectively. It is also remarkable that, in comparison with sample K-70SS-laser, samples F-70SS-laser and CF_x-70SS-laser outperform the water and oil repellence observed in the (SLIPS) sample.

The water repellence of the fluorinated hierarchical SS surfaces was further exemplified by strategically dripping large water droplets (10 µl) on their surfaces and measuring the water rolling-off angles values. The sequential snapshots in **Figure 5 c)**, illustrate that water droplets roll off effortlessly on the tested surfaces, leaving them dry without only residual liquid traces. Moreover, the water rolling-off angles values presented in **Table 3** show the differences between samples CF_x-70SS-laser, F-70SS-laser, and 70SS-laser, and the other samples, including sample K-70SS-laser.

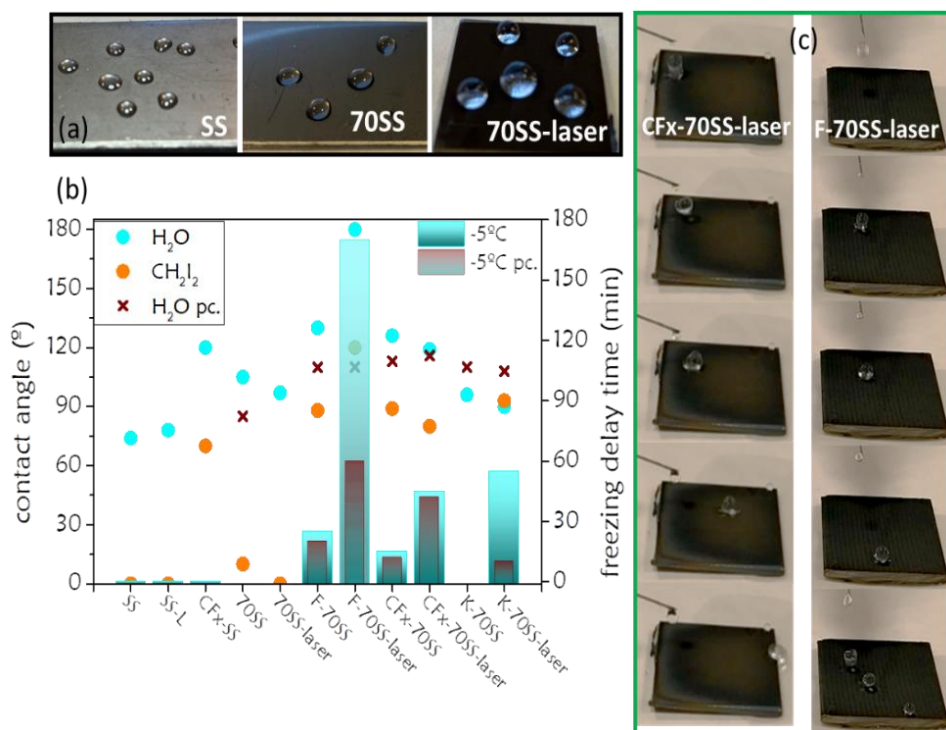


Figure 5. a) Pictures of stored, pristine prepared, SS substrates (i.e., samples SS, 70SS and 70SS-laser) with several water droplets left on their surface to assess their wetting behaviour. b) Contact angles with water and diiodomethane (WCA and DCA) and FD times for samples SS, SS-laser, 70SS-laser as prepared and after fluorination with a CF_x thin film (i.e., CF_x-70SS and CF_x-70SS-laser samples), infusion of Krytox to get SLIPS (i.e., K-70SS and K-70SS-laser samples) and grafting with perfluorinated molecules (i.e., F-70SS and F-70SS-laser). Plot with red cross dots (i.e. labelled pc) corresponds to values measured after corrosion tests; the two sets of bar plots for FD time correspond to samples before and after (i.e., labelled pc) corrosion tests. c) Dripping experiment to demonstrate the superhydrophobic behaviour of fluorinated samples with hierarchical topography. Snapshots sequence corresponding to the rolling-off of water droplets on the CF_x-70SS-laser and F-70SS-laser surfaces.

The low rolling-off angles observed for the two former samples contrast with the 90° angle values showed by the others except for sample K-70SS-laser, which displayed a high rolling-off angle of 60°. These variations in water sliding demonstrate that a dual scale roughness is required for achieving a pronounced water slippery behaviour. Furthermore, it is noteworthy that filling the surface porosity with Krytox (as observed in samples K-70SS-laser and K-70SS) seems detrimental for the water droplet repellence, mainly due to the relatively flat outer surface of these samples infused with liquid.

Table 3. Rolling-off angle values of 10 μl droplets of different liquids on SS, SS-laser, 70SS-laser samples as prepared and after fluorination by deposition of a CF_x thin film, Krytox incorporation in the form of SLIPS and grafting with perfluorinated molecules.

Rolling-off angle ($^\circ$)	Water	Diiodo-methane	Humic acid	Sodium alginate	Bovine serum
SS	-	-	-	-	-
SS-laser	-	-	-	-	-
70SS	90	-	30	30	20
70SS-laser	<2	-	20	20	20
F-70SS	90	90	90	90	90
F-70SS-laser	<2	70	<2	<2	<2
CF_x -70SS	90	90	90	90	90
CF_x -70SS-laser	<2	35	<2	<2	<2
K-70SS	90	90	90	90	90
K-70SS-laser	60	45	70	30	50

4.3.4 Self-cleaning and anti-fouling properties of low fluorinated hierarchical (SS) surfaces

The biofluid-repellent nature of fluorinated SS hierarchical surfaces was validated by exposing them to the interaction with various fouling simulators. The notable differences in rolling-off angles, detailed in Table 3, offer additional support for the self-cleaning and anti-fouling behaviors of these surfaces. Table 3 illustrates that the tested droplets presented a pinning response on the SS and SS-laser samples (i.e., surfaces without laser treatments show rolling-off angles as high as 90°), whereas they only exhibited rolling-off behavior after the deposition of the nanocolumnar SS layer and the fluorination treatments. Data in Table 3 also shows that the rolling-off angle is closely linked to the surface topography and the specific type of fluorination treatment. Moreover, fluorination had a high impact, reducing the rolling-off angles of biofluid simulants and transforming the surface state into an anti-fouling one for samples F-70SS-laser and CF_x -70SS-laser as it is shown in the **Figure 6**.

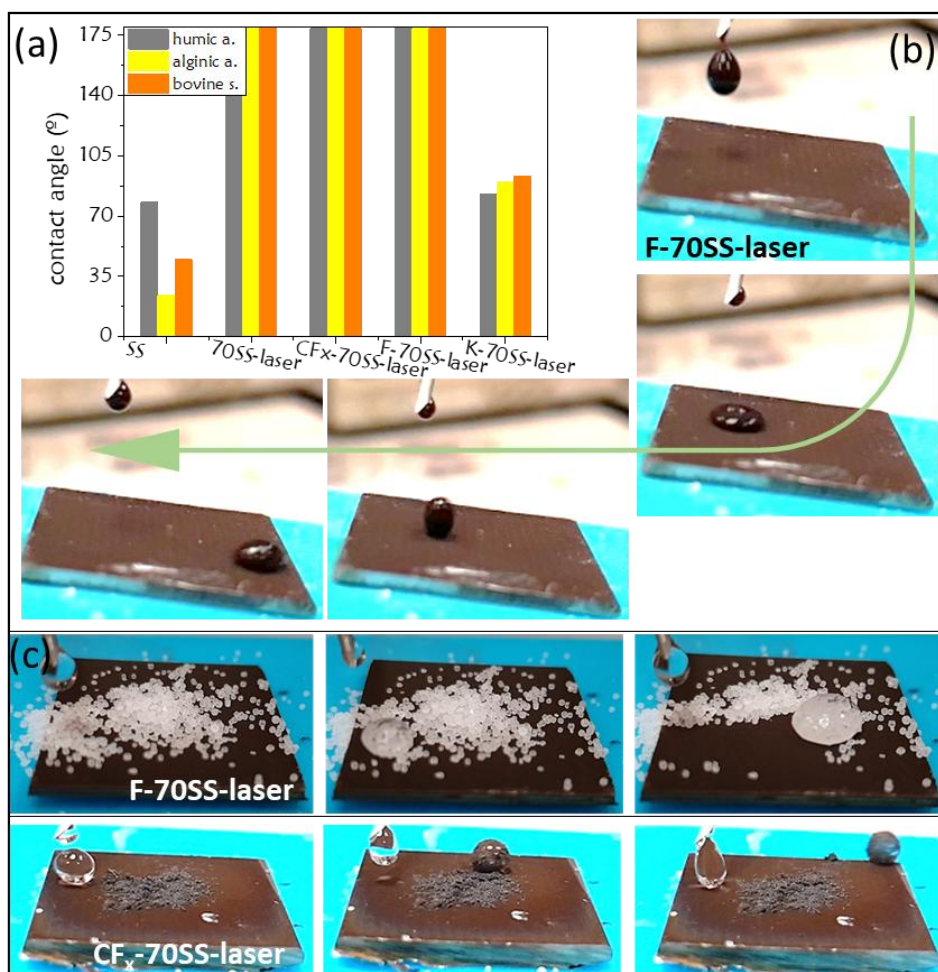


Figure 6. a) Contact angles of 2 μl fouling fluid droplets on fluorinated hierarchical SS surfaces. Data are shown the following simulated fouling agents: humic acid, alginate and bovine serum albumin. b) Pictures showing the anti-fouling response of sample F-70SS-laser against humic acid. c) Snapshots sequence corresponding to the self-cleaning behaviour with water droplets of F-70SS-laser and CF_x-70SS-laser surfaces contaminated with salt and graphite powder.

Figure 6 provides additional insights into biofluid repellence. Wetting contact angles in this figure reveal that fluorinated hierarchical SS samples, obtained through dry methods such as Teflon-like coating and perfluorinated molecules, exhibited anti-fouling behaviour, characterized by high CA values for the different proposed liquids, as well as showing complete repellence, causing the droplets of these liquids to stick on the dispensing needle⁷⁴. That is the opposite behaviour of the flat SS reference that became wetted, particularly with sodium alginate (contact angle around 20°). It is noteworthy that the SS SLIPS (K-70SS-

laser sample) displays the lowest wetting contact and rolling-off angles, seeming contradictory to its sliding surface character. It could be related to the absence of enough Krytox infused on porous SS nanocolumns due to the liquid mobility, as well as different densities values for these fouling agents and Krytox (1.2-1.5 g/cm³ for humic, sodium and bovine solution and values of 1.9-2.0 g/cm³ for Krytox)⁷⁵. According to data in Table 3, Figure 6 b), shows images of the F-70SS-laser sample tilted at 5°, where 10 µl humic acid droplets efficiently roll off onto the surface, while the snapshots demonstrated that the surface remained dry and clean after continuous dosing the fouling agents.

To expand the studies about omniphobic properties of different fluorinated hierarchical SS surfaces, immersion tests were carried out at room conditions employing bovine serum and humic acid for 30 minutes. Pictures about these immersion tests are shown in **Figure 7**. After 30 minutes of immersion in the biological fluids, stains or liquid accumulations, or alterations in wetting behaviour were not detected for F-70SS-laser and CFx-70SS-laser samples, showing an effective anti-fouling character presented in Figure 7 and **Table 4**. It is noteworthy that after immersion tests, samples were cleaned with water to remove humic acid and bovine serum rest. WCA values were similar than before immersion as it is shown in the Table 4. Experiments demonstrated the capability to recover the omniphobic character after several minutes of tests (30 min), in biological liquids to check the anti-fouling properties of the samples. In addition, related to anti-fouling capacity, snapshots in Figure 6 c), exhibited self-cleanability and these tests confirm that water droplets of varying volumes effectively remove solid contaminants like salt or carbon powder when it is sliding onto the surface.

Data in Table 4 shows omniphobic memory for these both fluorinated hierarchical SS surfaces after immersion tests highlighting the superhydrophobic behaviour for F-70SS-laser sample.



BOVINE SERUM



HUMIC ACID

Figure 7. Images corresponding to the immersion tests for F-70-SS-laser in bovine serum and humic acid.

Table 4. Wettability values of fluorinated hierarchical SS surfaces before and after immersion tests.

Water contact angle (°)	Bovine serum		Humic acid	
	Before immersion	After immersion	Before immersion	After immersion
F-70SS-laser	~180	~180	~180	~180
CF _x -70SS-laser	168	168	162	160

Surface structuration via chemical⁷⁶ or mechanical⁷⁷ methods has previously proven as effective in conferring anti-fouling properties to SS. In this study, we demonstrate that an enhanced anti-fouling capacity is the result of both hierarchical surface topography and fluorination. But, contrary to other reported findings^{78,79} the current SLIPS with a reduced amount of incorporated lubricant were found less suitable for anti-fouling, compared to the samples where fluorination was achieved through the grafting of fluorocarbon silicon molecules⁸⁰. Even more, the fluorine content in the grafted sample is comparatively negligible in relation to the fluorine amount incorporated in the SLIPS.

4.3.5 Durability and stability characterization of the low fluorinated SS hierarchical surfaces

A crucial issue for the practical use of the nanostructured and hierarchical SS sample is their resilience to erosion and abrasion processes under working conditions. To assess this aspect micro- and nano-textured SS surfaces, both with and without fluorination, were subjected to the series of standardized rain erosion and abrasion tests, detailed in the **Figure 8** and **Table 5**.

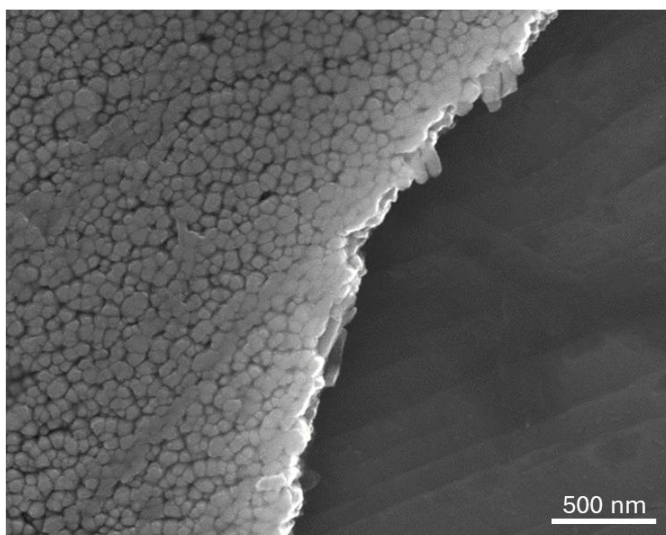


Figure 8. SEM micrograph corresponding to sample 70SS subjected to abrasion for 100 cycles taken in a zone where coating has been delaminated on purpose (i.e., at the boundary between coating and bare stainless steel).

These abrasion tests were carried out with a standardized 1720 abrasion and wash-ability tester with a load of 0.05 Kfg cm^{-2} for 100 cycles, the necessary value of cycles to observe minor physical damages on the surface of samples. This Figure 8 and Table 5 demonstrate that this kind of hierarchical surfaces are poised to resist the risk of harsh conditions typical of real-world working environments. It is apparent that the tip of the nanocolumns have been slightly rounded, although the integrity of the coating is maintained.

Table 5. Effect of rain erosion tests on the integrity and functionality of SS-laser, hierarchical SS-laser and fluorinated (CF_x-) SS-laser surfaces.

Sample/ droplet velocities	N° impacts for visible damage			N° impacts for wettability change		
	165m/s	180m/s	225m/s	165m/s	180m/s	225m/s
SS-laser	>2000	>2000	>2000	>2000	>2000	>2000
70SS-laser	<20	<20	<20	>2000	>2000	>2000
CF_x-SS-laser	~200	~200	~125	>2000	>2000	>2000

Rain erosion tests were carried out in Airbus Central R&T Materials Laboratory in Germany with a specific protocol¹⁶. Rain erosion experiments are specially employed in aeronautics due to the importance of rain erosion effect in harsh environments. These tests were conducted on icing wind tunnel⁸¹. A given number of water droplets (average diameter 260 μm) was sent at different velocities (as it is shown in Table 5) on the samples. Number of required impacts to observe visible damages was the key parameter at different velocities. It is possible to differentiate firstly that the number of impacts required to observe visible damage (presence of scratches on surfaces) in the samples was much higher for the coated microstructural SS, either in the form of SS nanocolumns or CF_x thin film on the laser-treated SS surface. The presence of a coating deposited on the hierarchical SS surface compared to the resistance of the uncoated SS-laser one was confirmed according to Table 5. However, to identify changes in the wettability of the tested surfaces, the number of required impacts must be higher than 2000 for all cases since, the robust superhydrophobicity of the hierarchical surfaces were demonstrated. Therefore, it is worth emphasizing that the hierarchical SS sample exhibited satisfactory performance in these assessments.

4.3.5 Anti-icing capacity

This CF_x thin film, consisting of a Teflon-like coating rich in -CF₂ and -CF₃ functional groups^{41,43,52}, has previously been employed as anti-icing coating on hierarchically rough alumina/aluminium substrates. In general, the assessment of surface's anti-icing capabilities encompasses various phenomena that show

the characteristics of the ice-substrate interface, including ice adhesion, ice accretion⁸², and FD time. In this study, we investigate the anti-icing properties of the hierarchical SS surfaces by focusing on their FD capacity and ice adhesion capabilities⁸³. Figure 5 b) presents the FD times determined for the fluorinated 70SS and 70SS-laser surfaces and references. The reported values, particularly the one obtained for sample F-70SS-laser (i.e; 170 minutes), indicate that the combination of fluorination and hierarchical surface roughness achieved by the combination of nano- and micro-structures, positively impact the anti-icing capacity of stainless steel. Based on these parameter values, the anti-icing performance of sample F-70SS-laser appeared superior to that of the other fluorinated hierarchical samples.

Notably, the long FD times of the fluorinated hierarchical SS surfaces were reproducible under freezing/thawing cycles, as illustrated in **Figure 9** for sample CF_x-70SS-laser. After 5 heating/cooling cycles with a 2 µl water droplet deposited on the surface and temperature changes from -5 ° to 20 °C, the water contact angle of the droplet only changed by 14 degrees, the surface keeping its original hydrophobicity. In addition, the FD time remained constant (worsening by 1 minute) after these 5 freeze/thaw cycles. The reproducibility in FD times for these surfaces support their long-term stability, comparing favourably with similar studies conducted on other materials such as SiO₂, Al₂O₃ and TiO₂ nanostructured surfaces^{84,85}, (note that there are limited studies available on the anti-icing capacity for nanostructured SS surfaces^{86,87}). It is noteworthy that K-70SS-laser samples are susceptible to losing the Krytox lubricant after successive icing tests, a risk not encountered with the other two fluorination methods. We hypothesize that the surface modifications resulting from low fluorination play a crucial role in decreasing FD times to values exceeding 60 minutes for sample CF_x-70SS-laser. When substrate thermal conductivity is equivalent, the primary factor controlling FD response is the time required to create the first ice nuclei either inside the water droplets or at specific hierarchical SS surfaces sites (i.e; homogeneous and heterogeneous nucleation, respectively)⁸⁸.

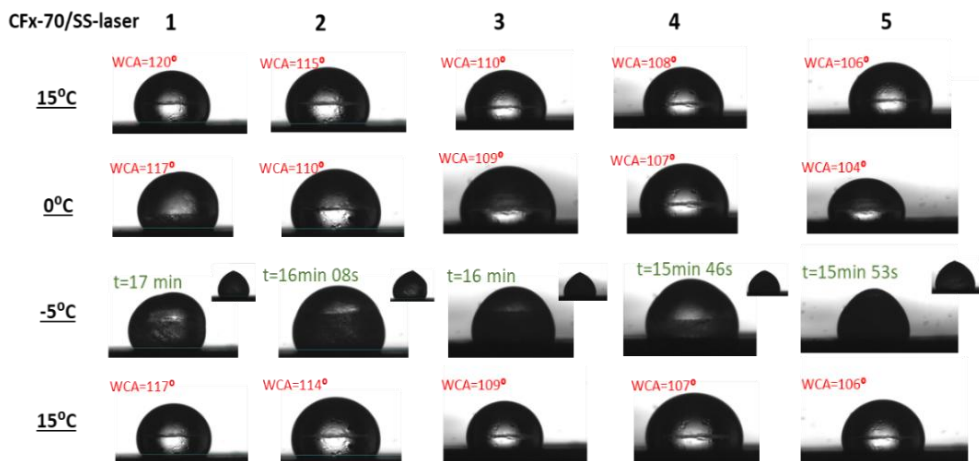


Figure 9. Snapshots corresponding to five freezing / thawing cycles on the CF-70SS-laser surface. Water contact angle and freezing delay time values are included in each temperature phase.

Previous research has indicated that heterogeneous nucleation requires a minimum size to proceed and that surfaces with hydrophobic characteristics, especially those that are heterogeneous and rough, often inhibit these size requirements^{89,90}. Therefore, long FD times were observed for sample F-70SS-laser (and to a lesser extent, samples CF_x-70SS-laser, as seen in the Figure 5 b)) from the modification of its surface state through the grafting of freely moving PFOTES molecules, where difficulty finding a free surface size to initiate the ice nucleation process.

Fluorination played an important role to decrease the strength of ice adhesion. As a fundamental principle, increasing surface roughness typically leads to increase ice adhesion strengths^{91,92}. This observation results true when comparing the values determined for flat stainless steel (SS) and the hierarchical SS samples, which are shown in the **Table 6**. Comparing the ice adhesion strength values, the sequence 70SS << SS << 70SS-laser was evident, with all samples displaying values exceeding the threshold of 100 kPa, considered the limit between low and high ice adhesion surfaces⁹³.

Table .6 Ice adhesion strength of the CF_x-, F- and K- hierarchical SS substrates compared to the SS ones without laser treatment and the pristine SS substrate. A Teflon foil reference was employed for comparison.

Samples	Ice adhesion strength (kPa)
SS	135 ±7
70SS	125 ±6
70SS-laser	241 ±12
F-70SS	69 ±3
CF _x -70SS	109 ±4
K-70SS	44 ±2
F-70SS-laser	98 ±5
CF _x -70SS-laser	210 ±11
K-70SS-laser	89 ±4
Teflon reference	15 ±1

Fluorination induced a substantial reduction in these values, with the order K-70SS-laser << F-70SS-laser <<< CF_x-70SS-laser, with values failing below 100 kPa for the first two samples in the sequence and close to it for the last one (it is worth nothing that SLIPS sample generally exhibit low adhesion strength as ice forms directly in contact with the infused fluorinated liquid, indicating ice adhesion values in the same range as the Teflon reference). It is attributed both, the extended FD times measured and its remarkably low adhesion strength, to the influence of the grafted PFOTES molecules for sample F-70SS-laser. These molecules probably contribute to avoiding ice nucleation and, once ice is formed, reducing its adhesive force with the surface.

4.3.6 Functionality after corrosion tests

The long-term preservation of the functional properties of SS surfaces is crucial for their practical utility^{94,95,96}. Here, we examine the functionality of F-70SS-laser and CF_x-70SS-laser samples after the corrosion testing. Figure 5 displays water and diiodomethane contact angles, as well as FD times for samples subjected to the corrosion essays. Interestingly, the contact angle and FD values for the CF_x-70SS-laser sample after corrosion remained quite like those ones before the corrosion test, indicating minimal, if any, impact on the water repellence of this low fluorinated hierarchical SS surface. However, samples K-70SS-laser and F-70SS-laser, subjected to corrosion testing, exhibited significant

degradation in superhydrophobicity and/or FD time values, suggesting a substantial deterioration of their original surface state. This effect is more pronounced for the SS SLIPS, where contact with the water solution may induce some lubricant migration during the test⁷⁹. The increase observed in water contact angle after the corrosion test (Figure 5 b)) likely reflects the influence of the bare nano- and micro-SS surface after the loss of infused liquid. Notably, both CF_x- and F- hierarchical surfaces maintained their original anti-fouling response after corrosion testing, as indicated by the determination of very small rolling-off angles for droplets of the bio-fluid simulants used in this study shown in **Table 7**.

Table 7. Wetting contact angle and rolling-off angle (in brackets) values of droplets of 2 and 10 μ l, respectively, for fluorinated and nanostructured SS surfaces after being subjected to the corrosion test.

Wetting CA (RoA) /°	Wetting CA			
	Water	Humic acid	Sodium alginate	Bovine serum
70SS	85(90)	50(90)	49(90)	45(90)
F-70SS-laser	110(90)	~180(<2)	~180(<2)	~180(<2)
CF_x-70SS-laser	116(90)	160(<2)	160(<2)	170(<2)
K-70SS-laser	60(80)	70(80)	70(70)	50(70)

SEM analysis revealed that surface topography shown in **Figure 10** corresponding to the post-corrosion (p.c.) test surfaces involved some scratches from the sample handling itself but from the point of view of the integrity of the developed hierarchical surface no major changes were detected. CF_x-70SS-laser p.c. showed the fluorinated coating remaining homogeneous after the corrosion test. On the other hand, F-70SS-laser hierarchical structure presented the same topography shown in Figure 2 c). Finally, the presence of the fluorinated liquid with low surface tension was missed after this post-corrosion test (K-70SS-laser), as it has been previously commented that despite its great sliding capacity as SLIPS, the concepts of stability and durability must still be worked on due to the possible loss of the liquid infiltrated in the quite open porous hierarchical surfaces.

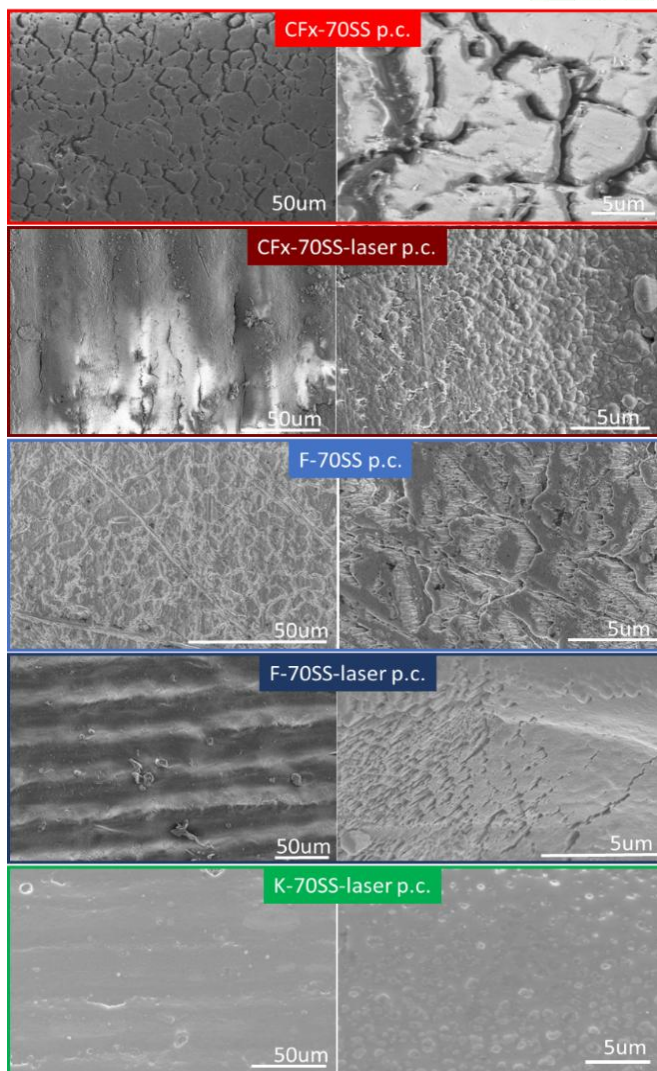


Figure 10. SEM micrographs of the top view for CF_x-, F- and K- 70SS surfaces after the corrosion test at two magnification levels.

The surface state of the fluorinated SS hierarchical F-70SS-laser and CF_x-70SS-laser surfaces after corrosion testing was analysed using XPS and it is shown in the **Figure 11**.

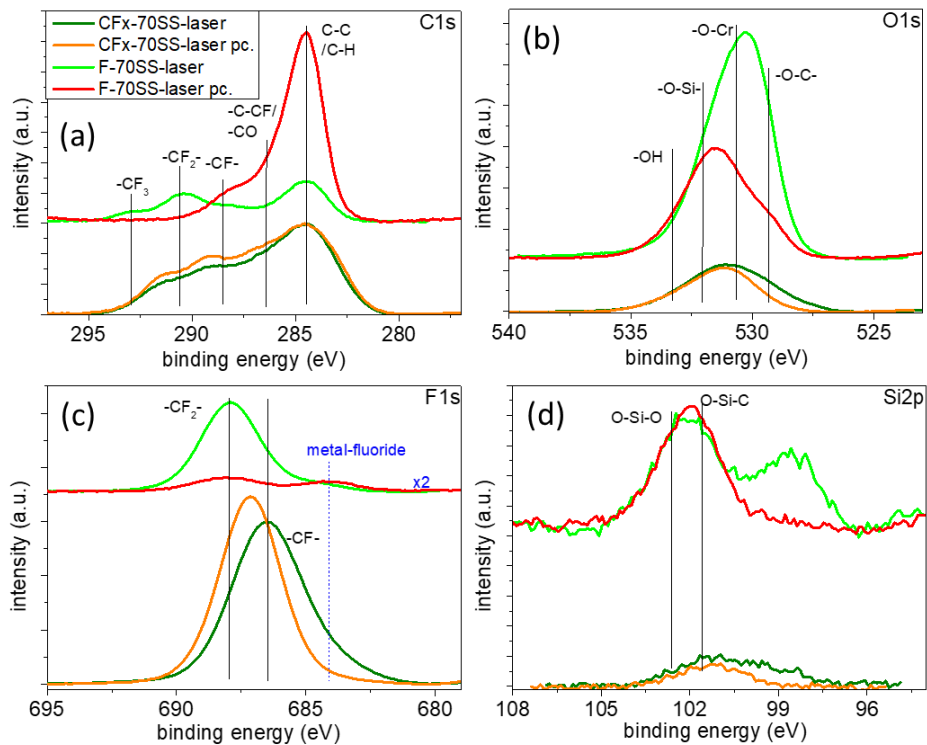


Figure 11. XPS photoelectron spectra of fluorinated samples before and after the corrosion test as indicated: high resolved binding energy regions for C 1s a), O 1s b), F 1s c) and Si 2p d) signals. The attribution of spectral feature to given functional groups bonds is indicated. It is noted that F-70SS-laser p.c. appear as x2 in the graph.

Figure 11 reveals significant differences in the F 1s, C 1s, O 1s, and Si 2p spectra of the two examined surfaces before and after corrosion testing. The analysis of the CF_x-70SS-laser sample in its original state indicated that it was uniformly covered by a continuous Teflon-like film, as evidenced by the low percentage of iron/chromium and oxygen atoms detected at the surface shown in **Table 8**.

Table 8. Atomic percentages determined by XPS analysis of the CF_x-70SS-laser and F-70SS-laser surfaces before and after the corrosion test.

At%	CF _x -70SS-laser	CF _x -70SS-laser p.c.	F-70SS-laser	F-70SS-laser p.c.
C	43.3	45.5	19.2	54.4
N	1.4	1.5	0.1	3.0
O	11.6	8.2	41.7	31.2
F	41.2	42.0	27.3	4.1
Si	0.6	0.7	3.8	4.3
Cr	0.1	0.5	1.8	1.5
Fe	1.8	1.5	6.1	1.5

A highly intense F 1s spectrum and the characteristic shape of the C 1s spectrum further confirmed the presence of a CF_x layer. Thus, the C 1s spectral shape of this sample (Figure 11 a)) is indicative of a fluorinated polymeric film with distinctive features attributed to CF₃ (293.0 eV), -CF₂ (290.8 eV), -CF (288.6 eV), C-CF (286.4 eV), and C-C/C-H (284.5 eV) functional groups⁹⁷. Interestingly, these XPS photopeaks were minimally affected by the corrosion tests, both in terms of the C 1s and F 1s spectral shape, width at half height and the relative percentages of detected elements (Table 8). The preservation of a similar fluorinated surface state in this sample explains the consistent wetting, freezing delay and anti-fouling behaviours observed before and after corrosion testing. It demonstrates the high chemical stability of the CF_x coated hierarchical SS surface where corrosion likely occurring beneath the Teflon-like thin film or in the form of localized pitting processes at specific sites on the surface.

In contrast to the CF_x-70SS-laser, F-70SS-laser sample revealed notable differences in surface element percentages (refers to Table 8) and the chemical characteristics of functional groups before and after corrosion testing. In its pristine state, the C 1s spectrum of this sample exhibited bands attributable to the CF₂/CF₃ functional groups of the PFOTES molecule (290.8/293.0 eV) and surface contamination by airborne hydrocarbons (284.5 eV). This finding, coupled with the relatively high intensity of the F 1s peak (Figure 11 c) and Table 8), supports the effective grafting of PFOTES molecules onto the surface of the nanostructured SS. Additionally, the Si 2p spectrum of this sample in Figure 11 d) suggest the incorporation of Si-O and C-Si-O groups onto the surface during the functionalization process (note that the peak around 99 eV corresponds to

an overlap with the Fe 3s signal⁹⁸. Furthermore, the Fe 2p and Cr 2p photoelectron spectra indicated that the two primary metal components of SS, Fe and Cr, exhibited a similar oxidation state before and after corrosion testing as it is shown in **Figure 12**. Comparing values shown for SS-laser in Table 1 related to Cr/Fe ratio, lower values for this ratio were detected in Table 8. It could be due to different chemical heterogeneities for the fluorination strategies since the growth of SS nanostructures using AISI 301 commercial pellets exhibited Cr-Fe ratio values comparable to those of the pristine substrate⁴⁸.

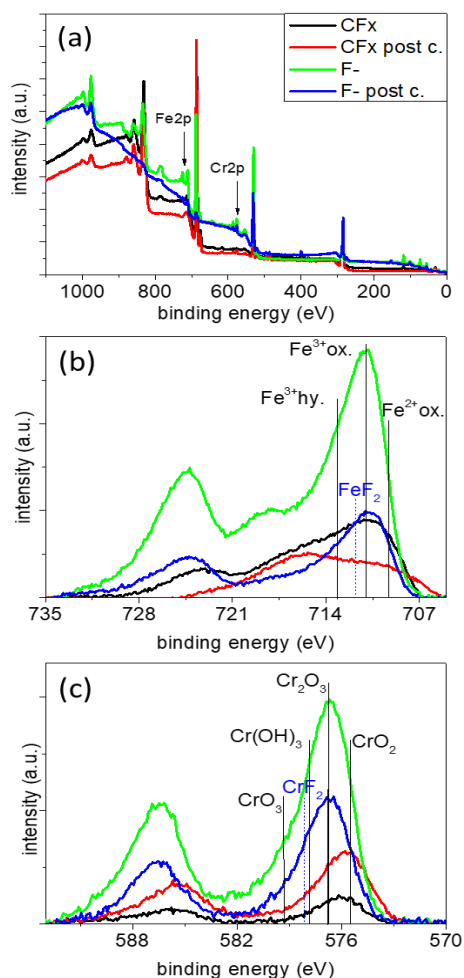


Figure 12. General survey a), Fe 2p b) and Cr 2p c) XPS spectra of fluorinated SS surfaces before and after the corrosion test.

Quantitative analysis (Table 8) revealed that the intensity of distinct photoemission signals roughly corresponds to the contribution of one silicon

atom (from the PFOTES molecule) per two Cr/Fe atoms at the surface of the fluorinated surfaces. However, this may not accurately reflect the true situation due to shadowing effects resulting from silicon and the anchoring oxygen atoms situated atop Cr/Fe atoms that could drastically reduce the spectral contribution of these elements. Consequently, the actual ratio is likely much lower, in the order of one silicon atom per 4/6 Cr/Fe atoms, respectively. In other words, one PFOTES molecule per 2-3 nm², equivalent to thirteen fluorine atoms per this surface area, a significantly lower amount of fluorine than that incorporated through fluorinated liquid immersion or the coating with a CF_x layer. A significant reduction in the fluorine content (refer to Table 8 and Figure 11 c)) and alterations in the C1s component at 284.5 eV should be attributed to carbon contamination, while the photopeak around 288 eV suggests carbonate-like or C-F bonded species. Confirmation by EDX revealed the presence of fluorine at the surface, primarily in the internal regions of the hierarchical stainless steel functional layer how it can be checked in **Table 9**.

Table 9. Atomic percentages determined by EDX analysis of the CF_x-, F- and SS-laser surfaces after the corrosion analysis compared to the SS substrate.

At.% (EDX)	C	O	F	Fe	Cr	Si	Ni	Mn
SS-laser (p.c.)	40.0	19.2	-	28.4	9.0	0.1	1.9	1.5
F/SS-laser (p.c.)	42.1	21.6	4.0	20.6	8.2	0.5	1.6	1.3
CF _x /SS-laser (p.c.)	36.8	13.3	23.0	16.3	6.6	-	0.8	0.5

All silicon contribution appeared oxidized after the corrosion test, evidenced by the Si 2p broad band centred at 102.0 eV⁹⁹. Additionally, the O 1s peak shifted to higher binding energy after corrosion, indicating the formation of oxyhydroxides (and carbonate in the case of sample F-70SS-laser) species at the surface¹⁰⁰. XPS analysis of samples subjected to the corrosion tests offers insights into the corrosion mechanisms in each case and the subsequent modification of their functional properties. In the case of CF_x-SS70-laser, the CF_x protecting layer appeared stable and largely unaffected on the surface, suggesting that corrosion primarily occurred beneath it and had a minimal impact on the functional wetting and icing properties. Conversely, sample F-70SS-laser exhibited the

highest pitting potential among the series (refer to Table 2), suggesting that the grafted PFOTES molecules confer a high chemical stability against corrosion to the SS. However, upon reaching the critical potential (E_c), XPS data indicate detrimental effects on the native oxide layers of the SS hierarchical surfaces and Si-O-Metals and F-C bonds of the grafted molecules. Consequently, it appears that some fluorine atoms remain on the surface, contributing to a certain passivation through the formation of stable (O)Fe-F or Cr-F bonds. Moreover, the formation of new Si-O-Cr (Fe) bonds may also contribute to this passivation process after reaching the high E_c potential during corrosion testing^{101,102}. Therefore, the loss of superhydrophobicity and the significant decrease in FD time observed in the sample F-70SS-laser after the corrosion test (refer to Figure 5 and Table 3) can be attributed to the partial removal of the grafted PFOTES molecules. However, the residual fluorination of the surface in the form of direct F-Metals bonds, along with the preserved hierarchical structure, appears sufficient to keep the repellence of this sample towards water and other liquids, as evidenced by Figure 5 b) and Table 7.

Overall, these results support the wide spectrum of functionalities offered by the fluorinated hierarchical SS surfaces developed in this study. Notably, their multifunctional character and robust performance in terms of anti-fouling, anti-icing, anti-corrosion or abrasion resistance properties stand out. While most literature focuses on one or another of these functionalities, few aim to address them simultaneously. A comparative analysis of these results from previous studies with respect to these achieved here using the hierarchical plus stable low fluorination approaches developed in this work, is shown in **Table 10**.

Table 10. Comparative analysis of multifunctional properties of low fluorinated hierarchical SS surfaces with those of the present work (reference numbers as used in the main text).

Surface config./processing	Wetting behavior	Other properties	Ref.
Spray-coating + dip coating / SS meshes 304SS	Superhydrophobic WCA ~160°	Selective wetting (Oil/water separation)	5
Femtosecond laser treatment + air aging / 316SSL	Superhydrophobic WCA ~160°	Anti-fouling(Ecoli counts decrease)	9
Fluorosilane coating/SiO₂NPs+silicone matrix/ 304SS	Superomniphobic CA ~160°	Anti-icing (supercooled droplets rolling off in cold environment - 18°C), wear resistance (100 cycles10mN), corrosion protection (1% HCl, 3 days)	19
Oil layer/ SAM-functionalized 316LSS	Hydrophobic WCA ~100°	Anti-fouling(E.coli adhesion reduction)	23
Fluoroalkylsilane coating / SiO₂NPS /nanosecond laser treatment/ SS316L	Superhydrophobic WCA ~150°	Wear resistance in water environment (5000 cycles at 5N)	28
N-alkylated PDMAEMA grafted-Polydopamine coating/SS304	Hydrophilic WCA	Anti-fouling (marine bacteria); anti-corrosion (0.5·10 ⁻⁶ A/cm ² , - 0.236V)	30
Perfluorinated lubricant oil/PFG grafted-APTES SAM/polydopamine coating/SS316L and SS304 SLIPS	Slippery–rolling off angle <3°	Anticoagulant and anti-fouling; anti-icing (40min at -5°C, tilted angle 10°, ice adhesion strength 12kPa at - 25°C)	44
Picosecond laser treatment + air aging /SiC sanded SS302	Superhydrophobic WCA ~160°	Abrasion resistance (4.7m at 5.5kPa), thermal stability (150min at 100°C), anti-icing (500min at -8.5°C)	58
Stearic acid coating/Zn coating/sandblasted SS SAE630/17-4	Superhydrophobic WCA~ 150°	Anti-icing (4.64x10 ⁶ s/kg at 15°C)	59
Femtosecond laser treatment + air aging/SS430	Superydrophobic WCA~149°	Anti-icing (363s at - 10°C, 60% area frost coverage at 50min)	60
SiO₂ powder/PDMS-PVDF coating/Sandblasted SS304	Superydrophobic WCA~160°	Anti-icing (46kPa at - 35°C)	94

F-grafting/SS nanocolumns/ nanosecond laser treatment/SS304	Superhydrophobic WCA~180° Omniphobic, DCA ~120°	Anti-fouling/self- cleaning (CA~180°);	This work
--	--	---	----------------------

4.4 Conclusions

The results have illustrated the efficient development of hierarchical SS surfaces through a method combining laser treatment of SS flat substrates with porous, thin film deposition using oblique angle evaporation. It is relevant to note that this technique for growing nanostructures with varying degrees of porosity has demonstrated excellent adhesion to the reference substrate. This enables the creation of hierarchical surfaces with well-integrated nanostructures that are compatible with the reference material, highlighting experiments on wetting responses with different liquids (anti-fouling) as well as the evaluation of ice adhesion strength for the first time within the research group where this work has been developed.

This approach has proven to be highly effective in achieving dual-scale roughness and showing different wetting and anti-freezing properties. Furthermore, we have demonstrated that low fluorination of such hierarchical surfaces confers specific functionalities, including superhydrophobicity, omniphobicity, self-cleaning, freezing delay, low ice adhesion, and efficient anti-fouling response. Notably, these functionalities are achieved with a relatively small amount of fluorine atoms incorporated into the samples, as compared to SLIPS produced by the infusion of fluorinated liquid Krytox. This superior performance, particularly evident in sample F-70SS-laser is attributed to the surface grafting of PFOTES molecules into the hierarchical surface structure of the sample, presenting values of WCA around 170° and FD times around 175 minutes. We propose that these fluorinated molecules preserve their free movement after anchorage to the surface, preventing water and other liquids wetting and the ice nucleation steps required for freezing. Good performance was also shown in the ice adhesion tests conducted in our universal machine, with values comparable to the Teflon reference in the case of K-70SS-laser, and values not exceeding 100 kPa for F-70SS-laser sample.

The repellence properties against various liquids, as well as the self-cleaning ability, have been demonstrated for these hierarchical metallic surfaces with different fluorinated strategies. High contact angle values with various bio-fouling simulants have been observed, highlighting the superomniphobicity of these systems and their self-cleaning capability with graphite powder and salt, being the best responses for CF_x -70SS-laser and F-70SS-laser samples.

These low fluorinated hierarchical surfaces remained stable even after 30 min of immersion in the biofouling fluids.

Regarding anti-corrosion properties, our findings indicate that fluorination can preserve or even enhance the corrosion resistance of hierarchical SS surfaces, particularly exemplified by the grafted sample F-70SS-laser which exhibited significantly higher potentials required to initiate the pitting process. Notably, wetting, anti-fouling, and anti-icing functionalities do not completely degrade after corrosion, likely due to the preservation of the hierarchical microstructure of the samples and the direct attachment of some fluorine atoms to their surface, thereby maintaining a certain hydrophobic character checked by wetting tests after corrosion experiments as well as SEM images and XPS characterization. Of particular interest is the observation that the CF_x coated hierarchical SS surface remained largely unaltered after corrosion test, thereby maintaining its functional properties. Collectively, these findings lead to the conclusion that nanostructuring and low fluorination procedures provide protection against corrosive and abrasive environments, while maintaining anti-fouling, anti-icing, and self-cleaning capabilities. The significant reduction in the incorporation of fluorine atoms into these materials represents an additional advantage of the experimental strategy developed here.

Bibliography

1. Hemmasian Etefagh, A., Guo, S. & Raush, J. Corrosion performance of additively manufactured stainless steel parts: A review. *Additive Manufacturing* vol. 37 (2021).
2. Fujiike, K., Kaneko, T. & Izaki, H. Product Development on Market Trend of Stainless Steel and Its Future Prospect. *Nippon Steel Technical Report* No. 99 (2010).
3. Lutey, A. H. A. *et al.* Towards laser-textured antibacterial surfaces. *Sci Rep* **8**, (2018).
4. Bobaru, S., *et al.* Electron beam evaporated vs. magnetron sputtered nanocolumnar porous stainless steel: Corrosion resistance, wetting behaviour and anti-bacterial activity. *Mater Today Commun* **31**, (2022).
5. Zhang, Z. H. *et al.* One-step fabrication of robust superhydrophobic and superoleophilic surfaces with self-cleaning and oil/water separation function. *Sci Rep* **8**, (2018).
6. Cremaldi, J. & Bhushan, B. Fabrication of bioinspired, self-cleaning superliquiphilic/phobic stainless steel using different pathways. *J Colloid Interface Sci* **518**, 284–297 (2018).
7. Tlili, B., Barkaoui, A. & Walock, M. Tribology and wear resistance of the stainless steel. The sol–gel coating impact on the friction and damage. *Tribol Int* **102**, 348–354 (2016).
8. Podgornik, B. & Hogmark, S. Surface modification to improve friction and galling properties of forming tools. *J Mater Process Technol* **174**, 334–341 (2006).
9. González S., A. *et al.* Functional Antimicrobial Surface Coatings Deposited onto Nanostructured 316L Food-Grade Stainless Steel. *Nanomaterials* **11**(4), 1055 (2021).
10. Maller R.R. Passivation of SS. *Trends in Food Science and Technology* **18**, 112–115 (2010).
11. Yuan, X., Wang, X., Cao, Y. & Yang, H. Natural passivation behavior and its influence on chloride-induced corrosion resistance of stainless steel in simulated concrete pore solution. *Journal of Materials Research and Technology* **9**, 12378–12390 (2020).
12. Liu, Y. *et al.* Effect of Pre-passivation on the Corrosion Behavior of PH13-8Mo Stainless Steel in Industrial—Marine Atmospheric Environment. *Front Mater* **6**, (2019).
13. Pérez, H., Vargas, G. & Silva, R. Use of Nanotechnology to Mitigate Biofouling in Stainless Steel Devices Used in Food Processing, Healthcare, and Marine Environments. *Toxics* **10**, 35 (2022).
14. Fihri, A., Bovero, E., Al-Shahrani, A., Al-Ghamdi, A. & Alabedi, G. Recent progress in superhydrophobic coatings used for steel protection: A review. *Colloids and Surfaces A: Physicochemical and Engineering Aspects* **520**, 378–390 (2017).
15. Wood, M. J., Brock, G., Debray, J., Servio, P. & Kietzig, A. M. Robust Anti-Icing Surfaces Based on Dual Functionality—Microstructurally-Induced Ice Shedding with Superimposed Nanostructurally-Enhanced Water Shedding. *ACS Appl Mater Interfaces* **14**, 47310–47321 (2022).
16. Rico, V. *et al.* Robust anti-icing superhydrophobic aluminum alloy surfaces by grafting fluorocarbon molecular chains. *Appl Mater Today* **21**, (2020).
17. Wasser, L. *et al.* Bio-inspired fluorine-free self-cleaning polymer coatings. *Coatings* **8**, (2018).
18. Long, Z. *et al.* A Durable Fluorine-Free MOF-Based Self-Cleaning Superhydrophobic Cotton Fabric for Oil-Water Separation. *Adv Mater Interfaces* **9**, (2022).
19. Huang, K. W., Huang, B. W., Chen, H. T., Lu, S. C. & Chen, H. H. Super-omniphobic surface prepared from a multicomponent coating of fluoro-containing polymer and silica nanoparticles. *Prog Org Coat* **173**, (2022).
20. Žemaitis, A. *et al.* Controlling the wettability of stainless steel from highly-hydrophilic to super-hydrophobic by femtosecond laser-induced ripples and nanospikes. *RSC Adv* **10**, 37956–37961 (2020).
21. Kim, A., Lee, C. & Kim, J. Durable, scalable, and tunable omniphobicity on stainless steel mesh for separation of low surface tension liquid mixtures. *Surf Coat Technol* **344**, 394–401 (2018).
22. Wang, L., Xing, Y., Liu, X., Zheng, H. & Song, J. Fabrication of Superhydrophobic Surfaces on Stainless Steel Mesh Substrates via Electro-brush Flow Plating Technology. in *Procedia CIRP* **68**, 232–236 (2018).

23. Resnik, M. *et al.* Strategies for improving antimicrobial properties of stainless steel. *Materials* **13**, (2020).
24. Arulvel S., Dsilva D., R., Jain, A., Kandasamy, J. & Singhal, M. Laser processing techniques for surface property enhancement: Focus on material advancement. *Surfaces and Interfaces* **42**, 103293 (2023).
25. Barati Darband, G., Aliofkhaezraei, M., Khorsand, S., Sokhanvar, S. & Kaboli, A. Science and Engineering of Superhydrophobic Surfaces: Review of Corrosion Resistance, Chemical and Mechanical Stability. *Arabian Journal of Chemistry* **13**, 1763–1802 (2020).
26. Sciancalepore, C., Gemini, L., Romoli, L. & Bondioli, F. Study of the wettability behavior of stainless steel surfaces after ultrafast laser texturing. *Surf Coat Technol* **352**, 370–377 (2018).
27. Kietzig, A. M., Hatzikiriakos, S. G. & Englezos, P. Patterned superhydrophobic metallic surfaces. *Langmuir* **25**, 4821–4827 (2009).
28. Gregorcic P. & Setina-Batic B. Controlling the stainless steel surface wettability by nanosecond direct laser texturing at high fluences. *Appl Phys A* **123**, 766-774 (2017).
29. Lee, B. S. *et al.* Engineering Antifouling and Antibacterial Stainless Steel for Orthodontic Appliances through Layer-by-Layer Deposition of Nanocomposite Coatings. *ACS Appl Bio Mater* **3**, 486–494 (2020).
30. Cao, P., Cao, Z. & Yuan, C. Stainless steel coated by Cu NPs via dopamine coupling for antifouling application. *Surface and Interface Analysis* **51**, 809–816 (2019).
31. Barish, J. A. & Goddard, J. M. Anti-fouling surface modified stainless steel for food processing. *Food and Bioproducts Processing* **91**, 352–361 (2013).
32. Bekmurzayeva, A., Duncanson, W. J., Azevedo, H. S. & Kanayeva, D. Surface modification of stainless steel for biomedical applications: Revisiting a century-old material. *Materials Science and Engineering C* **93**, 1073–1089 (2018).
33. Erdogan, Y. K. & Ercan, B. Anodized Nanostructured 316L Stainless Steel Enhances Osteoblast Functions and Exhibits Anti-Fouling Properties. *ACS Biomater Sci Eng* **9**, 693–704 (2023).
34. Zhang, H. *et al.* Durable microstructure-based superhydrophobic composite with photothermal performance for multifunctional application. *Prog Org Coat* **197**, 108764 (2024).
35. Xue, X., Zhang, J., Sun, X. & Zhang, B. Facile spraying prepared superhydrophobic coating with self-cleaning, corrosion resistance, and increased buoyancy. *Mater Today Commun* **40**, 109689 (2024).
36. Krishnan, A., Krishnan, A. V., Ajith, A. & Shibli, S. M. A. Influence of materials and fabrication strategies in tailoring the anticorrosive property of superhydrophobic coatings. *Surfaces and Interfaces* **25**, 101238 (2021).
37. Pendurthi, A. *Thesis Fabrication of Omniphobic and Superomniphobic Surfaces Submitted By.* (2017).
38. Bekmurzayeva, A., Duncanson, W. J., Azevedo, H. S. & Kanayeva, D. Surface modification of stainless steel for biomedical applications: Revisiting a century-old material. *Materials Science and Engineering C* **93**, 1073–1089 (2018).
39. Emelyanenko, K. A., Emelyanenko, A. M. & Boinovich, L. B. Laser Obtained Superhydrophobic State for Stainless Steel Corrosion Protection, a Review. *Coatings* **13**, 194 (2023).
40. Barranco, A., Borrás, A., Gonzalez-Elipe, A. R. & Palmero, A. Perspectives on oblique angle deposition of thin films: From fundamentals to devices. *Prog Mater Sci* **76**, 59–153 (2016).
41. Rico, V. J. *et al.* Hydrophobicity, Freezing Delay, and Morphology of Laser-Treated Aluminum Surfaces. *Langmuir* **35**, 6483–6491 (2019).
42. Kim, A., Lee, C. & Kim, J. Durable, scalable, and tunable omniphobicity on stainless steel mesh for separation of low surface tension liquid mixtures. *Surf Coat Technol* **344**, 394–401 (2018).
43. Pendurthi, A. *et al.* Supporting Information Fabrication of Nanostructured Omniphobic and Superomniphobic Surfaces with Inexpensive CO₂ Laser Engraver. *ACS Appl Mater. Interfaces* **9**, 25656-25661 (2017).

44. Li, S. *et al.* Slippery liquid-infused microphase separation surface enables highly robust anti-fouling, anti-corrosion, anti-icing and anti-scaling coating on diverse substrates. *Chemical Engineering Journal* **431**, (2022).
45. Basu, S. *et al.* Laboratory and Field Testing Assessment of Next Generation Biocide-Free, Fouling-Resistant Slippery Coatings. *ACS Appl Polym Mater* **2**, 5147–5162 (2020).
46. Guo, C. *et al.* Multifunctional superamphiphobic fluorinated silica with a core-shell structure for anti-fouling and anti-corrosion applications. *Colloids Surf A Physicochem Eng Asp* **615**, (2021).
47. Sanchez-Cano, C. & Carril, M. Recent developments in the design of non-biofouling coatings for nanoparticles and surfaces. *International Journal of Molecular Sciences* **21**, 1007 (2020).
48. *Properties and Selection: Irons, Steels, and High-Performance Alloys.* (ASM International, 1990).
49. Sreeramagiri, S. V. Biomimetics: Applications in Structural Design an overview Biomimetics: Applications in Structural Design. *International Journal of Innovative Research in Science, Engineering and Technology* **10**, 1478-1486 (2021).
50. Blackstock, J. J. *et al.* Ultraflat Carbon Film Electrodes Prepared by Electron Beam Evaporation. *Anal Chem* **76**, 2544–2552 (2004).
51. Pakman Y., *et al.* Tunable hydrophilicity in a surface nano-textured stainless steel thin film deposited by DC magnetron sputtering. *Appl Surf Sci* **30**, 149705 (2021).
52. Terriza, A. *et al.* C-C4F8 plasmas for the deposition of fluorinated carbon films. *Plasma Processes and Polymers* **11**, 289–299 (2014).
53. Horcas, I. *et al.* WSXM: A software for scanning probe microscopy and a tool for nanotechnology. *Review of Scientific Instruments* **78**, (2007).
54. Bousser, E., Martinu, L. & Klemberg-Sapieha, J. E. Solid particle erosion mechanisms of protective coatings for aerospace applications. *Surf Coat Technol* **257**, 165–181 (2014).
55. Huang, X. *et al.* A survey of icephobic coatings and their potential use in a hybrid coating/active ice protection system for aerospace applications. *Progress in Aerospace Sciences* **105**, 74–97 (2019).
56. Ruan, H. *et al.* Preparation and characterization of an amphiphilic polyamide nanofiltration membrane with improved antifouling properties by two-step surface modification method. *RSC Adv* **8**, 13353–13363 (2018).
57. Edyvean, R. G. J. & Videla, H. A. Biological Corrosion. *Interdisciplinary Science Reviews* **16**, 267–282 (1991).
58. Sales, W. F., Schoop, J., da Silva, L. R. R., Machado, Á. R. & Jawahir, I. S. A review of surface integrity in machining of hardened steels. *J Manuf Process* **58**, 136–162 (2020).
59. Li, L., Breedveld, V. & Hess, D. W. Creation of superhydrophobic stainless steel surfaces by acid treatments and hydrophobic film deposition. *ACS Appl Mater Interfaces* **4**, 4549–4556 (2012).
60. Sciancalepore, C., Gemini, L., Romoli, L. & Bondioli, F. Study of the wettability behavior of stainless steel surfaces after ultrafast laser texturing. *Surf Coat Technol* **352**, 370–377 (2018).
61. Jung, R. H., Tsuchiya, H. & Fujimoto, S. XPS characterization of passive films formed on Type 304 stainless steel in humid atmosphere. *Corros Sci* **58**, 62–68 (2012).
62. Guo, L. Q., Qin, S. X., Yang, B. J., Liang, D. & Qiao, L. J. Effect of hydrogen on semiconductive properties of passive film on ferrite and austenite phases in a duplex stainless steel. *Sci Rep* **7**, (2017).
63. Elsener, B., Addari, D., Coray, S. & Rossi, A. Nickel-free manganese bearing stainless steel in alkaline media - Electrochemistry and surface chemistry. *Electrochim Acta* **56**, 4489–4497 (2011).
64. Welch, R. H. & Speliotis, D. E. Oblique Incidence Evaporated Iron Films. *J Appl Phys* **41**, 1254–1256 (1970).
65. Kivaisi, R. T. Optical properties of obliquely evaporated aluminium films. *Thin Solid Films* **97**, 153–163 (1982).

66. Karabacak, T., Wang, G.-C. & Lu, T.-M. Physical self-assembly and the nucleation of three-dimensional nanostructures by oblique angle deposition. *Journal of Vacuum Science & Technology A: Vacuum, Surfaces, and Films* **22**, 1778–1784 (2004).
67. Muñoz-Piña, S. *et al.* Thin film nanostructuring at oblique angles by substrate patterning. *Surf Coat Technol* **436**, (2022).
68. Vu, H. H., Nguyen, N. & Kashaninejad, N. Re-Entrant Microstructures for Robust Liquid Repellent Surfaces. *Adv Mater Technol* **8**, (2023).
69. Burkert, A., Klapper, H. S. & Lehmann, J. Novel strategies for assessing the pitting corrosion resistance of stainless steel surfaces. in *Materials and Corrosion* vol. **64** 675–682 (2013).
70. Dhaiveegan, P., Elangovan, N., Nishimura, T. & Rajendran, N. Corrosion behavior of 316L and 304 stainless steels exposed to industrial-marine-urban environment: Field study. *RSC Adv* **6**, 47314–47324 (2016).
71. Husain, E. *et al.* Corrosion behavior of AISI 316 stainless steel coated with modified fluoropolymer in marine condition. *J Coat Technol Res* **15**, 945–955 (2018).
72. Miki N., Maeno M., *et al.* Fluorine Passivation of Metal Surface for Self-Cleaning Semiconductor Equipment. *IEEE Transactions on Semiconductor Manufacturing* **3**, (1990).
73. Terriza, A. *et al.* Roughness assessment and wetting behavior of fluorocarbon surfaces. *J Colloid Interface Sci* **376**, 274–282 (2012).
74. Barish, J. A. & Goddard, J. M. Anti-fouling surface modified stainless steel for food processing. *Food and Bioproducts Processing* **91**, 352–361 (2013).
75. Deng, R. *et al.* Slippery liquid-infused porous surfaces (SLIPSs): A perfect solution to both marine fouling and corrosion? *Journal of Materials Chemistry A* **8**, 7536–7547 (2020).
76. Xu, S., Wang, Q. & Wang, N. Chemical Fabrication Strategies for Achieving Bioinspired Superhydrophobic Surfaces with Micro and Nanostructures: A Review. *Adv Eng Mater* **23**, 1–21 (2021).
77. Sui, R., Zhang, G. & Liu, H. Anti-Fouling Behaviors of a Modified Surface Induced by an Ultrasonic Surface Rolling Process for 304 Stainless Steel. *Coatings* **13**, (2023).
78. Tesler, A. B. *et al.* Extremely durable biofouling-resistant metallic surfaces based on electrodeposited nanoporous tungstite films on steel. *Nat Commun* **6**, (2015).
79. Zouaghi, S. *et al.* Antifouling Biomimetic Liquid-Infused Stainless Steel: Application to Dairy Industrial Processing. *ACS Appl Mater Interfaces* **9**, 26565–26573 (2017).
80. Conradi, M., Drnovšek, A. & Gregorčič, P. Wettability and friction control of a stainless steel surface by combining nanosecond laser texturing and adsorption of superhydrophobic nanosilica particles. *Sci Rep* **8**, (2018).
81. Gohardani, O. Impact of erosion testing aspects on current and future flight conditions. *Progress in Aerospace Sciences* **47**, 280–303 (2011).
82. Meuler, A. J. *et al.* Relationships between water wettability and ice adhesion. *ACS Appl Mater Interfaces* **2**, 3100–3110 (2010).
83. Tourkine, P., Merrer, M. Le & Quéré, D. Delayed freezing on water repellent materials. *Langmuir* **25**, 7214–7216 (2009).
84. Jian, Y., Gao, H. & Yan, Y. Fabrication of a superhydrophobic micron-nanoscale hierarchical structured surface for delayed icing and reduced frosting. *Surfaces and Interfaces* **34**, 102353 (2022).
85. Vercillo, V. *et al.* Durability of superhydrophobic laser-treated metal surfaces under icing conditions. *Materials Letters: X* **3**, 100021 (2019).
86. Boinovich, L. B., Emelyanenko, A. M., Ivanov, V. K. & Pashinin, A. S. Durable icephobic coating for stainless steel. *ACS Appl Mater Interfaces* **5**, 2549–2554 (2013).
87. Moon, C. H. *et al.* Icephobic Coating through a Self-Formed Superhydrophobic Surface Using a Polymer and Microsized Particles. *ACS Appl Mater Interfaces* **14**, 3334–3343 (2022).
88. Peleka, E. N. & Matis, K. A. Water separation processes and sustainability. *Ind Eng Chem Res* **50**, 421–430 (2011).
89. Heydari, G. *et al.* Wetting hysteresis induced by temperature changes: Supercooled water on hydrophobic surfaces. *J Colloid Interface Sci* **468**, 21–33 (2016).

90. Heydari, G., Thormann, E., Järn, M., Tyrode, E. & Claesson, P. M. Hydrophobic surfaces: Topography effects on wetting by supercooled water and freezing delay. *Journal of Physical Chemistry C* **117**, 21752–21762 (2013).
91. He, Z., Zhuo, Y., Zhang, Z. & He, J. Design of icephobic surfaces by lowering ice adhesion strength: A mini review. *Coatings* **11**, 1343 (2021).
92. Memon, H., Wang, J. & Hou, X. Interdependence of Surface Roughness on Icephobic Performance: A Review. *Materials* **16**, 4607 (2023).
93. Kreder, M. J., Alvarenga, J., Kim, P. & Aizenberg, J. Design of anti-icing surfaces: Smooth, textured or slippery? *Nature Reviews Materials* vol. **1**, 15003 (2016).
94. Bhushan B. & Multanen V. Designing liquid repellent, icephobic and self-cleaning surfaces with high mechanical and chemical durability. *R Soc A* **377**, 20182770 (2018).
95. Gregorčič, P. Wettability and friction control of a stainless steel surface by combining nanosecond laser texturing and adsorption of superhydrophobic nanosilica particles. *Sci Rep* **8**, (2018).
96. Wang, H., He, M., Liu, H. & Guan, Y. One-Step Fabrication of Robust Superhydrophobic Steel Surfaces with Mechanical Durability, Thermal Stability, and Anti-icing Function. *ACS Appl Mater Interfaces* **11**, 25586–25594 (2019).
97. Sanchez-Cano, C. & Carril, M. Recent developments in the design of non-biofouling coatings for nanoparticles and surfaces. *International Journal of Molecular Sciences* **21**, Preprint (2020).
98. Song, Y. *et al.* The influence of surface structure on H₄SiO₄ oligomerization on rutile and amorphous TiO₂ surfaces: An ATR-IR and synchrotron XPS study. *Langmuir* **28**, 16890–16899 (2012).
99. Riabov, D., Rashidi, M., Hryha, E. & Bengtsson, S. Effect of the powder feedstock on the oxide dispersion strengthening of 316L stainless steel produced by laser powder bed fusion. *Mater Charact* **169**, (2020).
100. El-Katori, E. E., Nessim, M. I., Deyab, M. A. & Shalabi, K. Electrochemical, XPS and theoretical examination on the corrosion inhibition efficacy of stainless steel via novel imidazolium ionic liquids in acidic solution. *J Mol Liq* **337**, (2021).
101. Shinonaga, Y. & Arita, K. Surface modification of stainless steel by plasma-based fluorine and silver dual ion implantation and deposition. *Dent Mater J* **28**, 735–742 (2009).
102. Miki, N., Maeno, M., Maruhashi, K., Nakagawa, Y. & Ohmi, T. Passivation of SS. *Corrosion Science* vol. 31 (1990).



“Somewhere, something incredible is waiting to be discovered.”

(Carl Sagan)

5

Superhydrophobic, anti-fogging and anti-icing transparent glass surfaces prepared by laser patterning and low fluorination

Abstract

This work addresses the fabrication of transparent glass surfaces with outstanding water-repellence (i.e., superhydrophobicity), and related functional properties, mainly omniphobicity and anti-icing responses. These surfaces have been obtained by means of mild femtosecond laser treatments combined with low fluorinated surface functionalization. A fine control of the pattern design and surface roughness can be achieved tuning the laser overlapping and lateral distances of the marked grooves. A compromise between laser parameters and topography design makes compatible a high transparency with water repellence over large glass plates of around 10 cm x 5 cm. This is demonstrated for square pattern with grooves separated by 50 μm or parallel line pattern of 100 μm , which present a stable Cassie-Baxter state, a very low ice-adhesion strength and a 70-80% total transmittance depending on the surface pattern. This laser patterned glass was also prone to be infiltrated with a transparent lubricant liquid to fabricate SLIP surfaces with an even higher transmittance and remarkable anti-icing properties. Anti-fouling tests, as well as freezing/thawing cycles have revealed the notable self-cleaning and durable anti-icing capacities of the developed transparent surfaces. Water condensation experiments under controlled environments and in an environmental microscope have unraveled key issues about the formation and slippery of supercooled water droplets on the superhydrophobic patterned surfaces, showing that the continuity breakdown of surface properties due to the patterned grooves is key to prevent fogging and water accumulation on the surface for low temperature applications.

5.1 Introduction

Glass is a universal material, which was invented and manufactured since the antique times, that has been continuously growing in applications and demand for new properties. Its modern use for window walls and display lids relies on its high transparency, chemical and environmental resistance and the capacity of modern industry to prepare it in the form of large area laminates. Moreover, the functionalization of glass with the incorporation of protective, conductive, anti-reflective, low-emissive or self-cleanable coatings has added specific functionalities that have opened wide fields of application in many industrial sectors, including energy, construction, communication, and electronics. Unlike specifically coated glasses, bear glass laminates are partially hydrophilic and as such rather prone to become covered with ice, fog or fouling agents, events that suppose clear limitations for the transparency and prolonged cleanness of architectural glass, photovoltaic panels, or optical systems working in the exterior. In this context, control of wetting properties of glass is of paramount importance and a topic of maximum interest for many industrial applications.

For non-transparent materials such as metals¹, ceramic² or even polymers³, surface modification procedures are already in place to transform their surface into hydrophobic or superhydrophobic and bestow them with specific anti-stain⁴, water repellent⁵ or anti-icing properties⁶. These procedures usually entail the surface texturing and/or roughening of the materials accompanied by the modification of their surface chemical composition, both strategies aiming at achieving a superhydrophobic and omniphobic state. However, these surface modifications inevitably produce a change in optical properties, which in the case of glass can degrade its transparency due to light scattering and, therefore, preclude their use for key applications.

Addressing this problem, recent works have proposed the application of laser as a method to create surface roughness and topographic texturing to confer specific wetting and anti-icing functionalities to the surfaces of treated materials^{7,8,9}. The wetting properties and the transformations from hydrophilic to hydrophobic experienced by the treated surfaces exposed to the ambient atmosphere have been usually discussed in terms of Wenzel and Cassie-Baxter wetting regimes. It has been also reported that a way of stabilizing a hydrophobic or superhydrophobic state in these materials consists of the surface grafting of tethered molecules on these lasers treated surfaces^{8,9,10,11}. Therefore, similar

procedures relying on laser texturing to control wetting and icephobic properties have been also proposed for glass^{12,13}. However, in these previous investigations little or no attention has been paid to the possible modifications of optical properties, the most widely topic of investigation when talking at fundamental level about glass-laser interactions^{14,15,16}.

In the present work we propose a specific procedure based on the femtosecond laser patterning of borosilicate glass combined with the grafting of fluorinated molecules to confer superhydrophobicity, anti-icing and anti-fouling properties, as well as anti-fogging potential (i.e. tailor the water condensation behavior on the surface) to this material, while preserving the maximum transparency into the visible spectral range. The borosilicate glass composition includes silicon dioxide (SiO_2) in a range from about 60% to 74% by total composition weight; boric oxide (B_2O_3) in a range from about 9% to 25% by total composition weight; and aluminium oxide (Al_2O_3) in a range from about 7% to 17% by total composition weight. B_2O_3 is one of the reasons for the better chemical stability of borosilicate glass compared to soda-lime, which has been commercially used for a long time^{17,18}, making it less susceptible to sudden temperature changes. Another reason for choosing borosilicate glass in this work is its lower thermal expansion¹⁷ compared to soda-lime¹⁹, reducing the risk of thermal fractures since it will be employed in laser processing. The work provides a critical assessment of the influence of the pattern motifs, size and geometry on both optical and wetting properties, i.e. the surface interactions with water (liquid, ice, and vapor), and biological simulants. In addition, it carries out a critical analysis of the possibilities of laser-based procedures to induce specific surface functionalization of glass without significantly altering its transparency.

5.2 Experimental Section

5.2.1 Materials and samples preparation

Borofloat®33 (VIDRASA S.A.), a floated borosilicate flat glass, was used such as transparent substrate. Borosilicate glass plates have been used rather than soda-lime glass because the superior mechanical strength and reduced thermal stress of the former that make it easier its handling and treatment with a laser beam as previously indicated. Plates of these substrates with dimensions 10 cm x 5 cm were cleaned using detergent water solutions, isopropanol and a N_2 dry flow. Laser

patterns were generated with a femtosecond (fs) laser (Carbide model, Light Conversion, Lithuania), using its third harmonic (UV range) at 343 nm. At the working distance, the laser beam exhibited a spatially Gaussian energy profile with an elliptical spot, where $1/e^2$ beam dimensions were $2a = 60 \mu\text{m}$ (long semi-axis) and $2b = 36 \mu\text{m}$ (short semi-axis) (**Figure 1**). This laser offers the possibility of using a Pulse Peak Divider (PPD) option to reduce the effective frequency of the laser treatment. The following working conditions were used for the treatments: 6.07 W laser power, 200 kHz oscillator frequency, 10 kHz effective frequency, 25 mm/s laser scan rate, and 238 fs pulse duration inspired by the previous work where laser parameters were optimized to generate superhydrophobicity on aluminum alloy surfaces²⁰. With these laser processing parameters, the energy per pulse is $30.35 \mu\text{J}/\text{pulse}$. Two hatching configurations were tested consisting of cross and lines varying the distance between scanning lines from $10 \mu\text{m}$ to $500 \mu\text{m}$. Considering that the laser scanning speed is the same in both directions, when the laser scans parallel to the $2b$ semi-axis, the maximum fluence at the centre of the line is $53.55 \text{ J}/\text{cm}^2$, while when the laser scans parallel to the $2a$ semi-axis, the overlapping between consecutive pulses is lower and the maximum fluence is reduced to $32.13 \text{ J}/\text{cm}^2$. For some testing experiments, the laser scanning protocol has been repeated from 1 to 5 times.

Laser treated borosilicate surfaces were functionalized by the grafting of 1H,1H,2H,2H-Perfluoro-octyltriethoxysilane 98% (PFOTES) molecules following the procedure described in Chapter 2 (Figure 1).

Borosilicate samples used as reference have been designated as *glass ref.*, and the laser treated samples have been identified according to the following labeling: laser cross and line patterned surfaces as *C-distance* and *L-distance*, respectively, where *distance* expressed in microns refers to the distance between centres of contiguous laser scanned lines; and with *F-glass*, *F-C-distance* and *F-L-distance*, where *F* refers to the low fluorination treatment. This labeling assumed that the laser scanning process was repeated five times. When for specific experiments the number of laser scans was a relevant experimental parameter, it has been added to the previous labeling as (*x number*). For example, *F-C-100 (x3)* means a sample with a fluorinated square pattern and lines separated by $100 \mu\text{m}$ repeating the laser protocol three times to mark the grooves. Finally, the *K-C/L-distance* label designates an infiltrated patterned surface with a fluorinated lubricant: Krytox

(refractive index around 1.296-1.301) according to the procedure described in Chapter 2.

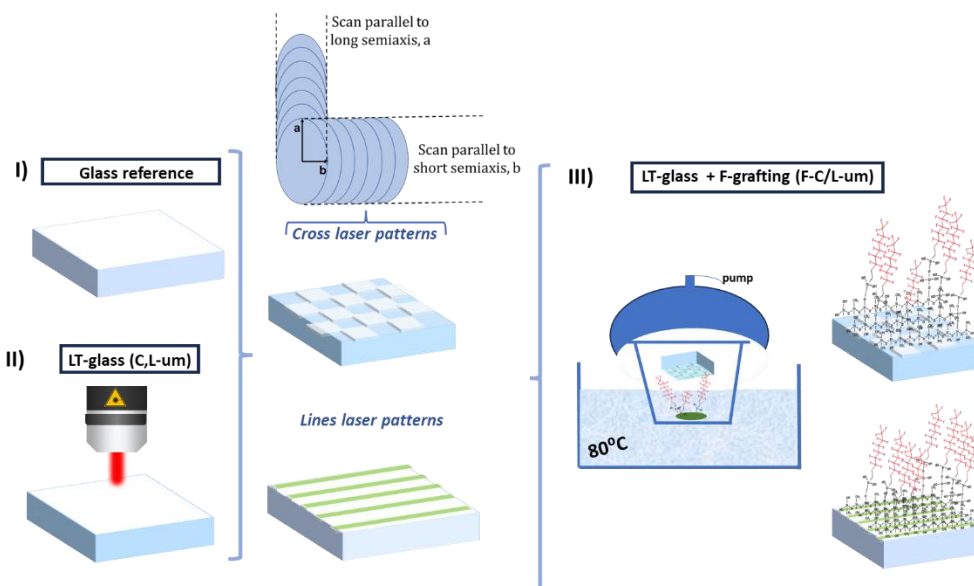


Figure 1. Main scheme of the steps to achieve fluorinated laser processed glass substrates: I) cleaning of the pristine glass; II) gentle laser treatment to generate square or parallel line patterns including a representation of the two scanning directions along the long and the short elliptical semi-axes of the laser spot; III) laser patterned surface grafting with perfluorinated molecules.

5.2.2 Surface characterization

Surface morphology of reference and laser treated samples was examined by confocal (Sensofar PL μ 2300) and scanning electron microscopes (SEM, Hitachi S4800) detailed in Chapter 2. Width and depths of the patterned surfaces were estimated as an average over 3 different measurements. The optical properties of the modified glasses were determined in transmission mode in the UV-vis-nIR range between 200 and 900 nm using a Perkin Elmer Lambda 750 spectrometer equipped with a 60 mm diameter integrative sphere.

ImageJ was used for the calculation of the percentage of laser treated surface, with distance between laser patterns varying from 10 to 500 μm , and the laser trace depends on scanning parallel to the short semiaxis or to the long semiaxis, being 37 μm and 25 μm respectively, for the surface treatment with 5 laser cycles. The, the area of treated surface was normalized to 1 cm^2 , according to the width and number of squares or lines for each laser pattern.

5.2.3 Wetting properties

Wetting properties were measured with the sessile droplet method in an OCA 20 DataPhysics Instruments (described in Chapter 2), depositing different volumes (2 μl for CA and 15 μl for RoA) of bi-distilled water and different organic liquids on the surface. The reported data are an average on a minimum of 10 experimental values per surface. Microliter droplets were obtained by controlling the dose rate through the electronic component and syringe, DS500/GT, provided with a 0.5 mm diameter needle (more detailed in Chapter 2). The organic liquids used as fouling simulants for wetting analysis were humic acid, sodium alginate and bovine serum (Sigma Aldrich).

Water condensation experiments were carried out in an OCA 25 DataPhysics environmental chamber provided with a temperature control modulus, and a humidity generator (described in Chapter 2). Monitoring was possible thanks to a high-resolution side and a front optical cameras. From a microscaled point of view, water condensation was also characterized in an Environmental Scanning Electron Microscope (ESEM) (Quanta FEG250 system from FEI and Thermofisher QuattroS) by placing the sample on the top of a thermoelectric modulus while the environmental water vapor pressure is controlled. The temperature stabilized at 2 $^{\circ}\text{C}$ and the water condensation was monitored as a function of water vapor pressure (Figure 8 in Chapter 1) under the continuous electron beam scanning.

5.2.4 Icing tests

Freezing Delay Time (FDT) measurements were carried out in the OCA 20 DataPhysics system thanks to a controlled environmental chamber, monitoring the water droplet deposited on the top of the cold surface during the icing process. The surface temperature stabilized with a thermoelectric modulus and was tracked with a thermocouple placed on the surface at 1 mm from the water droplet. To perform the freezing experiments, a flow of dry nitrogen (~ 10 sscm) was cooled at 0 $^{\circ}\text{C}$ before passing through the chamber (details in Chapter 2). A 2 μl water droplet was deposited on the surface at 25 $^{\circ}\text{C}$ and then the temperature was decreased to a fixed value of -10 $^{\circ}\text{C}$ with a variation ramp of -1 $^{\circ}\text{C}/\text{s}$ until 0 $^{\circ}\text{C}$ and -0.1 $^{\circ}\text{C}/\text{s}$ for subzero temperature.

Ice adhesion tests were carried out by the pull-off method described in Chapter 2. The pull-off adhesion experiment was performed inside the Universal Material Testing Machine at $-13\text{ }^{\circ}\text{C}$. The applied force perpendicular to the sample (tensile mode) required to detach the ice block was determined by the dynamometer. The adhesion strength was obtained by normalization of this force to the area of the ice cylinder and expressed in units of MPa (N/m^2).

5.3 Results and discussion

5.3.1 Control of surface morphology by laser patterning

Tuning the laser parameters allows the development of regular replicas of surface motifs over large transparent surface areas ($10\text{ cm} \times 5\text{ cm}$) with reproducible size and depth at the microscale. Particularly, the width and separation distance between motifs, as well as the laser overlapping and scanning direction, have been the main process variables optimized in this work for the generation of a hydrophobic surface state. The first parameter of the laser treatment directly related to the wetting response of glass is the distance between the pattern motifs^{21,22}. **Figure 2** shows the confocal images for the obtained pattern designs: parallel lines and asymmetric square micropillars resulting from laser cross-scans in normal directions. For each pattern design, configurations with different sizes/distances have been tested. To ensure a good definition and reproducibility of the groove depth and width, laser scanning process was repeated up to five times. Figure 2 a)-d) correspond to a selection of images of the *L-50/100* and *C-50/100* samples obtained after the fifth repetitions. Otherwise, differences in the groove depths were obtained as a function of the number of repetitions as exemplified in Figure 2 e)-h) for sample *C-100*.

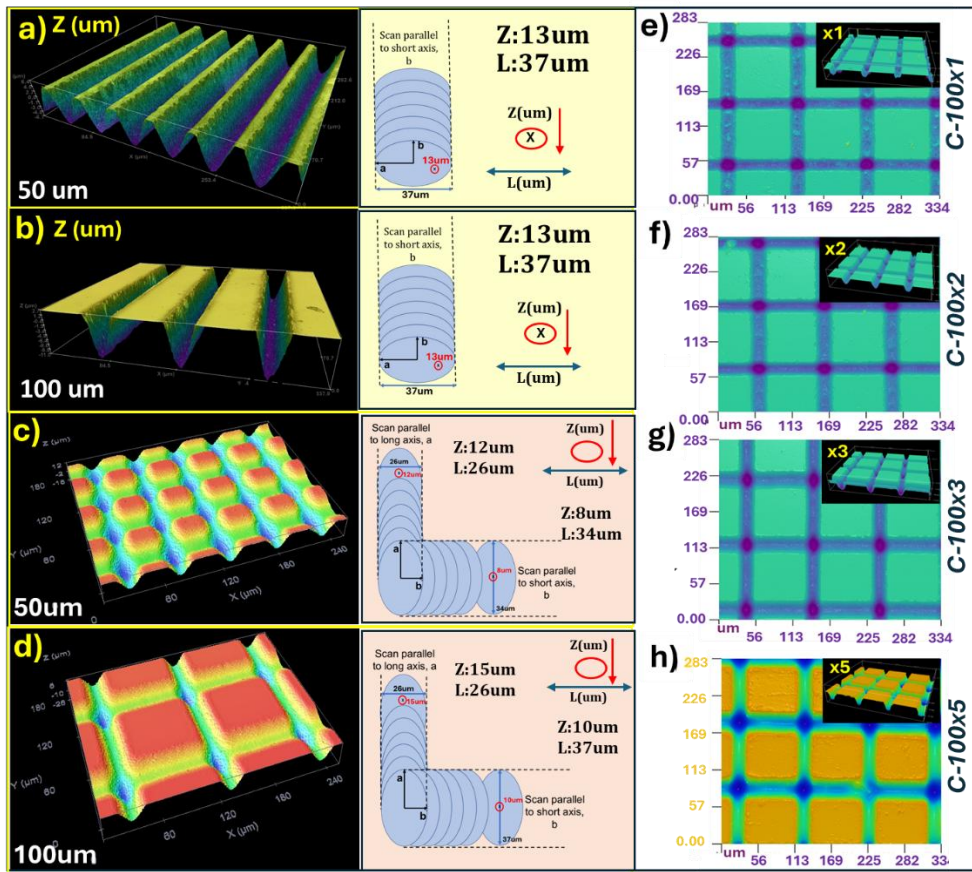


Figure 2. 3D maps by confocal microscopy: a), b) L-50/100 samples, c), d) C-50/100 samples, respectively, where depth and width are indicated for each laser direction (a and b long and short semi-axes); e)-h) 2D maps (arbitrary colour scale bar) for sample C-100 varying the number of laser repetitions from 1 to 5.

In the case of *L* samples, the laser scan direction was parallel to the long laser beam axis, $2b$. Regular grooves of $13 \mu\text{m}$ depth and $37 \mu\text{m}$ width are obtained by the laser line patterning after 5 repetitions, where a subsequent scan over a previously treated region increases the energy absorption. However, for the case of *C* samples, a similar topography is obtained when equivalent lines are machined, while in the perpendicular direction, that is when the scanning is parallel to the long axis $2a$, the accumulated laser fluence is higher and, after five repetitions, grooves of smaller width, i.e. $26 \mu\text{m}$ (laser spot diameter is around $25 \mu\text{m}$) and depths around $12\text{-}15 \mu\text{m}$ depending on the separation between motifs, were induced. Figure 2 e)-h) evidence that, although square motifs preserve their dimensions ($\sim 74 \mu\text{m} \times 63 \mu\text{m}$ for $100 \mu\text{m}$ of laser groove

separation), it is under 5 repetitions when the anisotropic dimensions between laser scanning normal directions becomes more significant, especially for scratched depths. As can be seen in **Figure 3**, the lines marked in the direction parallel to the short laser beam semiaxis resulted in grooves with larger width and lower depth, whereas the grooves generated in the normal direction present smaller width values and similar or even slightly higher depths. Z ablation depth is not considerably affected by the distance between lines or motifs when five laser scans are applied to draw the grooves. However, groove depth and width were quite dependent on the number of scans varying from 1 to 5 repetitions, as it is observed in Figure 3 and **Table 1**.

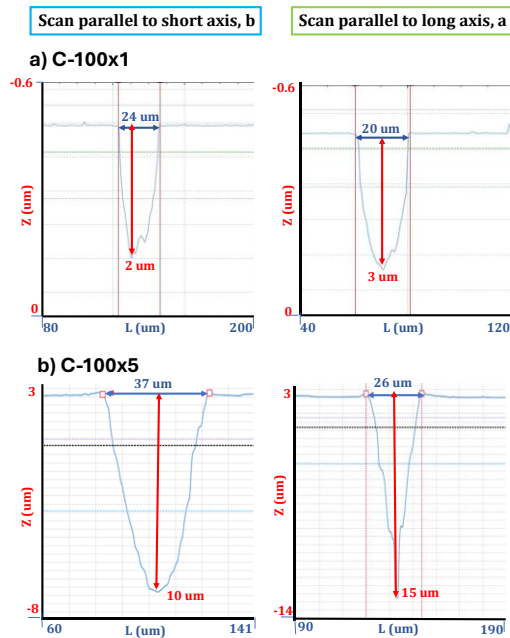


Figure 3. Confocal topographical profiles for the C-100 pattern a) from scan parallel to the long and short laser spot axis with a) 1 repetition and b) 5 repetitions. (Different values in the scales have presented since the images shown were taken from the confocal microscope software).

This is consequence of the elliptical shape of the laser beam, making that the depth and width of the grooves vary from 24 μm to 37 μm or from 20 μm to 26 μm and from 2 μm to 10 μm or from 3 μm to 15 μm when the laser scanning was applied in along the short or long axis and increased number of repetitions, respectively.

Table 1. Different widths and depths for different laser treatment repetitions for the C-100 sample.

Patterned surfaces	Scan parallel to short axis laser, b		Scan parallel to long axis laser, a	
	Width (L) (μm)	Depth (Z) (μm)	Width (L) (μm)	Depth (Z) (μm)
C-100x1	24	2	20	3
C-100x2	26	5	23	5
C-100x3	28	8	24	8
C-100x5	37	10	26	15

For this C-100 sample, there is not a significant difference between the depth of grooves generated in both scanning directions, since the material begins to melt and being micro-/nano-structured gradually with each additional repetition, which causes much of the fluence to be absorbed in the melted laser material rather than cutting to a greater depth. Therefore, it is after 5 repetitions when notable changes in roughness and the appearance of micro-/nano- structures are achieved, as will be presented below.

Therefore, the overall effect of the laser treatment is that the original flat glass surface in a patterned surface, regular or anisotropic, where flat regions coexist with the laser textured grooves. In the course of this investigation, it has been indicated that rather than average roughness, a relevant parameter to correlate optical and wetting properties of the patterned surfaces is the percentage of treated surface with the laser and that therefore is occupied by the grooves²⁰. The estimated percentages of laser-treated glass surface over 1 cm x 1 cm are presented in **Table 2**. For 10 μm and 25 μm, the smaller separations between laser pattern motifs, there is no practically untreated flat areas remaining on the glass. This must be attributed to the overlapping of the grooves corresponding to two adjacent lines caused by the laser spot size limitation. For higher separations, L-50 and L-100, laser treated surface percentages reach 50% and 25%, whereas higher values of 87% and 53% were maintained for the samples C-50 and C-100, respectively. Treated surface area percentages decreased drastically for larger line distances up to 500 μm both for C- and, particularly L-samples.

Table 2. Laser treated surface area percentage values normalized to a 1 cm² for different laser patterned glass surfaces after having repeated the process 5 times.

Lines (L-) / Cross (C-) samples x5	Laser-treated surface percentage (%)
L-10	100
L-25	100
L-50	50
L-100	25
L-200	13
L-300	9
L-500	5
C-10	100
C-25	100
C-50	87
C-100	53
C-200	29
C-300	19
C-500	12

At this point, it is clear than for the same distance between grooves, in C- samples the percentage of laser treated surface area has been always higher than in L- samples. Rivera-Saun et al.²⁰ have found that 200 μm distance between consecutive lines minimized thermal interaction working at low frequency which is established as a threshold from which the percentage of treated surface decreases drastically.

Laser processing parameters affect also the surface roughness. Results presented in **Table 3** have been obtained by confocal microscopy measurements over a 283 μm x 334 μm scanned area, expressed in terms of the arithmetical mean heigh (S_a) and root mean square height (S_q) roughness parameters.

Table 3. Roughness parameters of the laser treated glass samples deduced from the confocal microscopy measurements for different laser treatment repetitions, patterns and distances between motifs.

Samples	S_a (μm)	S_q (μm)
Glass ref.	0.50	0.54
Line-distances x5		
L-10	0.49	0.63
L-25	3.40	3.89
L-50	3.60	4.00
L-100	4.00	4.29
L-200	1.09	2.43
L-300	1.00	2.20
L-500	1.00	2.30
Cross- distances x5		
C-10	0.53	0.63
C-25	2.90	3.50
C-50	2.00	2.25
C-100	3.00	3.20
C-200	2.26	3.40
C-300	1.50	2.00
C-500	2.30	3.20
Laser repetitions		
C-100x1	1.14	1.35
C-100x2	2.32	2.70
C-100x3	2.50	3.00
C-100x5	3.00	3.20

Table 3 presents a clear increase in roughness from around 1 μm to 3 μm as the number of laser scan repetitions increases. On the other hand, roughness data reveal that roughness parameters reach maximum values for L-100 and C-100 samples (around 4 μm and 3 μm for S_a and S_q , respectively). Then, for larger distances, the practically constant values of roughness parameters of 1 μm and 2.3-2.4 μm for S_a and S_q parameters can be correlated with the almost constant

percentage of treated surface area of these surfaces. Thus, roughness parameters appeared to be higher for the C-patterns compared to the L-ones for separations above 200 μm in agreement with the higher treated surface area percentage values. However, for smaller separations, the situation is reversed, possibly related to the fact that, although the percentage of treated surface in line patterns is lower, the width of grooves and the greater depth may be affecting in terms of roughness.

Interestingly, the femtosecond laser treatment of glass surfaces also induced a second order texture inside the grooves as it can be seen in **Figure 4**.

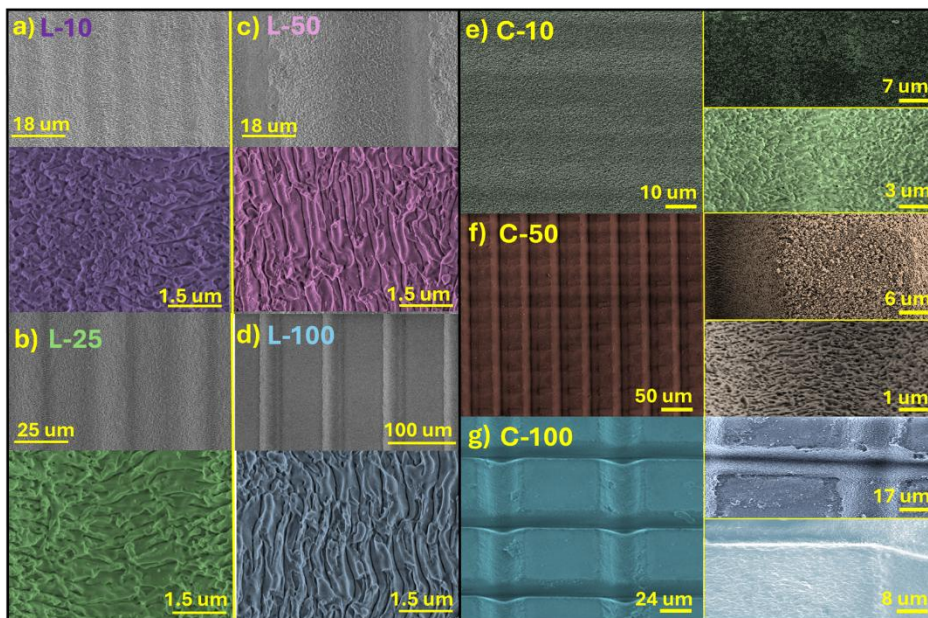


Figure 4. SEM micrographs at different zoom scales for patterned samples: a) L-10, b) L-25, c) L-50, d) L-100, and e) C-10, f) C-50, and g) C-100. Laser treatments were carried out applying five laser repetitions to draw the different motifs.

The SEM analysis of L-samples in Figure 4 a)-d) reveal that, due to the superposition of grooves, sample L-10 presents no pattern, but a continuous rough surface characterized by a grain-like morphology (Figure 4 a)). Only for a distance between lines close to the size of the laser spot (25 μm) a pattern of defined grooves starts to emerge on the surface. Effectively, on sample L-25, and with greater clarity in samples L-50 and L-100, well defined grooves appear in which interior elongated nanostructured features, of around 1 μm long and 0.3

μm width, appear to have developed, also observed for larger distances in **Figure 5**.

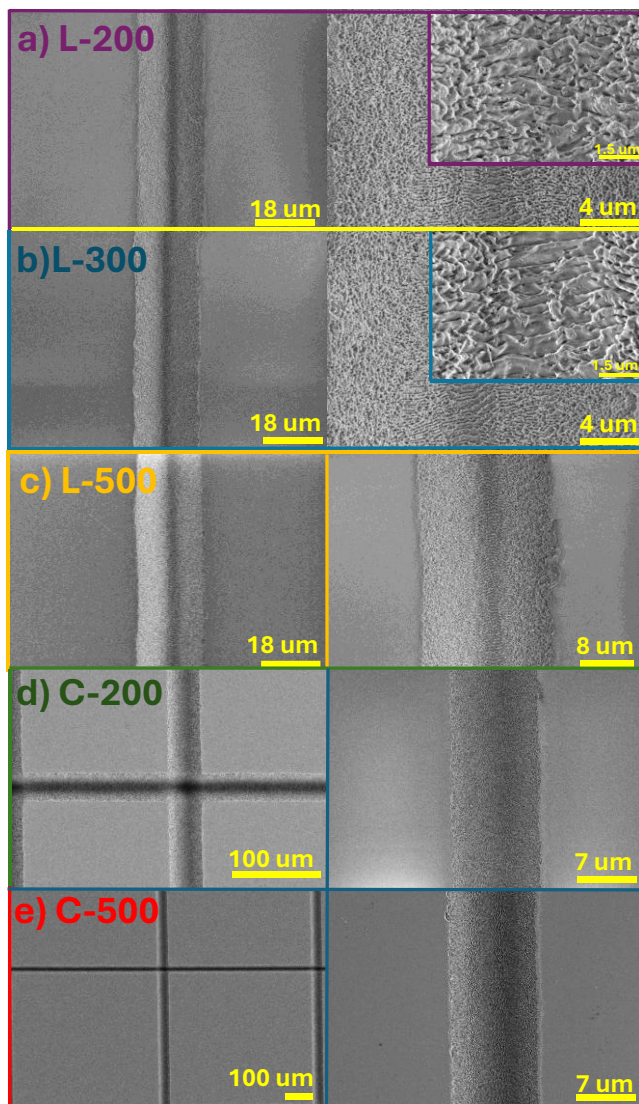


Figure 5. SEM images for line and cross laser patterns with larger distances between them: a) L-200 μm , b) L-300 μm , c) L-500 μm , d) C-200 μm , and e) C-500 μm after 5 repetitions.

As it is observed in Figure 4 b)–d) and 5, elongated nanostructures, well defined, and independent of the larger distance between lines until 500 μm , were developed, with groove widths slightly increasing from 0.3 to 0.5 μm corresponding to separations from L-100 to L-500 respectively. In agreement

with previous works²³, the previous results show that the combination of micro-(laser patterned motifs) and nano-(inside the grooves) structuration of glass surfaces is possible by fs laser treatments leading to different roughness scales, in the way of topographical hierarchy, on these transparent substrates^{24,25}.

A similar SEM analysis than that carried out for L-samples is presented in Figure 4 e)–g) for C- samples. For the five laser scanned samples, it is apparent that C-10 sample, where separation between groove distance is smaller than the groove width, did not develop a well-defined pattern. Instead, a continuous rough surface was obtained. Meanwhile, samples C-50 and C-100 present well-defined squares of untreated surface micropillars, result that extends to greater distances as shown in the Figure 5 d) and e).

A closer observation of what happens inside the grooves can be seen in **Figure 6**, with an increased surface roughness resulting from the accumulation of elongated nanostructures when the treatment is repeated on a previously modified region. As laser treatments are superimposed, a better-defined region of elongated nanostructures inside the grooves is being defined. This region is around 12 μm of the 28 μm width corresponding to the whole groove after 3 laser repetitions. It is possible to distinguish that the nanostructures placed at the bottom of the groove over measured around 0.4 μm width. Observing the images of the limit region between the generated groove and the pristine glass surface, the transition from the untreated region to an in-depth treated one with one or two different defined nanostructures can be recognized in function of the overlapped laser scans.

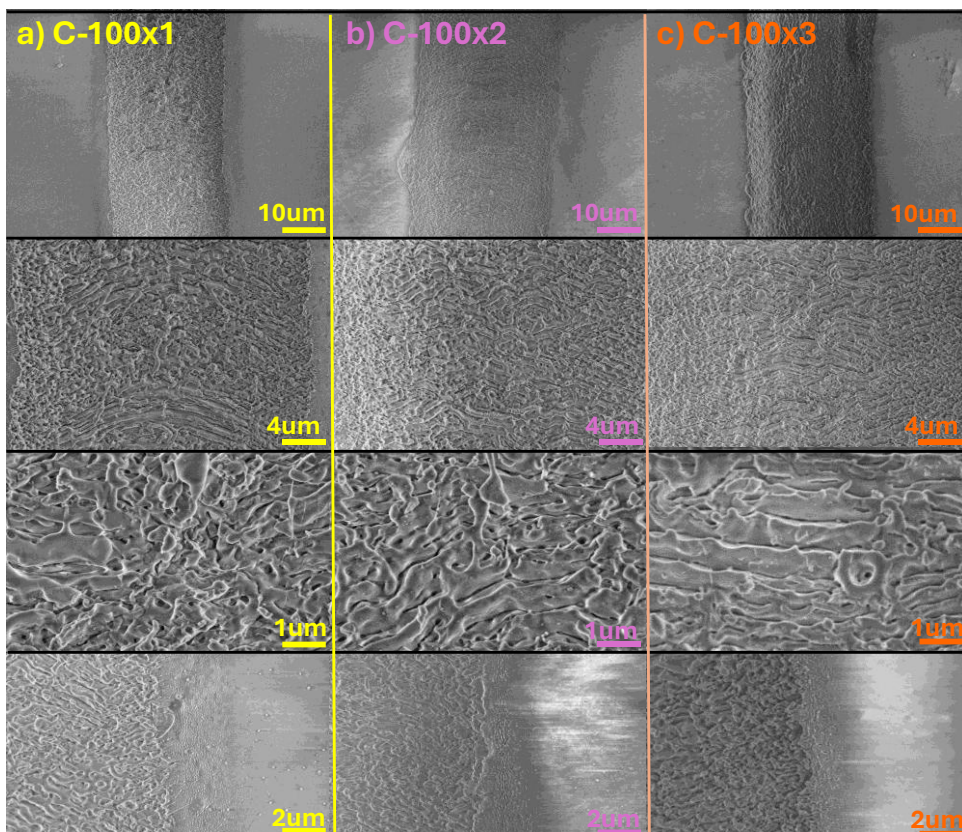


Figure 6. SEM images of cross laser grooves with fixed distance between lines (C-100 sample), and at different magnifications in function of repetitions: a) 100 μm between cross motifs with one laser scan, b) with two laser scans, and c) using 3 overlapping laser times. Last images correspond to the groove-flat glass surface frontier.

5.3.2 Optical properties of laser patterned glass surfaces

Optical transmittance analysis has been performed to evaluate the effect of patterning the transparent borosilicate. **Figure 7** indicates that, in agreement with the treated surface area percentage in Table 2, line patterns preserve better the optical transmittance of the glass substrate. What can be highlighted is that the cross-hatching, which doubles the percentage of treated surface compared to the line pattern, does not proportionally harm the optical transmittance, but rather maintains a high level above 70% for the entire visible region. Moreover, a brief demonstration is presented of the effect that subsequent surface functionalization, with the aim of making the surface repellent as will be

explained in the following section, has on laser-treated substrates is included in Figure 7.

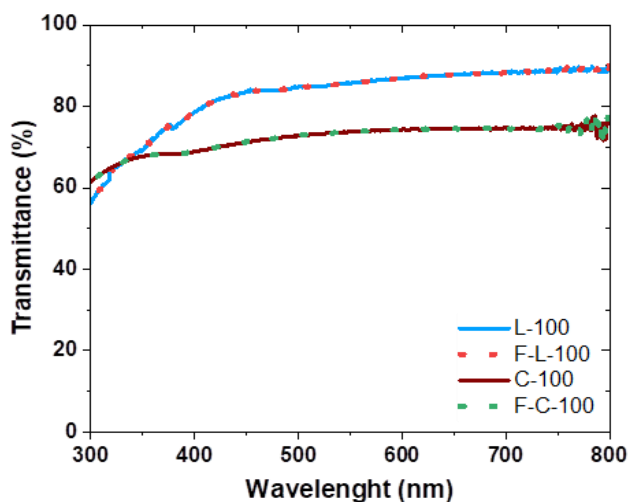


Figure 7. Optical properties before and after fluorination treatment of L-100 and C-100 patterned surfaces.

Figure 7 shows that the low surface fluorination process of the laser treated surfaces has not affected the optical properties for either of the two, line and cross, laser patterns.

UV-visible spectra of patterned and fluorinated glass samples are reported in **Figure 8** to assess the influence of the type of patterning on their optical properties. A general assessment of the set of spectra of samples F-L (Figure 8 a)), indicates that they maintain a high degree of transparency in the visible range, whereas a decrease in total transmission is found in the UV region and to a lesser extent in the visible region at low wavelengths. We attribute this effect to light scattering effects, which are more important for this range of wavelengths and are known to depend on feature shape, size and distribution^{26,27,28}. From the observation of the spectra in Figure 8 a), it appears that the magnitude of light attenuation transmission in the UV range correlates directly with the percentage of laser treated area of the borosilicate plates. Unlike this dependence in the UV range, in the visible region for $\lambda > 500-550$ nm most F-L samples present a high transparency. An exception to this behaviour was found in sample F-L-25 where distance between grooves coincides with the size of the laser spot ($25 \mu\text{m}$) and where a 100% of surface area was subjected

to the action of the laser and the average roughness presented one of the highest values as it was shown in Table 2 and Table 3, respectively.

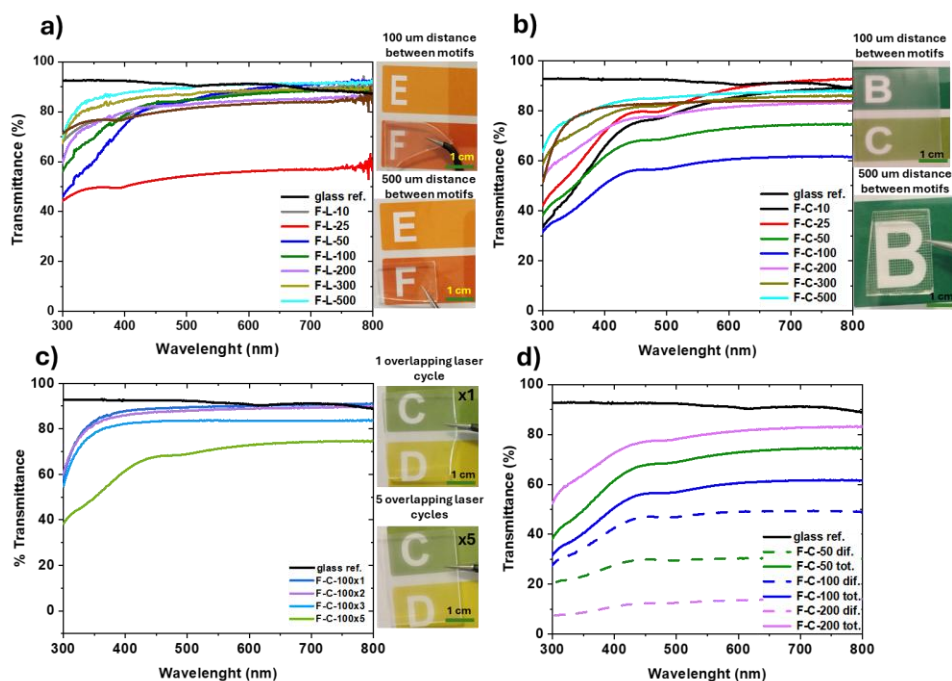


Figure 8. UV-visible transmission spectra of patterned and fluorinated glass samples: Total transmittance of F-L a) and F-C b) samples in function of the groove separation, compared to a reference sample, c) total transmission spectrum of samples F-C-100 depending on the number of laser repetitions. Photographs of coloured letter motifs are included to directly assess the visible light transmission through the patterned glass samples, d) examples of the total (tot.) and diffuse (dif.) transmittances for F-C- surfaces in function of the separation between motifs.

Figure 8 b) showcases that the optical behaviour of samples F-C vary with the dimension of the square micropillars patterned on the borosilicate plates. The spectra reveal an inverse correlation between the pattern size and the relative decrease in transmission intensity below 400 nm. This selective decrease in the UV region, is particularly intense for samples F-C-25 and F-C-10. In addition, there is a general decrease of the transmittance level, both in the visible and UV regions for samples F-C-50 and F-C-100 that reaches a maximum decrease of 40% in the latter sample. Transmission in the visible range increases for the other samples, particularly for samples F-C-200/300/500, characterized by a percentage of laser treated surface smaller than 30% as it is reflected in Table 2. The transmission spectra in Figures 8 a) and b), correspond to patterns drawn by scanning five times the laser. Further analysis revealed that the optical

transmission increased for patterns manufactured with less laser scans. Figure 8 c) presents a thorough analysis of this effect for sample F-C-100, the one depicting the lowest transmission from the whole series. The recorded transmission experienced a significant increase for the sample prepared with three and particularly two or one scan, in which case a transmission close to that of the reference sample was found for the whole range of visible wavelengths. It is assumed that the decrease in optical transmission with the number of laser scans is due to the progressive nanostructuration induced into the grooves with the number of laser scans (Figure 6). It is noteworthy though that even for sample F-C-100 where light transmission is the smallest, photographs in this figure demonstrate that samples present sufficient transparency for their use as transmission windows. As can be seen in Figure 8 d), for selected representative C-laser patterns, there is a non-negligible diffuse transmittance component when square patterns are generated which appears to be maximum for the separation value of $100\ \mu\text{m}$. Above this value, the untreated surface (71%) with larger motifs of full transparency becomes more important and seems to be less affected by the scattering phenomena caused by the roughness induced in the grooves. However, for shorter distances, even though the percentage of treated area is greater, the line width (37 and $26\ \mu\text{m}$ depending on the scanning direction) is more similar to the value of the distance between lines ($50\ \mu\text{m}$), making the untreated motifs, although smaller ($\sim 13 \times 24\ \mu\text{m}^2$), closer to each other. Therefore, when the distance is $100\ \mu\text{m}$, the more separated bigger untreated motifs ($\sim 63 \times 74\ \mu\text{m}^2$) together with the rough grooves of different depths (10 and $15\ \mu\text{m}$ depending on the scanning direction) appears to give rise to a critical value of light diffusion effects.

Scattering can be significantly reduced by incorporating to the pattern surface a fluid with a refraction index like that of glass (1.47)²⁹. This strategy might be used with a thin polymeric layer or other conformal coating deposited onto the laser treated glass surface serving as host scaffold. As an example of this, a fluorinated lubricant, Krytox, has been infiltrated in two laser patterns to form SLIPS. The optical properties of these slippery surfaces are shown in the **Figure 9**.

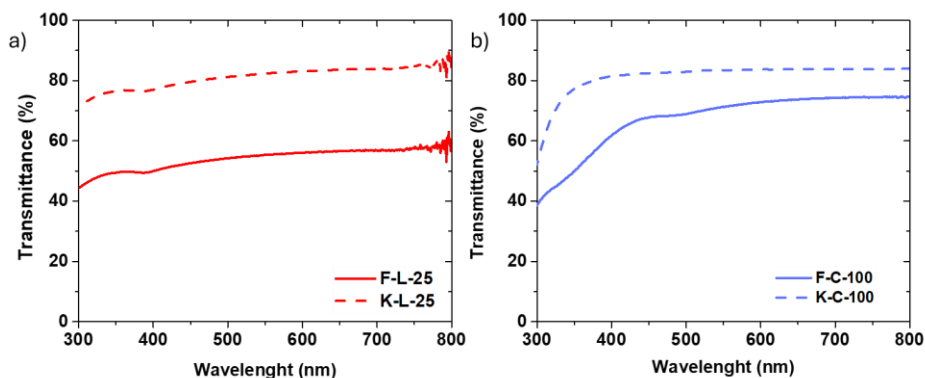


Figure 9. Optical transmittance of a) line and b) cross glass laser patterns infiltrated with the Krytox lubricant liquid, compared to those without it.

Figure 9 supports the enhancement of the optical transmittance reaching a level of 80% for the entire visible spectral region when air pores are replaced by the liquid of refractive index around 1.296-1.301 in both the lower transmittance treated cases: F-C-100 and F-L-25 surfaces.

5.3.3 Wetting and anti-icing properties of transparent patterned glass surfaces

Pristine glass surfaces present a WCA lower than 60° for droplets of $2\ \mu\text{l}$. However, the patterned samples L- and C- become superhydrophilic, as expected for their very roughness under the premises of the Wenzel model³⁰. This superhydrophilic state lasted more than 3 months for samples stored under normal environmental conditions. To permanently convert the surfaces of patterned samples into hydrophobic without affecting their optical properties as it happens with common coatings^{31,32}, we proceed to anchor perfluorinated molecules over the entire borosilicate surface (Chapter 2). This procedure has been, previously used for the fabrication of self-cleaning, anti-fouling and anti-icing alumina³³ and stainless-steel hierarchical surfaces (Chapter 4). It was found that grafting of PFOTES molecules on flat borosilicate surface induce a net and permanent increase in WCA from 60° to 97° as it is represented in **Figure 10**.

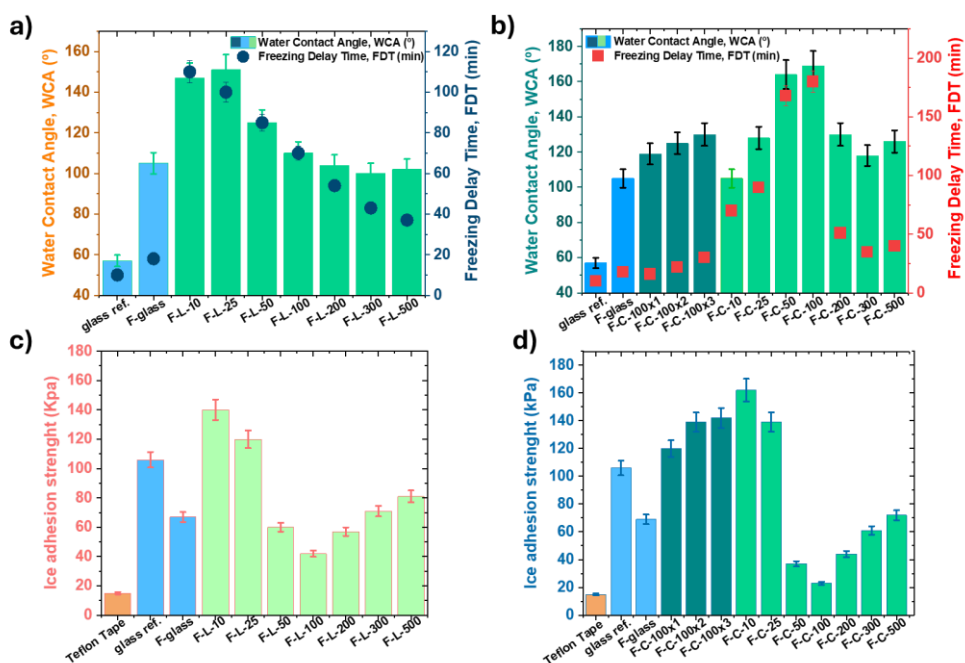


Figure 10. Water contact angles (columns) and freezing delay times (spots) graphs for a) F-L- and b) F-C- patterns; ice adhesion stress (compared to a Teflon reference) graphs for c) F-L- and d) F-C- samples. Data for an untreated flat and glass reference are included for comparison.

An increase in wetting angle must be associated to the modification in surface composition, a feature that was also observed when the patterned samples were subjected to a similar grafting process. To be able to check this phenomenon, XPS spectrum and chemical element quantification were carried out for glass ref., F-glass, C-100 and F-C-100 samples (**Figure 11** and **Table 4**). Surface composition determined by XPS for laser patterned samples reveal a small increase of the carbon content while the O/Si ratio remaining virtually constant with values around 2 typical of SiO_2 as it is shown in Figure 11 c). However, surface functionalization of the reference and laser treated samples by grafting PFOTES molecules lead to the incorporation onto the surface of a considerable amount of fluorine (21.4% and 27.8% atomic on pristine and laser treated surfaces), which appears in the form of $-\text{CF}_2$ and $-\text{CF}_3$ functional groups³⁴ (Figure 11 b)). This and other changes in the atomic percentages and chemical state of C, O and Si suggest that a high concentration of tethered PFOTES molecules have been grafted onto the surface of borosilicate glass.

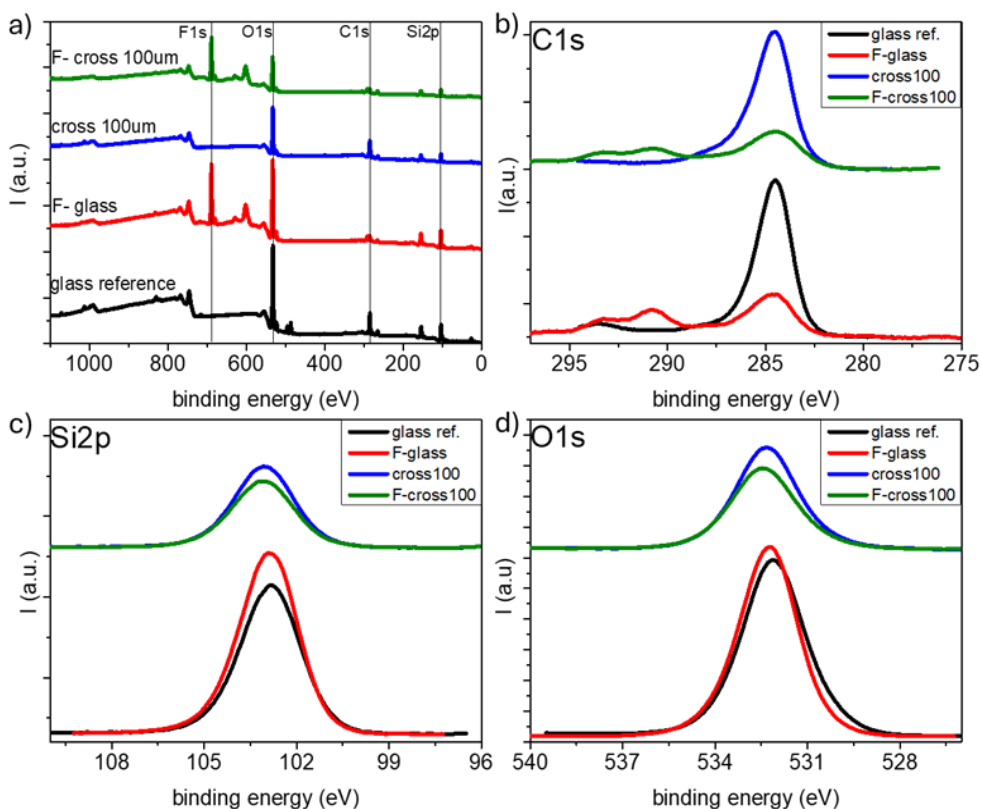


Figure 11. XPS analysis of the glass surface and the cross laser patterned one after the fluorinated grafting: a) survey, b) C 1s, c) Si 2p and d) O 1s spectra.

Table 4. Effect of the fluorination on the atomic concentration expressed in percentages of the laser treated glass surface compared to the pristine reference.

Atomic composition (%)	C	O	Si	F
glass ref.	28.8	46.3	24.9	-
F-glass	17.9	37.1	23.6	21.4
C-100	41.3	39.1	19.6	-
F-C-100	25.1	30.2	16.9	27.8

Dates on the wetting behavior (static and dynamic) of samples F-L and F-C prepared applying five laser scans are shown in Figure 10 a) and b) and **Table 5**. Samples F-L are hydrophobic with WCAs higher than 100°, approaching 150° for sample F-L-10 and a virtual superhydrophobic state for samples F-L-25. As discussed in previous section, 100% of this sample has been laser treated, and its overall roughness has the maximum value from the whole series (Table 3). On

the other hand, all F-L samples except F-L-500, present no sliding against 15 μ l of water droplets as it can be seen in the Table 5, for different organic liquids studied with 15 μ l of droplet volume, no difference whether sliding takes place along the direction of grooves or perpendicular to them.

Table 5. Rolling-off angles values of 15 μ l droplets of different liquids on line laser patterns in function of the line separation before and after fluorination measured in parallel (and normal in brackets) direction respect to the laser patterns.

Rolling-off angle /° (15 μ l)	water	diiodo-methane	humic acid	sodium alginate	bovine serum
glass ref.	57	43	41	47	47
L -10	-	-	-	-	-
F-L -10	90 (90)	49 (47)	90 (72)	90 (90)	90 (90)
L -25	-	-	-	-	-
F- L -25	90 (90)	42 (20)	30 (90)	40 (90)	20 (90)
L-50	-	-	-	-	-
F- L-50	90 (90)	62 (35)	55 (90)	62 (90)	60 (90)
L-100	-	-	-	-	-
F- L-100	90 (90)	75 (30)	45 (90)	55 (90)	60 (90)
L-200	-	-	-	-	-
F- L-200	90 (90)	15 (15)	60 (90)	60 (90)	57 (90)
L-300	-	-	-	-	-
F- L-300	90 (90)	16 (90)	44 (90)	45 (90)	50 (90)
L-500	-	-	-	-	-
F- L-500	23 (90)	39 (90)	40 (90)	40 (90)	40 (90)

Only in sample F-L-500, water droplets readily slit along the direction of grooves (RoA of 23°) but become blocked in the perpendicular direction. A selective directional sliding of water droplets has been reported for other systems with directional patterns or drawings and attributed to the asymmetric wetting of water droplets³⁵. Other liquids including diiodomethane and biological fluid simulants to study anti-fouling behaviour, slit more readily than water (presenting RoAs smaller than 90°) and an anisotropic behavior that depended on rolling direction, particularly for samples with a distance between grooves equal or higher than 300 μ m (Table 5). Increasing the distance between lines and grooves that generate a pinning effect seems to favor the decrease of water droplets sliding angle in the longitudinal direction. Since the sliding is possible due to a force-unbalance between the gravitational force and the surface tension

of the droplet, whereas the general hydrophobic state is quite similar for L-surfaces of larger micro-separations, it must be a topographical effect influencing the droplet movement on the predetermined direction along the grooves. Besides for F-L-500 the untreated flat surface area becomes predominant, and the droplet overcomes interfacial friction resistance due to the rough grooves surfaces³⁶.

In the case of the anisotropic laser patterned surface, the WCAs of samples F-C are reported in Figure 10 b). Wetting data for the F-C-100 pattern prepared applying from 1 to 5 laser scans to draw the grooves is also included (Figure 10 c)). All F-C samples were hydrophobic (generally with a higher WCA than the equivalent F-L samples with grooves separated by the same distances), reaching a state close to superhydrophobicity for samples F-C-100 and F-C-50. It is noteworthy that this close to superhydrophobic state found in sample F-C-100 was achieved applying five laser scans according to a progressive increase with the number of cycles that induced changes of the in-depth grooves from 2-3 μm to 10-15 μm (according to the laser scan direction) and, consequently, an enhanced roughness of the groove path. A rough estimation of the number of contacted square motifs under a 2 μl or 15 μl droplet when the WCA of the F-C-100 is around 170° represents around 36 or 40 square micropillars, respectively, as the optimum condition for superhydrophobic laser treated glass surfaces³⁷. Thus, lower WCA values for higher distances between motifs implies larger contact surface area of the droplet that cover an order of magnitude greater number of flat motifs. While in the opposite trend, smaller separations for similar contact surface area of the droplet (similar WCA) involves several thousand motifs included under the drop, i.e. multiplies the presence of micro-/nano-rough grooves acting as pinning points predicted by the Wenzel model. According to Rivera-Saun et al.²⁰ it is possible to relate the roughness factor and the surface fraction in contact to the liquid, of the Wenzel and Cassie-Baxter models respectively (Chapter 1) with morphological parameters of the developed patterns, i.e., distance between lines, grooves depth and widths of grooves and untreated regions in both laser scanning directions. For the F-C-100 surface, these factors take the values of 1.15 (Wenzel factor) and 0.47 (Cassie-Baxter factor) that tends to approach to a Cassie-Baxter behaviour. Whereas, for the other laser patterns, the morphological features dimensions lead to a predominance of the roughness level induced by grooves depths lower than 20

μm pointing to a Wenzel response²⁰. Therefore, this wetting state results from the anchoring of tethered PFOTES molecules on the surface characterized by a micro-roughness of the laser pattern and a high nano-roughness at the grooves in a hierarchical version, with a minimum contribution of the untreated borosilicate surface regions.

As it is observed in **Table 6**, most fluorinated cross patterned surfaces present a pinning droplet effect that cannot be able to rolling-off the surface, except for the F-C-50 and 100 cases that represent the most optimal distances between grooves for decreasing RoAs values. Particularly, for most biofouling agents, RoAs values lower than 2° indicate total repellence and superomniphobicity when combines with the contact angle measurements. However, for distances smaller and greater than 50 - 100 μm , a “*petal-like*” wetting is exhibited.

Table 6. Rolling-off angles values of 15 μl droplets of different liquids on cross laser patterns samples in function of the line separation before and after surface fluorination.

Rolling-off angle /° (15 μl)	water	diiodo- methane	humic acid	sodium alginate	bovine serum
glass ref.	57	43	41	47	47
C -10	-	-	-	-	-
F-C -10	90	90	87	90	90
C -25	-	-	-	-	-
F- C -25	90	-	90	90	90
C-50	-	-	-	-	-
F- C-50	<2	70	<2	<2	<2
C-100	-	-	-	-	-
F- C-100	<2	79	<2	<2	<2
C-200	-	-	-	-	-
F- C-200	90	60	90	90	90
C-300	-	-	-	-	-
F- C-300	90	30	90	90	90
C-500	-	-	-	-	-
F- C-500	90	39	90	90	90

The anti-icing properties of samples have been evaluated through the determination of FDTs shown in Figure 10 a) and b), and ice adhesion strength results in Figure 10 c) and d). F-L samples with grooves separated by small distances depicted the longest FDTs around 100 and 110 min for a 2 μl water droplet deposited on the surface at -10°C , this magnitude decreasing as the distance between grooves increases. Meanwhile all F-C samples presented FDTs

longer than one hour, following again the trend of WCAs. Values were slightly higher than those found with F-L samples with equivalent groove distances. Outstanding FDTs of 180 and 168 min were found for samples F-C-100 and F-C-50, respectively. Compared to current transparent anti-icing proposals in the literature, mainly based on coatings, the FDT values presented here are an order of magnitude longer at the same freezing temperature, demonstrating the anti-icing potential of the combination low fluorination + laser pattern^{38,39}. This behaviour suggests a clear correlation between FDT and hydrophobicity/roughness through the surface treated area percentage in contact with the water droplet as predicted eq. 4-6 in Chapter 1. Added to this is the fact that borosilicate glasses have usually very low heat transfer coefficient ($\sim 1,2 \text{ Wm}^{-1}\text{K}^{-1}$) that tends to increase with the surface roughness⁴⁰. However, these low fluorinated patterned glass surfaces presented remarkable retards of the icing phenomena.

Supporting this anti-icing promising behaviour, ice adhesion strength at $-13 \text{ }^{\circ}\text{C}$ (Figure 10 c) and d)) presents a minimum for sample F-L-100 ($\sim 41 \text{ kPa}$, close to the Teflon reference), increasing for samples with higher or smaller distances between grooves. And, for the cross patterned surfaces, the remarkable icephobic character, particularly of sample F-C-100 prepared with five laser scans, is confirmed by a value of 23 kPa , quite similar to the Teflon tape reference. F-C-100 samples prepared applying fewer laser repetitions or the other F-C samples with smaller and larger groove distances presented higher ice adhesion strengths. This ice adhesion strength response can be related to the interlocking mechanism that occurs between the micro-/nano- roughness and the ice when interacting grooves have developed less depth (n° repetitions) or if there are structured grooves closer together compared to the $100 \text{ }\mu\text{m}$ distance case, as well as if larger separations between motifs reduce the effect of the topographical hierarchy (surface treated area percentage) on the wettability trending to present similar adhesion strength values than that obtained for the fluorinated flat glass reference. Therefore, it is required a compromise between specific roughness levels and surface chemical modification on these borosilicate glass to achieve low ice adhesion results in line with what was indicated in the eq. 7 from Chapter 1. It should be noted that the potential anti-icing SLIPS based on the development transparent glass that presented ice adhesion strength values of 32 and 18 kPa for the F-L-25 and F-C-100 samples, respectively.

5.3.4 Water condensation on patterned glass surfaces

Water condensation experiments were carried out in an environmental chamber and in an environmental electron scanning electron microscope to, respectively, follow the water condensation capacity at the macro-scale on samples F-C-100 and F-L-100 and at the micro-scale on sample F-C-100. These samples present highly hydrophobic or superhydrophobic states and the best anti-icing performance (Figure 10). Water condensation is highly dependent on temperature and relative humidity (RH) conditions of environment. Experiments were carried out at 2 °C and different degrees of RH. **Figure 12** displays a series of images taken at 2 °C and 90% RH for the investigated samples in a vertical configuration. According to images in Figure 12 a1)-a4), taken from 2 to 60 min of exposure to the humid and cold conditions, a considerable amount of water condenses and forms a continuous layer on the reference sample placed in a vertical position. A rough estimation of the amount of water condensed on this sample is around 1 $\mu\text{l}/\text{cm}^2$ after 60 min. Unlike this, much less water accumulated on the surface of the hydrophobic laser patterned surfaces was observed for similar time intervals, where their distribution took the form of isolated or separated droplets, depending on the analysed pattern, instead of a continuous layer⁴¹. By eye inspection, the water accumulation degree over the observed surface area follows the order: ref-glass \gg F-L-100 (horizontal) > F-L-100 (vertical) > F-C-100. Interestingly, only small differences were found for sample F-L-100 oriented with their grooves in horizontal or vertical positions, indicating that laser patterning did not function as an effective drainage system of the accumulated water giving its wetting behaviour in the typical Wenzel state. It should be noted that the condensation of macroscopic water droplets only starts on sample F-C-100 for RH degrees higher than 60%, unlike what happens on other surfaces. Therefore, a high level of humidity was established as represented in Figure 12 b), where small droplets on the F-C-100 surface began to appear after 17 min of stay under condensation conditions. A rough estimation of water surface coverage from Figure 12 b3) was 68%, meaning 0.6 $\mu\text{l}/\text{cm}^2$.

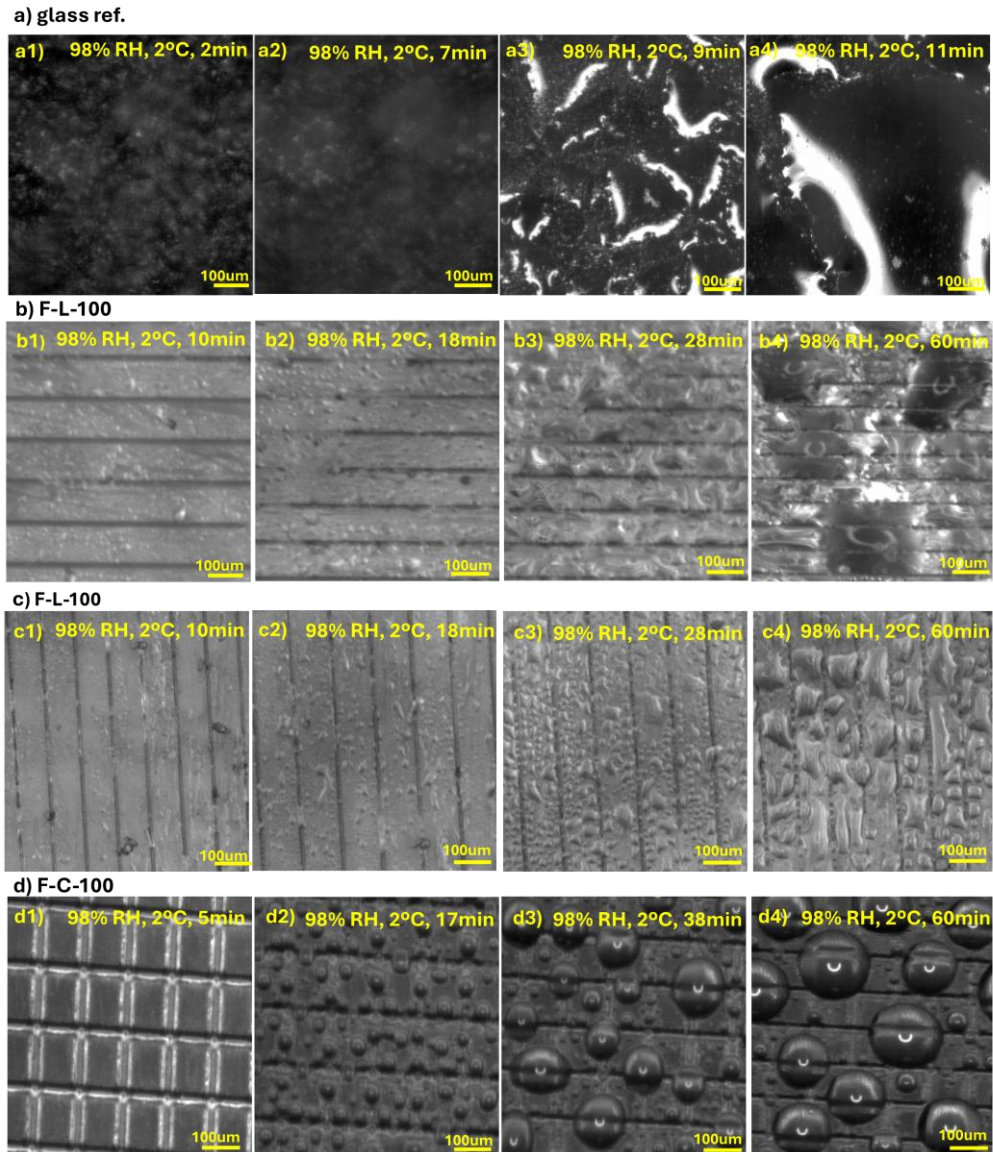


Figure 12. Water condensation experiment at 2 °C and 90% RH for the samples placed in vertical position. Snapshots were taken for the indicated times from 2 to 60 min for: a) glass ref., b) and c) F-L-100 with the grooves placed in horizontal or vertical direction, respectively, and d) F-C-100.

The diameter of these primary observed droplets was approximately of 25 μm and, assuming a spherical shape, it had a volume of approximately $8 \times 10^{-6} \mu\text{l}$. Augmenting the condensation time provoked an increase of the droplet size until 100 μm diameter corresponding to a volume of $5 \times 10^{-4} \mu\text{l}$, accompanied by a decrease in the number of droplets on the surface in what it appears to be a kind of Ostwald ripening process. It is defined as a physical process where larger

particles tend to grow at the expense of smaller ones. This phenomenon is related to the difference in vapor pressures between the small and large particles. Small particles have a greater curvature and, therefore, higher surface tension. This creates a higher vapor pressure inside them compared to what happens in larger particles. The higher vapor pressure promotes the transfer of material from these small droplets to the larger ones^{42,43}. Therefore, after 60 min these droplets had approximate diameters of 500 μm and an estimated volume of $65 \times 10^{-3} \mu\text{l}$. It is relevant to stress that the overall amount of condensed water did not increase significantly from the situations in Figure 12 d2) to Figure 12 d4).

All long this latter experiments the water droplets, albeit the vertical position of samples, did not slide away from the surface, not even on the surface of superhydrophobic behaviour (F-C-100). This is likely related with their small volume and the fact that gravity forces are not enough to overpass the adhesion forces with the substrates. A completely different situation was the one encountered for the rolling of angle measurements where 15 μl water droplets readily slide-off at angles as small as 5° .

Water condensation proceeds differently for a RH smaller than 60%. For example, in experiments carried out at 48% of RH at 2°C , considerable water condensation could be observed on the glass-ref sample, while no macroscopic water droplets remained on sample F-L-100 where they readily slide-off even for surface inclinations as small as $1-2^\circ$ at it is shown in **Figure 13**. The snapshots show that after 10 min, water droplets of 25 μm diameter were visible on the bear glass reference surface. A progressive accumulation of water droplets continued to occur on this sample, while no water droplets could be detected on the F-L-100 patterned surface (note that condensed water droplets traces can be seen on the back of sample F-L-100 due to its transparency). Interestingly, a “reality show” experiment carried out with this sample consisting of its exposure to falling snow at temperatures around -4°C showed no accumulation of snow after more than 18 min and for samples orientation close to tilted position around 45° facing the direction of arrival of the snowflakes.

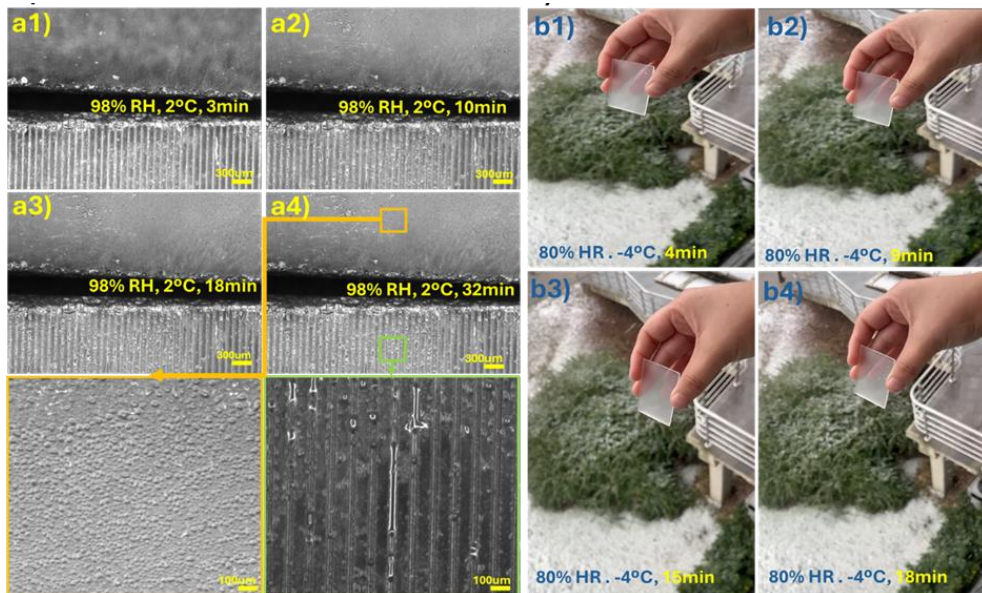
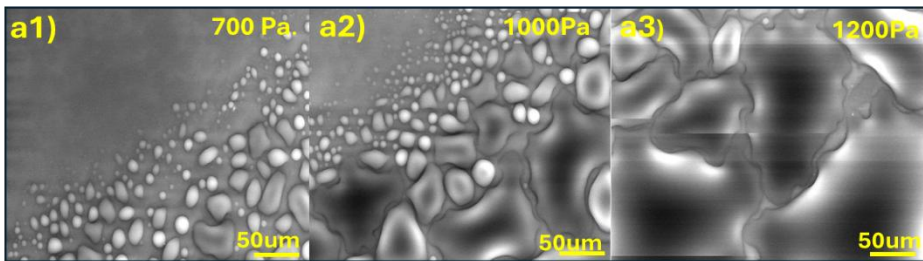


Figure 13. a) Sequence of images of a water condensation test in a controlled environmental chamber at 2 °C and 98% RH and increasing times for a reference sample (top) and F-L-100 sample (bottom) including two respective zoomed regions of the last time event; b) sequence of images of a real experiment in Poland was carried out for F-L-100 sample at -4 °C for different ice exposition times.

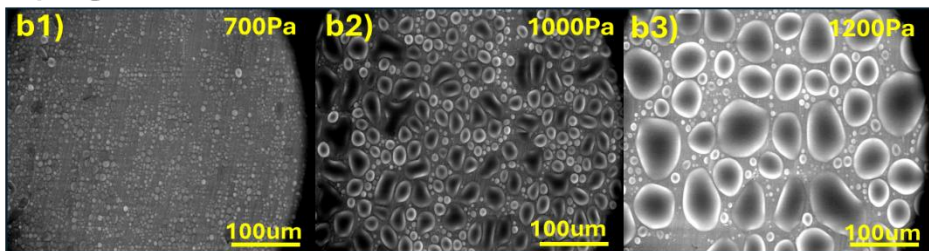
To get deeper into the water condensation behaviour on the patterned glass surfaces (its reluctance to accumulate macroscopic water layers onto their surfaces), a study at the microscale in an environmental microscope following the water condensation on the samples kept at 2 °C and increasing water vapor pressures in the microscope chamber were performed as it is shown in **Figure 14**. This figure shows a series of ESEM images describing the condensation behaviour on samples glass ref. and F-glass and samples C-100 and F-C-100. Vapor pressure inside the chamber was varied from 700 Pa (water saturation pressure at 2 °C, according to Figure 8 in Chapter 1) to values as high as 1200 Pa (note that the walls of the microscope chamber were not cooled, only the sample holder).

On the glass reference, even for the smallest vapour pressure of 700 Pa, water forms large condensates that enlarge its size and eventually form big water accumulations in a film wise mode at the highest water pressure of 1200 Pa. This behaviour is characteristic of a hydrophilic surface and reproduce well the condensation behaviour in air at the macroscale.

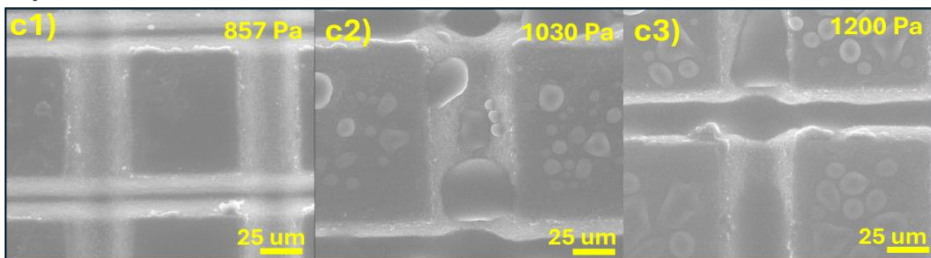
a) glass ref.



b) F-glass



c) C-100



d) F-C-100

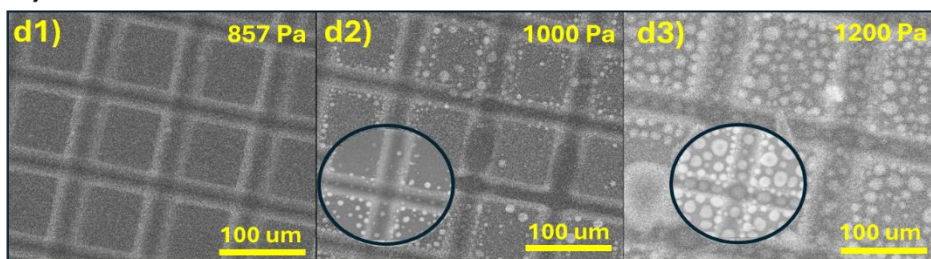


Figure 14. ESEM images at different water vapor pressures evolution of the water condensation phenomena onto the following surfaces at 2°C: a) glass ref., b) F-glass, c) C-100 and d) F-C-100.

On the fluorinated flat glass reference, between 700 and 1000 Pa of vapor pressure in the ESEM chamber, condensation proceeds through the formation of small and spherical droplets, which are distinctive of a hydrophobic behaviour and grew with the vapour pressure rise. Thus, droplets increased in volume and coalesced with the neighbouring ones at 1200 Pa but keeping always a diameter

smaller than 100 μm as it is reflected in Figure 14 b). ESEM images of the water condensation on the highly hydrophilic sample C-100 reveals two well-differentiated regions (Figure 14 c)): initially water accumulates in the form of a continuous pool inside the grooves, followed by the formation of small droplets on top of the flat surface of square micropillars. On the highly hydrophobic/superhydrophobic F-C-100 sample shown in Figure 14 d), the formation of very small spherical droplets was only observed for a water vapor pressure around 1000 Pa, above the water saturation pressure at the temperature of the sample (Figure 14 d2)) and was slightly more favourable on the flat surface of micropillars. Further increasing the vapor pressure to 1200 Pa produced an increase in the size of microdroplets, although their size was much smaller than that found on sample F-glass for the same conditions. It could be proposed that the presence of grooves separating the micropillars in sample F-C-100 prevents the coalescence of microdroplets into larger droplets as it happens in sample F-glass. This effect would be like the one observed for this sample in the cooling chamber at atmospheric pressure (Figure 12 d3) and d4)), where grooves seem to prevent the coalescence of droplets because they remain fixed by the grooves. To account for the difference in the size of water droplets formed on sample F-C-100 in the experiment in air and the one in the microscope, we hypothesize that in the former case growth of water droplets is possible through the already mentioned Ostwald ripening mechanism, while it would be hindered in the ESEM. This would be the case provided that the droplet growth through ripening takes place by an evaporation-condensation mechanism⁴⁴. This would be possible in the air experiment where the RH is 98% but would be hindered in the case of the ESEM where the water vapour pressure is higher than the water saturation pressure at the sample temperature. In this regard, the ESEM experiments suggests that the low surface energy and superhydrophobic character of samples F-glass and particularly F-C-100 efficiently hinders the formation of water droplets on their surfaces even for vapour pressures above the saturation pressure of water at the temperature of surfaces.

5.3.5 Anti-fouling response of transparent patterned glass surfaces

The wetting behaviour of the patterned glass samples has been further characterized with simulated fouling fluids. **Figure 15** shows the contact angles of droplets of polar (water) and non-polar liquid as well as other fluid agents such as proteins dispersions deposited on the pristine glass reference sample compared to the laser patterned ones: C-100 and F-C-100 surfaces.

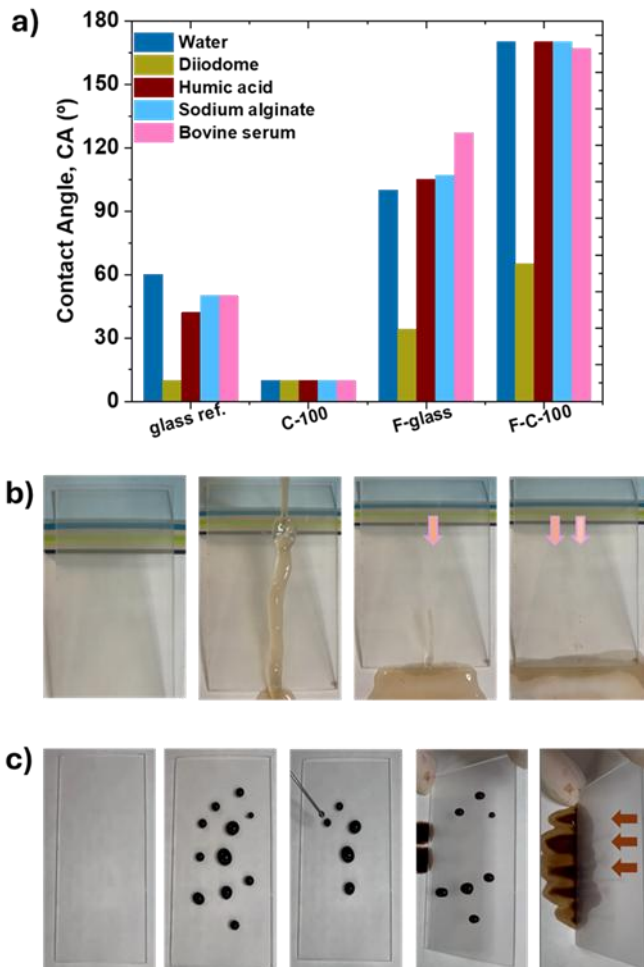


Figure 15. a) Anti-fouling response through wetting measurements with polar, non-polar and organic liquids for glass ref., C-100, F-glass and F-C-100. Sequence of images of anti-fouling behavior using b) bovine serum (blood simulator), and c) humic acid (mud simulator) for the F-C-100 sample.

Data in this figure reveal fouling agents on the untreated reference sample depict wetting angles between 50° and 60° (partially omniphilic). Unlike this behaviour, sample C-100 was omniphilic, because there was a complete spreading of the liquids on its surface, in agreement with the high RoA values collected in Table 5. After fluorine surface functionalization, the wetting drastically changed. Figure 15 a), showcases contact angles values around $115\text{--}125^{\circ}$ for the fluorinated flat surface and a superomniphobic behaviour, with contact angles higher than 150° , on sample F-C-100. This supports a notable anti-fouling response and self-cleaning capacity in line with what was predicted by equation 2 of Chapter 1, a behaviour that was further confirmed by the series of picture sequences presented in Figure 15 b) and c), also in agreement with the sliding behaviour reflected in Table 5.

Finally, Table 4 reveals that the line laser pattern allows the obtention of a selective repellent/attractive behaviour to fouling agents: it is possible to retain the sliding of $15\ \mu\text{l}$ fouling simulant fluid droplets in the direction perpendicular to the lines while, on the line parallel one, the sliding is allowed almost independently on the distance between them. This could have potential applications in microfluidics and smart windows/displays.

5.4 Conclusions

In this chapter, it is shown how, through focused laser technology using a femtosecond laser on a transparent substrate, it is possible to control the micro- and nano-structuration of the surface based on patterns from the perspective of biomimetics, aiming for achieving superhydrophobicity.

Two laser patterns were studied: parallel lines and asymmetric square micropillars, through the variation of two main laser parameters, i.e., the distance between laser generated grooves and the laser overlapped repetitions, focused on the control of the wetting properties while preserving the transparency.

It has been proven that the parametrization of the UV femtosecond (fs) laser technology manages to minimize the alteration of the optical properties of these transparent glass substrates in the form of diffuse scattering. Moreover, transparency was not at all affected by the chemical functionalization with fluorinated molecules.

Borosilicate glass has been chosen as reference substrates due to their low thermal expansion coefficient and resistance to thermal shocks compared to commonly used substrates as promising anti-icing candidate, however its surface exhibited hydrophilic behavior even after the morphological changes induced by the laser treatment. A subsequent fluorine-based surface functionalization through chemical anchoring of fluorinated molecules has been proposed to promote a transition from a Wenzel-type wetting response of rough patterned surfaces (superhydrophilic) to a Cassie-Baxter-type one (superhydrophobic). Besides, related properties such as anti-fouling, anti-fogging and anti-icing have been able to be observed.

Regarding the laser treatments with line and square patterns, the variation of the distance between motifs from 10 μm to 500 μm has been explored, finding a trend from 100% to 5% or 12%, depending on the respective pattern, for the percentage of laser-treated surface. Therefore, specific laser patterning conditions have been found with 5 repetitions (depths around 10 – 15 μm) and distances between 50 and 100 μm to develop the highest water contact angles values, better anti-fouling response, longer freezing delay times, lower ice adhesion strength response, and better resistance to water condensation. The best performance corresponded to the F-C-100 glass surface with around 53%

of laser treated surface of micro-/nano- roughness generation, exhibiting a Cassie-Baxter-type behaviour.

In general, square patterns had better wetting derived functionalities compared to the line ones. Nevertheless, an anisotropic sliding behaviour, which has had an impact on the anti-fouling capacity, has been revealed for the line laser patterned transparent surface, allowing the control of the fluid droplets movement along or across the surface.

Bibliography

1. Montes, L. *et al.* Long-lasting low fluorinated stainless steel hierarchical surfaces for omniphobic, anti-fouling and anti-icing applications. *Surfaces and Interfaces* **46**, (2024).
2. Li, Y. *et al.* Robust super-hydrophobic ceramic coating on alumina with water and dirt repelling properties. *Journal of the American Ceramic Society* **102**, 6267–6274 (2019).
3. Kumar, A., Mishra, V., Negi, S. & Kar, S. A systematic review on polymer-based superhydrophobic coating for preventing biofouling menace. *Journal of Coatings Technology and Research* vol. 20 1499–1512 (2023).
4. Thennakoon, C. A., Rajapakshe, R. B. S. D., Rajapakse, R. M. G. & Rajapakse, S. Anti-stain and durable superhydrophobic/antistatic dual functionality surface for fabric materials based on F-ZnO/TiO₂ composite. *J Solgel Sci Technol* **101**, 529–538 (2022).
5. Tourkine, P., Merrer, M. Le & Quéré, D. Delayed freezing on water repellent materials. *Langmuir* **25**, 7214–7216 (2009).
6. Guo, P. *et al.* Icephobic/anti-icing properties of micro/nanostructured surfaces. *Advanced Materials* **24**, 2642–2648 (2012).
7. Ijaola, A. O. *et al.* Wettability Transition for Laser Textured Surfaces: A Comprehensive Review. *Surfaces and Interfaces* **21**, 100802 (2020).
8. Rico, V. J. *et al.* Hydrophobicity, Freezing Delay, and Morphology of Laser-Treated Aluminum Surfaces. *Langmuir* **35**, 6483–6491 (2019).
9. Pan, R., Zhang, H. & Zhong, M. Triple-Scale Superhydrophobic Surface with Excellent Anti-Icing and Icephobic Performance via Ultrafast Laser Hybrid Fabrication. *ACS Appl Mater Interfaces* **13**, 1743–1753 (2021).
10. Ouchene, A. *et al.* Roughness and wettability control of soda-lime silica glass surfaces by femtosecond laser texturing and curing environments. *Appl Surf Sci* **630**, (2023).
11. Psarski, M. *et al.* Vapor phase deposition of fluoroalkyl trichlorosilanes on silicon and glass: Influence of deposition conditions and chain length on wettability and adhesion forces. *Mater Chem Phys* **204**, 305–314 (2018).
12. Cleaver, A.J. *et al.* The influence of Relative Humidity on Particle Adhesion-A Review of Previous Work. *Chem Proc Eng* **24**, (2004).
13. Nguyen, H. H. *et al.* Surface characteristics and wettability of superhydrophobic silanized inorganic glass coating surfaces textured with a picosecond laser. *Appl Surf Sci* **537**, (2021).
14. Dinh, T. H., Ngo, C. V. & Chun, D. M. Direct laser patterning for transparent superhydrophobic glass surfaces without any chemical coatings. *Appl Phys A Mater Sci Process* **126**, (2020).
15. Tan, D., Sharafudeen, K. N., Yue, Y. & Qiu, J. Femtosecond laser induced phenomena in transparent solid materials: Fundamentals and applications. *Progress in Materials Science* vol. 76 154–228 (2016).
16. Richardson, M. C. *et al.* Ablation and optical property modification of transparent materials with femtosecond lasers, **472** (2004).
17. Johanns, K. E. *et al.* *Strength and Contact Damage Responses in a Soda-Lime-Silicate and a Borosilicate Glass. Proceedings of the 2006 Army Science Conference* (2006).
18. Lee, J. E., Kim, E., Hwang, J. B., Choi, J. C. & Lee, J. K. Flake formation and composition in soda-lime-silica and borosilicate glasses. *Heliyon* **9**, (2023).
19. Pawar, P., Ballav, R. & Kumar, A. Review on Material Removal Technology of Soda-Lime Glass Material. *Indian J Sci Technol* **10**, 1–7 (2017).
20. Rivera-Sahún, J., Porta-Velilla, L., de la Fuente, G. F. & Angurel, L. A. Use of Green Fs Lasers to Generate a Superhydrophobic Behavior in the Surface of Wind Turbine Blades. *Polymers (Basel)* **14**, (2022).
21. Ancona, A. *et al.* Laser surface texturing for superhydrophobic, icephobic and friction reduction functionalization. *IOP Conf Ser Mater Sci Eng* **1296**, 012042 (2023).

22. Peethan, A., Unnikrishnan, V. K., Chidangil, S. & George, S. D. Laser-Assisted Tailoring of Surface Wettability - Fundamentals and Applications. in *Progress in Adhesion and Adhesives* 331–365 (2020).
23. Heltzel, A., Battula, A., Howell, J. R. & Chen, S. Nanostructuring Borosilicate Glass With Near-Field Enhanced Energy Using a Femtosecond Laser Pulse. *J Heat Transfer* **129**, 53–59 (2007).
24. Hansch, T. W. *et al. Springer Series In.* www.springer.com/series/624.
25. Luo, H., Zhang, Y., Yu, J., Dong, X. & Zhou, T. Additive, subtractive and formative manufacturing of glass-based functional micro/nanostructures: A comprehensive review. *Mater Des* **233**, 112285 (2023).
26. Sugioka, K., Michael, M. & Pique, A. *Laser Precise Microfabrication. Book* (2010).
27. Park, K. W. & Na, S. J. Theoretical investigations on multiple-reflection and Rayleigh absorption-emission-scattering effects in laser drilling. *Appl Surf Sci* **256**, 2392–2399 (2010).
28. Wang, J. *et al.* Effects of laser processing parameters on glass light guide plate scattering dot performance. *Opt Laser Technol* **115**, 90–96 (2019).
29. J.R. Philip. The Scattering Analog for Infiltration in Porous Media. *Reviews on Physics* **27**, 431–448 (1989).
30. Han, T. Y., Shr, J. F., Wu, C. F. & Hsieh, C. Te. A modified Wenzel model for hydrophobic behavior of nanostructured surfaces. *Thin Solid Films* **515**, 4666–4669 (2007).
31. Vüllers, F. *et al.* Bioinspired Superhydrophobic Highly Transmissive Films for Optical Applications. *Small* **12**, 6144–6152 (2016).
32. Nguyen-Tri, P. *et al.* Recent progress in the preparation, properties and applications of superhydrophobic nano-based coatings and surfaces: A review. *Prog Org Coat* **132**, 235–256 (2019).
33. Rico, V. *et al.* Robust anti-icing superhydrophobic aluminum alloy surfaces by grafting fluorocarbon molecular chains. *Appl Mater Today* **21**, (2020).
34. Terriza, A. *et al.* C-C4F8 plasmas for the deposition of fluorinated carbon films. *Plasma Processes and Polymers* **11**, 289–299 (2014).
35. Kumar, M., Bhardwaj, R. & Sahu, K. C. Motion of a Droplet on an Anisotropic Microgrooved Surface. *Langmuir* **35**, 2957–2965 (2019).
36. Ding, Y. *et al.* Anisotropic wetting characteristics of droplet on micro-grooved surface. *Colloids Surf A Physicochem Eng Asp* **633**, (2022).
37. Fan, C. F. & Çağın, T. Wetting of crystalline polymer surfaces: A molecular dynamics simulation. *J Chem Phys* **103**, 9053–9061 (1995).
38. Liu, M. *et al.* Transparent superhydrophobic EVA/SiO₂/PTFE/KH-570 coating with good mechanical robustness, chemical stability, self-cleaning effect and anti-icing property fabricated by facile dipping method. *Colloids Surf A Physicochem Eng Asp* **658**, (2023).
39. Guo, W. *et al.* A highly transparent and photothermal composite coating for effective anti-/de-icing of glass surfaces. *Nanoscale Adv* **4**, 2884–2892 (2022).
40. Everts, M. & Mahomed, F. The effect of high values of relative surface roughness on heat transfer and pressure drop characteristics in the laminar, transitional, quasi-turbulent and turbulent flow regimes. *Heat and Mass Transfer/Waerme- und Stoffuebertragung* **60**, 1173–1193 (2024).
41. Ghosh, A., Beaini, S., Zhang, B. J., Ganguly, R. & Megaridis, C. M. Enhancing dropwise condensation through bioinspired wettability patterning. *Langmuir* **30**, 13103–13115 (2014).
42. Aoki, S., Uematsu, K., Suenaga, K., Mori, H. & Sugishita, H. A study of hydrogen combustion turbines. *Proceedings of the ASME Turbo Expo* **3**, 231–252 (1998).
43. Kabalnov, A. Ostwald ripening and related phenomena. *J Dispers Sci Technol* **22**, 1–12 (2001).
44. Tokuyama, M. Statistical Physics Theory of Ostwald Ripening. *Dynamics of Ordering Processes in Condensed Matter* 63–70 (1988).



“With each passing day, humanity becomes more and more victorious in its struggle against space and time”

(Guillermo Marconi)

6

Anti-icing and omniphobic performance of scalable hierarchical surfaces with permanent Cassie-Baxter wettability

Abstract

Relevant sectors like aeronautics demand reliable ice-repellent surfaces. However, existing solutions lack for durability, reproducibility, adaptability to complex geometries, and environmental sustainability. Biomimetic approaches to water-repellent phenomena have been inspired by animal and plant textures that feature nano-microscale roughness and a particular chemical functionalization to create highly effective surfaces with icephobic purposes. In this chapter, we propose the exploitation of hierarchical surfaces based on supported 1D core@shell nanofibers grown by combining vacuum and plasma-assisted deposition with a soft-template method. This protocol has been applied to medium-scale substrates and 3D aeronautics profiles. Anti-icing properties have been tested using advanced techniques, especially ice-wind tunnel facilities, and environmental electron microscopies. The developed hierarchical surface has exhibited stable superhydrophobic and omniphobic behaviour consequently with a permanent Cassie-Baxter wetting state even at low temperature, humid and windy environments. In addition, these surfaces were tested as anti-fouling, self-cleanable, and icephobic, revealing potential implementation in outdoor protective applications.

6.1 Introduction

In cold seasons, as well as in working conditions where the altitude is high, and temperatures decrease, effects related to ice formation and ice accumulation, frost, and fogging phenomenon are highly significant for applications such as aeronautics, where ice accreted on different parts of aircraft can produce several damages affecting aerodynamics, communications, and damage of different sensors. Ice accumulation on aircraft can disrupt airflow, reducing lift and increasing drag, which creates dangerous flying conditions. Other application fields -affected by low temperature working conditions- could be related to wind energy, power transmission systems, outdoor security cameras, commercial and domestic refrigeration systems, traffic, construction, and food cold chain among others^{1,2,3}. For example, ice buildup on transmission lines can cause them to sag or break, resulting in power outages and potential hazards to nearby structures and people. Other reasons why icing issues should be solved are related to economic impact, efficiency, and environmental considerations. Such scenarios, endangering mainly safety and reliability in their respective fields, highlight the need to find systems capable of preventing the formation and accumulation of ice.

To prevent ice formation and accumulation (anti-icing passive capability) or remove ice efficiently once it has been formed (de-icing active performance), the most sensitive devices are equipped with ice protection systems (IPSs)⁴. Presently, these IPSs, are classified as active systems, as they require external energy to function. The most widely used active systems employ mechanical⁵, chemical⁶, or thermal methods^{7,8}, with thermal technology being the most advanced and commonly implemented in the aviation industry, for wing surfaces, leading edges, engines (air inlets), propellers and rotors and sensors and pitot tubes⁹. However, in certain places of aircraft, IPSs are not viable or efficient due to limitations such as weight, space, or energy requirements, making passive systems more suitable. For example, the phenomena known as secondary or runback icing occurs when melted ice coming from active IPSs moves to downstream areas of thermally covered zones in both aircraft and wind turbines, reaching sensors and other operational devices. Through these secondary processes, the liquid water flows to unprotected regions and refreezes beyond the ice protected areas¹⁰. Other crucial aerodynamic surfaces, like wing leading edges and control surfaces, rely on passive ice protection to

avoid compromising stability from added weight or vibrations. Small external sensors, such as those for temperatures, pressure, and airspeed, also require passive solutions, as active systems could interfere with their functionality. Other engine components, including air intakes and fan blades, can benefit from passive methods by maintaining airflow efficiency and reducing energy use. Even active systems, to be more energy efficient, also require passive surfaces, protective and preventive ones, that reduce interaction with ice. In this chapter, we propose nanostructured multicomponent passive solutions capable of reducing interaction with ice, thus addressing one of the hybrid solutions outlined in the SoundofIce project.

Superhydrophobic surfaces, exhibiting remarkable water repellency with a contact angle (CA) greater than 150° and a rolling-off angle (RoA) below 10° , known as a Cassie-Baxter (CB) state^{11,12,13} have been identified as promising solutions for icephobic applications^{3,14}. Typically, that repellent wetting behavior is achieved through micro-nano structured configuration combined with low surface energy chemical termination, what significantly reduces the solid-liquid contact area partly thanks to the ability to trap air, which in turn could decrease the thermal exchange required for the phase transition at low temperatures (take into account the low thermal conductivity of stationary air, around $0.026 \text{ Wm}^{-1}\text{K}^{-1}$)¹⁵. Although it is commonly assumed that the thicker the passive system, the lower the heat transfer through it to prevent the ice formation, the thermal conductivity of the materials does not depend on the insulating thickness. So, in a porous surface, the thermal conductivity of trapped air plays a fundamental role, that depends inversely on the air molecule mean free path (a few tens of nanometres) to the pore size ratio¹⁵. Since low temperatures lead to lower air thermal conductivity¹⁶ they are the solid surface contact points that promote the ice nucleation degrading the icephobic properties. Therefore, by minimizing the contact points of water / surface interaction, superhydrophobic porous surfaces should minimize the probability of heterogeneous ice nucleation at cold environments, thus preventing ice formation.

Additionally, moisture content can reduce the surface thermal resistance because the thermal conductivity of water is 20 times greater than that of room air. So, at low temperatures and under notable humid conditions, water absorption in porous structures leads to an increase in the effective thermal conductivity of the surface¹⁷ allowing the condensation of water in the pores,

which would reduce the number of open pores in the structure. Also, surface tension increases when the temperature decreases that affect the wettability, that is, promoting the Cassie-Baxter (“*lotus-like*”) superhydrophobic to hydrophobic Wenzel (W, “*petal-like*”) behaviours transition^{18,19}, which increases the water/surface contact area, being enhanced if roughness is present, promoting freezing. Thus, the CB to W transition accelerates the heterogeneous ice nucleation and increases the strength of ice adhesion to the porous surfaces²⁰. Even if the temperature returning to room values, the reverse transition could not occur²¹ due to a high surface free energy state and structural changes. Returning to the C-B state would require removing this additional surface free energy or restoring air pockets, now filled with water, what is challenging without active intervention. Therefore, the surfaces lose their water repellency and become sticky, compromising their icephobic properties or the repellent, antimicrobial response as biomaterials^{22,23}. This irreversibility is crucial for applications needing stable water interactions, whether to repel or retain water²⁴. Current strategies used to mitigate the transition from CB to W states include surface texturing and surface chemistry modification using low surface free energy coatings, molecules, and liquids in order to stabilize the water repellence capability^{22,23,25}.

It should be noted that the roughness at the nanoscale can also play a key role in the ice nucleation, as exposed in Chapter 1, because concave motifs at low temperature seem to reduce the energy barrier of water molecules to organize themselves and give rise to ice crystals. However, the influence of the roughness on the ice formation from water liquid droplets, specially on superhydrophobic surfaces, is still uncertain or unconcluded, sometimes due to the difficulty of distinguishing topographical from chemical effects²⁶. On the contrary, the interfacial free energies between vapor/liquid and solid surface seem to govern the different freezing events since vapor to surface interfacial energy is higher than the nucleus to surface corresponding one. Therefore, an ice nucleus from the liquid phase is expected to have a larger contact angle than one from the vapor phase, and consequently, the reduction of the energy barrier to trigger freezing due to the topography is less important when ice nucleation comes from a liquid droplet. Moreover, water droplet temperature has an influence in the freezing mechanism since supercooled water presents higher viscosity and surface tension than room temperature water²⁷.

However, the Achilles heel of icephobic surfaces is stability and durability. It is well known that the mechanical properties and thermal performance of passive surfaces age. One of the main effects is the wear of insulating agents or the infusion of ambient air that can absorb moisture into the porous structure. Both passive and passive-protected active systems to mitigate ice accumulation must be designed to ensure stability, durability and substrate compatibility, particularly in aeronautical applications where a diverse range of materials is involved, including different metallic alloys, composites and laminates. Extending these concerns to other substrates, such as glass or polymeric surfaces, highlights the challenges of developing systems that prevent ice formation while ensuring compatibility and transparency. These configurations are also applied in other fields, such as the automotive industry for heated windshields, displays and outdoor screens and architectural glazes²⁸. Therefore, the strategies to overcome applied incompatibilities must be adaptable to any type of substrate and surface.

In this chapter, icephobic passive surfaces based on hybrid hierarchical nano-micro-structures are proposed and studied to prevent ice formation on medium area samples and cylindrical geometries. We propose the use of laser patterning of metallic substrates (aeronautical substrates) and the development of supported 1D core@shell nanofibers to produce superhydrophobic surfaces, even at low temperatures. This approach provides a surface development with permanent Cassie-Baxter wettability by combining three levels of roughness with a peculiar chemical modification. Particularly, the method involves nanosecond IR laser treatments of AL6061 substrates followed by the application of the soft-template method for the formation of core@shell nanofibers with tunable morphology, density and composition^{29,30}.

Laser technology is applied in metallic substrates to achieve aleatory or ordered roughness at the microscale. Herein, we advance over the results presented in Chapter 3, extending the growth of core@shell nanofibers to laser treated alloys at larger scales and on complex substrates shapes and morphologies, including airfoils. We take advantage of the combination with low free energy materials in small content/concentration, like PDMS and fluorinated molecules grafting to produce highly robust and omniphobic hierarchical surfaces. On a step forward, we test the anti-icing capability under harsh environmental conditions employing advanced large facilities and aeronautical conditions.

As explained in Chapter 2, the nanofibers resulting from the soft-template method³¹ were developed using two organic molecules with different sublimation temperatures to provide different parameter options related to nanofiber density, diameters, and lengths, particularly different surface aspect ratio. The sublimation temperature depends on the molecule employed as a building block of the organic nanowires and can be compatible with temperature-sensitive substrates. Thus, the results gathered in this chapter can be straightforwardly extended to glass and polymeric substrates to allow for transparent and flexible anti-icing surfaces. Finally, the proposed passive surface will be tested as universal protective ending of active de-icing systems governing by two different fundamentals: electrothermal heating and surface acoustic waves.

6.2 Experimental Section

6.2.1 Materials and samples preparation

AL6061 polished plates of 10 x 5 cm² and aeronautics profiles of 2 cm of diameter and 10 cm of length were supplied by INTA (National Institute of Aerospace Technology) as shown in **Figure 1 a**). These substrates were cleaned using detergent water solutions.

Laser treatments of these substrates were performed at room temperature using a 20 W diode-pumped Nd laser operating at 1064 nm with a pulse width of 100 ns (see Chapter 2). It was the first step of generating a first level of micro-roughness. The next steps devoted to the obtention of a hierarchical surface that combines nanowires of nanostructured surface are included in the growth of nanostructures by the soft-template method using OPVD technique (Chapter 2) with two different organic molecules: 1,5-diaminoanthraquinone (DAAQ) and free metal phthalocyanines (H₂Pc) (see Figure 1 b)), with 150°C and 350°C sublimation temperature, respectively, at the working pressure of 10⁻³ mbar of Ar.

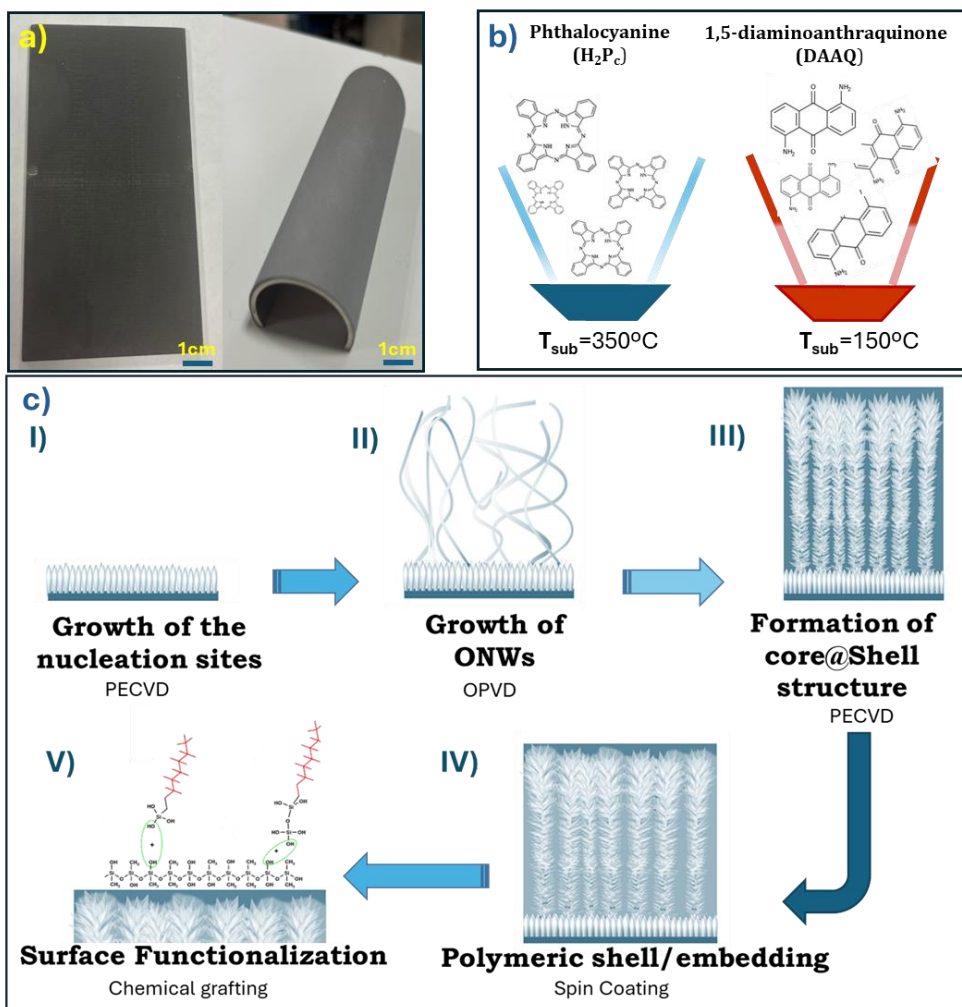


Figure 1. a) AL6061 polished plates and aeronautic profiles after a mild laser treatment; b) different organic molecules (free phthalocyanine and 1,5-diaminoanthraquinone) employed for organic nanowires grow by OPVD process; c) schematic of the core@shell nanofibers deposition including PDMS embedding and fluorine-based grafting.

Both molecules present one-dimensional growth of organic nanowires (ONW) directed by π -conjugated stacking. Substrate temperatures above 200 °C and 60 °C for H₂Pc and DAAQ were fixed, respectively. It is worth noting that in the case of the DAAQ, temperatures as low as 60 °C make the growth of ONWs compatible with temperature-sensitive substrates, such as polymers. TiO₂ seed layers and shells were fabricated by PECVD (Chapter 2) as shown in Figure 1 c). The shell thickness was controlled by the growth duration and rate of the TiO₂ on the ONWs decorated substrates, being the 250 nm the nominal thickness of the TiO₂

shell. The final steps involve the formation of a thin layer of PDMS (80 nm thickness), working as hydrophobic and protective coating to enhance the substrate adhesion, the nanostructures flexibility, (according to results in Chapter 3) and expected resilience to ice accretion and impact. PDMS was functionalized by grafting of 1H,1H,2H,2H-Perfluorooctyltriethoxysilane (PFOTES) molecules. This protocol allowed the comparison of surfaces with different morphologies, and nanofibers density and surface aspect ratio (defined as the nanowires length /diameter ratio) while keeping the same chemical modification.

Hereafter, the following labeling is employed to include the multi-step processing of the surfaces: AL - aluminum substrates, L- laser treatment, P- PDMS layer, and F- fluorinated grafted molecules. Thus, the samples were mentioned as AL-L-DAAQ@TiO₂-P-F or AL-L-H₂Pc@TiO₂-P-F depending on the used organic precursor. Reading the label from left to right represents the step-by-step processing of the substrate (except for the formation of the TiO₂ seed thin film (TF) not included as it is inherent to all the surfaces) to end up in the chemical functionalization of the external shell.

6.2.2 Surface characterization: morphology, wetting, environmental stability, durability and anti-icing capability

The morphological aspects of the hierarchical surface have been explored by SEM analysis in both cross section and top view configurations. Surface aspect ratio was estimated by means of SEM image treatments using ImageJ software. The wetting properties of the potential passive surfaces were evaluated by contact angle measurements using 2 µl polar (water contact angle - WCA) and non-polar liquid (diiodomethane contact angle - DCA) droplets in a contact angle goniometer (Chapter 2). Data presented is an average over 3 measurements per condition. Omniphobic properties were also evaluated through rolling-off angle (RoA) measurements with biological fluid simulants described in Chapter 2. To evaluate the stability of the hydrophobic state and to check the possible C-B to W transition, evaporation process monitoring³² of 5 µl bidistilled water droplet deposited on the surface at low temperature were carried out in terms of finding correlations between WCAs, Triple-Phase-Contact-Line (TPCL) diameter and Laplace pressure (details included in Chapter 2).

Durability tests (detailed in Chapter 2) were conducted on both hierarchical systems through exposure to UV-vis light using a 300 mWcm^{-2} light source for 90 min at a 30 cm distance between light source and faced samples. Thermal cycling in a conventional laboratory oven was performed for 3 cycles from room temperature to $150 \text{ }^{\circ}\text{C}$ for 120 min. Immersion tests were carried out in two different solvents (50 ml of isopropanol and acetone, respectively) for 30 minutes. Additionally, rain erosion tests were conducted in the universal machine at $5 \text{ }^{\circ}\text{C}$ using two different working modes: water jet and water dripping with 30° tilting and 50 cm distance between sample and water dispenser, for 90 min in each working mode. Measuring WCA before and after durability experiments was used to verify the wetting stability of the passive surface.

Environmental stability and anti-fogging behavior were evaluated through microscopic observation of the water vapor condensation on the surface carried out by “in situ” Environmental Scanning Electron Microscopy (ESEM)^{33,34} performed at INSA as well as at BIONAND, operating at 30-35 kV, with pressure values from 300 Pa to 1500 Pa to achieve water condensation and sample temperature kept at $2 \text{ }^{\circ}\text{C}$. In the annex supporting this chapter, Environmental Transmission Electronic Microscopy (ETEM)³⁵ study of the water/nanofibers interaction at high resolution depending on their wetting state is included, having also been performed at INSA (experiments detailed in Chapter 2).

The anti-icing capability of the hierarchical surfaces was evaluated through freezing delay experiments, pull-off ice adhesion and complemented by advanced tests carried out at the Icing Wind Tunnel (IWT) at INTA simulating real flight conditions. Freezing delay was performed under dry conditions using a nitrogen flow in a sealed chamber, with $2 \text{ }\mu\text{l}$ of bidistilled water droplets, at a temperature of $-5 \text{ }^{\circ}\text{C}$. Pull-off ice adhesion experiments were carried out in the Universal Material Testing Machine at $-13 \text{ }^{\circ}\text{C}$ with 90% relative humidity using 1 ml of bidistilled water, Teflon cantilevers, and waiting for more than 20 min for the complete freezing process of ice particle. Two icing tests were performed in the IWT: centrifugal ice adhesion and ice accretion experiments to evaluate the anti-icing properties under harsh conditions. Ice adhesion experiments were conducted using a centrifugal mode (300 rpm) with glaze ice blocks of about $2.75 \text{ cm} \times 5 \text{ cm}$ formed at -5°C and 70 m/s of air speed, Liquid Water Content (LWC) around 1 g/m^3 and Mean Volume droplet Diameter (MVD) of $20 \text{ }\mu\text{m}$. Ice accretion experiments were realized with a medium distance of 50 cm between the sample

and the supercooled droplet injector, at -5°C without collimators, working with the same glaze ice formation parameters that in the ice adhesion test. Once the ice is generated, the experimental setup is placed inside the cold chamber where the tunnel is located, maintaining the same temperature as the ice formation conditions³⁶, to perform both adhesion and accretion experiments.

6.3 Results and discussion

6.3.1 Hierarchical surfaces: topography and morphology

Figure 2 shows characteristic SEM and confocal images of the morphology of the laser-treated aluminum alloys.

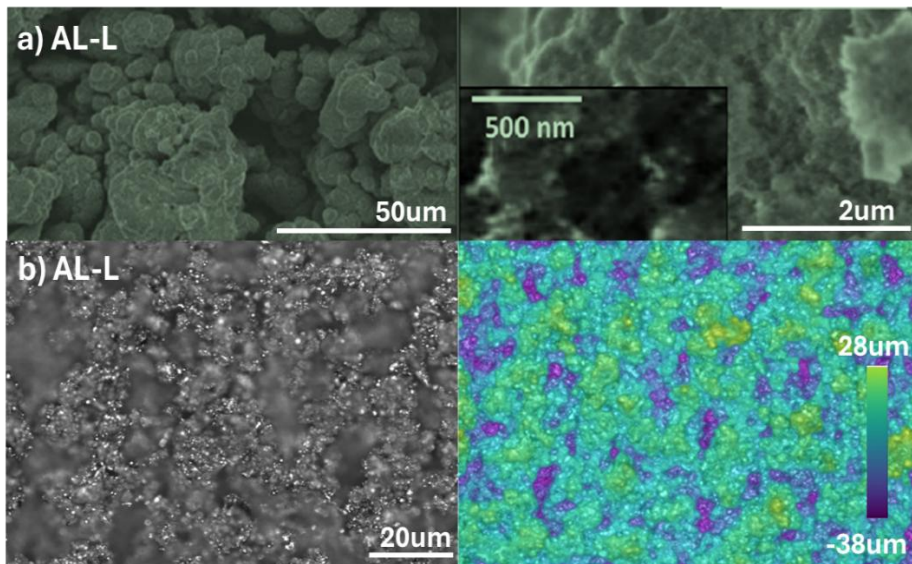


Figure 2. a) Top-view SEM micrographs of AL-L at different magnifications; b) confocal and 2D map images of AL-L surface.

Figure 2 a) presents SEM micrographs of the AL-L sample surface at different magnifications fabricated under the so called “explosive” laser conditions (described in Chapter 2). It exhibits a micro-scale porous random roughness, i.e., without an orderly pattern, with medium size grooves in the range between 10 and 20 μm . The surface microstructure consists of deep, narrow features, with valleys of 65 μm in depth shown in the confocal image and 2D profile at the micro-scale (Figure 2 b)). The main roughness parameters, S_q (root mean square

height) and S_a (arithmetical mean height) are 13 μm and 10 μm , respectively, reaching a surface roughness scale of tens of microns. The next step to achieve the hierarchical surfaces (combination with the nanoscale) is the growth of nanostructures exploiting the soft-template method. **Figure 3** a)-c) shows the nanofibers grown on a reference Si(100) wafer, with phthalocyanine ONWs and a TiO_2 shell nanostructure. Figure 3 d)-f) display the 1,5-diaminoantraquinone core-based nanofibers finished with similar TiO_2 conformal coating grown on the laser treated substrate.

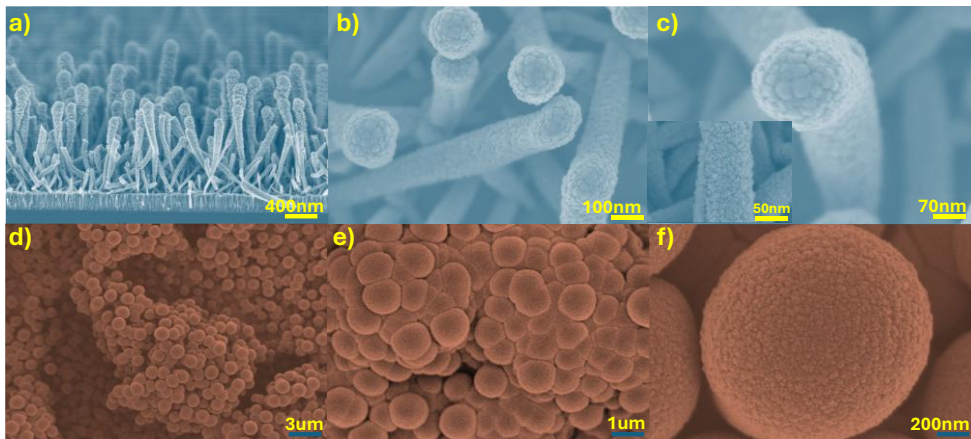


Figure 3. Microstructural characterization by SEM images at different magnifications for: a-c) $\text{Si-H}_2\text{Pc@TiO}_2$ (flat silicon reference substrate), and d-f) AL-L-DAAQ@TiO_2 (laser treated aluminum substrate).

Figure 3 a) shows the preferential vertical alignment of the nanofibers on the substrates. This alignment is related to both the presence of the electrical field in the plasma sheath and the enhanced stiffness of the nanofiber upon the formation of the TiO_2 shell. Figure 3 b) presents the formation of high density DAAQ@TiO_2 nanofibers obtained on the microstructured laser treated substrate. As it has been previously reported³⁷ the ONW density is enhanced on laser grooves due to a high number of nucleation sites and exalted supersaturation conditions. The formation of 1D-aligned nanofibers does not clog the laser grooves but produces two new levels of roughness, i.e., in the microscale, related to the nanofibers' length and at the nanoscale, given the nanofibers' surface roughness. Both SEM zoomed images (Figure 3 c) and f)) highlight the nanostructure of the conformal TiO_2 shell with a cauliflower-like configuration

generated by the nanocolumnar arrangement of the TiO₂ nanocolumns. This nanostructured morphology depends on the plasma conditions during the formation of the shell and is equivalent for both organic cores. However, in the example in Figure 3 d)-f) the TiO₂ deposition conditions lead to a thicker shell of 200 - 250 nm (compared scale bars between panels c) and f)). Therefore, the nanostructured surface provides a third scale of roughness to the system in the range of the tens of nm that is conditioned to the used ONW core, which may define the roughness hierarchy needed for a superhydrophobic Cassie-Baxter surfaces^{29,34,38}. Employing different organic molecules allows for controlling the density, and length of nanofibers. Thus, the average nanofiber length and diameter for the H₂Pc were 1 μm and 60-70 nm, respectively, in comparison with DAAQ core, showing 600 nm and 90-100 nm, respectively. This phenomenon is related to the π-conjugated specifications and single-monocrystalline growth of this organic molecules according to different variables such as seed layers, temperature of the deposition, deposition rate and work pressure³⁹. From those average length and diameter as well as the shell thickness, aspect ratio values can be estimated. Thus, the hierarchical samples formed by supported 1D core@shell nanostructures using H₂Pc and DAAQ exhibits aspect ratio values of 9 and 1.5, respectively.

The nanofibers were subjected to a hybrid chemical surface modification, previously explored in Chapter 3, in order to enhance substrate adhesion, mechanical and repellence properties. **Figure 4** shows the hierarchical surfaces after embedding in PDMS and perfluorinated grafting, i.e., AL-L-DAAQ/H₂Pc@TiO₂-P-F. The surface nanoroughness, although softened, is still respected when the nanofibers were coated with the PDMS layer as observed in Figure 4 d) and h).

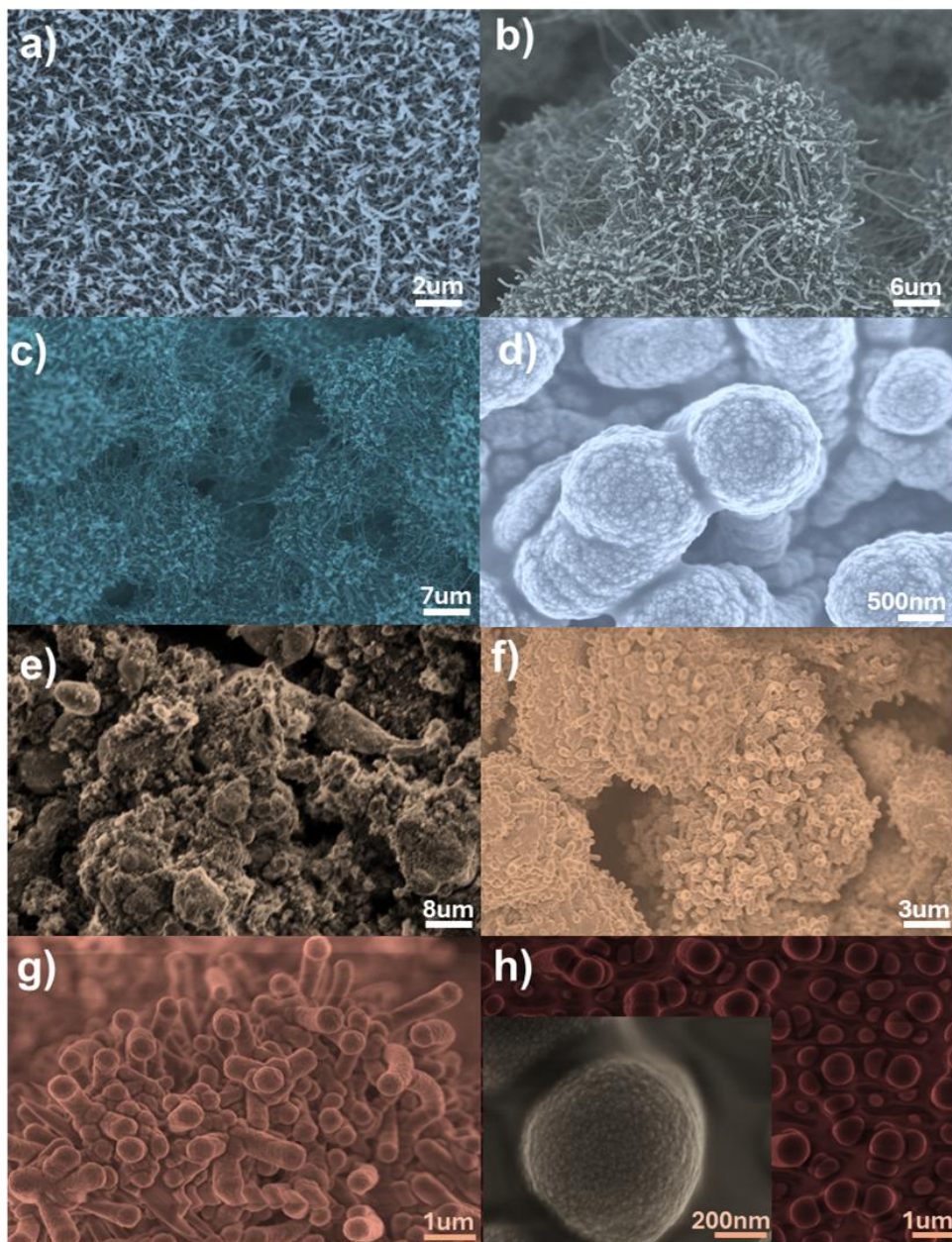


Figure 4. SEM microstructural characterization of the hierarchical surfaces in function of the core organic nanowires, both coated and modified with PDMS and fluorine molecules, respectively: a)-d) AL-L-H₂Pc@TiO₂-P-F and e)-h) AL-L-DAAQ@TiO₂-P-F.

Although the deposition of PDMS by spin coating was optimized to achieve a suitable thickness to preserve the generated micro- and nano-roughness, the different core@shell nanostructure aspect ratio promotes different degrees of

polymeric coverage: from conformal coatings to partially embedded nanofibers, as is the case with shorter DAAQ@TiO₂ nanofibers. The average thickness of the PDMS is 80 nm which results in a mean thickness increase of ca. 40 nm for both AL-L-H₂Pc@TiO₂-P-F and AL-L-DAAQ@TiO₂-P-F nanostructures. It should be noted that the incorporation of perfluorinated molecules to the surface does not affect the nanostructure since its estimated length is around 15 Å. The free movement and flexible characteristics of these fluorinated chains well anchored to the surface are responsible for preventing interaction with external agents⁴⁰. This type of hierarchical porous surface morphology has been proposed as an effective approach to achieve superhydrophobicity and to mitigate ice formation by reducing heat transfer to the substrate^{34,41,42}. In the following sections, we thoroughly analyse the wetting and anti-icing properties of our hierarchical nanostructures and present their compatibility with different active de-icing approaches.

6.3.2 Wetting properties of hybrid hierarchical surfaces

The wetting properties were evaluated through static contact angle measurements using polar and non-polar liquids at room temperature and water at subzero temperature. As shown in **Figure 5**, the water and diiodomethane contact angle measurements were obtained for different levels of surface hierarchy from aluminum reference to complete hybrid core@shell systems (AL-L-H₂Pc/DAAQ@TiO₂-P-F). The AL sample exhibited a partial hydrophilic state with WCA value of approximately 70°. After laser treatment, hydrophobicity slightly increased reaching WCA~90°, likely related to a higher surface roughness and presence of carbonaceous species due to storage and aging under room conditions⁴³. The deposition of TiO₂ thin films, which were later used as a nucleation seed layer for the growth of the supported 1D core@shell nanostructures, involved a decrease of the contact angle on both Al reference and laser treated substrates, which did not exceed 80° (AL-TiO₂ TF and AL-L-TiO₂ TF). This evolution responds to the lower contact angle corresponding to TiO₂ surfaces, which present hydrophilic behavior just after deposition under plasma conditions and evolve toward a higher contact angle upon exposure to room environment.

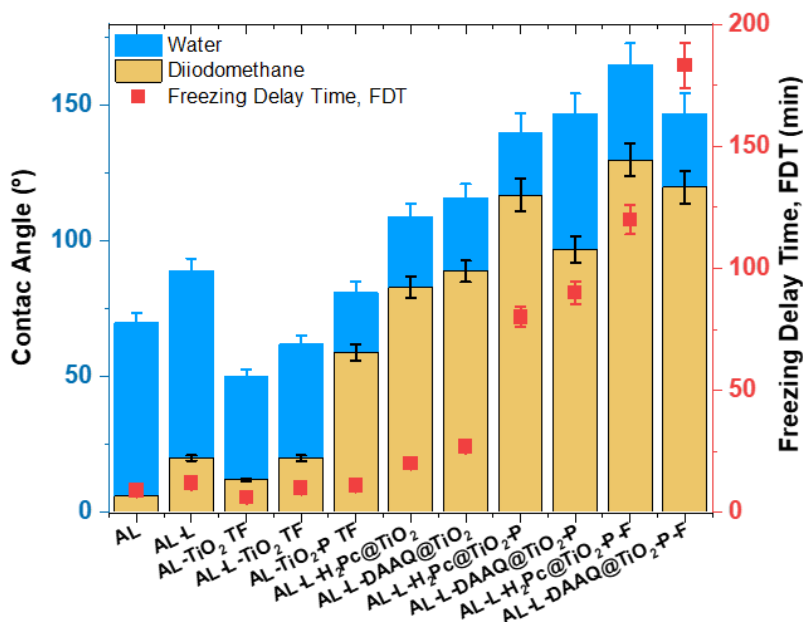


Figure 5. Contact angle measurements for increased complexity of surface hierarchy, characterized by sessile droplets of 2 μl , including bi-distilled water and diiodomethane. Freezing delay time was estimated for bi-distilled droplets of 2 μl and surface temperature of $-5\text{ }^{\circ}\text{C}$. (The statistics in each experimental data are reflected by a $\pm 5\%$ error).

Contact angles below 70° were observed for diiodomethane ($\sim 51\text{ mNm}^{-1}$ of surface tension) for the reference substrate, AL-L and TiO_2 seed layers, highlighting the amphiphilic nature of this type of metal oxides (TiO_2)⁴⁴.

As the roughness scales with the growth of core@shell nanostructures, the contact angle increases for both water and diiodomethane droplets. Particularly, the contact angle values of AL-L-DAAQ@ TiO_2 and AL-L- H_2Pc @ TiO_2 samples may be compatible with a typical *petal-like* wetting behavior⁴⁵, (i.e., lower than 150°) but still far from the reported *lotus* effects⁴⁶.

There is a substantial enhancement of both hydrophobicity and oleophobicity behaviors for samples coated with the PDMS thin film. While the interaction with water seemed to be more influenced by surface chemistry (PDMS) in view of the similar WCA values within the margin of error, the higher surface aspect ratio has promoted greater repellency to diiodomethane droplets. Despite PDMS is one of the *petal* effect model materials⁴⁶, its combination with a structural hierarchy provides contact angle values in the range expected for the *lotus* effect,

particularly for the AL-L-DAAQ/H₂Pc@TiO₂-P surface with 150° and close to 120° of WCA and DCA values, respectively. In general, both passive strategies using DAAQ and H₂Pc as organic cores for nanostructures growth obtained notable improvements of repellency (superhydrophobicity and oleophobicity) with the presence of fluorinated molecules anchored to the PDMS surface (last two bars in Figure 5). The highest WCA and DCA values were obtained with the hybrid surface modification (F+P) of the H₂Pc core-based hierarchical samples. This result is in good agreement with the lower solid fraction expected from the H₂Pc-based nanofibers endowed with a higher aspect ratio than the DAAQ ones. Moreover, both modified hierarchical surfaces (AL-L-H₂Pc/DAAQ@TiO₂-P-F) exhibit RoA values (related to water and diiodomethane droplet sliding) lower than 5°, which indicates a full repellence (superoleophobic response) as it is collected in the **Table 1**.

To evaluate the wetting stability of the developed hierarchical surfaces in comparison to the AL reference sample, evaporation experiments at 0 °C were carried out. 5 µl of bidistilled water were used in a dry atmosphere supplied by N₂ gas flow. The objective was to differentiate superhydrophobic from hydrophilic wetting responses by analysing the influence of Laplace pressure during the droplet evaporation process when it is deposited on these special open porous hierarchical structures. Laplace pressure, detailed in Chapter 2, states that the pressure difference between the inside and outside of a drop increases with the liquid surface tension (γ) and decreases with the droplet curvature radius (R). This pressure is the result of the liquid's tendency to reduce its surface area due to surface tension acting towards the interior of the liquid to maintain its ideal spherical shape. Typically, rough wettable surfaces create negative Laplace pressures, enabling capillary wicking, while rough non-wettable surfaces create positive Laplace pressures, exhibiting fluid repellency⁴⁷. Particularly, superhydrophobic nanostructures lead to high Laplace pressure values on water droplets resulting in bouncing and sliding phenomena on these non-sticking surfaces⁴⁸.

The droplet evaporation evolution has been typically used as indicative parameter of the stability of a Cassie-Baxter state. Thus, if the pressure of the liquid can overcome the surface tension of the air trapped in the pores during the evaporation, the wettability evolves towards Wenzel-type, as water can

penetrate and fill the pores. This feature allows to identify the transition from superhydrophobic to hydrophobic/hydrophilic behaviours.

Table 1. Rolling-off angle values of 10 μl droplets of different liquids on the hierarchical surfaces compared to the substrate reference.

Rolling-off angle ($^{\circ}$)/10 μl	Water	Oil	Humic acid	Sodium alginate	Bovine serum
AL	>90	>90	>90	>90	>90
AL-L	>90	>90	>90	>90	>90
AL-TiO ₂ TF	>90	>90	>90	>90	>90
AL-L-TiO ₂ TF	90	90	90	90	90
AL-TiO ₂ -P TF	71	59	75	75	77
AL-L-DAAQ@TiO ₂	38	53	51	53	50
AL-L-H ₂ Pc@TiO ₂	45	49	50	53	49
AL-L-DAAQ@TiO ₂ -P	15	29	27	25	24
AL-L-H ₂ Pc@TiO ₂ -P	38	45	41	42	42
AL-L-DAAQ@TiO ₂ -P-F	<2	<2	<2	<2	<2
AL-L-H ₂ Pc@TiO ₂ -P-F	<2	9	6	7	6

Figure 6 shows the trend of the WCA and the TPLC diameter of a 5 μl water droplet deposited on the AL-L-DAAQ@TiO₂-P-F hierarchical surface as function of the Laplace pressure compared to the case on the reference Al6061 surface during the evaporation event at temperature close to 0 $^{\circ}\text{C}$.

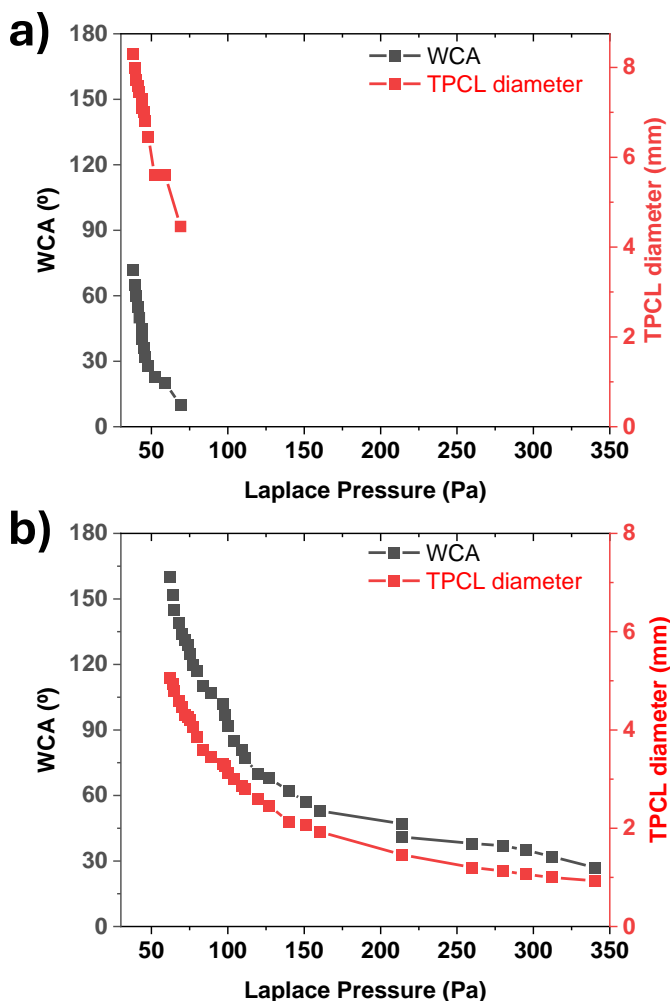


Figure 6. Evolution of the water contact angle and triple phase contact line diameter of a 5 μl water droplet as a function of the Laplace pressure approximately according to $P=2Y/R$, deposited on a) AL6061 ref. surface (hydrophilic) and b) AL-L-DAAQ@TiO₂-P-F hierarchical surface (superhydrophobic) during evaporation at 0 °C in dry environment.

Depending on the way the droplet evaporates, the TPCL evolution will be different, whether the change in volume (droplet radius) or the change in surface tension (contact angle) predominates⁴⁹. It should be noted that the evaporation rate must compete with the cooling and freezing processes at low temperature. Moreover, a dry environment tends to favour the evaporation due to the difference in humidity between the droplet and the surrounding air as well as the higher water vapor pressure.

For the reference surface, a hydrophilic behaviour was reflected by low WCA values (around 70°) at the beginning of the experiment, decreasing to values close to 10° by the end of the evaporation process at 0°C in dry atmosphere. The surface tension of a droplet typically increases as the temperature decreases. For water, the surface tension goes from 72.8 to 75.5 mNm^{-1} when the temperature drops from room to 0°C . Since the liquid surface tension is indicative of the cohesive forces between liquid molecules at the contact solid surface, these become stronger at low temperature and resist spreading out over the surface. Besides, at lower temperatures, the reduced molecular motion allows intermolecular forces to dominate, resulting in higher surface tension. This fact would result in the measurement of greater contact angles, which should be maintained as the volume of the drop is reduced by undergoing at low-temperature evaporation process. However, as the water evaporates, the amount of water molecules near the surface decreases, what, at low temperature, due to lower thermal movement, establishes stronger adhesive interactions with the surface reducing the water contact angle. Also, since the water droplet contour decreases as evaporation occurs together with the increase of water viscosity at low temperature, the droplet shape can change influencing the contact angle. On the other hand, most solid surfaces also increase their surface free energy at low temperatures that enhances the affinity to be wet. Therefore, the competition between all of these factors is involved in the resulting trend in the Figure 6. There was a fast drop for both WCA and TPCL diameter evolution consistent with such a hydrophilic behaviour of the flat reference. During evaporation, the droplet kept a low curvature shape defined by higher radius values at low Laplace pressure values (see first points in Figure 6 a)). In this region, the maximum Laplace pressure that the droplet deposited on the surface could withstand before the final changes in surface tension (caused by droplet disappearance) was around 60 Pa .

In contrast, the first WCA measurement on the hierarchical surface leads to a higher Laplace pressure as a consequence of a smaller droplet curvature (TPCL diameter) due to the more spherical shape adopted when deposited on a superhydrophobic surface. Also, slower and more gradual decrease of both WCA and TPCL diameter was observed in Figure 6 b) for the superhydrophobic AL-L-DAAQ@TiO₂-P-F surface, where the evaporation process lasted for 3 hours. In this case, WCA and TPCL diameter values presented extremely slow fall for

higher Laplace pressure values in comparison with the reference. Hence, the hierarchical sample with a characteristic Cassie-Baxter wettability has endowed with an outstanding resilience to the Laplace pressure influence⁵⁰. The multiscale roughness and chemical functionalization of this hierarchical system were able to delay the Cassie-Baxter to Wenzel transition at 0 °C until to 100 Pa. After that, the hierarchical surface delayed for longer time the droplet volume decrease until 350 Pa at the dry and cold environment.

6.3.3 Anti-fouling characterization

The ability to repel fluids simulating fouling agents can be used to demonstrate the anti-fouling capacity of surfaces. Various organic simulants of surface tension values lower than that corresponding to water, around 50-65 mNm⁻¹, were employed to assess this bio-fouling repellence similarly to that protocol previously presented in Chapter 4. **Figure 7** shows the contact angle measurements using different organic solutions together with different snapshots of the droplet interaction with the developed hierarchical surfaces. Contact angle values were quite low for the reference surfaces, with or without TiO₂ coating and even with the induced roughness state by the laser treatment. Meanwhile, a notable increase has been observed when a PDMS thin film was included, reaching values between 80-100° with various organic liquids droplets. The presence of nanostructures enhanced the repellency behavior, improving the omniphobicity for both nanofibers grown with DAAQ and H₂Pc cores, as shown in Figure 7. Besides, wrapping the supported 1D core@shell nanostructures with the polymeric coating did not include significant improvements in the anti-fouling response unless combined with the fluorinated functionalization. In fact, for fluids with similar surface tension, such as diiodomethane and bovine serum, both the hierarchical structures and those coated with PDMS showed a worse affinity for diiodomethane droplets, which are denser and more viscous compared to the bovine serum ones.

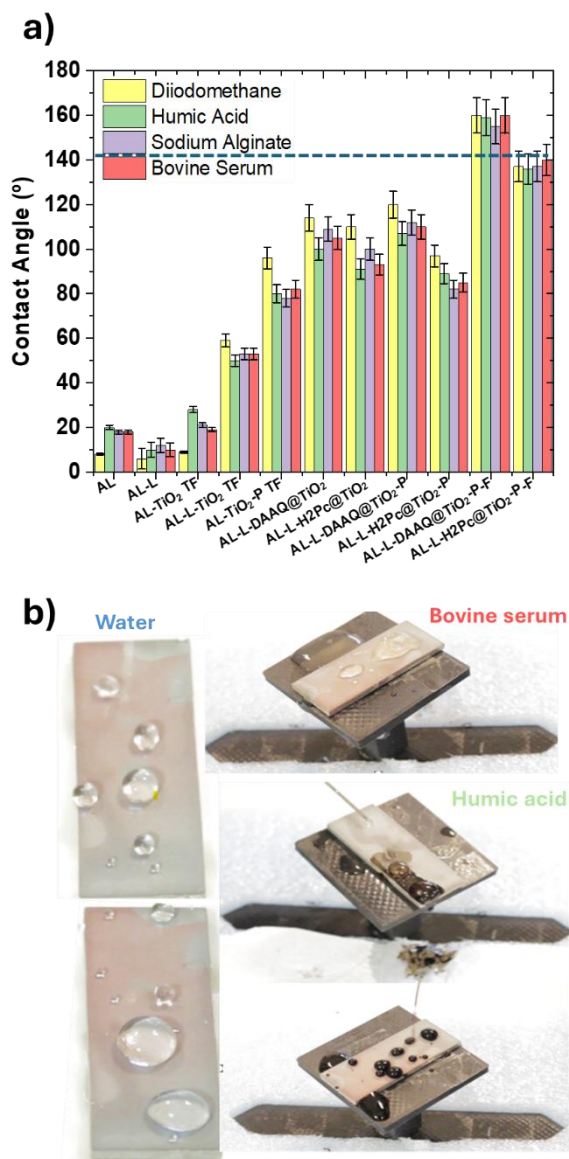


Figure 7. a) Contact angles of 2 μl droplets on the surfaces with different complex hierarchy. Data are shown for the following simulated fouling agents: diiodomethane, humic acid, sodium alginate, and bovine serum. b) Snapshots showing the anti-fouling response of the AL-L-DAAQ@TiO₂-P-F sample to different liquid droplets of 10 μl as labeled.

However, the presence of perfluorinated molecules leads to a well-defined anti-fouling properties regardless of the used fouling fluid. Particularly, the sample AL-L-DAAQ@TiO₂-P-F reached contact values close to 170°. This result agrees with the current literature that points to the surface chemical modification

necessary to achieve a total repellence (superomniphobic behavior)⁵¹, and its optimal combination with nanostructures⁵².

Table 1 presents the rolling-off angle values of larger droplets on the studied surfaces. The experience confirmed the repellent response of AL-L-DAAQ@TiO₂-P-F and AL-L-H₂Pc@TiO₂-P-F surfaces, with RoA values lower than 2° and around 6-9°, respectively, since a complete organic liquid droplet sliding on those surfaces. For the other hierarchical surfaces, such as the AL-L-DAAQ@TiO₂-P sample, the RoA values were ~ 25° for the different biological simulators, whereas higher values (~ 50°) were found for the bare hierarchical surface. The images in Figure 7 b) depict the complete droplet sliding behavior on the surface of the best anti-fouling surface, i.e., AL-L-DAAQ@TiO₂-P-F, which preserved superhydrophobic behavior even after the anti-fouling experiments.

6.3.4 Water condensation experiments

“In-situ” water condensation observation was carried out using environmental electron microscopy (ESEM). ESEM images sequence of the omniphobic AL-L-DAAQ@TiO₂-P-F and AL-L-H₂Pc@TiO₂-P-F surfaces in a supersaturated humid environment are presented in **Figure 8**. After 5 minutes (Figure 8 top) I-II) the water vapor pressure increased from dry conditions (~350 Pa) to wet conditions (~800 Pa) with no impact on the AL-L-H₂Pc@TiO₂-P-F surface, as evidenced by the absence of microdroplets in the micrographs. According to Figure 8 in Chapter 1, at 2°C the saturated vapor pressure corresponds to a value around 706 Pa. It is worth stressing that the electron beam scanning could be influencing the water condensation on the region under observation. Therefore, nearby unexposed areas with equivalent focus planes were periodically checked to see if water evaporation could occur due to continuous scanning³⁴. After 7 minutes, and increasing of the water vapor pressure until 1401 Pa, the surface remains unchanged (blurring is due to the water vapor supersaturated environment).

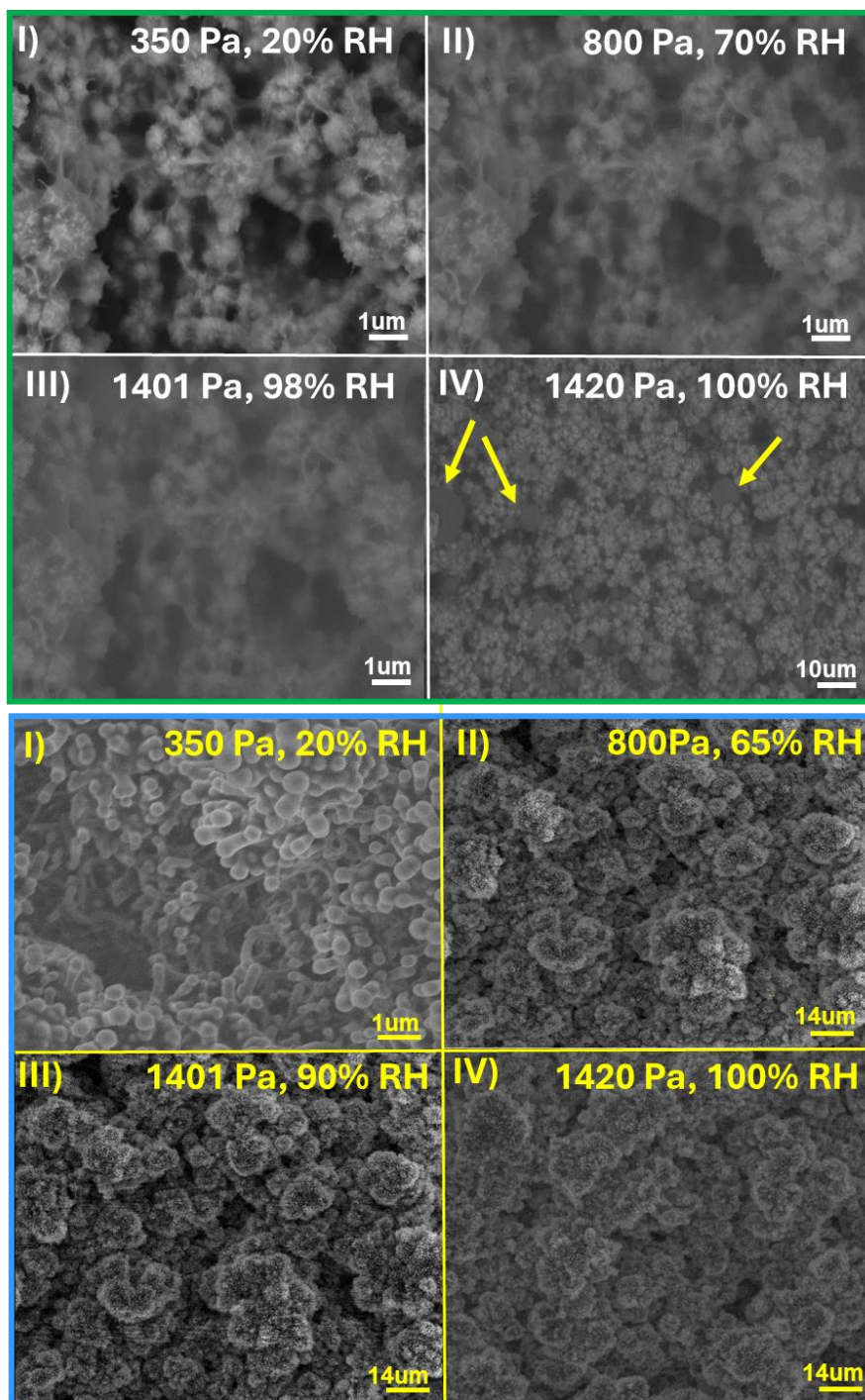


Figure 8. Top view ESEM micrographs for AL-L-H₂Pc@TiO₂-P-F (top green square) and AL-L-DAAQ@TiO₂-P-F (blue square bottom) surfaces at 2 °C for increasing water vapor pressure and relative humidity conditions (RH) as labelled.

At 1400 Pa of water vapor pressure, sample temperature increased until 6 °C (theoretical water vapor pressure of 935 Pa) and the relative humidity rose to 98% without any signs of water condensation on the cold hierarchical surface. Finally, after approximately 12 minutes at 100% RH, isolated spherical droplets (with an estimated diameter of 8 μm) began to be visible (see yellow arrows).

Figure 8 bottom) gathers the results of an equivalent experiment for the hierarchical surface of lower aspect ratio (i.e., from DAAQ organic cores). In this case, the surface resisted more than 40 minutes under higher water vapor pressure and high relative humid conditions without evidence of water condensation. At stages I) and II), the dual-scale roughness of this surface was clearly resolved, and even at 1400 Pa and 98% relative humidity, no microdroplets were observed. Considering the phase diagram of water from Figure 8 in Chapter 1, at high-pressure values such as 1400 Pa, liquid water should start to be present between 0 °C and 15 °C, with a humidity percentage of 98%. In conclusion, the superhydrophobic behaviour prevented the water condensation on the surface under severe temperature, pressure and relative humidity conditions. It should be noted that since water condensation is an exothermic process^{53,54} even with the little increase of the surface temperature, condensation on it was not appreciated unlike other more hydrophilic regions inside the microscope.

To understand the anti-fogging response, it should be considered the differences in thermal conductivity of the hierarchical surface materials. Standard thermal conductivity of AL6061 is 152 W mK⁻¹, meanwhile, the corresponding to amorphous TiO₂ (seed layer and shell) is in the range 0.2-0.7 W mK⁻¹, and even lower for PDMS, i.e. 0.15-0.2 W mK⁻¹^{55,56,57}. Since the cooling of the samples was carried out by using a Peltier plate below them (temperature sensor was placed there), water condensation could occur not only at the interior of the laser groove defects, but also at the sides and sample holder acting as low-temperature points of hydrophilic behaviour.

It is expected that the superhydrophobic Cassie-Baxter wettability of these hierarchical surfaces will induce different water condensation mechanisms based on the final combination of surface hierarchy and chemical functionalization⁵⁸. The surface modification is equivalent for both types of hierarchical surfaces, including PDMS and PFOTES grafting. Therefore, the differences in the condensation are likely related to the differences in

morphology, aspect ratio, and density of the nanofibers. We hypothesize that the lower aspect ratio of the DAAQ-based nanofibers allows for higher coverage of the nanoroughness, specially of the deepest laser groove regions, by the PDMS and perfluorinated grafting, reducing the nucleation sites available for heterogeneous water condensation. As stated in Chapter 1, according to eq. 3, the expected critical size radius for temperature differences between 5-10°C from 0°C would be around 4.6-9 nm⁵⁹, what is in the range of the roughness scale developed with the TiO₂ shell nanostructures.

6.3.5 Icing behavior of the hybrid hierarchical surfaces

Experiments aimed at determining the freezing delay time (FDT) (the duration a surface at -5 °C in a dry atmosphere can prevent ice formation when 2 µl water droplet is deposited on it) have been previously illustrated in Figure 5. All surfaces without nanostructures, including AL, AL-L, AL-TiO₂ TF, and AL-L-TiO₂-P TF, showed a freezing delay time of less than 26 minutes. This maximum time corresponds to the FDT of the PDMS-coated sample. The hydrophilic nature of the surfaces, combined with a roughness topography in the microscale (even flatter when coated with PDMS), results in a larger water-surface interface area. This larger area facilitates heat exchange and promotes a quick freezing from the cold interface toward the top of the liquid droplet^{60,61}.

Hierarchical surfaces presented similar FDT values, ranging from 20 to 26 minutes to those of the smooth low surface free energy PDMS surface. The presence of air pockets should slow down heat exchange due to the low thermal conductivity of air (0.025 W mK⁻¹), making cooling condition difficult. Besides, the TiO₂ nanostructured shell has a high surface tension and hydrophilic behaviour. This structure can create defects that serve as initiation sites for ice nucleation. The presence of air pockets in hierarchical surfaces contributes to the increase of the WCA until it reaches a superhydrophobic behavior, decreasing the surface tension upon contact with water, which is not affected by the decrease in temperature below 0°C. This favors a very reduced physical contact between the perfect spherical water droplet and the surface, only through pinning points of nanometric dimensions that, added to the low thermal conductivity of the air located in the porosity, makes it difficult for a stable Cassie-Baxter to Wenzel state transition even at -5 °C. Taking into account that

nominal thermal conductivity values of the materials employed in the development of the hierarchical surfaces are higher than that of the air present in the pores of the structure, and decreases linearly as temperature decreases¹⁷. Liu et al.⁶² found that the air thermal conductivity is not affected by the pore size at the microscale and thus the effective thermal resistance of a microstructure may increase with the microporosity. Otherwise, regarding the effect of the pore size in the nanoscale, when air molecules mean free path and the pore size of the TiO₂ shell are of the same order of magnitude, the effective thermal conductivity of the nanoporous structure would be practically determined by that of the trapped gas in the open pores, which would tend to decrease. The other critical parameter is the moist environment since the effective thermal conductivity of porous surfaces tends to increase with the ambient humidity¹⁷.

Consequently, combining topographic hierarchy with chemical modification is necessary to obtain anti-icing performance. Longer FDTs were observed when a thinner PDMS encapsulation on both hierarchical surfaces was added, reaching values of 90 and 81 minutes for AL-L-DAAQ@TiO₂-P and AL-L-H₂Pc@TiO₂-P samples, respectively. Finally, a fluorinated surface termination through the anchoring of fluorinated molecules allowed the longest FDTs: 182 and 119 min for the AL-L-DAAQ@TiO₂-P-F and AL-L-H₂Pc@TiO₂-P-F surfaces, respectively. Even without considering the effect of the PDMS embedding, the nanostructure with lower surface aspect ratio (DAAQ core) has been found to be more beneficial in delaying freezing. Consequently, the physicochemical nature of PDMS (surface tension and heat thermal conductivity around 20-25 mNm⁻¹ and 0.15-0.2 W mK⁻¹, respectively) together with the coverage of deeper structural defects and the known water repellency of perfluorinated molecules contributed to inhibiting ice nucleation in icing environments.

To further evaluate the icephobic behavior of the AL-L-DAAQ@TiO₂-P-F surface, ice accretion, and centrifugal ice adhesion experiments were conducted in an icing wind tunnel (IWT) at the INTA facilities. **Figure 9** presents the results of the ice accretion tests, which were carried out using glaze ice formed at -5 °C and a wind speed of 70 m/s, as detailed in Chapter 2.

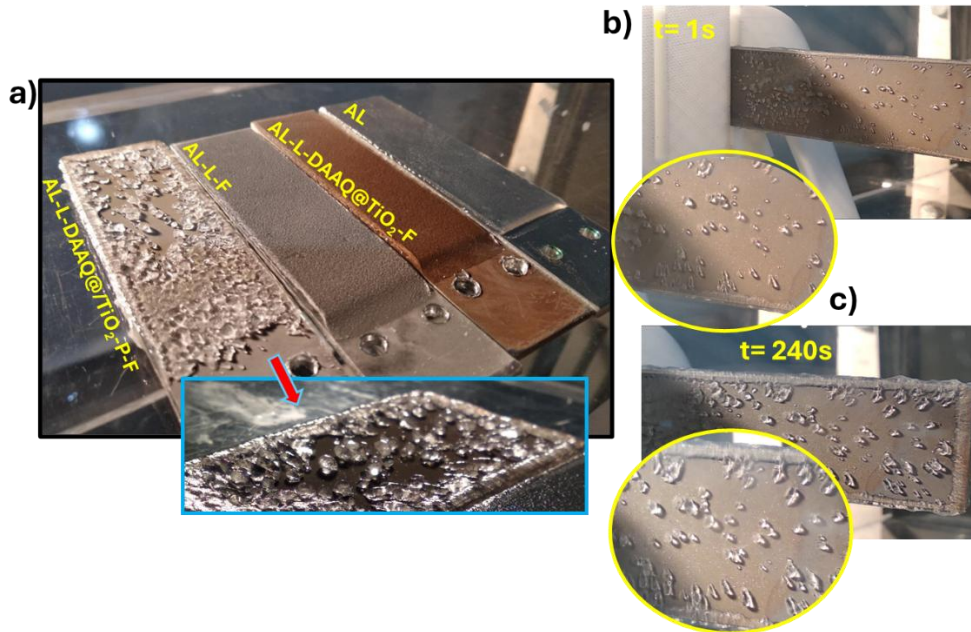


Figure 9. Pictures of ice accretion experiments at -5°C , 70 m/s of airspeed and glaze ice for AL-L-DAAQ@TiO₂-P-F hierarchical surface (top left panel a)) as well as zoomed regions at posterior event times (panels b) and c)), compared to other surfaces, from right to left in panel a): AL6061 reference sample, AL-L-DAAQ@TiO₂-F, and AL-L-F.

It is known that the higher air speed moving across a surface, the higher the rate of heat transfer through the surface and, consequently, the faster the freezing triggering. However, the hybrid hierarchical surface, as illustrated in Figure 9, shows clean areas free of ice particles compared to the other tested surfaces that display a continuous layer of several millimeters of glaze ice on top characteristic of a film-wise water accumulation when high-speed supercooled water droplets impact on them. These results stress the role of the surface hierarchy and chemical termination in reducing heterogeneous ice nucleation and accretion⁶³. In contrast, the exposition of the AL-L-DAAQ@TiO₂-P-F surface to freezing conditions resulted in an extremely low ice coverage through the unusual formation of ice particles keeping quasi-spherical drop-like shapes. This fact indicates that the Cassie-Baxter regime was stable under severe icing conditions for more than 240 s. The accreted ice content on the hybrid hierarchical sample after 240 seconds represented approximately 40% less of the surface area of the sample compared to the others. This performance was even more impressive considering its reproducibility after three cycles, which confirms the stability of

its anti-icing capability. The result indicates the synergetic combination of the chemical modification with the hierarchical structure that supports stress accumulation and topographical damage that typically affect rigid superhydrophobic surfaces under ice particle formation and/or impact conditions⁶⁴.

It is important to note that the literature indicates that one of the disadvantages of using superhydrophobic rough surfaces in anti-icing applications is their generally low performance when it comes to ice adhesion. To shed light on this issue, ice adhesion tests using a centrifugal ice adhesion method were performed (see Chapter 2). The acceleration speed was settled at 300 rpm for all the samples. Collimators were employed to provide normalized glaze ice accretion area on the surfaces. The samples were weighed before and after the experiment to determine the amount of accumulated ice mass, calculating the angular velocity for each of these samples and their adhesion values^{65,66}. **Figure 10** presents images of the ice adhesion state before and after the surfaces, including as references the AL6061 substrate and two low-adhesion aeronautical coatings (paints). The estimated ice adhesion strength is 260 ± 54 kPa for the aluminum reference and 88 ± 5 kPa for the aeronautical paints.

Figure 10 i) shows the equivalent amount of ice accreted for all the surfaces at the initial step of the experiment. Meanwhile, Figure 10 iii) displays the final stage, showing the presence of visible ice residues on the tested surfaces. Particularly the ice weighed after the centrifugal test was 7.0 g, 8.0 g and 7.3 g for the AL-L-F, AL-L-DAAQ@TiO₂-F, and AL-L-DAAQ@TiO₂-P-F samples, respectively, corresponding to ice adhesion strength values of 400 kPa, 628 kPa, and 439 kPa, respectively. Although these values are far from the slippery references, are in the same order of magnitude than that corresponding to the flat aluminum, even better than other literature proposals, such as silane-based patterned surfaces^{67,68,69}.

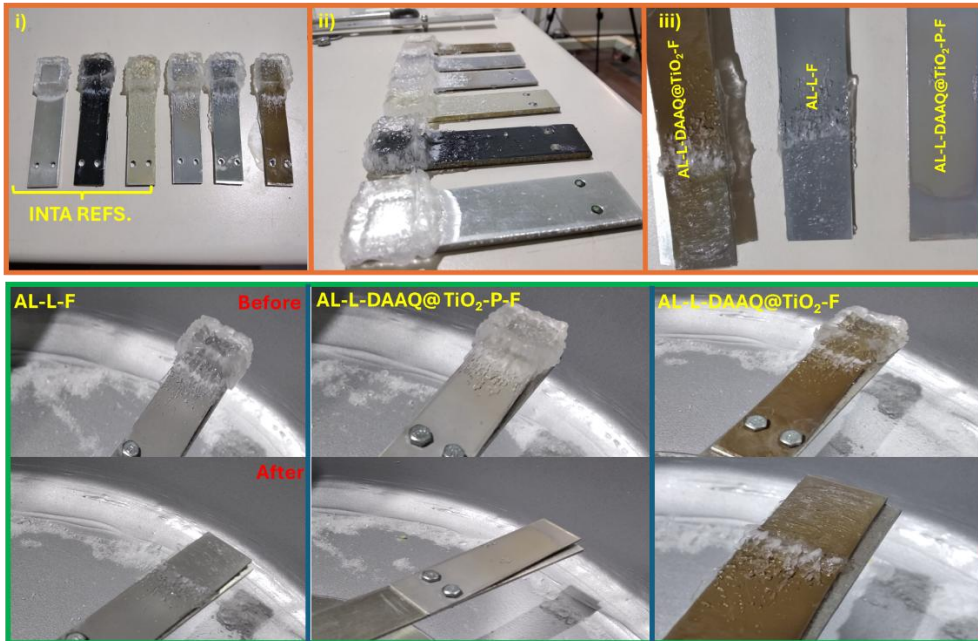


Figure 10. Pictures of the centrifugal ice adhesion tests at -5°C and 300 rpm, using glaze ice of the proposed surfaces: AL-L-F, AL-L-DAAQ@TiO₂-F and AL-L-DAAQ@TiO₂-P-F compared to the aeronautical references.

The reason why the fluorinated hierarchical sample without the PDMS coating showed higher ice adhesion values compared to the same coated hierarchy lies in the insufficiently smoothed roughness at the nanoscale or the lack of concealment of defects from the laser treatment still exposed. Roughness may be harmful to promote a mechanical interlocking of the ice nuclei within the micro, and mainly nano-scales^{70,71}. It has been reported that laser-induced morphology, combined with the presence of nanostructures, creates an interlocking mechanism that traps ice nuclei within the surface roughness. Other adverse factor to improving anti-adhesion properties is the use of sticking polymers of similar chemical nature than the high density PDMS⁷². However, it is worth highlighting the good performance of this hierarchical surface in ice accretion experiments conducted in the IWT, as well as the promising results in runback experiments like those previously reported with another functionalized hierarchical structure previously developed by the research group, using the same chemical modification on oriented nanocolumnar Al₂O₃ coatings deposited on laser treated aluminum aeronautical substrates^{10,73}. Other factor of

improvement to reduce these ice adhesion values include reducing the density of PDMS reaching a liquid-like slippery termination^{74,75}.

6.3.3 Durability and stability characterization of the hybrid hierarchical surfaces

The durability test matrix of physical and chemical essays representing the real-life applications detailed in Chapter 2 has been applied to the best performance anti-icing surfaces, i.e., AL-L-DAAQ@TiO₂-P-F and AL-L-H₂Pc@TiO₂-P-F. **Figure 11** summarizes the positive results obtained after these aging and durability tests.

TESTS	Possible effects	PASS/NO PASS	
UV-Vis irradiation	Coating changes in physical appearance (colour,gloss...)	AL-L-H ₂ Pc@TiO ₂ -P-F	AL-L-DAAQ@TiO ₂ -P-F
		PASS	PASS
Thermal cycling 150°C (2h, 3 cycles)	Coating integrity: blistering/delamination /cracks	PASS	PASS
Solvent immersion (30 min)	Coating changes in physical and chemical properties (loss of functionalization, microstructure)	PASS	PASS
Rain erosion test of 3h with water dripping (0.01 ml/s)	Wettability changes	WCA before: 160° WCA after: 160° PASS	WCA before: 163° WCA after: 163° PASS
Rain erosion test of 3h with water jet (0.1 ml/s)	Wettability changes	WCA before: 160° WCA after: 159° PASS	WCA before: 163° WCA after: 158° PASS

Figure 11. Summary about durability tests for AL-L-DAAQ@TiO₂-P-F and AL-L-H₂Pc@TiO₂-P-F samples checking the surface integrity and wetting stability.

As shown in Figure 11, both hybrid hierarchical surfaces exhibited positive results concerning changes in wettability and physical alterations after the proposed tests. Notably, no loss of coating integrity was observed after three hours of rain erosion experiments, which were conducted under two working modes: dripping and jet dosing. In the same way, the surfaces resisted adequately the interactions with solvents, UV light, and under thermal cycling.

To further evaluate the durability of the fluorinated surface functionalization of the hierarchical surfaces, we followed the evolution of surface chemistry during the aging of the samples. Considering that the perfluorinated molecules grafted feature long, and flexible C-F chains that can evolve upon aging, we monitored periodically the chemical composition (XPS) and the wettability of the surfaces. This analysis is also relevant in the context of the new European regulations aimed at reducing the use of perfluorinated and polyfluoroalkyl substances (PFAS), defined as forever chemicals. Looking also for alternatives to the extended use of the (1H,1H,2H,2H-Perfluoro-octyltriethoxysilane 98% (PFOTES)) precursor, we have also included in the study two other fluorinated molecules considered more environmental-friendly due to their shorter carbon chains and, therefore, fewer C-F bonds, or promoter of stronger bonds to the surface: 1H,1H,2H,2H-Perfluorodecyl-triethoxysilane 97% (PFDTES), and Trichloro(1H,1H,2H,2H-Perfluorooctyl)silane 97% (TCPFOS).

XPS spectra and quantitative analysis of the surface atomic concentration have been obtained for different time intervals (1 month, 5 months, 9 months and 13 months) of air storage in hermetic boxes, as well as the corresponding WCA analyses were studied. Stability of the molecular anchoring is assessed through the silanol groups of these perfluorinated molecules and the hydroxyl groups (-OH) on the pre-activated surfaces with mild plasma, or ozoniser treatments. **Figure 12** gathers the XPS spectra corresponding to the survey, and high resolved binding energy regions of interest (C 1s and F 1s) for each of these molecules for different intervals until 13 months from the first measurement (the corresponding atomic concentration is collected in **Table 2**).

Just after performing the chemical derivatization with the different perfluorinated molecules, the surface state was quite similar. It was notable the incorporation of fluorine atoms bound to carbon ones and for the presence of silicon or chlorine at binding energies corresponding to -O-Si- and -Cl-Si-species^{76,77} depending on the used molecule (see Figure 12 panels a-c)). Fluorine incorporation varied from 28% to 34% when PFOTES or PFDTES was employed in good agreement with the higher fluorine content of the precursors (13 F atoms versus 17 ones, respectively).

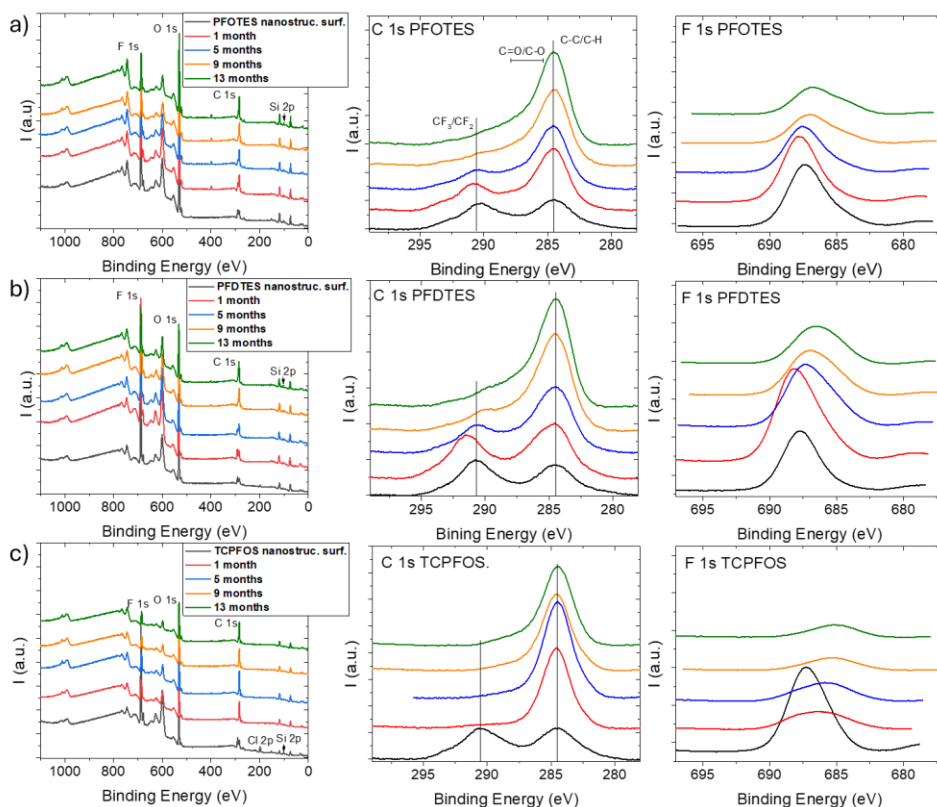
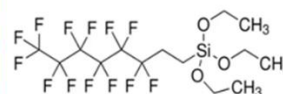


Figure 12. XPS survey spectra and high resolution XPS spectra corresponding to C 1s and F 1s regions at different aging times for functionalized hierarchical surfaces: a) PFOTES, b) PFDTES and c) TCPFOS.

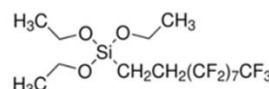
The primary highest incorporation of fluorine at the surface was observed with the TCPFOS precursor, which also has 13 F atoms per molecule, reaching 39% atomic concentration. This result might indicate that after surface activation with oxygen plasma, the link through the formation of Si-O bonds to the surface by the loss of a chlorine atom (~ 380 kJ/mol Si-Cl bond energy) would be more efficient than that through the loss of the oxygen linked to a methyl groups (~ 450 kJ/mol Si-O bond energy)⁷⁸. F 1s spectra in Figure 12 a)-c), corroborate the incorporation of fluorine on the surface with binding energies between 687.8 – 687.3 eV assigned to the presence of covalent C-F bonds⁷⁹. The increase of the fluorine content is also accompanied by an increase in carbon concentration (Table 2 and Figure 12 a)-c)).

Table 2. Atomic concentration of the elements: F, C, O, Si and Cl by XPS by progressive aging time intervals of the fluorinated functionalized hierarchical passive surface. Representation of the chemical formula of the molecule is also included as an illustration of each fluorinated precursor.

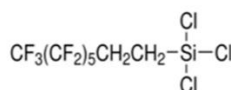
PFTOES	F (%)	C (%)	O (%)	Si (%)
Ref.	28.3	22.1	31.0	2.6
1 month	25.4	27.3	26.4	5.4
5 month	20.0	28.4	28.0	6.3
9 month	17.6	44.7	36	6.6
13 month	14.5	41.3	36.3	6.0



PFDTES	F (%)	C (%)	O (%)	Si (%)
Ref.	34.1	25.5	24.3	1.1
1 month	38.3	25.4	18.0	5.8
5 month	32.4	28.2	22.3	1.6
9 month	26.0	43.7	27.4	4.0
13 month	21.4	40.2	30.1	6.0



TCPFOS	F (%)	C (%)	O (%)	Si (%)	Cl (%)
Ref.	39.1	29	15.7	5.5	3.6
1 month	15.4	40	25.1	4.04	3.2
5 month	13.1	40	27.8	27.8	--
9 month	9.0	47	27.0	27.0	--
13 month	7.8	54	32	32	--



C 1s XPS spectra have a common appearance for the derivatized surfaces with the three precursors consisting of two main peaks located around 290.5 eV and 284.5 eV related to the CF₃/CF₂ and C-C/C-H functional groups, respectively⁸⁰. Both contributions present similar intensities of the C 1s photopeak except for the PFDTES surface functionalization, where the fluorinated carbon band, at higher binding energies, was a bit higher than that corresponding to the aliphatic carbon bonds. Besides, in the case of the TCPFOS grafting, the fluorinated carbon band was slightly wider towards higher values of binding energy consistent with a greater contribution of CF₃ bonds added to the majority presence of CF₂ ones. After a month of air storage, the surface chemical functionalization appeared to be quite stable when using PFOTES and PFDTES molecules in the grafting process. In contrast, the TCPFOS precursor showed a significant decrease in the atomic fluorine percentage, dropping from 38% to 15%. Besides, it can be seen how the increase in the atomic concentration of carbon of spurious origin hid the signal corresponding to fluorinated groups in the C 1s spectrum after 1 month of aging. This trend has continued for 13 months, with a fluorinated contribution

on the surface decreasing to 7%. On the contrary, the CF band was still clearly visible in the C 1s spectra of both PFOTES and PFDTES grafted surfaces after 5 months have passed, being around 20%-30% of fluorine content. This XPS signal was still evident after 9 months for the fluorinated surface through the PFDTES grafting. And after 13 months of aging, C 1s spectra was similar for both PFOTES and PFDTES grafted surfaces made up of a main photopeak centered at 284.5 eV and a notable tail extending beyond the 290 eV of binding energy. The envelope of this tail would have contributions from possible oxygen-containing functional groups coming from the environment in addition to the remnant of fluorinated groups resisting on the surface. That is justified by the increase in the presence of oxygen from 31% to 36% and from 24% to 30% (Table 2) on the aged, fluorinated surfaces after the grafting with PFOTES or PFDTES, respectively. It should be mentioned that the surface that has incorporated the most oxygen atomic percentage after the aging time was the one functionalized with TCPFOS, confirming that it was this fluorine-based grafted surface the most sensitive to environmental contamination. During the entire analysis time and for all the grafted surfaces, the main O 1s photopeak has been located on the binding energy corresponding to -O-Si- species at 531.5 eV. However, full width at half maximum around 3.5-3.8 eV depending on the perfluorinated molecules, suggests the incorporation of -O-C- groups over 530 eV⁸¹. Finally, as an additional effect of the aging, F 1s spectra indicated a slight shift to lower binding energies as time has passed, especially accentuated in the case of the TCPFOS grafted surface in almost 2 eV. Some works in the literature refer to the formation of C-F bonds that are less strong than the covalent/organic type (around 687.5 eV), called semi-ionic C-F bonds appearing close to 685.5 eV⁷⁹.

In Table 2, it can be observed that, generally, the three fluorinated molecules exhibit a decrease in the percentage of fluorine on the surface over time, while the percentage of carbon tends to increase for all of them. This carbonaceous contamination of the surface can be also responsible for maintaining the high-water contact angles⁸². Thus, the reduction of exposed F content was compensated by the increase of spurious carbon on the surface, which ultimately would benefit water repellence^{82,83}. In fact, after 13 months, wetting properties were measured with water droplets and other simulators of biological agents, resulting contact angles ca. 150°. This highlights that the carbon accumulation

also sustains the omniphobic character of the surfaces to inspire reviewing eco-friendly alternatives to PFAS^{84,85,86}.

6.3.6 Permanent Cassie-Baxter hybrid hierarchical surface as passive protective termination in active de-icing systems

After conducting a thorough study of hierarchical surfaces as icephobic passive systems, we have demonstrated their impressive performance in terms of durability, stability and compatibility to be implemented in active de-icing systems. For this section, we have selected AL-L-DAAQ@TiO₂-P-F surface as a proposal to be tested due to the demonstrated permanent Cassie-Baxter state at icing conditions. This sample will be implemented into two de-icing solutions, namely, as icephobic coating and protective layer (passive system) on an electrothermal ice protection system (IPS) and on a thickness-shear mode acoustic de-icing device.

In the case of the electrothermal IPS, the hybrid hierarchical surface was scaled to substrates with complex geometries, such as AL6061 semicylinders. Joule heating was provided by a 0.5 mm thick steel serpentine, which is secured with a temperature-resistant material. The electrothermal IPS experiments were conducted in the IWT at INTA. Two working modes were proposed as follows:

- Anti-icing mode, where the resistive heating was activated before water droplets injection in the IWT and kept during the posterior interaction with the exposed surface. While the surface was hot (values between 0 and 5 °C), water was sprayed onto it, and then, the input power was gradually reduced until ice formed on the surface, calculating the required minimum input power to avoid ice accumulation.
- De-icing mode, where ice was allowed to accrete for 2 minutes without de-icing applied power, and then, the electrothermal heater was activated at a fixed power (1.8, 2.5 or 3.5 kW/cm²) to determine the de-icing time.

Aerodur and others commercial polyurethane (PU) paints with thickness ~ 100 µm (compare to the 7-10 µm thickness of our hierarchical system), were used as

references. Two different types of ice were formed for both specific experiments: glaze ice (transparent denser crystalline ice), which was formed at $-5\text{ }^{\circ}\text{C}$, with a LWC of 1 g/m^3 and MVD of $80\text{ }\mu\text{m}$, and rime ice (white lighter amorphous or polycrystalline ice), which required severe icing conditions to be achieved ($-15\text{ }^{\circ}\text{C}$, LCW: 1 g/m^3 , and MVD of $30\text{ }\mu\text{m}$)⁸⁷. Temperature values and ice types were chosen to mimic severe icing conditions. **Figure 13** illustrates the experimental setup, and the semicylinders in the configuration of electrothermal de-icing systems.

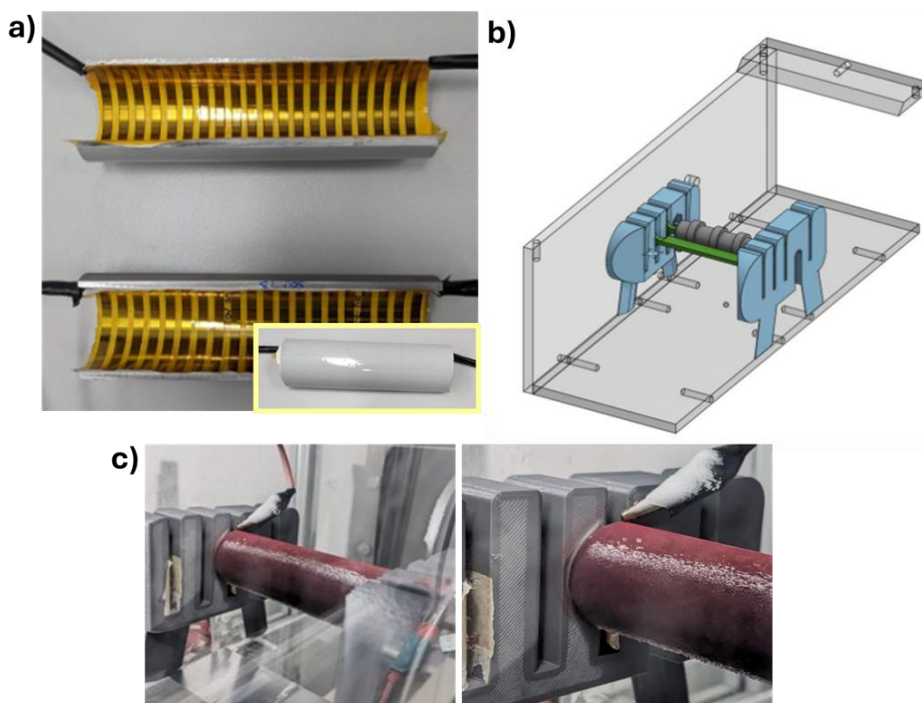


Figure 13. a) Details of the electrothermal de-icing system mounted on the aluminum semicylinder covered with the Aerodur paint aeronautical reference; b) Schematic of the experimental setup in the icing wind tunnel; c) Pictures of the AL-L-DAAQ@TiO₂-P-F hierarchical surface on the semicylinder assembled with the electrothermal protection system during the anti-icing mode experiment.

At first, Figure 13 a) presents the Aerodur coating on this 3D complex geometry such as reference sample whereas the Figure 13 c) illustrates the AL-L-DAAQ@TiO₂-P-F hierarchical surface deposited on the AL6061 semicylinder. This picture demonstrates the compatibility of the laser and hybrid micro-/nano-structured fabrication protocol with 3D substrates. The red colour observed is attributed to the organic π -conjugated molecules (DAAQ)

incorporated within the nanofibers which would be easily removed by heating to remove organic content from the nanofibers. Figure 13 b), show the final set up, illustrating how the studied surfaces are positioned for both anti-icing and de-icing experiments, where supercooled droplets under the wind action attacks are concentrated on the front sections thanks to the use of collimators. This faced area received the impact of supercooled droplets at 70 m/s, causing drag towards the lateral substrate ends.

Table 3 presents the results of the anti-icing mode experiments with both types of ice, with the comparison between the most representative anti-icing power values of the PU paint reference (Aerodur), 1.0 W/cm² for rime ice, which is defined as the minimum power required for the anti-icing effect to occur with this coating, and 0.5 W/cm² for glaze ice. These values can be compared to those needed for the hybrid hierarchical surface. This indicates that if the power values are lower than those specified, the anti-icing effect will not be achieved with this type of coating. Anti-icing power value for bare AL6061 reference was 1.03 W/cm² under extreme conditions (-15 °C, rime ice).

Table 3. Anti-icing experiments at -15 °C (rime ice) and -5 °C (glaze ice) comparing anti-icing power values of the hybrid hierarchical surface with the reference sample in 4 tests.

Anti-icing experiments (-15 °C) → Rime ice		Anti-icing experiments (-5 °C) → Glaze ice	
F-P-L-AL-DAAQ@TiO ₂	Power (W/cm ²)	F-P-L-AL-DAAQ@TiO ₂	Power (W/cm ²)
Essay 1	1.1*	Essay 1	0.54*
Essay 2	1.0*	Essay 2	0.47
Essay 3	0.9*	Essay 3	0.51*
Essay 4	0.8	Essay 4	0.53*

*Indicates that with this input power, it was not formed ice on the samples.

An overall conclusion of this table is that the implementation of the passive anti-icing coatings is not only compatible with the electrothermal protection system, but also improves its energy efficiency. The results of the hybrid hierarchical surface at -15 °C (rime ice) indicate an anti-icing power value of approximately 1 W/cm² across four reproducible tests, which is comparable to or even lower than the industrial paint reference with a thickness of ca. 100 μm. Essay 4

showed that the applied power could not be lowered to 0.8 W/cm² to prevent rime ice formation, representing the limited minimum power required. Similarly, in the anti-icing experiment at -5°C with glaze ice, the power values obtained with the hybrid hierarchical coating were also very close to those of the paint reference across four tests. This suggests that the hierarchical surfaces have a great potential as passive protective coatings in active anti-icing electrothermal systems.

The second test consisted of the electrothermal de-icing at two different temperatures, -15 °C and -5 °C, depending on the type of ice. For these experiments, supercooled droplets with LWC of 1 g/m³ impacted the surface at 70 m/s during 2 minutes without any applied power. Once the ice has been formed, a reference fixed power value was applied⁸⁸, whereas the time needed for the surface to thaw was registered. The key parameters in this experiment were the de-icing time and the energy consumption (E) for each de-icing test. These values were estimated by the product of the fixed consumed power by the de-icing time, measured in J/cm². Results are shown in **Table 4**.

Table 4. De-icing experiments at -15 °C (rime ice) and -5° C (glaze ice) comparing de-icing energy consumption of the hybrid hierarchical surface with the reference sample in 3 powered de-icing conditions.

De-icing experiments (-15 ⁰ C)→ Rime ice			De-icing experiments (-5 ⁰ C)→ Glaze ice		
Fixed Power (W/cm ²)	Energy consumed (J/cm ²) E=P·t _{de-ice}		Fixed Power (W/cm ²)	Energy consumed (J/cm ²) E=P·t _{de-ice}	
	AERODUR (PU paint)	F-P-L-AL- DAAQ@TiO ₂		AERODUR (PU paint)	F-P-L-AL- DAAQ@TiO ₂
1.85	20.67	22.31	1.12	10.08	11.65
3.35	20.13	14.04	1.75	8.75	8.64

Two limits, low power of 1.85 W/cm² and 1.12 W/cm² and high-power of 3.35 W/cm² and 1.75W/cm² values were used for de-icing experiments with rime and glaze ice, respectively. Table 4 illustrates that at low power levels, the Aerodur reference required an energy consumption like that of the hybrid hierarchical surface at -15°C to remove rime ice from it. In the case of high-power values, the hybrid hierarchical surface required lower energy consumption compared to the

aeronautical reference sample, that is, 14.04 J/cm² against 20.13 J/cm², respectively. It should be noted that AL6061 reference consumed around 39 J/cm² at low power and 54.3 J/cm² for the high applied power in rime de-icing experiments. The hierarchical system also significantly reduced the de-icing time, which is extremely important in aeronautical applications, as shorter de-icing times are crucial for minimizing mechanical and aerodynamic issues⁸⁹. For example, since rime de-icing took 21 s for the aluminum sample at low applied power, the hybrid hierarchical surface managed to de-ice in 11 s, whereas at 3.35 W, de-icing was performed in 6 s compared to the 16 s that the bare sample needed. Hence, in de-icing experiments with rime ice, the permanent Cassie-Baxter surface presented a greater benefit with lower energy consumption values associated to shorter de-icing times even compared to the aeronautical paint in high applied power conditions: a reduction of 58% of de-icing time comparing the 11 s required with the Aerodur surface respect to the 4 s of the hierarchical system, associated to a reduction of 30% of energy consumption. The experiments conducted at -5 °C at the two limit powers for de-icing glaze ice showed that the energy consumed by Aerodur surface and the hybrid hierarchical one was comparable for both limits applied power conditions.

To further demonstrate the compatibility of the developed passive system with an alternative electromechanical de-icing system, the hybrid hierarchical coating was integrated in an active anti-/de-icing system working by the application of Surface Acoustic Waves (SAW), developed in the framework of the European project SoundofIce. The use of these repellent hierarchical coatings on piezoelectric substrates were proposed as anti-icing protective layer. The active anti-/de-icing system is formed of a piezoelectric substrate (LiNbO₃) with a ZnO layer deposition by PECVD (piezoelectric material), whose effectiveness for de-icing and its compatibility with other passive systems such as fluorinated coatings have been previously demonstrated⁹⁰. In this case, instead of using TiO₂ seeds and shells to grow nanostructures, piezoelectric ZnO was employed following the same soft template method. This choice is based on the previous results found by the research group indicating a proper acoustic propagation on the polycrystalline ZnO layers. Then, the supported 1D core@shell nanostructures, keeping a dual scale roughness formed by the microscale dimension of the nanofibers in combination with the nanostructure of the shell, were deposited on the piezoelectric plate and then modified with the PDMS

coating and PFOTES surface termination ($\text{H}_2\text{Pc@ZnO-P-F}$). **Figure 14** presents a scheme of the final design for implementing this nanostructured system as a passive coating in an active anti-/de-icing (SAW) system as well as of the experimental set-up.

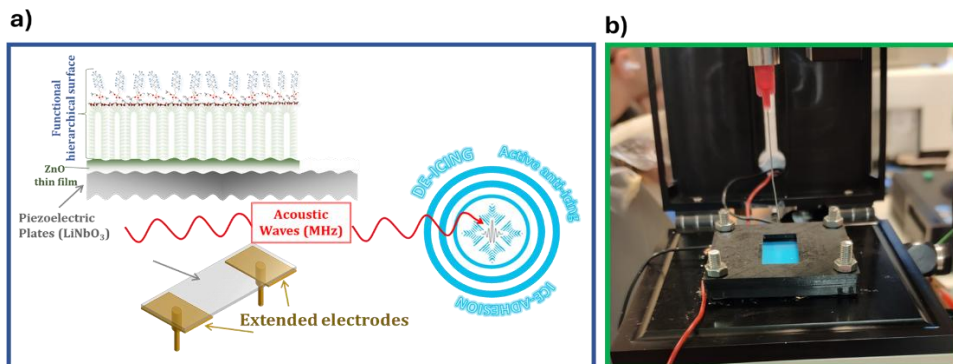


Figure 14. a) Scheme to integrate the anti-icing coating such as protective layer on the top of the active de-icing system to be conducted by acoustic waves, b) experimental set-up for de-icing by acoustic waves in room environment when the sample stays at $-5\text{ }^\circ\text{C}$.

Figure 15 showcases different snapshots of the de-icing process acquired in the environmental chamber of the OCA 20 DataPhysics (shown in Figure 14 b)). This experiment was performed at $-5\text{ }^\circ\text{C}$ under room humidity level ($\sim 40\%$ RH), applying voltages of $70\text{ V}_{\text{p-p}}$ (peak-to-peak) through a RF source and an amplifier as detailed in reference⁹⁰. The surface in stage I) appeared completely covered with frozen droplets of different volumes. When the acoustic wave-assisted device was activated by applying voltage to the bottom part of the piezoelectric plate, the ice particles began to melt, forming supercooled water droplets on the surface. These droplets exhibit spherical shapes typical of being deposited on a superhydrophobic surface. Over time (57 s until stage VI), these droplets gradually began to slide and disappear out the surface slightly tilted, leaving clean and dry areas at the same time as other droplets, due to the enhanced mobility on the repellent surface, tended to coalesce between them.

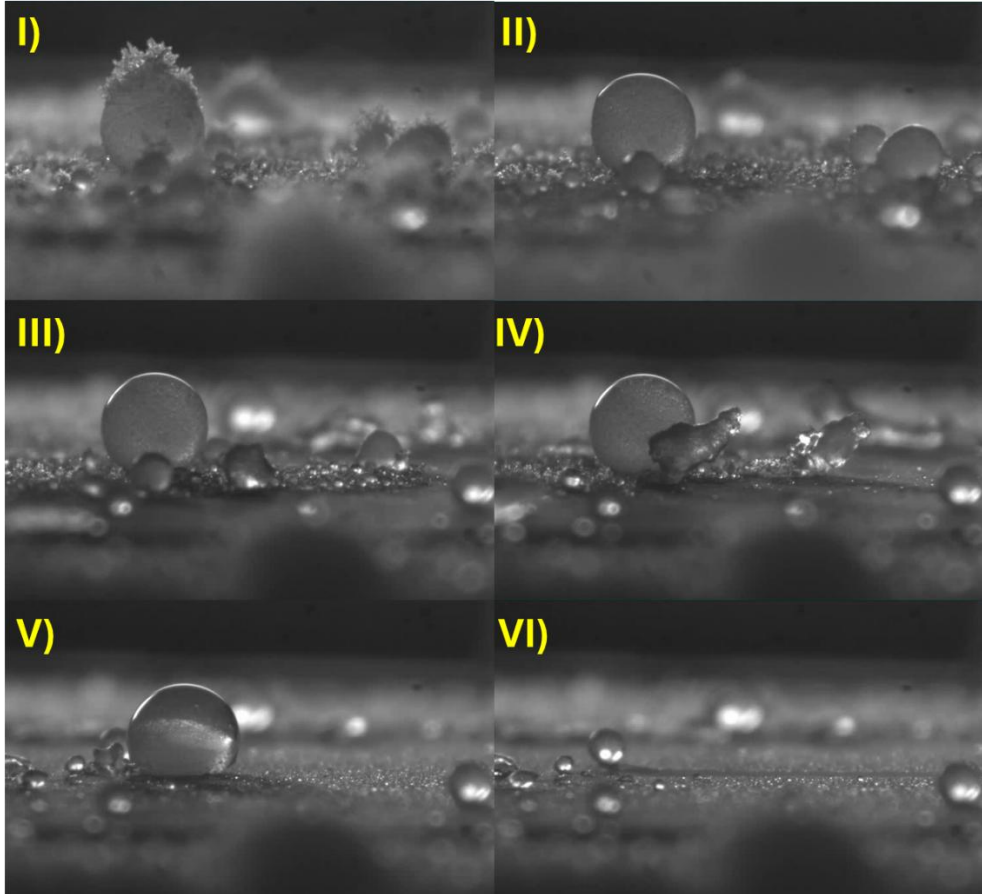


Figure 15. De-icing sequence using $\text{H}_2\text{Pc@ZnO-P-F}$ as passive protective coating on an acoustic wave assisted active de-icing device at $-5\text{ }^\circ\text{C}$ and room humidity environment.

Therefore, the protective repellent hybrid hierarchical surface has been fully compatible with the propagation of acoustic waves through the piezoelectric plate and the surface, inducing the melting of droplet contours and interfaces with the surface and facilitating the droplets and partially melting ice particles removing without the need to achieve a complete ice fusion. It should be noted that according to reference⁹⁰, $40\text{ V}_{\text{p-p}}$ and 41 s were required to melt an ice aggregate formed on the pristine piezoelectric plate at $-5\text{ }^\circ\text{C}$, quite similar values than those reported here for the combined passive hierarchical surface and the acoustic active de-icing device.

6.4 Conclusions

Hierarchical surfaces, combining two or even three roughness levels, from the grow of supported 1D core@shell nanofibers of a few micrometres length and a few hundred of nanometres diameter, with a special nanostructured surface made by vacuum and plasma techniques, to the combination with random roughness at the microscale induced by laser treatments, have proven to be compatible with substrates of medium size dimensions and complex geometries of interest in industrial applications such as aluminum aeronautical alloys. The selection of the π -conjugated organic precursor to fabricate the single-monocrystalline core of the nanofibers allowed to tune the surface aspect ratio, a crucial factor to control the wetting properties, as well as the processing temperature what is a promising result to implement the hierarchical surface on sensible and flexible substrates, like polymers.

Hierarchical surfaces of developed triple level roughness have presented hydrophobic and almost oleophobic response which thanks to a special surface modification with PDMS coating and fluorinated molecules grafting scaled to superhydrophobic and oleophobic behavior, particularly noteworthy with the surface of lower aspect ratio, and, by extension, at an omniphobic, fully fluid repellent, function. That meant an anti-fouling surface checked with bovine serum, humic acid and alginic acid agents. Besides, the superhydrophobic behavior has been shown to be stable by low temperature evaporation experiments up to 350 Pa of Laplace pressure values. Consequently, it seems that these hybrid hierarchical surfaces are of a permanent Cassie-Baxter state.

Other evidence of this fact has come from the monitoring of water vapor condensation experiments in ESEM, where both high and low surface aspect ratio hybrid hierarchical surfaces withstood supersaturated humid environmental conditions without signs of water condensation on its surfaces, remaining at a low temperature. And only in the case of the less PDMS embedding, i.e. the hierarchical surface of lower aspect ratio, after 12 minutes at 1420 Pa of water vapor condition, 100% RH, and 6 °C, began to present water microdroplets of spherical shape between the larger pores of the structure. Therefore, it has been verified that the greater coverage with the PDMS thin film (respecting the topographic hierarchy) out the free defects that could have remained from laser machining guaranteed the anti-fogging capacity. Under the same arguments, the hybrid hierarchical surfaces demonstrated a remarkable

anti-icing capacity by a discontinuous ice accretion, and longer freezing delay times, particularly in the case of the lower surface aspect ratio sample. This result adds to the preservation of a Cassie Baxter state even when working under adverse environmental conditions of supercooled droplets impact under the action of high wind currents at temperatures below 0 °C. However, the anti-adhesion to ice property, although with tolerable values regarding the literature, they are far from being comparable to the aeronautical paint references. Here, the roughness at the nanoscale may promote a mechanical interlocking of the ice nuclei of similar sizes, whose prevention can be addressed from the surface modification with slippery alternatives.

The stability of the hybrid hierarchical surfaces was also confirmed through several durability tests, where, after solvent immersion, temperature cycling, UV-Vis illumination, and rain erosion essays, the surfaces were able to maintain the superhydrophobicity, as well as the omniphobicity.

Finally, the hybrid hierarchical configuration was integrated as protective coating of two different de-icing systems, based on surface acoustic waves and electrothermal heating devices, and checked in scalable facilities under realistic aggressive environmental icing conditions. Regarding the electrothermal de-icing actuation, the hybrid hierarchical surface of an aluminum semicylinder was tested as active anti-icing and de-icing performances at two different temperatures (-5 °C and -15 °C) and different type of ice particles (rime and glaze), compared to an aeronautical reference. On one hand, the developed surface required similar values of applied power to prevent ice accumulation as the reference, while on the other, the de-icing times were of the same order or even shorter than those of the references, particularly with rime ice and higher applied power conditions, which resulted in a reduction in the energy consumed around 30%. So these surfaces are potentially interesting to adapt in aeronautical applications, where it is preferable to apply higher power values in the electrothermal system for shorter periods of time to have the lowest energy consumption.

Regarding the second de-icing device, the implementation of the hybrid hierarchical passive surface on piezoelectric layers as a final protective layer resulted compatible with the acoustic wave transmission responsible to the ice detachment at the ice/surface interface. And, due to the stable superhydrophobic behaviour even at low temperatures, the de-icing process was facilitated

combining a minimal ice melting, particularly at the interface, to promote the droplets removing as partially melting ice particles.

Bibliography

1. Golovin, K., Dhyani, A., Thouless, M. D. & Tuteja, A. Low-Interfacial Toughness Materials for Effective Large-Scale Deicing. *Science* **26**, 371-375 (2019).
2. Wong, T. S. *et al.* Bioinspired self-repairing slippery surfaces with pressure-stable omniphobicity. *Nature* **477**, 443-447 (2011).
3. Lynch, F. T. & Khodadoust, A. Effects of Ice Accretions on Aircraft Aerodynamics. *Progress in Aerospace Sciences* **37**, 669-767 (2001).
4. Heinrich, A., Ross R., Zumwalt, G., Provorse & Padmanabhan V. *Aircraft Icing Handbook Volume 1* (1991). National Technical Reports Library.
5. Endres, M., Sommerwerk, H., Mendig, C., Sinapius, M. & Horst, P. Experimental study of two electro-mechanical de-icing systems applied on a wing section tested in an icing wind tunnel. *CEAS Aeronaut J* **8**, 429-439 (2017).
6. Goraj Z., An Overview of the De-icing and Anti-icing Technologies with Prospects for the Future. *24 th International Congress of the Aeronautical Sciences, (2003)*.
7. Mohseni, M. & Amirfazli, A. A novel electro-thermal anti-icing system for fiber-reinforced polymer composite airfoils. *Cold Reg Sci Technol* **87**, 47-58 (2013).
8. Park, M. S. *Aircraft De-Icing System Using Thermal Conductive Fibers*.
9. Huang, X. *et al.* A survey of icephobic coatings and their potential use in a hybrid coating/active ice protection system for aerospace applications. *Progress in Aerospace Sciences* **105**, 74-97 (2019).
10. Mora, J. *et al.* Setting a comprehensive strategy to face the runback icing phenomena. *Surf Coat Technol* **465**, (2023).
11. Lafuma, A. & Quéré, D. Superhydrophobic states. *Nature Materials* **2**, 457-460 (2003).
12. Rauter T.M., Schnell K., Signe Kjelstrup. Cassie-Baxter and Wenzel States and the Effect on Interfaces on Transport Properties across Membranes. *The Journal of Physical Chemistry B* **125**, 12730-12740 (2021).
13. Wang, D. *et al.* Design of robust superhydrophobic surfaces. *Nature* **582**, 55-59 (2020).
14. Liao, D., He, M. & Qiu, H. High-performance icephobic droplet rebound surface with nanoscale doubly reentrant structure. *Int J Heat Mass Transf* **133**, 341-351 (2019).
15. Shen Y. & Garrett R. Combined effects of pores and cracks on the effective thermal conductivity of materials. *J. Matter Sci: Mater Eng.* **183**, 19-25 (2022).
16. Stephan, K. & Laesecke, A. The Thermal Conductivity of Fluid Air. *J Phys Chem Ref Data* **14**, 227-234 (1985).
17. Hung Anh, L. D. & Pásztor, Z. An overview of factors influencing thermal conductivity of building insulation materials. *Journal of Building Engineering* **44**, 234 (2021).
18. Irajizad, P., Hasnain, M., Farokhnia, N., Sajadi, S. M. & Ghasemi, H. Magnetic slippery extreme icephobic surfaces. *Nat Commun* **7**, 13395 (2016).
19. Chu, F., Wu, X. & Wang, L. Meltwater Evolution during Defrosting on Superhydrophobic Surfaces. *ACS Appl Mater Interfaces* **10**, 1415-1421 (2018).
20. Ling, E. J. Y., Uong, V., Renault-Crispo, J. S., Kietzig, A. M. & Servio, P. Reducing Ice Adhesion on Nonsmooth Metallic Surfaces: Wettability and Topography Effects. *ACS Appl Mater Interfaces* **8**, 8789-8800 (2016).
21. Tavakoli, F. & Kavehpour, H. P. Cold-induced spreading of water drops on hydrophobic surfaces. *Langmuir* **31**, 2120-2126 (2015).
22. Giacomello, A., Meloni, S., Chinappi, M. & Casciola, C. M. Cassie-baxter and wenzel states on a nanostructured surface: Phase diagram, metastabilities, and transition mechanism by atomistic free energy calculations. *Langmuir* **28**, 10764-10772 (2012).
23. Park, I. W., Ribe, J. M., Fernandez, M. & Dorao, C. A. The Criterion of the Cassie-Baxter and Wenzel Wetting Modes and the Effect of Elastic Substrates on It. *Adv Mater Interfaces* **10**, (2023).
24. Bormashenko, E. Progress in understanding wetting transitions on rough surfaces. *Advances in Colloid and Interface Science* **222**, 92-103 (2015).

25. Heo, K. J. *et al.* Transition from the Wenzel to Cassie-Baxter state by PFOTES/TiO₂ nanoparticles leading to a mechanically robust and damage/contamination-recoverable surface. *J Mater Chem A Mater* **12**, 3886–3895 (2024).
26. Campbell, J. M., Meldrum, F. C. & Christenson, H. K. Is ice nucleation from supercooled water insensitive to surface roughness? *Journal of Physical Chemistry C* **119**, 1164–1169 (2015).
27. Zhang, X., Liu, X., Wu, X. & Min, J. Impacting-freezing dynamics of a supercooled water droplet on a cold surface: Rebound and adhesion. *Int J Heat Mass Transf* **158**, 119997 (2020).
28. Koutsoloukas, L., Nikitas, N. & Aristidou, P. Passive, semi-active, active and hybrid mass dampers: A literature review with associated applications on building-like structures. *Developments in the Built Environment* **12**,100094 (2022).
29. Li, X. *et al.* A Novel Icephobic Strategy: The Fabrication of Biomimetic Coupling Micropatterns of Superwetting Surface. *Adv Mater Interfaces* **6**, (2019).
30. Li, X. *et al.* Fabrication of bio-inspired non-fluorinated superhydrophobic surfaces with anti-icing property and its wettability transformation analysis. *Appl Surf Sci* **505**, (2020).
31. Borrás, A., Gröning, O., Aguirre, M., Gramm, F. & Gröning, P. One-step dry method for the synthesis of supported single-crystalline organic nanowires formed by π -Conjugated Molecules. *Langmuir* **26**, 5763–5771 (2010).
32. Nix, W. D. Interface Stresses. *Encyclopedia of Materials: Science and Technology* 4136–4141 (2001).
33. Chatre, C. *et al.* Influence of Surface-Active Substances and Substrates on the Wettability of Individual Aerosol Particles during Condensation by Environmental Scanning Electron Microscopy Influence of Surface-Active Substances and Substrates on the Wettability of Individual Aerosol Particles during Condensation by Environmental Scanning Electron Microscopy. *Langmuir* **39**, (2023).
34. Macías-Montero, M. *et al.* In Situ Determination of the Water Condensation Mechanisms on Superhydrophobic and Superhydrophilic Titanium Dioxide Nanotubes. *Langmuir* **33**, 6449–6456 (2017).
35. Jornsano, P. *et al.* Electron tomography combining ESEM and STEM: A new 3D imaging technique. *Ultramicroscopy* **111**, 1247–1254 (2011).
36. García, P. *et al.* Passive Ice Protection Systems Lab Scale Testing Methodology. *SAE International Conference* (2023).
37. García-Casas, X. *et al.* Plasma engineering of microstructured piezo – Triboelectric hybrid nanogenerators for wide bandwidth vibration energy harvesting. *Nano Energy* **91**, (2022).
38. Filippin, A. N. Development of Supported 1D Nanomaterials by Vacuum and Plasma Technologies: From Sensors to Nanogenerators. *A Thesis doctoral by* (2015).
39. Borrás, A. *et al.* Synthesis of Supported Single-Crystalline Organic Nanowires by Physical Vapor Deposition. *Chem. Mater* **20**, 7371-7373 (2008).
40. Wang, Y., Zhang, F., Li, C. & Zhao, Y. Long-chain alkyl groups enhance the water-repellent properties of short-chain perfluoroalkyl compounds: An experimental and computer simulation study. *Colloids Surf A Physicochem Eng Asp* **698**, (2024).
41. Wang, L., Gong, Q., Zhan, S., Jiang, L. & Zheng, Y. Robust Anti-Icing Performance of a Flexible Superhydrophobic Surface. *Advanced Materials* **28**, 7729–7735 (2016).
42. Wang, L. *et al.* The investigation of de-icing and uni-directional droplet driven on a soft liquid-metal chip controlled through electrical current. *J Taiwan Inst Chem Eng* **106**, 191–197 (2020).
43. Rodic P. *et al.* Anti-corrosion and Anti-icing properties of superhydrophobic Laser-Treated Aluminum Surfaces. *Surf. Coat. Tech.* **494**, 131325 (2024).
44. Huang, J. Y. *et al.* Multifunctional superamphiphobic TiO₂ nanostructure surfaces with facile wettability and adhesion engineering. *Small* **10**, 4865–4873 (2014).
45. Feng, L. *et al.* Petal effect: A superhydrophobic state with high adhesive force. *Langmuir* **24**, 4114–4119 (2008).

46. Chen, C. H., Cheng, I. C. & Chen, J. Z. Facile method to convert petal effect surface to lotus effect surface for superhydrophobic polydimethylsiloxane. *Surfaces and Interfaces* **30**, 101901 (2022).
47. Wilke, K. L., Song, Y., Lu, Z. & Wang, E. N. Enhanced Laplace Pressures for Functional Surfaces: Wicking, Switchability, and Selectivity. *Adv Mater Interfaces* **10**, (2023).
48. Zhou, X., Yang, G., Li, C. & Wu, J. Functional microdroplet self-dislodging icephobic surfaces: A review from mechanism to synergic morphology. *Applied Thermal Engineering* **215**, Preprint (2022).
49. Shirtcliffe, N. J., McHale, G., Newton, M. I. & Perry, C. C. Wetting and wetting transitions on copper-based super-hydrophobic surfaces. *Langmuir* **21**, 937–943 (2005).
50. Pan, R. *et al.* Extremely high Cassie-Baxter state stability of superhydrophobic surfaces via precisely tunable dual-scale and triple-scale micro-nano structures. *J Mater Chem A Mater* **7**, 18050–18062 (2019).
51. Sfameni, S. *et al.* Design and Development of Fluorinated and Biocide-Free Sol–Gel Based Hybrid Functional Coatings for Anti-Biofouling/Foul-Release Activity. *Gels* **8**, 538 (2022).
52. Shi, X. *et al.* Advanced strategies for marine antifouling based on nanomaterial-enhanced functional PDMS coatings. *Nano Materials Science* **6**, 375–395 (2024).
53. Zhang, Z. *et al.* In Situ Observation of Ice Formation from Water Vapor by Environmental SEM. *Cryst Growth Des* **18**, 6602–6608 (2018).
54. Masenelli-Varlot, K. *et al.* Wet-STEM tomography: Principles, potentialities and limitations. *Microscopy and Microanalysis* **20**, 366–375 (2014).
55. Gao, T. & Jelle, B. P. Thermal conductivity of TiO₂ nanotubes. *Journal of Physical Chemistry C* **117**, 1401–1408 (2013).
56. Wei, J. *et al.* Enhanced thermal conductivity of polydimethylsiloxane composites with carbon fiber. *Composites Communications* **17**, 141–146 (2020).
57. Krishna, M., Shridhar, T. N. & Krishnamurthy, L. Microstructural Characterization and Investigation of Thermal Conductivity Behaviour of Al 6061-SiC-Gr Hybrid Metal Matrix Composites. *Indian Journal of Engineering & Materials Sciences* **23**, (2016).
58. Rico, V. J. *et al.* Hydrophobicity, Freezing Delay, and Morphology of Laser-Treated Aluminum Surfaces. *Langmuir* **35**, 6483–6491 (2019).
59. Campbell, J. M., Meldrum, F. C. & Christenson, H. K. Is ice nucleation from supercooled water insensitive to surface roughness? *Journal of Physical Chemistry C* **119**, 1164–1169 (2015).
60. Nistal, A., Sierra-Martín, B. & Fernández-Barbero, A. On the Durability of Icephobic Coatings: A Review. *Materials* **17**, Preprint (2024).
61. Oberli, L. *et al.* Condensation and freezing of droplets on superhydrophobic surfaces. *Advances in Colloid and Interface Science* **210**, 47–57 Preprint (2014).
62. Liu, H. & Zhao, X. Thermal Conductivity Analysis of High Porosity Structures with Open and Closed Pores. *Int J Heat Mass Transf* **183**, (2022).
63. Maeda, N. Brief overview of ice nucleation. *Molecules* **26**, Preprint (2021).
64. Kulinich, S. A., Farhadi, S., Nose, K. & Du, X. W. Superhydrophobic surfaces: Are they really ice-repellent? *Langmuir* vol. 27 25–29 Preprint (2011).
65. Rehfeld, N., Speckmann, B. & Stenzel, V. Parameter Study for the Ice Adhesion Centrifuge Test. *Applied Sciences (Switzerland)* **12**, (2022).
66. Vicente, A. *et al.* Icephobic Coating Based on Novel SLIPS Made of Infused PTFE Fibers for Aerospace Application. *Polymers (Basel)* **16**, (2024).
67. Momen, G., Jafari, R. & Farzaneh, M. Ice repellency behaviour of superhydrophobic surfaces: Effects of atmospheric icing conditions and surface roughness. *Appl Surf Sci* **349**, 211–218 (2015).
68. He, Z., Zhuo, Y., Zhang, Z. & He, J. Design of icephobic surfaces by lowering ice adhesion strength: A mini review. *Coatings* **11**, 1343 (2021).
69. Xu, Z. *et al.* Enhanced stability and durability of Cassie-Baxter state in aluminum-based superhydrophobic surfaces fabricated via nanosecond laser ablation. *Journal of Materials Research and Technology* **33**, 7586–7595 (2024).

70. Chen, J. *et al.* Superhydrophobic surfaces cannot reduce ice adhesion. *Appl Phys Lett* **101**, 223 (2012).
71. Kim, W. S., Yun, I. H., Lee, J. J. & Jung, H. T. Evaluation of mechanical interlock effect on adhesion strength of polymer-metal interfaces using micro-patterned surface topography. *Int J Adhes Adhes* **30**, 408–417 (2010).
72. Blackford, J. R., Skouvaklis, G., Purser, M. & Koutsos, V. Friction on ice: stick and slip. *Faraday Discuss* **156**, 243 (2012).
73. Tong, W. *et al.* Direct laser texturing technique for metal surfaces to achieve superhydrophobicity. *Materials Today Physics* **23**, 100651 (2022).
74. Zhang, Y. *et al.* A simple fabrication of liquid-like polydimethylsiloxane coating for resisting ice adhesion. *J Chem Phys* **160**, (2024).
75. Zehui, Z. *et al.* Liquid-like slippery surface with passive-multi active strategy integration for anti-icing/de-icing. *Chemical Engineering Journal* **474**, (2023).
76. Maharjan, S. *et al.* Self-cleaning hydrophobic nanocoating on glass: A scalable manufacturing process. *Mater Chem Phys* **239**, (2020).
77. Lee, M. V., Hussein, G., Sautter, K. & Linford, M. R. Gas Phase Deposition of Trichloro(1H,1H,2H,2H-perfluorooctyl)silane on Silicon Dioxide, by XPS. *Surface Science Spectra* **17**, 87–92 (2010).
78. Luo, Y.-R. *Comprehensive Handbook of Chemical Bond Energies*. (2007).
79. Zhang, B. *et al.* Micro-nano textured superhydrophobic 5083 aluminum alloy as a barrier against marine corrosion and sulfate-reducing bacteria adhesion. *J Taiwan Inst Chem Eng* **97**, 433–440 (2019).
80. Liu, J. *et al.* Super-hydrophobic/icephobic coatings based on silica nanoparticles modified by self-assembled monolayers. *Nanomaterials* **6**, (2016).
81. Montes, L. *et al.* Long-lasting low fluorinated stainless steel hierarchical surfaces for omniphobic, anti-fouling and anti-icing applications. *Surfaces and Interfaces* **46**, (2024).
82. Terriza, A. *et al.* Roughness assessment and wetting behavior of fluorocarbon surfaces. *J Colloid Interface Sci* **376**, 274–282 (2012).
83. Terriza, A. *et al.* C-C4F8 plasmas for the deposition of fluorinated carbon films. *Plasma Processes and Polymers* **11**, 289–299 (2014).
84. Sarkar, P. K. & Kandasubramanian, B. Fluorine-free superhydrophobic characterized coatings: A mini review. *Maritime Technology and Research* **3**, 365–376 (2021).
85. Foorginezhad, S. & Zerafat, M. M. Fabrication of stable fluorine-free superhydrophobic fabrics for anti-adhesion and self-cleaning properties. *Appl Surf Sci* **464**, 458–471 (2019).
86. Ezeorba, T. P. C. *et al.* Emerging eco-friendly technologies for remediation of Per- and poly-fluoroalkyl substances (PFAS) in water and wastewater: A pathway to environmental sustainability. *Chemosphere* **364**, (2024).
87. Liu, H. & Ma, Xiaohui. *Experimental Researches on Micro-Droplet Freezing on a Solid Surface Under Atmospheric Conditions: Part I*. (2008).
88. García, P. *et al.* Passive Ice Protection Systems Lab Scale Testing Methodology. *SAE Technical Papers* (2023).
89. Yamazaki, M., Jemcov, A. & Sakaue, H. A review on the current status of icing physics and mitigation in aviation. *Aerospace* **8**, Preprint (2021).
90. del Moral, J. *et al.* A Holistic Solution to Icing by Acoustic Waves: De-Icing, Active Anti-Icing, Sensing with Piezoelectric Crystals, and Synergy with Thin Film Passive Anti-Icing Solutions. *Adv Funct Mater* **33**, 2209421 (2023).

A.1 Water condensation on core@shell nanostructures monitoring at the nanoscale by STEM and ETEM analysis

To study in a more fundamental point of view the interaction of water vapor with the nanostructured shell of the core@shell nanofibers depending on the wetting behavior, Environmental SEM in STEM¹ (Scanning Transmission Electron Microscopy) mode and ETEM² (Environmental Transmission Electron Microscopy) studies were performed using holey carbon TEM grids as supports where the core@shell nanofibers can be individually characterized. Experiments were conducted at temperatures close to 0 °C and varying the water vapor pressure (from dry conditions at 300 Pa to 900 Pa) to achieve water vapor saturation conditions to promote the condensation on the cold surface. To find differences between hydrophobic and hydrophilic nanostructured surfaces, functionalized core@shell nanofibers collected in the TEM grids were exposed to an “in situ” plasma cleaning for 30 seconds at 6 W power. Therefore, the plasma discharge can hydroxylate the nanostructured TiO₂ shell leading to a hydrophilic state. **Figure A1** presents a sequence of the ESEM in STEM mode and ETEM experiments, comparing the fluorinated (hydrophobic surface), and plasma activated (hydrophilic surface) H₂Pc@TiO₂ nanofibers. As is seen in Figure A1 top a) and b) for STEM mode in ESEM, at high water vapor pressure (900 Pa) and low temperature, water droplets began to condense on the hydrophilic holey carbon grid, but no water condensation signs were detected around the hydrophobic nanofibers. Meanwhile, in Figure A1 bottom d) and e), water droplets were well appreciated around all nanofibers at the beginning of the experiment (600 Pa) giving rise to the formation of water meniscus between hydrophilic nanofibers. At higher resolution analysis by ETEM, at the initial state it was possible to observe a well-defined nanostructure of the TiO₂ shell as external part of the hydrophobic nanofibers with the core filled with organic molecules as appreciated by a darker contrast in Figure A1 c). After 1.73 s at 900 Pa, the organic core suddenly disappeared (isthmus left in the center marked with a yellow arrow) in agreement with a previous study³ whereas the nanostructured TiO₂ shell remained well resolved. From the following snapshot taken at 3.70 s until the last one at 4.60 s, it was clearly visible how the outside porous shell nanostructure was blurring.

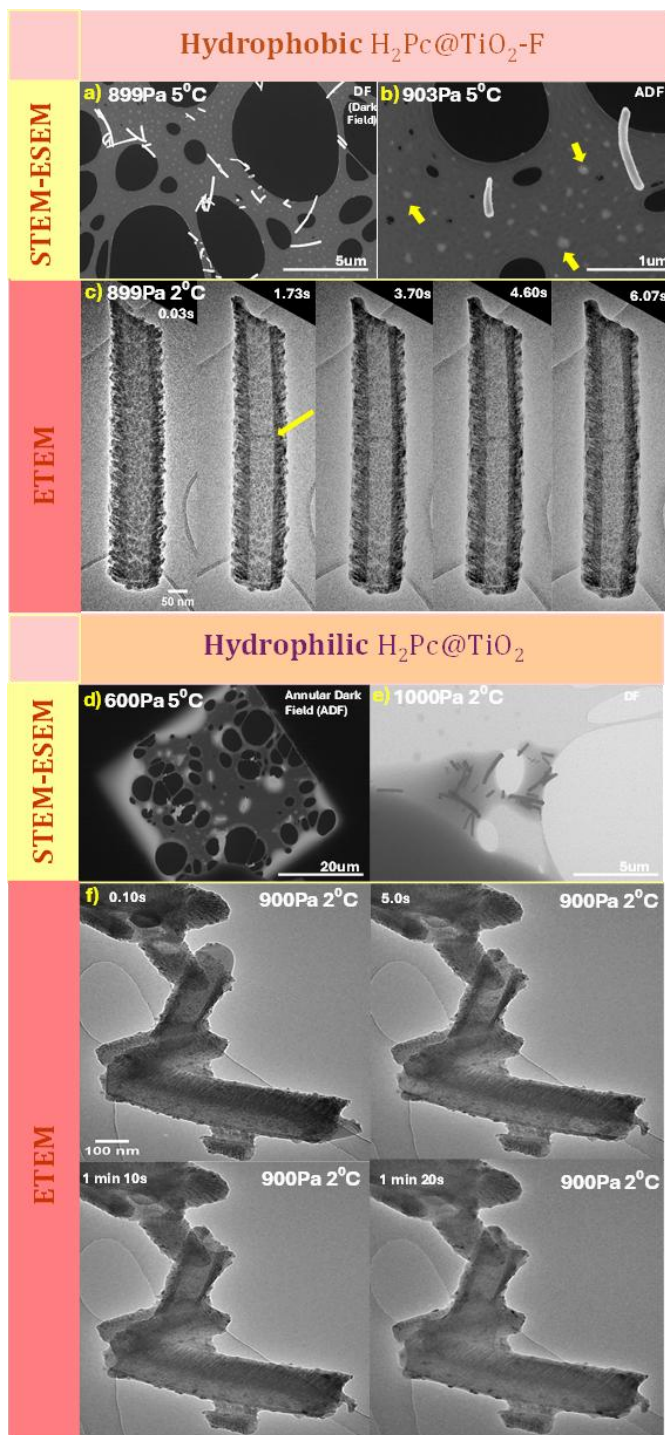


Figure A1. Sequence of STEM-ESEM images in a-b) and d-e) and ETEM images in c) and f) for hydrophilic $H_2Pc@TiO_2$ nanofibers (top) and hydrophobic $H_2Pc@TiO_2-F$ nanofibers (bottom), respectively.

In the absence of testing with empty nanofibers (although there was a clear difference between the darker contrast expected for water compared to a lighter contrast corresponding to the organic material), the hypothesis is that the interface between the nanofiber and the holey carbon grid presented condensed water filling the TiO₂ wall nanopores (blurred and darker contrast) while the core remained empty (even with one end open: the one above the observed nanofiber). On the contrary, the ETEM experiments for hydrophilic nanofibers showed water flooding from the initial state. The presence of water film in the TiO₂ nanostructured walls forming menisci between nanofibers was clearly observed. After 5.00 s, the core also partially disappeared (lighter inner contrast) and after 80 s, water also reached the hole core, facilitating the growth of the water menisci between nanofibers.

In conclusion, when water condensation occurs on the hydrophilic holey carbon grid, it can propagate through capillarity onto the nanofibers. In this scenario, fluorinated molecules serve as barriers to repel water. In contrast, water condensation on hydrophilic nanofibers could easily occur at lower partial pressures, with water molecules condensing at every defect at the nanoscale, including the nanostructured shell and the empty core.

It is important to note that during the ETEM process, the inner core was affected due to the combination of a high-voltage electron beam (300 kV) and the presence of water vapor. However, it was preserved inside the core@shell nanofiber operating at lower magnification (30 kV) in ESEM. Therefore, it is presumed that the surface functionalization with fluorinated molecules could be compromised during the ETEM experiment although for analysis prolonged for an hour, evident differences between the hydrophobic and hydrophilic core@shell interaction with water could be detected.

1. Masenelli-Varlot, K. *et al.* Wet-STEM tomography: Principles, potentialities and limitations. *Microscopy and Microanalysis* **20**, 366–375 (2014).
2. Jinschek, J. R. Advances in the environmental transmission electron microscope (ETEM) for nanoscale in situ studies of gas–solid interactions. *Chem. Commun.* **50**, 2696–2706 (2014).
3. Filippin, A. N. *et al.* Self-Assembly of the Nonplanar Fe(III) Phthalocyanine Small-Molecule: Unraveling the Impact on the Magnetic Properties of Organic Nanowires. *Chemistry of Materials* **30**, 879–887 (2018).

7

General conclusions and future perspectives

7.1 General conclusions

In this thesis, advanced methodologies have been developed to fabricate multifunctional hierarchical surfaces with multiscale roughness, employing the combination of laser treatments or porous substrates, supported nanomaterial deposition by vacuum and plasma techniques and surface chemical modification of low fluorine content. These surfaces, designed following biomimetic principles, exhibit outstanding control of the wetting properties, and, particularly related to repellence as superhydrophobicity, omniphobicity, self-cleaning, anti-fouling, anti-fogging and anti-icing responses.

A central focus has been the controlled fabrication of surface structures in the micro- and nano- scales by three main strategies: supported 1D core@shell nanostructures, and oriented porous nanocolumnar thin films by plasma assisted vacuum approaches, and surface patterning by laser treatments. These methodologies allow a precise control over the final wetting properties. Multiscale roughness configurations have been combined with surface chemical modification in pursuit of the ecofriendly requirements based on the merging of PDMS thin films with low fluorinated terminations, compatible with any kind of substrate material and geometry, from flexible porous cellulose membranes and SS filters to transparent glass plates and aeronautical alloys plates and semicylinders. The hybrid hierarchical surfaces were tailored to diverse operational contexts, from harsh environment conditions to active de-icing demonstrators to prove their reliability, stability and durability.

The most notable results include:

- ❖ **Controlled wettability:** tuning from hydrophilicity to superhydrophobicity and omniphobicity, permanent even under severe environmental conditions.
- ❖ **Anti-icing capability:** surfaces exhibit repellent properties that delay ice formation, reduce ice accretion, and provides lower energy consumption in active de-icing systems.
- ❖ **Durability and stability:** functional properties were preserved after corrosion tests, rain erosion aging, solvent immersion, UV radiation, thermal cycling, and ice particle / supercooled water droplet impact in

icing wind tunnel experiments, confirming their potential for industrial applications.

- ❖ **Processing versatility:** the employment of dry, clean, and efficient deposition by vacuum and plasma techniques supported by laser treatments enabled work with a wide variety of materials and complex geometries, demonstrating scalability and adaptability to specific requirements.

A summary about the specific conclusions for each chapter is listed below:

CHAPTER 3

3.1 This work presents the innovative combination of the soft-template method by vacuum and plasma techniques, enabling the synthesis of supported 1D core@shell nanowires and nanofibers. The integration of plasma-enhanced chemical vapor deposition (PECVD) at room temperature for the formation of metal oxides seeds and decoration with nanostructured shells, especially amorphous TiO₂, proves to be effective for controlling surface roughness at micro- and nano- scales devoted to generation of hierarchical porous structures from π -conjugated organic nanowires templates. This method is adaptable for diverse substrates, including metal grids and cellulose filters.

3.2 The 1D supported nanofibers exhibit a unique cauliflower-like topography that contributes to a triple scaled roughness when combined with porous substrates, raising a superhydrophobic behaviour. This is particularly effective for separating polar and non-polar liquids and a self-cleaning capability. The surface modification with low surface free energy materials, particularly a thin PDMS coating and fluorinated molecules termination, also assisted by plasma pre-activation, ensures a firm omniphobic state without occlusion of the membrane pores, and stable even under UV exposition.

3.3 The hybrid nanomembranes demonstrate significant potential in microfluids, particularly for controlling droplets movement, and oil/water separation. The TiO₂ photoactivity can be used to promote a selective wetting to be employed for potential applications such as on-demand liquid release and efficient droplet manipulation in biomedical devices.

CHAPTER 4

4.1 This study demonstrates the successful creation of hierarchical stainless steel (SS) surfaces using a combination of laser treatment and oblique angle evaporation for porous oriented nanocolumnar thin film deposition. The method yields nanostructures of similar composition to the bare substrate, what ensures the compatibility and good adhesion, with varying porosity levels to be available for allocating functional agents, particularly the integration of different low fluorinated strategies at the nanoscale.

4.2 It has been shown that reducing fluorine surface content is effective to achieve enhanced surface wetting related properties, such as superhydrophobic, omniphobicity, self-cleaning, anti-fouling, and anti-icing. Specifically, the grafting of PFOTES molecules onto the hierarchical SS surface is revealed as the best repellent performance compared to the fluorinated coating, and SLIPS approaches.

4.3 Low fluorination process lets to preserve or even enhance the corrosion resistance of the SS hierarchical surface, which in principle could have been counterproductive due to the high concentration of topographic defects available to be attacked by corrosive agents. Thus, the fluorinated grafted hierarchical SS surface exhibit a remarkable resistance to pitting corrosion while its superhydrophobicity is maintained even after the corrosion test. These findings suggest that the combination of micro- and nano-structuring and low fluorination of stainless steel offers substantial benefits such as long-term protection in corrosive and abrasive environments with industrial interest.

CHAPTER 5

5.1 The research demonstrates how bioinspired mild laser technology, specifically femtosecond laser treatment, on transparent substrates can control the structuring of surfaces to achieve repellent properties while maintaining transparency. By tuning laser treatment parameters, particularly the distance between laser-generated grooves and the number of laser repetitions in two different laser patterns: parallel lines and asymmetric square micropillars,

structured surfaces at the micro- and nano- scales can be obtained without compromising the optical properties of the transparent borosilicate glass.

5.2 Since the borosilicate glass, despite its low thermal expansion coefficient and resistance to thermal shock ideally suitable for anti-icing applications, is hydrophilic even after laser treatment, its surface requires a low fluorinated functionalization by chemical grafting to reach a superhydrophobic behaviour. This functionalization combined with the micro-structured patterning resulted in additional properties, such as anti-fouling, anti-fogging, and anti-icing, thereby enhancing the versatility of the transparent treated substrates.

5.3 The best performance conditions included 5 laser pattern repetitions and groove distances between 50 and 100 μm to get the highest water contact angle value, improved anti-fouling response, and longer freezing delay times. Furthermore, square micropillar patterned surface exhibit better wettability-derived functionalities compared to the line patterned one, although the latter allows for the anisotropic movement of droplets, positively impacting the anti-fouling capacity.

CHAPTER 6

6.1 Hierarchical surfaces, which combine multiple roughness levels ranging from supported 1D core@shell nanofibers to microstructured surfaces by vacuum and plasma techniques supported with soft laser treatments, guarantee compatibility with substrates of medium size and complex geometries, such as aluminum aeronautical alloy plates and semicylinders. By selecting the appropriate π -conjugated organic precursor for the growth of nanofibers, the surface aspect ratio and processing temperature can be controlled, allowing the development of hierarchical surfaces of outstanding repellent properties on sensitive and flexible substrates, like polymers.

6.2 The developed triple-level roughness surfaces present both hydrophobic and oleophobic responses, which were further enhanced to omniphobicity through the exploited surface modification with thin PDMS coating and fluorinated

molecules grafting. Consequently, the hybrid hierarchical surfaces have excellent anti-fouling properties against bovine serum, alginic acid and humic acid.

6.3 It has been found that the higher PDMS embedding that promotes the low surface aspect ratio hierarchical surface together with the fluorine-based termination induces a stable superhydrophobicity under low-temperature evaporation tests, and longer delay of water condensation in a supersaturated humid and low temperature environment, what confirms the obtention of a permanent Cassie-Baxter state with anti-fogging activity.

6.4 The hybrid hierarchical surfaces possess excellent anti-icing properties, as demonstrated by long freezing delay times, and low ice accretion in severe windy, humid and cold conditions, produced in a heterogeneous way checked in Icing Wind Tunnel facility, what indicates the robust superhydrophobic behaviour of the developed surface. Meanwhile the anti-adhesion to ice performance is promising, it does not yet meet the standards due to the impossibility of avoiding mechanical interlocking in the exposed nanostructure. The surface's ability to remain in a Cassie-Baxter state under challenging weather conditions highlights its potential in aerospace applications.

6.5 Durability and long-term stability of the hybrid hierarchical surfaces is accordingly confirmed since maintaining the superhydrophobic and omniphobic characteristics after exposition to harsh environments and interaction with aggressive agents.

6.6 Additionally, the integration of the hybrid hierarchical surfaces into de-icing active systems, particularly an electrothermal heating mechanism, and an assisted acoustic wave piezoelectric device, implies significant protective action and energy consumed reduction, offering an efficient solution for ice prevention and de-icing in aeronautical applications, and potentially transferred to other ones.

7.2 Future perspectives

Given the current climatic conditions we are facing and the urgent need to address or find short-term solutions to the associated challenges, it is essential to develop scalable, high-performance methods that are environmentally friendly and energetically efficient, making the most of possibilities offered by the nanotechnology and surface engineering worlds. The modification of surfaces to control the wetting behaviour can be achieved through invasive techniques that create micrometric roughness or non-invasive deposition methods that preserve the material's integrity and adopt to various substrates. In the context of this thesis, the proposed approaches to keep repellent surfaces working at low-temperature calls to explore its scalability on other substrates and geometries, accessible thanks to the advances in laser technology and plasma and vacuum techniques to be compatible with flexible and soft materials. Furthermore, the processing optimization could take advantage of new artificial intelligence routines to design the parametrization of new hierarchical structures.

Particularly, addressing the challenges of roughness hierarchy generation for repellent and anti-icing purposes, involves the need to adapt laser treatments conditions (wavelength and pulse duration) and the design of supported nanostructures by vacuum and plasma methodologies that ensure a conformal coverage devoted to enhancing the ice anti-adhesion properties. Besides from the point of view of surface modification to count with hybrid hierarchical surfaces, other solutions to the interlocking mechanism can be explored with liquid-like material coatings.

From the perspective of surface chemical termination, it is advisable to adopt fluorine-free approaches. These include using low surface free energy materials like silicone-based or wax-based coatings and exploring chemical anchoring with shorter fluorine chains, that also could be supported by artificial intelligence tools intended for finding new stoichiometries and chemical design to get effective low surface free energy combinations.

Moreover, the development of gradient materials, both for the chemistry and the topography configurations, inspired in the *Janus* approach, allows the conjunction of -fobic and -filic wetting behavior on the same surface, which would provide responses to the interaction with the environment or other agents depending on the location. At the very least, this would ensure the best

adhesion and adaptability of the generated surface to any substrate while maintaining external repellence or could be applied to direct with high precision the interaction with fluids. From a fundamental point of view, advanced analysis by wet-STEM and ETEM facilities on empty and stable repellent nanostructures will shed light on the understanding of how water-porous surface interaction occurs at low temperatures at the nanoscale.

Finally, the integration of the hybrid hierarchical passive surfaces as protective element into de-icing systems could be optimized, helped by the artificial intelligence assistance and even extrapolated to other external activation devices. This includes testing other scalable substrate geometries and different electrothermal and acoustic waves transmission configurations, evaluating performance at low temperatures and humid conditions and incorporating the interaction of contaminants and fouling agents to the icing processes for a better simulation of the real outdoor application environment.

Laura Montes Montañez

Ph.D. thesis